

Biophysical Studies of *de-novo* Designed Antimicrobial peptides: Correlation with Biological membranes

Thesis Submitted for the Degree of

Doctor of Philosophy (Science)

of

Jadavpur University



By

Sk Abdul Mohid

Department of Biophysics

Bose Institute

Kolkata – 700091

India

बसु विज्ञान मंदिर
BOSE INSTITUTE



(विज्ञान एवं प्रौद्योगिकी विभाग, भारत सरकार के एक स्वायत्त संस्था)
(An Autonomous Institute of Department of Science & Technology, Govt. of India)

मुख्य कैंपस Main Campus :

93/1, आचार्य प्रफुल्ल चंद्र रोड़, कोलकाता - 700 009
93/1, Acharya Prafulla Chandra Road, Kolkata - 700 009
ग्राम/Gram: Bostute, फोन/Phone: 2350-7073 (निदेशक/Director)
इपीएबीएक्स/EPABX : 2350-6619/6702/2402/2403, 2303-0000/1111
फैक्स/Fax : 91-33-2350-6790

शतवार्षिकी भवन Centenary Building :


पी-1/12, सी.आई.टी. स्कीम-VII-एम, कोलकाता - 700 054
P-1 / 12, C.I.T. Scheme VII-M, Kolkata - 700 054
फोन/Phone: 2355-7434(निदेशक/Director), 2355-0595(रजिस्ट्रार/Registrar)
इपीएबीएक्स/EPABX : 2355-9416/9219/9544, 2569-3271, फैक्स/Fax : 91-33-2355-3886

संदर्भ सं. / Ref. No. _____

दिनांक / Date :

CERTIFICATE FROM THE SUPERVISOR

This is to certify that the thesis entitled “Biophysical Studies of de-novo Designed Antimicrobial peptides: Correlation with Biological membranes” submitted by Sri Sk Abdul Mohid who got his name registered on 16th September 2019, For the award of Ph. D. (Science) degree of Jadavpur University, is absolutely based upon his own work under the supervision of Prof. Anirban Bhunia, Department of Biophysics, Bose Institute Unified Academic Campus, Kolkata - 700091 and that neither this thesis nor any part of it has been submitted for either any degree / diploma or any other academic award anywhere before.

 21/7/2022

.....
DR. ANIRBAN BHUNIA
Professor
Dept. of Biophysics
BOSE INSTITUTE
Kolkata, India
.....

(Signature of the Supervisor with date and official seal)

∞ Dedication ∞

*To My Beloved Parents and
Morseda, Teachers, Well Wishers and
The Curious Minds Who Want to
Unveil the Unknowns*

∞ Acknowledgements ∞

This thesis, titled "Biophysical Studies of de-novo Designed Antimicrobial Peptides: Correlation with Biological Membranes," is the most important scientific achievement of my life, and it would not have been possible without the tremendous contributions and support of a great number of individuals. It has always been tough for me to convey my thanks to those who deserve it because I am not a particularly vocal person. As a result, I want to use this occasion to convey my heartfelt gratitude to everyone who has assisted me in finishing this fascinating Ph.D. journey.

Being the first member from a family where nobody pursued higher studies in science and specially a Ph.D., I had no clue what I was getting myself into when I declared my intention to pursue a Ph.D. It has been a long trip since then, and it has changed me a lot as a person. I have learned many valuable life lessons. There were times when I felt dejected, lost patience, and had writer's block during my Ph.D. tenure. In the end, I learnt that it is hard to fail but it is worse never to have tried to succeed.

*I would like to start with expressing my deepest thanks to my Ph.D. supervisor **Prof. Anirban Bhunia**, Chairman of Biophysics Department, Bose Institute Unified Campus, Kolkata. During past 7 years of being part of his lab (first as the M.Sc. dissertation student and then as a Ph.D. scholar), I have got the opportunity to learn from him, the true meanings of dedication, attentiveness, enthusiasm, patience and pursuance toward science. From giving the sovereignty of crucial thinking and constant guidance through the experimental sessions to shaping my writing and presentation skills, he has always been a great support. It was a delight to acquire the profound life lessons that he has easily imparted throughout the years, in addition to his scientific temperament. Maintaining a*

healthy work-life balance, remaining cool and composed in the face of adversity, and being polite and modest are just a few examples. I feel myself extremely privileged to be a member of his lab. I owe him a debt of gratitude for allowing me sufficient academic independence in my studies. The completion of this thesis was made possible by his vision and direction during my tenure.

I am especially grateful to **Prof. Uday Bandyopadhyay** for awarding me an institutional Ph.D. fellowship, a travel grant to attend the International Conference on "Innovative Approaches in Applied Sciences and Technologies" in Singapore, and an extended fellowship for an extra six months. My sincere thanks go to **Prof. Gautam Basu**, ex-chairman of the Department of Biophysics and also my teacher during my Masters. His unique style has always contributed to breaking up the routine of daily study life while simultaneously leading and instructing.

I am also grateful to **Prof. Kaushik Biswas** (Division of Molecular Medicine, Bose Institute), **Prof. Anup Kumar Mishra** (Chairman of Division of Molecular Medicine, Bose Institute), **Professor Achintya Singha** (Department of Physics, Bose Institute) and their scholars **Abhisek Sarkar**, **Arin Gucchait** and, **Sreyan Raha** respectively, for their collaboration and support to finish my research works. My PhD work is the result of a variety of collaborative assistance and advice. In this regard, I would like to express my gratitude to **Professor DongKuk Lee** (Department of Fine Chemistry, Seoul national University of Science and Technology, Seoul, South Korea) and his students **TaeJun Won**, **MinSook Kim**, **JiHey Choi** and **HaSun**. I have gathered my first hands-on-training in solid-state NMR and several sweet memories during my short visit in his lab. Working with him and his students was an enriching and learning experience. I would also like to thank **Dr. Anupam Midya** (School of Nanoscience and Nanotechnology, IIT Kharagpur, India) and his student **Dr. Arup Ghorai** for their valuable

collaborations. They first introduced me to the fascinating world of nanotechnology. A special thanks to **Dr. Arup Ghorai (Arup Da)** for all the arrangements (lodging and meals) he had done during my every visit to IIT Kharagpur Campus. Another special thanks go to **Dr. Soumya De**, (School of Bio Science, IIT Kharagpur) and his students **Dr. Aditya Jyoti Basak**, **Dr. Snigdha Maiti** and **Mr. Soumendu Boral** for their assistance and help in accessing the 600 MHz NMR and hostel facility in the IIT Kharagpur Campus. I want to express my gratitude to **Dr. Sanhita Roy** (L V Prasad Eye Institute, India) and her students for rescuing me by collaborating with us with her in-vivo experiment facilities. I am grateful to **Prof. Nikhil R. Jana** and his student **Dr. Haydar Ali** (Centre for Advanced Materials, IACS) for helping me with DLS data acquisition. I will also extend my gratitude to **Dr. Jayanta Mukhopadhyay** and his student **Dr. Arkajyoti Dutta** (Department of Chemistry, Bose Institute) for helping me perform specific molecular biology experiments in his lab. I want to express my gratitude to **Dr. Viji Sarojini** (University of Auckland, New Zealand), **Prof. Rajamani Lakshminarayan** (Singapore Eye Research Institute, Singapore), **Dr. Debarun Dutta** (Aston University, UK), **Dr. Nirakar Sahoo** (UTRGV, USA), **Prof. Charles G. Cranfield** (UoT, Sydney, AU), **Prof. Dr. Bernd Reif** (TUM, Germany), **Prof. Dr. Samit K. Ray** (SNBNCBS, Kolkata), and **Prof. Enrico Leipold** for their valuable collaborations, suggestions and, guidance during my PhD tenure.

I began my studies at the Bose Institute in 2014 as an integrated MSc-PhD student. For the past eight years, I have spent most of my time in this institute. This institute is connected with so many memories and learning experiences for me. I am immensely thankful to all of the scientists who educated us and enabled us to work in their laboratories to study or perform my research experiments.

I am grateful to everyone at the Central Instrument Facilities and the Bose Institute Library, especially Rina di, Barun da (NMR), Soumya da (NMR), Swapan

Da (NMR and Liquid Nitrogen), Tanmoy da (Peptide Synthesis and HPLC), Swaroop da (HPLC, Fluorescence, and CD Spectroscopy), Mrinal da (DNA Sequencing), Smriti da (FPLC), Ranjan Da (Millipore water and FACS), Narayan da (Autoclaving), Prabir da, Gaurav Da, Mrityunjay Da (Department of Chemistry), and Tanima di (SEM imaging). I'd also want to thank and express my appreciation to Dibakar da, Suman da, Ganesh da, Pranab da, Gouranga da, Behera da, and all the other support workers. All of these folks have been really helpful to me since I began as a student at Bose Institute. Their assistance in obtaining this doctorate degree is unparalleled.

I will always be grateful to my professors in Bachelor who taught me how to become a good thinker and researcher. I would like to thank **Prof. Swapan Bhattacharyya**, **Dr. Soma Pal Saha**, **Dr. Rini Roy**, **Dr. Samudra P. Banik**, **Dr. Suchitra Sarkar** and **Dr. Bikash Kundu** for their guidance and encouragement. A special thank goes to **Dr. Amitava Ghorai**, Associate professor of Physics Department, Maulana Azad College, Kolkata, for his assistance and guidance in completing my first scientific project and my first publication in a scientific journal. Last but not the least, I would like to mention the name of **Dr. Subhamoy Das**, Associate Professor of Mahishadal Raj College, Midnapore, who coloured my dreams to become a scientist one day. I am greatly thankful for his continuous inspiration and motivational talks when I was a school student.

I gratefully acknowledge the generous help and support of my past & present lab members. I would like to thank my seniors **Dr. Anirban Ghosh**, **Dr. Rajiv Kumar Kar**, **Dr. Aritreyee Dutta**, **Dr. Bhisma Narayan Ratha**, and **Dr. Swapna Bera** for their guidance, support, motivations and all the scientific discussions that we had during their tenure. I am also thankful to my present lab mates, **Ms. Dipita Bhattacharyya**, **Ms. Shruti Mukherjee**, **Mr. Dibakar Sarkar**, **Mr. Ranit Pariary**, **Ms. Dipanwita Roy**, and **Ms. Karishma Biswas**. They are like

my brothers and sisters and, I am fortunate to have them who always bring fresh air to the day-to-day boredom of life. Their continuous help and support made the hardship of PhD journey more comfortable. We have a lot of shared memories, both good and unpleasant. In these six and half years, I have learnt something new from every one of them, and I'm grateful to have discovered people who have gone above and beyond to assist me. I also want to thank my trainees, **Nabarupa, Debottam, Teresa and Aishi**, for joining me on this adventure and giving me the chance to learn new things while being of service to them. I would like to especially mention Dipita, Shruti, Madhura, and Monalisa for all the good memories, beyond the lab discussions and continuous moral supports during all these years. A special note of thanks goes to **Dr. Humaira Ilyas** who was my lab mate cum best friend and a strong pillar of support from my college days to PhD journey. I will always be thankful to her for all the scientific discussions, troubleshooting during any experiments and the funs that we had together in and outside of our lab. It is really difficult for me to put into words how I truly feel about my friends and about everyone else who has supported me through my darkest moments. I'm delighted to reiterate their warmest sympathies at this very moment.

Whatever I am and what I hope to be in the future are the result of the unwavering support and encouragement I have gotten from my parents (**Sk Abdus Sadek** and **Tahura Bibi**) and my life partner (**Morseda Khatun**). Their gracious collaboration aided me in completing my Ph. D. studies, and no words can adequately express my gratitude.

Sk Abdul Mohid

July, 2022

Kolkata, WB

List of Abbreviations

- ALS: asymmetric least squares
- AMP: Antimicrobial Peptide
- CD: Circular Dichroism
- CFU: Colony Forming Unit
- CHAPSO: 3-[(3-cholamidopropyl)dimethylammonio]-2-hydroxy-1-propanesulfonic acid
- CHL: Cholesterol
- CMC: Critical Micelle Concentration
- CSP: Chemical Shift Perturbation
- D₂O: Deuterium oxide
- D8PG: Dioctanoyl Phosphatidylglycerol
- DLS: Dynamic Light Scattering
- DMF: Dimethyl Formamide
- DMSO: Dimethyl Sulfoxide
- DOPC: 1,2-Dioleoyl-sn-glycero-3-phosphocholine
- DOPE: 1,2-dioleoyl-sn-glycero-3-phospho ethanolamine
- DOPG: 1, 2-dioleoyl-sn-glycero-3-phospho-(1'-racglycerol)
- DPC: Dodecyl Phosphocholine
- DIPEA: N, N-Diisopropylethylamine
- ERG: Ergosterol
- GUV: Giant unilamellar vesicle
- HCEC: Human corneal epithelial cells
- HDP: Host Defense Peptides
- hERG: hydrogenated ergosterol
- HPLC: High Performance Liquid Chromatography
- HSQC: Heteronuclear Single Quantum Coherence
- ILE-6: Interleukin 6
- IL-1 β : Interleukin 1 β
- ITC: Isothermal titration calorimetry
- LA: Luria Agar
- LB broth: Luria-Bertani broth
- LPS: Lipopolysaccharide
- LUV: Large Unilamellar Vesicles
- MD: Molecular Dynamics
- MDR: Multidrug Resistance
- MIC: Minimal Inhibitory Concentration
- MIC_{99%}: Minimal inhibitory concentration for 99% killing
- MTT: Methylthiazolyldiphenyl-tetrazolium
- NB: Nutrient Broth
- NMR: Nuclear Magnetic Resonance
- NOE: Nuclear Overhauser Effect
- NOESY: Nuclear Overhauser Effect Spectroscopy
- NPN: N-Phenyl-1-naphthylamine
- O.D.: Optical Density
- OM: Outer Membrane
- PBS: Phosphate Buffer Saline

- PDI: Polydispersity Index
- PI: Propidium Iodide
- POPE: 1-palmitoyl-2-oleoyl-sn-glycero-3- phosphoethanolamine
- POPG: 1-palmitoyl-2-oleoyl-sn-glycero-3- phospho-(1'-rac-glycerol)
- PRE: Paramagnetic Relaxation Enhancement
- RMSD: Root Mean Square Deviation
- ROS: Reactive oxygen species
- RP-HPLC: Reverse Phase High Performance Liquid Chromatography
- SDS: Sodium Dodecyl Sulfate
- SEM: Scanning Electron Microscopy
- STD: Saturation Transfer Difference
- TEM: Transmission Electron Microscopy
- TFA: Trifluoroacetic Acid
- TOCSY: Total Correlation Spectroscopy
- *tr*NOESY: *transferred* Nuclear Overhauser Effect Spectroscopy
- TSP: 3-Trimethylsilyl propionic-2, 2, 3, 3-d4 acid
- $\mu\text{M}/\text{mM}$: Micro/ Millimolar
- 1D/2D: One/Two Dimensional
- Å: Angstrom

Abstract

Title: Biophysical Studies of *de-novo* Designed Antimicrobial peptides: Correlation with Biological membranes

Index no.- 93/19/Life Sc./26

The fast rise in drug-resistant infections has posed a significant challenge to antimicrobial treatments. The need for new antibiotics has driven researchers to find new ways to combat pathogenic microorganism, resulting in a boom of research focusing on antimicrobial peptides (AMPs) and their therapeutic potential. While these AMPs have a few basic characteristics and structural motifs, their sequences, activity, and targets differ significantly. AMPs, in fact, are less vulnerable to bacterial resistance than standard antibiotics. These diverse functions have sparked tremendous interest in research aimed at understanding AMP activity, and various protocols have been described to assess different aspects of AMP function, such as screening and evaluating the activities of natural and synthetic AMPs, measuring interactions with membranes, optimizing peptide function, and delivering the AMPs to their target sites. NMR spectroscopy has revealed a strong association between the structure and biological properties of distinct classes of AMPs, which is being used to build novel peptide-based antibiotics. In addition to its ability to offer high-resolution structures, NMR is particularly effective in investigating dynamics, opening the door to understanding the mechanism of complicated *in situ* physiological processes. Despite substantial development over the last decade, notably in AMP optimization, their routes of action, particularly *in vivo* as well as drug delivery, remain unknown because the peptides either undergo enzymatic destruction or exhibit high toxicity towards the host cells.

In this context, the objectives of this work are divided into six chapters. (I) The first chapter covers the brief introduction of the AMPs and its therapeutic potentials in combination with nanoparticles. (II) The second chapter is focused on the structure-activity relationship (SAR) of the AMPs derived from the human autophagy 16 (Atg16) polypeptide (K5). This study looked at the influence of various N-terminal fatty acids on the activity of a truncated counterpart of human Atg16. To further test and validate the peptide's potential to enter into and interact with the bacterial membrane, an analogue with the best therapeutic index (K30) was chosen for in-depth biophysical experiments. Following that, numerous biophysical approaches are used to study the impact of newly created N-trifluoroacetyl lysine and N-thioacetyl lysine peptides (KP 13, KP 15, and KP 24) and their cell-penetrating peptide conjugates as inhibitors of bacterial sirtuins. The conjugated peptides were efficiently absorbed and shown bacterial transcription inhibition, resulting in increased antibacterial effectiveness against Gram-negative and Gram-positive pathogens. (III) The subsequent studies focused on the fungal membrane specificity and interaction of VG16KRKP, a broad spectrum, nontoxic and non-hemolytic AMP derived from dengue virus fusion protein. Generation of mutant analogues and the high-resolution NMR studies revealed that the wild type peptide solely interacts with the membranes that contains ergosterol as major sterol component along with phosphatidylethanolamine (PE) as lipid moiety. (IV-V) In order to generate more potent AMPs with anti-pseudomonas activity, a bacterial lipopolysaccharide binding "KNKSR motif" was introduced in a shorter analog of VG16KRKP either at N- or C-terminal to generate KG18 and VR18 peptides, respectively. These two peptides showed excellent antifungal as well as antipseudomonal activity while keeping the low cytotoxicity and hemolytic profile. The VR18 peptide showed spectacular activity against invasive *Pseudomonas* strains in both *ex-vivo* and *in vivo* set up which led this peptide a suitable candidate to be used as a potent anti-keratitis agent in future. Additionally, both the peptides showed higher efficiency in combination with tungsten disulfide quantum dots (WS₂-QD) nanoparticles. The structure-function relationship of QD conjugates was further analyzed by low-resolution spectroscopic techniques and high-resolution NMR methods. (VI) Lastly, the innate immune system's ubiquitous antimicrobial enzyme lysozyme exhibits hereditary autosomal dominant amyloidosis, which causes multi-organ dysfunction. Designing of small synthetic molecules called HK compounds showed great efficacy to inhibit the aggregation propensity of lysozyme as revealed by NMR and biophysical techniques. This study paves the way to generate new anti-amyloidosis drugs to treat neurodegenerative disorders like Alzheimer's or Parkinson's disease in future.

Sk. Abdul Mohid. 25/07/2022

(Sk Abdul Mohid)

ABlie 21/7/22

(Sign of the Supervisor with Seal and Date)

DR. ANIRBAN BHUNIA
Professor
Dept. of Biophysics
BOSE INSTITUTE
Kolkata, India

Preface

The entitled thesis “**Biophysical Studies of *de-novo* Designed Antimicrobial peptides: Correlation with Biological membranes**” intended to be submitted by the investigator, **Sk Abdul Mohid**, under the supervision of **Prof. Anirban Bhunia**, in the Department of Biophysics, Bose Institute Unified Campus, Kolkata-700091, India, for the Ph.D. (Sc.) degree in the Jadavpur University, is summarized below.

CHAPTER I

Chapter I is a review of the literature and covers a brief introduction of the antimicrobial peptides (AMPs), nanoparticles and combination of these two distinct molecules in order to get potent and novel therapeutic agents to fight drug resistance pathogens as well as to develop new diagnostic tools. This chapter also explains about the background behind the work done in this thesis.

Parts of this chapter has been adapted from the following publications:

(A) **Mohid, S.A.** and Bhunia, A., **2020**. Combining antimicrobial peptides with nanotechnology: an emerging field in theranostics. *Current Protein and Peptide Science*, 21(4), pp.413-428. And, (B) Bhattacharjya, S., **Mohid, S.A.** and Bhunia, A., **2022**. Atomic-Resolution Structures and Mode of Action of Clinically Relevant Antimicrobial Peptides. *International Journal of Molecular Sciences*, 23(9), p.4558.)

CHAPTER II

Chapter II describes the biophysical analysis of two types of antimicrobial peptides curated from natural origins like the human autophagy 16 polypeptide and the substrate-mimic of sirtuins, a Histone deacetylase (HDAC) that regulates metabolic balance, genomic integrity and longevity and are highly conserved among various forms of life.

Firstly, the human autophagy 16 polypeptide has been used to create a synthetic antimicrobial peptide library. Acetylated peptides with varied chain length lipids produced peptides with higher potency than the original Atg16. The most powerful antibacterial, with low hemolysis, was a 21-residue fragment of Atg16 linked to 4-methylhexanoic acid (K30). Several investigations, including microscopy, dye leakage, and isothermal titration calorimetry (ITC), were carried out to acquire insight into the peptide's antibacterial mode of action. The peptide's selectivity towards bacterial cell membranes was further demonstrated using dye leakage experiments. ITC studies demonstrated that the peptide's binding interaction with D8PG micelles was exothermic. The three-dimensional solution NMR structure of K30 in association with Dioctanoyl phosphatidylglycerol (D8PG) micelles indicated that the presence of anionic membrane lipids, imitating bacterial

membranes, the peptide K30 adopts a helical hairpin or helix-loop-helix shape structure. The position of the peptide in the bound state was decoded by intermolecular NOEs between the peptide and lipid, which was further validated by the paramagnetic relaxation enhancement (PRE) NMR experiment. These findings reveal the structure-function interaction of the peptide in the bacterial membrane as a whole.

The substrate of sirtuins (a Histone deacetylase (HDAC) that regulates metabolic balance) was used as a template for another *de novo* created peptide library. Substrate-based sirtuin inhibitors target the bacterial genome and RNA, and if cellular internalization can be accomplished, they might be a potential way to combat bacterial resistance. N-trifluoroacetyl lysine and N-thioacetyl lysine peptides (KP 13, KP 15, and KP 24) as inhibitors of bacterial sirtuins and their cell-penetrating peptide conjugates Tat KP 13, Tat KP 15, and Tat KP 24 were developed in this area. Internalization of the conjugated peptides was effective, and evidence of bacterial transcription suppression were seen, leading in increased antibacterial activity against Gram-negative and Gram-positive pathogens. Calcein dye leakage analysis established the selectivity of these peptides to bacterial membranes. This study documents the first report of the application of substrate-based sirtuin inhibitors as antimicrobial therapeutics.

This chapter has been adapted from the following publications:

(A) Varnava, K.G., **Mohid, S.A.**, Calligari, P., Stella, L., Reynison, J., Bhunia, A. and Sarojini, V., **2019**. Design, synthesis, antibacterial potential, and structural characterization of N-acylated derivatives of the human autophagy 16 polypeptide. *Bioconjugate chemistry*, 30(7), pp.1998-2010. and (B) Patel, K.D., **Mohid, S.A.**, Dutta, A., Arichthota, S., Bhunia, A., Haldar, D. and Sarojini, V., **2021**. Synthesis and antibacterial study of cell-penetrating peptide conjugated trifluoroacetyl and thioacetyl lysine modified peptides. *European Journal of Medicinal Chemistry*, 219, p.113447.

CHAPTER III

The treatment of invasive drug-resistant and potentially life-threatening fungal infections is limited to few therapeutic options that are usually associated with severe side effects. The development of new effective antimycotics with a more tolerable side effect profile is therefore of utmost clinical importance. Chapter III describes a combination of complementary *in vitro* assays and structural analytical methods to analyze the interaction of the *de novo* antimicrobial peptide VG16KRKP with the sterol moieties of biological cell membranes. It has been demonstrated that VG16KRKP disturbs the structural integrity of fungal membranes both *in-vitro* and in model membrane system containing ergosterol along with phosphatidylethanolamine lipid and exhibits broad-spectrum antifungal activity. As revealed by systematic structure-function analysis of mutated VG16KRKP analogues, a specific pattern of basic and hydrophobic amino acid side chains

in the primary peptide sequence determines the selectivity VG16KRKP for fungal specific membranes.

This chapter has been adapted from the following publication:

(This chapter has been adapted from the following publication: **Mohid, S.A.**, Biswas, K., Won, T., Mallela, L.S., Gucchait, A., Butzke, L., Sarkar, R., Barkham, T., Reif, B., Leipold, E. and Roy, S., 2022. Structural insights into the interaction of antifungal peptides and ergosterol containing fungal membrane. *Biochimica et Biophysica Acta (BBA)-Biomembranes*, p.183996.)

CHAPTER IV

Contact lens wearers are at an increased risk of developing *Pseudomonas*-associated corneal keratitis, which can lead to a host of serious ocular complications. Despite the use of topical antibiotics, ocular infections remain a major clinical problem, and a strategy to avoid *Pseudomonas*-associated microbial keratitis is urgently required. The hybrid peptide VR18 (VARGWGRKCPLFGKNKSR) was designed to have enhanced antimicrobial properties in the fight against *Pseudomonas*-induced microbial keratitis, including contact lens-related keratitis. Chapter IV illustrates the VR18's modes of action against *Pseudomonas* membranes as shown by live cell Raman spectroscopy, live cell NMR, live-cell fluorescence microscopy and measures taken using sparsely tethered bilayer lipid membrane bacterial models to be via a bacterial-specific membrane disruption mechanism. The high affinity and selectivity of the peptide were then demonstrated using *in vivo*, *in vitro* and *ex vivo* models of *Pseudomonas* infection. The extensive data presented in this work suggests that topical employment of the VR18 peptide would be a potent therapeutic agent for the prevention or remedy of *Pseudomonas*-associated microbial keratitis.

This chapter has been adapted from the following publication:

Mohid, S.A., Sharma, P., Alghalayini, A., Saini, T., Datta, D., Willcox, M.D., Ali, H., Raha, S., Singha, A., Lee, D. and Sahoo, N., **2022**. A rationally designed synthetic antimicrobial peptide against *Pseudomonas*-associated corneal keratitis: Structure-function correlation. *Biophysical Chemistry*, 286, p.106802.

CHAPTER V

Two-dimensional (2D) tungsten disulfide (WS₂) quantum dots offer numerous promising applications in materials and optoelectronic sciences. Additionally, the catalytic and photoluminescence properties of ultra-small WS₂ nanoparticles are of potential interest in biomedical sciences. Addressing the use of WS₂ in the context of infection, the Chapter V describes the conjugation of two potent antimicrobial peptides with WS₂ quantum dots, as well as the application of the resulting conjugates in antimicrobial therapy and bioimaging. In doing so, we

determined the three-dimensional solution structure of the quantum dot-conjugated antimicrobial peptide by a series of high-resolution nuclear magnetic resonance (NMR) techniques, correlating this to the disruption of both model lipid and bacterial membranes, and to several key biological performances, including antimicrobial and anti-biofilm effects, as well as cell toxicity. The results demonstrate that particle conjugation enhances the antimicrobial and anti-biofilm potency of these peptides, effects inferred to be due to multi-dentate interactions for the conjugated peptides. As such, our study provides information on the mode-of-action of such conjugates, laying the foundation for their potential use in treatment and monitoring of infections.

This chapter has been adapted from the following publication:

Mohid, S.A.*, Ghorai, A.*, Ilyas, H., Mroue, K.H., Narayanan, G., Sarkar, A., Ray, S.K., Biswas, K., Bera, A.K., Malmsten, M. and Midya, A., **2019**. Application of tungsten disulfide quantum dot-conjugated antimicrobial peptides in bio-imaging and antimicrobial therapy. *Colloids and Surfaces B: Biointerfaces*, 176, pp.360-370.

CHAPTER VI

The formation and accumulation of amyloid aggregates are the phenomena that accompany amyloidoses, which are currently untreatable and include Alzheimer's and Parkinson's diseases, diabetes mellitus, non-neuropathic lysozyme systemic amyloidosis, and others. One of the very promising therapeutic approaches seems to be an inhibition of amyloid formation and/or clearance of amyloid aggregates. Small molecules have a great potential to interfere with amyloid fibrillation of peptides and polypeptides, which can be improved by connection of cyclic structures into single multicyclic molecules and their dimerization. In our study, we focused on heterodimers consisting of 7-methoxytacrine (7- MEOTA) and 2-aminobenzothiazole (BTZ) parent molecules connected by an aliphatic linker. Using in vitro and in silico methods, we investigated the ability of studied compounds to inhibit the amyloid aggregation of hen egg white lysozyme. Heterodimerization led to significant improvement of inhibitory activity compared to that of the parent molecules. The efficiency of the heterodimers varied; the most effective inhibitor contained the longest linker, eight carbons long. We suggest that binding of a heterodimer to a lysozyme blocks the interaction between the β -domain and C-helix region essential for the formation of amyloid cross- β structure. Elongation of the linker ultimately enhances the compound's ability to prevent this interaction by allowing the BTZ part of the heterodimer to bind more effectively, increasing the compound's binding affinity, and also by greater steric obstruction. This study represents an important contribution to the recent rational design of potential lead small molecules with anti-amyloid properties, and the heterodimers studied are prospective candidates for the treatment of systemic lysozyme amyloidosis and other amyloid-related diseases

This chapter has been adapted from the following publication:

Gancar, M., Ho, K., **Mohid, S.A.**, Thai, N.Q., Bednarikova, Z., Nguyen, H.L., Bhunia, A., Nepovimova, E., Li, M.S. and Gazova, Z., **2020**. 7-Methoxytacrine and 2-Aminobenzothiazole Heterodimers: Structure–Mechanism Relationship of Amyloid Inhibitors Based on Rational Design. *ACS Chemical Neuroscience*, *11*(5), pp.715-729.

Each chapter (chapter 2 to 6) begins with a short ‘Introduction’ followed by ‘Materials and methods’, ‘Results and discussion’ and ‘Conclusion’. For Convenience, ‘References’ are given at the end of the thesis. List of publications has been appended at the end of the thesis.

(* indicates equal contribution)

Contents

Biophysical Studies of <i>de-novo</i> Designed Antimicrobial peptides: Correlation with Biological membranes.....	1
Chapter I.....	1
1. Designing, characterization and translation of synthetic antimicrobial peptides for future theranostics	1
1.1. Global shortage of innovative antibiotics fuels the threat of antimicrobial resistance worldwide	1
1.2. Traditional antimicrobials vs development of resistance.....	2
1.3. Antimicrobial peptides as a potent antimicrobial agent.....	5
1.4. Nanotechnology and Peptides.....	10
1.5. Application in Therapy and Diagnostics	19
1.6. Understanding and unveiling the <i>de-novo</i> designed AMP-membrane interactions by employing biophysical techniques.....	25
Chapter II.....	29
2. <i>De-novo</i> Designing and Biophysical Characterization of Different Antimicrobial Peptides	29
2.1. Design, Synthesis, Antibacterial Potential and Structural Characterization of N-acylated Derivatives of Human Autophagy 16 Polypeptide	29
2.1.1. Introduction	29
2.1.2. Materials and methods.....	30
2.1.3. Results and discussion	37
2.1.4. Conclusions	53
2.1.5. Appendix II.....	55
2.2. Synthesis and antibacterial study of cell-penetrating peptide conjugated trifluoroacetyl and thioacetyl lysine modified peptides	63
2.2.1. Introduction	63
2.2.2. Materials and methods.....	64
2.2.3. Results and discussion	68
2.2.4. Conclusions	75
Chapter III.....	77
3. Structural Insights into the Interaction of Antifungal peptides and Fungal Membrane-specific Ergosterol.....	77
3.1. Introduction	77
3.2. Materials and methods.....	78
3.3. Results and discussion	86
3.4. Conclusion	102
3.5. Appendix III	104
Chapter IV	109
4. A rationally designed synthetic antimicrobial peptide to treat Bacterial Ocular Infections	109

4.1. Introduction	109
4.2. Materials and methods	110
4.3. Results and discussion	120
4.4. Conclusion	143
4.5. Appendix IV	145
Chapter V	149
5. Application of Tungsten Disulfide Quantum Dot-Conjugated Antimicrobial Peptides in Bio- Imaging and Antimicrobial Therapy.....	149
5.1. Introduction	149
5.2. Materials and methods	150
5.3. Results and Discussion	160
5.4. Conclusion	177
5.5. Appendix V.....	179
Chapter VI	183
6. 7-Methoxytacrine and 2-Aminobenzothiazole Heterodimers: Structure-Mechanism Relationship of Amyloid Inhibitors Based on Rational Design.....	183
6.1. Introduction	183
6.2 Materials and methods	186
6.3 Results and discussion	190
6.4 Conclusion	202
6.5. Appendix VI	204
Summary and future outlook	205
References	207
Peer-reviewed publications.	

Chapter I

1. Designing, characterization and translation of synthetic antimicrobial peptides for future theranostics

Parts of this chapter have been adapted from the following publications:

(A) **Mohid, S.A.** and Bhunia, A., 2020. Combining antimicrobial peptides with nanotechnology: an emerging field in theranostics. *Current Protein and Peptide Science*, 21(4), 413-428.

(B) Bhattacharjya, S., **Mohid, S.A.** and Bhunia, A., 2022. Atomic-Resolution Structures and Mode of Action of Clinically Relevant Antimicrobial Peptides. *International Journal of Molecular Sciences*, 23(9), 4558.

1.1. Global shortage of innovative antibiotics fuels the threat of antimicrobial resistance worldwide

Human civilization has faced the challenge of several pathogenic microorganisms since its beginning. The effect of infections and the related rate of morbidity or mortality during the pre-antibiotic era was severe when the history witnessed the deadliest epidemic diseases like plague and cholera [1]. However, a major milestone was reached when the famous German scientist Paul Ehrlich hypothesized the concept of ‘magic bullet’ [2] in 1900 and the first true antibiotic Penicillin was discovered by Alexander Fleming in 1928 [3]. This successfully cured numerous life-threatening infections for decades along with its modified derivatives. Following the ‘golden era’ of antibiotics [4] from 1950 to 1970, rapid emergence of multidrug or extensive drug resistant (MDR and XDR) pathogenic microorganisms started to emerge. Drug resistant virus, bacteria, fungus, and protozoa continue to be reported regularly against the first line clinical drugs while the arsenal for new and potent alternatives are very limited [5].

Drug-resistant microbes that have evolved novel resistance mechanisms, resulting in antimicrobial resistance, continue to jeopardise our ability to treat common ailments.[6] The rapid global spread of multi- and pan-resistant bacteria and fungi (often referred to as "superbugs"), which produce illnesses resistant to existing antimicrobial therapies such as antibiotics, is especially worrying [7]. According to the World Health Organization (WHO), the pipeline of new antimicrobials in clinical trials is exhausted. Only six of the 32 antibiotics under clinical development recognized by the WHO to be effective against the list of priority diseases were categorised as a novel in 2019 [8]. Furthermore, a lack of availability of high-quality antimicrobials is also a significant issue.

Among the several infectious diseases, microbial keratitis (MK) is a potentially sight-threatening ophthalmologic illness that affects people all over the world [9]. This infection can cause corneal perforation, infectious endophthalmitis, and even blindness [9]. Accurate and prompt diagnosis, timely treatment, and adequate follow-up are critical for preventing irreversible vision loss [10]. Before beginning antibiotic therapy for infectious disorders, the causal pathogen and its drug resistance profiles should be established [10]. Corneal culturing, on the other hand, is frequently not practicable in nontertiary hospitals, and bacterial or fungal growth on culture plates takes several days. To prevent treatment delays, doctors treat ocular infections based on clinical symptoms of corneal lesions and a history of antibiotic use in the patients. Because the clinical characteristics of corneal microorganisms vary, monitoring the pathogen spectrum is critical for the management of corneal infections [11]. The microbiological spectrum of corneal infections varies with weather and region, according to various investigations [11].

In South Asia, the incidence of corneal ulceration is reported to be between 113 and 799 per 100,000 person per year, more than ten times greater than in the United States [12]. It is the fifth leading cause of blindness globally, accounting for almost 3.2% of all cases [13]. The recent WHO report highlighted that around 6 million of the world's population are affected by cornea-related blindness or moderate/severe visual impairment, including 2 million of those who are affected by trachoma [13]. Antimicrobial treatment is used to treat corneal infections, which necessitates understanding of the local antimicrobial susceptibility patterns of different medications. There's evidence to believe this susceptibility profile has shifted in recent years [14]. In India, for example, oral antibiotic use has risen in recent years, with cephalosporins being particularly popular [15]. This increasing antibiotic intake may have selected for resistant bacteria strains, altering the susceptibility profile [15]. Despite the high prevalence of corneal ulcers in India, there is a scarcity of current surveillance data from the subcontinent.

1.2. Traditional antimicrobials vs development of resistance

Antibiotics save lives but the overuse or misuse of antibiotics can cause side effects and lead to antibiotic resistance [6]. Since the 1940s, antibiotics have greatly reduced illness and death from infectious diseases. However, as we use the drugs, germs develop defense strategies against them [16]. This makes the drugs less effective. Microbes are very small living organisms and the sizes ranges from nanometer (e.g., Viruses) to micrometer (bacteria and fungus) ranges. Most microbes are harmless and even helpful to humans, but

some can cause infections and diseases [6]. Drugs used to treat these infections are called antimicrobials. The most commonly known antimicrobial is antibiotics, which kill or stop the growth of bacteria. Fungi cause illnesses like athlete's foot and yeast infections. Fungal infections are treated with drugs called antifungals.

Antibiotics combat against pathogenic microorganisms (bacteria and fungi). Microbes, on the other hand, fight back and develop new methods to survive. Resistance mechanisms are the names given to their defence tactics. Bacteria develop resistance mechanisms by using instructions provided by their DNA. Often, resistance genes are found within plasmids, small pieces of DNA that carry genetic instructions from one germ to another. This means that some bacteria can share their DNA and make other germs become resistant. Table 1.1 describes the defence mechanisms that exerted by the resistant pathogens.

Table 1.1. Mechanisms of antibiotic resistance

Microbes can use several defense strategies to resist the effects of antibiotics. Here are a few examples.

RESISTANCE MECHANISM	DESCRIPTION	AFFECTED ANTIBIOTICS
PREVENTION OF CELLULAR UPTAKE AND/OR EFFLUX PUMPS	<ul style="list-style-type: none"> • Efflux pumps actively transport antibiotics out of the cells. • Inhibit accumulation of drugs. • prevents the drug from reaching its cellular target. • Decreasing the porin channel expression on the outer membrane. 	Fluoroquinolones, Aminoglycosides, Tetracyclines, β -lactams, macrolides,
INACTIVATING ANTIBIOTICS VIA ENZYMATIC REACTIONS	<ul style="list-style-type: none"> • A well-known mechanism of acquired antibiotic resistance in both gram-negative and gram-positive bacteria is the production of enzymes capable of introducing chemical modifications to the antibiotics. 	aminoglycosides, chloramphenicol, streptogramins, lincosamides β -lactams

<p>TARGET MODIFICATION</p>	<ul style="list-style-type: none"> • Most frequent biochemical modification includes: acetylation, phosphorylation and, adenylation. • Enzymatic degradation of antibiotic molecules (e.g., β-lactamases, carbapenemase etc.) 	
<p>BIOFILM FORMATION</p>	<ul style="list-style-type: none"> • Distinct antibiotics target different intra- or extra-cellular components to cause bacterial death, such as genetic material, proteins, the cytoplasmic membrane, and other cell wall components. • Protection of the target site to avoid the antibiotic from reaching its binding site. • Modification or mutation or complete replacement of the target site that result in lower affinity for the antibiotic molecule. 	<p>Tetracycline Fluoroquinolones Fusidic acid Rifampin oxazolidinones (linezolid and tedizolid)</p>
	<ul style="list-style-type: none"> • Complex surface-adhering microbial communities within a self-composed extracellular polymeric matrix. • 1% biofilm population contains dormant or persistent cells that are highly resistant to antibiotics. • Typically, a biofilm houses subpopulations of bacteria that are susceptible and resistant to an antibiotic, 	<p>Gentamicin β-lactams Vancomycin Daptomycin</p>

a phenomenon called ‘hetero-resistance’.

- Horizontal gene transfer occurs within and between the bacterial species residing under a biofilm.
- Accumulates antibiotic-degrading enzymes in the matrix.

1.3. Antimicrobial peptides as a potent antimicrobial agent.

1.3.1. Discovery

Antimicrobial peptides (AMPs) are ubiquitous molecules, found in organisms ranging from prokaryotes to humans. These are also known as cationic host defense peptides or cationic amphipathic peptides [17-19].

In 1922, Lysozyme was discovered from nasal mucus by Alexander Fleming. He observed that the protein has antimicrobial activity. But after finding penicillin from the mold *Penicillium notatum* in 1928, the above observation was overshadowed because of the excellent therapeutic potential of the antibiotic molecule. However, in the year 1939, Dubos isolated a compound from soil microbes, which showed promising activity against pneumococcal infection in mice. After a year, Hotchkiss and Dubos named this compound as gramicidin [20]. Despite some toxic effects in the intraperitoneal application, gramicidin successfully cured tropical skin diseases. In the following year two other antimicrobial compound, namely tyrocidine and purothionin was discovered from soil bacillus and maize plants, respectively [21,22]. However, the focus on AMPs was very little at that time (between 1940 to 1960) due to the dominating presence of several antibiotics in the market.

However, the excess and improper uses of antibiotics lead to the development of multidrug-resistant (MDR) microbial pathogens during the year 1960. Therefore, the researchers began to find a novel class of molecules to replace traditional medicines, which restarted with the interest in AMPs. Since then, AMPs have been isolated from almost all type of organisms. Table 1.2 shows the timeline of discovering AMPs that have been reported from 1922 to 1987 when the concept of peptide-based drugs was gradually established.

Table 1.2. Discovery of different AMPs by different scientific groups and their sources

AMP	YEAR	SOURCE	GROUP
LYSOZYME	1922	Nasal mucus	Alexander Fleming
GRAMICIDIN	1940	soil <i>Bacillus</i> strain	Hotchkiss and Dubos
TYROCIDINE	1941	Aerobic sporulating bacilli	Dubos RJ, Hotchkiss RD
PUROTHIONIN	1941	plant <i>Triticum aestivum</i>	Ohtani S, Okada T, Yoshizumi H, Kagamiyama H
DEFENSIN (PHAGOCYTIN)	1956	Rabbit leukocytes	HIRSCH JG
BOMBININ	1962	Frog epithelia	Kiss G., Michl H.
LACTOFERRIN	1965	cow milk	Groves ML, Peterson RF, Kiddy CA
CECROPIN	1981	Cecropia silk moth	Steiner H, Hultmark D, Engström A, Bennich H, Boman HG
MAGAININ	1987	<i>Xenopus laevis</i>	Zasloff M.

1.3.2. Properties and mode of actions

More than thirty thousand review articles on AMPs are available on PubMed (Figure 1.1), which indicates that enormous amount of work has been done in this field. A total amount of 12,400 AMPs has been reported by Database of Antimicrobial Activity and Structure of Peptides (DBAASP), where more than 2000 ribosomal, 80 non-ribosomal and 5700 synthetic peptides were collected from natural sources like animal, plants, protists, fungi, bacteria, and viruses as well as *de-novo* designed peptides synthesized by several scientific groups [23].

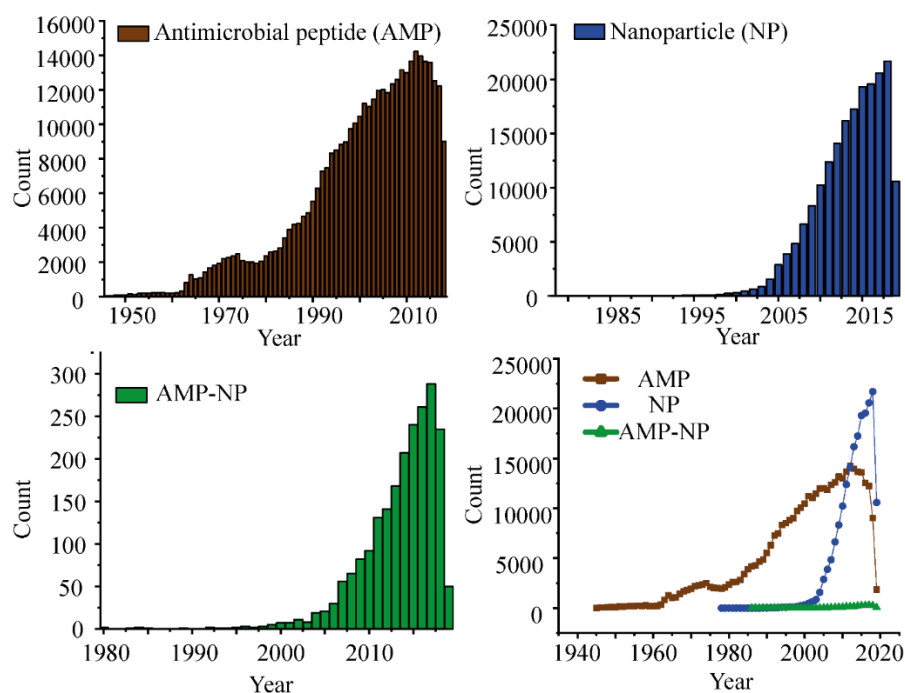


Figure 1.1. A statistical data of AMP, NP and NP-AMP conjugates available on PubMed server from 1945 to 2019.

AMPs can be found in all classes of the animal and plant kingdoms, known as a first line of defence against the microbes [24]. Due to their diverse sources and a broad range of activities, antimicrobial peptides are categorized by their physical and chemical attributes, such as charge, secondary structures, and target groups.

The main driving force for the activity of any AMP depends on its constituent amino acid residues, which contribute the net surface charge and amphipathicity of a particular peptide. Positively charged amino acids like Lysine, Arginine and Histidine-rich AMPs forms cationic AMP group and acidic amino acids like aspartate, and glutamate-rich AMPs produces anionic AMP group. Microbial membranes and cell walls are primarily composed of anionic lipids such as phosphatidylglycerol and negatively charged biopolymers such as lipopolysaccharide (LPS) and Teichoic acids, respectively [25]. These lipids serve as the primary target for most natural and synthetic cationic AMP families such as cecropin, magainin, indolicidin, and so on. However, anionic AMPs like dermcidin, maximin, and daptomycin also have different mechanisms to kill microbes and holds the potential to be used as a therapeutic agents [19].

To understand the structure-activity relationship of different AMPs, the secondary structure adopted by specific peptides in the presence of microbial membrane or target

molecules is crucial. There are four main classes of AMPs categorized by their secondary structures [26]; (i) alpha family [26], (ii) Beta family [26,27], (iii) Alpha-beta family [26], and (iv) Non-alpha-beta family [26].

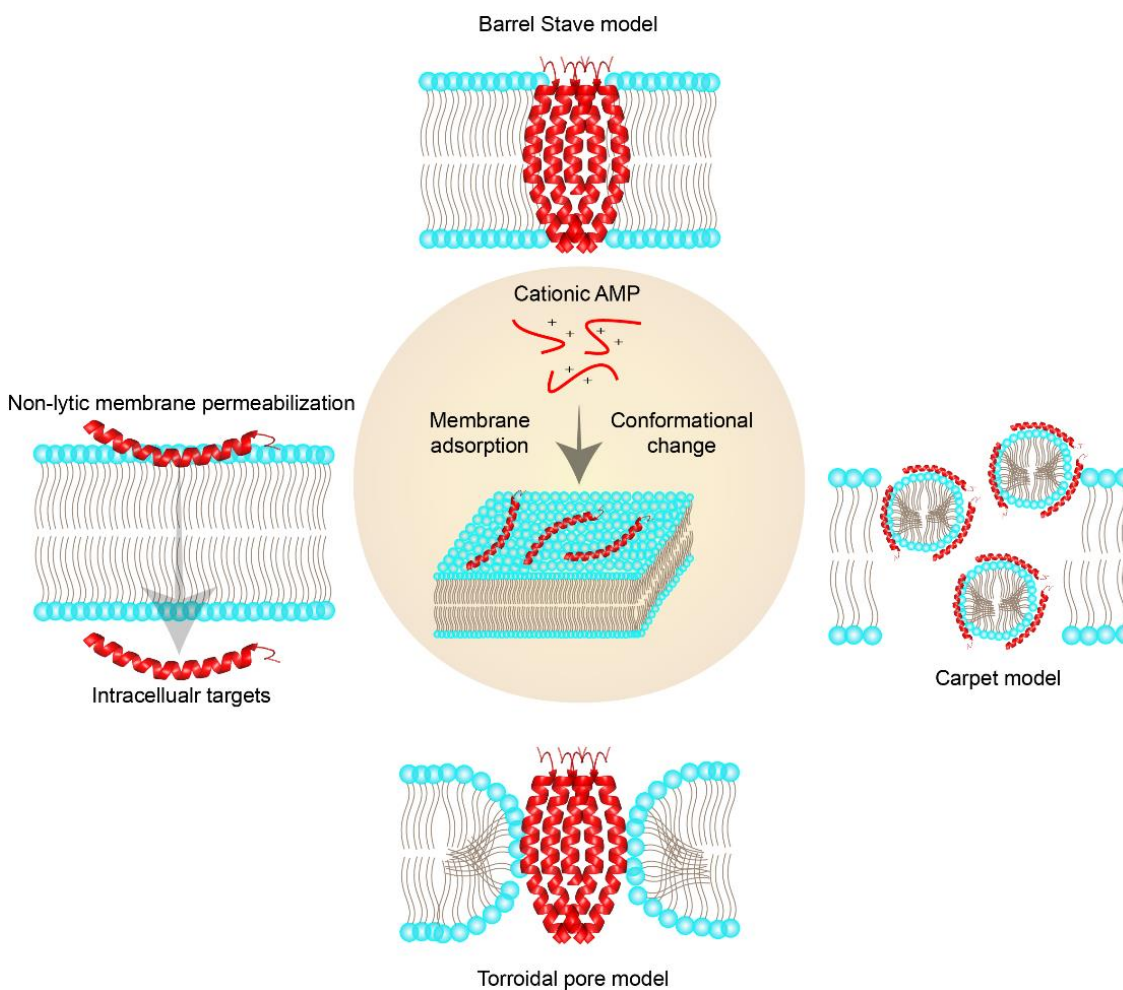


Figure 1.2. A schematic illustration of the mechanisms of action exerted by AMPs to kill the microbial cells.

Antimicrobial peptides are a diverse group of molecules and possess several different characteristics. Thus, it is very important to find out the mode of action or target of the interaction of AMPs to facilitate progress of designing novel therapeutic agents. Initially, it was perceived that membrane is the only target of all AMPs. With the increasing recent evidence, it is now clear that the AMPs employ a variety of antimicrobial mechanisms [28]. The mode of actions of all AMPs is divided into two major groups: direct and indirect pathways as shown in Figure 1.2. The direct path is mainly referred to as the killing mechanism where AMPs itself acts via membrane disruption or blocking intracellular pathways [29]. The cell membrane is critical in sustaining electrochemical

gradients and electron transport, and any malfunction, such as ion/metabolite leakage, leads to depolarization and loss of membrane-coupled respiration, finally resulting in cell death, either directly or indirectly. The Carpet model, Barrel-Stave model, and toroidal pore model are three of the most well-known processes by which AMPs damage their targets' lipid bilayer membranes [30]. In the Carpet model, AMPs concentrate on the surface and eventually "degrade" the cell membrane in a detergent-like way [30]. AMPs aggregate and are introduced into the bilayer of the cell membrane as multimers, arranged parallel to the phospholipids, and then create a channel in the Barrel Stave model [30]. In the toroidal model, the pore is partly composed of both peptide and phospholipid because AMPs cause the phospholipids from the two layers to form a curvature. After the peptides have accumulated, the peptides bend around a central channel, forming the transmembrane pore which eventually kills the microbial cell. Indirect pathways are driven via immune modulation where the AMPs interact with the immune cells and activates them by enhancing the immune response as well as controlling inflammation [29].

1.3.3. Limitations of AMPs

Despite discovering several AMPs in the past 30-40 years, there is still a prominent gap between the list of potential AMPs capable of therapeutic applications and the number of AMPs available after clinical trials [31]. The experimental, technical, and commercial challenges that limit the AMPs from successful therapeutic applications are summarized in Fig. (2). The first step to screen an AMP is to start with a naturally occurring biologically active sequence or *de-novo* designed peptide library. *In-vitro* optimization using standard minimal inhibitory concentration (MIC) or minimum bactericidal concentration (MBC) assays are conducted against a series of bacterial and fungal agents. However, these assays are highly dependent on environmental conditions, often the *in vitro* activity is not reflected by the subsequent *in vivo* efficacy studies, making it problematic for therapeutic application [32,33]. In addition, toxicity, serum binding, poor pharmacokinetics and stability are the major challenges observed with AMPs during clinical trials practical considerations [34,35].

Only a handful of scientific reports is currently available where a systematic toxicological or safety data has been published for a particular AMP [36]. Toxicity of AMPs can occur at different levels, few examples are, membrane toxicity, cellular toxicity, and systemic toxicity. Toxicity of the membrane relies on both the charge and hydrophobicity of a particular peptide sequence. It has been reported that increased charge can reduce mammalian membrane toxicity, but increasing hydrophobicity via long acyl chain

modification can accelerate the risk of membrane toxicity [37]. Cellular toxicity refers to the toxic effect on a single cell or cell lines, which can be analyzed via various laboratory assays such as cytotoxicity assay or measurement of total lactate dehydrogenase activity. However, it is highly challenging to assess for a multicellular organism without a long-term clinical trial. Systemic toxicity, on the other hand, arises from various factors. This includes activation or inhibition of transcription, binding and alteration of some receptor or change in metabolic pathways. Falagas et al. have shown that the intravenous administration of polymyxins may cause nephrotoxicity and neurotoxicity if administered with higher dose for a prolonged time [38]. Systemically administered AMPs are highly unstable due to their low metabolic stability because of the surrounding enzymatic environments. Poor penetration via intestinal mucosa makes these peptides unusable for oral administration [39]. The intravenous drug delivery is also a restricted option due to poor serum instability and degradation of AMP by the proteolytic enzymes present in the blood and they are excreted rapidly by hepatic or renal clearance [39]. However, topical applications such as dermal creams, emollients or spray are an exception, which may bypass these problems. Although they are still subject to tissue proteolytic enzymatic degradation that may reduce their therapeutic potential.

Various multidimensional approaches have been employed to enhance the stability of AMPs against the action of peptidases such as pepsin, trypsin, thrombin, plasmin etc. Several techniques like cyclization of peptides, mutation of crucial amino acids to either L- to D-isomer or non-natural analogs, peptide mimetics or combining nanotechnology either via organic or inorganic pathways [40] are used to overcome the above-mentioned problem. Malmsten et al. have shown end-tagging via oligomerization of tryptophan enhances the stability of AMPs from proteolysis [41]. The basic idea is to protect the N- and C-terminal end of the peptides from the active site of peptidases/proteases; to do this researchers have modified these terminals either by acetylation, or amidation, acylation, PEGylation etc [42,43]. However, the preparation of nanoparticles combining with AMPs or organic materials and conjugation with inorganic nanoparticles such as gold or silver has changed this scenario in the past two decades.

1.4. Nanotechnology and Peptides

Application of nanotechnology in the field of biologically active AMPs is diverse, and it includes several peptides and their modifications. Dipeptide, oligo-peptide, amyloid, antimicrobial, cyclic, lipid-associated, carbohydrate attachment is just few of them to

mention. Conjugation of different inorganic nanoparticles including gold (Au), silver (Ag), copper (Cu), titanium (Ti), zinc (Zn), iron (Fe), and transition metals has extended its application [44-48]. Every system has different properties and protocols for usage. Here, we will focus only on the AMPs and will discuss how nanotechnology has shaped a new platform for these peptides in drug designing to therapy and diagnostics.

1.4.1. Peptides and organic compounds as nanoparticles

Self-assembled peptides can obtain different shapes and sizes in nanoscale range depending on their amino acid compositions and three-dimensional structures such as nanotubes, nanofibers, nanoparticles, nanosphere, gels, and nanorods. However, the main driving force behind these self-assembled structures is entropy because only thermodynamically favorable shapes are taken by individual monomers rather than unfavorable condition in free solution. Nanotubes are extended tubular β -sheet like structures made by the self-assembly of planer, cyclic or disc-shaped peptide subunits [49]. The composition of these subunits are either alternating D- and L-amino acid residues or hetero-aromatic bicyclic bases stabilized via hydrogen bonding and hydrophobic packing as visualized by X-ray crystallography [50]. Nanofibers have mainly attracted attention because of its potential use as a biosensor. This type of assembly is also driven by several non-covalent interactions, and the most well-known member of this group is amyloid fibrils, which form insoluble aggregates by stacking its beta-sheet type monomers. Nanoparticles, nanosphere, and nanorods are a diverse group and cover the small, well-defined structures formed by different monomers. Liu et al. and Wang and co-workers used a short cationic peptide obtained by grafting cholesteryl chloroformate onto three glycine and six arginine residues (G_3R_6) that is attached with TAT (YGRKKRRQRRR) peptide. It can easily self-assemble to form core-shell structured micellar nanosphere [51,52]. They successfully showed that the nanoparticle is more active against a series of bacteria and fungus than its monomer and it can cross the blood-brain barrier (BBB) easily and thus can be used against brain inflammatory diseases such as meningitis and encephalitis. A star-shaped peptide polymer nanoparticle termed as 'Structurally Nano engineered antimicrobial peptide polymers' (SNAPPs) have been demonstrated by Lam et al. as superior antimicrobial agents with nanomolar range activity in *in vitro* and *in vivo* condition against Gram-negative pathogens, including multidrug-resistant species [53].

On the other hand, Mi et al. designed an amphiphilic peptide nanoparticle (APNP) rich in arginine residues, highly potent against Gram-positive bacteria including

methicillin-resistant *Staphylococcus aureus* (MRSA) but at the same time non-toxic to human fibroblasts [54]. Schneider et al. made 8 to 16 residue long beta-sheet peptide that can form distinct nanofiber and hydrogel depending on different physiological condition and is very useful for the purpose of wound healing [55]. Some researchers have used different organic molecule and scaffolds such as chitosan polymer, Polyglutamic (gamma-PGA)/ polylactic (PLA)/ polylactic-glycolic acid polymer and polyglycerol scaffold along with AMPs to form different nanostructures, which not only increases the potency of the peptides but also increases its bioavailability, serum stability, and reduced toxicity. For instance, Almaaytah et al. have reported an ultrashort AMP (RBRBR, R = arginine and, B = L-4-phenyl-phenylalanine) encapsulated via chitosan nanoparticle, capable of killing and removing MRSA and its biofilm for long duration due to its slow release [56]. In another study, Lauster et al. have synthesized a multivalent peptide-polymer nanoparticle based on dendritic polyglycerol scaffolds to inhibit virus particle from infection at the nano- to picomolar range in *in-vivo* condition [57].

1.4.2. Conjugation of iNP and AMP

Although inorganic nanoparticles (iNPs) gained significant attention in modern science, it has been used by ancient human civilization prior to the discovery of antibiotics. This is used in the form of metals, metallic oxides, and salts against pathogenic infections. This changed over the last few decades when several iNPs showed promising activity against MDR pathogens alone and in combination with antimicrobial drugs. Stimuli-responsive and carrier nanoparticles are also being considered for biomedical applications due to their efficiency in target cell killing in a localized area. However, prolonged use of iNPs have been associated with adverse effects [58].

Recent research has shown that conjugation of AMPs with iNPs may reduce systemic toxicity and may increase antimicrobial efficacy in addition to enhancement of proteolytic stability *in vivo* (Figure 1.3 and Table 1.3). Vignoni, M. et al. conjugated the human keratinocyte derived cathelicidin LL37 peptides with AgNP via thiol group (-SH) conjugation chemistry. The process resulted in enhanced activity of the system against Gram-positive and Gram-negative bacteria against *P. aeruginosa* biofilm while mitigating the anti-proliferative or toxic effects of ionic AgNPs [59]. Atreya and co-workers also attached AgNP to a potent AMP OA1 via cysteine residue, which exhibited significantly higher stability and activity of the conjugated system compared to that of the peptide alone [60]. Wadhvani et al. described that the conjugation of potent cationic AMPs to AuNP via

cysteine residue at the N-terminus does not change the antimicrobial activity and biologically active structure of the peptides but improved its proteolytic stability, solubility and lifetime in the *in vitro* system [61].

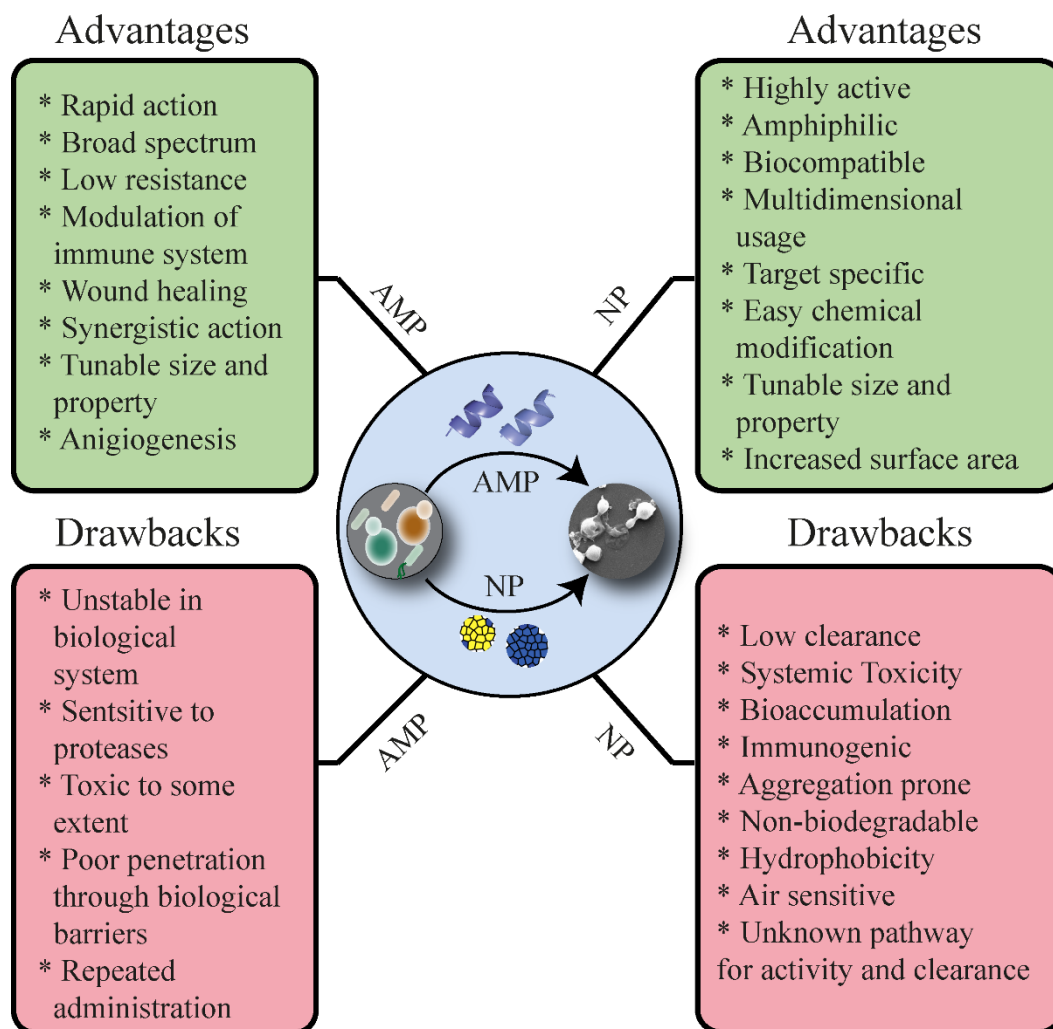


Figure 1.3. Advantages and disadvantages of AMPs and NPs as a drug in biological system.

Another study by Casciaro et al. has shown that a frog skin-derived AMP Esculentin (1-21) showed more than 15-fold increased activity than its free counterpart when conjugated with AuNP via poly (ethylene glycol) (PEG) linker. They also described that the system was highly stable against enzymatic degradation and showed no adverse effect on the human keratinocyte cell line while promoted wound healing in an *ex vivo* system [62]. Immobilization of cecropin-melittin (CM) via covalent bond on superparamagnetic FeO NP showed ten times lower MIC than free CM as depicted by Maleki et al [63]. This novel system can internalize itself by endothelial and macrophage cells and kills

intracellular pathogens while keeping low cytotoxic profile [63]. Finally, there are evidences supporting the fact where AMPs and NPs have been portrayed as a potent new generation drug where each member has complemented their limitations [64-66].

Table 1.3. Describes an overview of potent AMPs conjugated with different organic and inorganic nanoparticles for various purposes ranging from antimicrobial therapies to food contamination detection and wound healing.

AMPS AND SEQUENCE	NPS USED	CONJUGATION METHOD	TARGET ORGANISMS	MODE OF ACTION	REF.
INDOLICIDIN ILPWKWPWW PWRR-NH₂	Colloidal gold NP (AuNP)	Chemisorption via thiol group of 2-mercaptoethanol	Fluconazole resistant <i>Candida albicans</i>	Fungicidal, Suppresses iNOS gene in macrophages	[67]
PBP10 DERIVATIVES QRLFQVKGR R	Magnetic NP (MNP)	Iron oxide core functionalized with gold via K-gold process	<i>Staphylococcus aureus</i> , <i>MRSA Xen30</i> , <i>Pseudomonas aeruginosa Xen5</i> , <i>Candida albicans</i> , <i>Candida glabrata</i> , <i>Candida tropicalis</i> .	Membranolytic for both planktonic cells and biofilms, Inhibition of microbial cell division.	[68]
DAPTOMYCIN	Gold nanocluster (AuNC)	Covalent (amide) bond via 4,6-diamino-2-mercaptopyrimidine (DAMP) on AuNC	Methicillin-resistant <i>Staphylococcus aureus</i> (MRSA)	Disruption of the bacterial membrane via pore formation, Targets intracellular organelles and breaks the DNA of the Bacteria.	[69]
BACITRACIN A (BA) AND POLYMYXIN E (PE)	Silver NP (AgNP)	Reduction of AgNO ₃ was made via NaBH ₄ in presence of BA and PE	<i>Escherichia coli</i> , <i>Pseudomonas aeruginosa</i> , <i>Staphylococcus aureus</i> , <i>Bacillus amyloliquefaciens</i>	Bactericidal activity via membranolysis and shows wound healing property	[70]
BP100 (KKLFKKILK YL-NH₂),	Alumina NP	Disulfide-linked peptide-alumina nanoparticle via thiol group of cysteine and	<i>Escherichia coli</i> (ATCC 25922), <i>Salmonella typhimurium</i> (ATCC 14028)	It interacts with microbial inner membrane.	[71]

CAAA-BP100 (CAAACKLFLK KILKYL-NH₂) [PRA]GAAA- BP100 ([PRA]GAAAK KLFFKILKYL -NH₂) DERMADISTI NCTIN K (GLWSKIKAA GKEAAKAAA KAAGKAALN AVSEAV-NH₂)		Triazole linked peptide- alumina nanoparticle via a copper(I)-catalyzed azide-alkyne cycloaddition reaction (CuAAC)	<i>Staphylococcus aureus</i> (ATCC 29313) <i>Candida krusei</i> (ATCC 34135) and <i>Candida parapsilosis</i> (ATCC 22019)	
CERAGENIN CSA-13	Magnetic NP	Firstly, MNPs were treated with 3-aminopropyl trimethoxysilane (APTMS) to build the amine group linked with silica. Then aldehyde functionalization was done using glutaraldehyde. Lastly, imine bond was formed between aldehyde group and C3 of CSA-13	<i>Pseudomonas aeruginosa</i> PAO14	Disruption of the plasma membrane. [72]
ANDERSONIN- Y1 (AY1) [FLPKLFAKIT KKNMAHIR], CAY1 [CFLPKLFAKI TKKNMAHIR] AND AY1C [FLPKLFAKIT KKNMAHIRC]	AgNP	Mixing of aqueous or buffer solution of peptides (450 μ L of 0.3 mM) and AgNP (50 μ L of 50 μ g/mL) at 298K.	<i>Escherichia coli</i> DH5 α , <i>Pseudomonas aeruginosa</i> (ATCC 27853), <i>Salmonella typhi</i> (ATCC 14028), <i>Klebsiella pneumoniae</i> (ATCC 13883)	Lysis of bacterial cells. [45]

PEP-H OF HUMAN NEUTROPHIL PEPTIDE-1 (HNP-1) (RRYGTCIYQ GRLWAF)	Chitosan NP (CSNP) and AuNP	Pep-H was mixed in CSNP in solution, and sodium tripolyphosphate (STPP) was added to form the NPs. AuNP-Pep-H conjugate was prepared by mixing of peptide and AuNP solution at 298K and incubated for 30 min.	<i>Mycobacterium tuberculosis</i> (M. tb) H37Rv	Antimycobacterial activity	[73]
1018K6 (VRLIVKVRIRRR) (A MUTATED PEPTIDE DERIVATIVE OF BACTENECIN)	polyethylene glycol (PEG)-stabilized AuNP (hybrid AuNP)	Covalent conjugation of 1018K6 peptide to hybrid AuNP via the standard 1-ethyl-3-[3-(dimethylamino)propyl] carbodiimide hydrochloride (EDC)/N-hydroxysuccinimide (NHS) reaction.	<i>Listeria monocytogenes</i> (LM2 food-isolated strain), <i>Salmonella typhimurium</i> (ATCC 13311)	Alteration of the bacterial cell membrane	[74]
ESC(1-21) (GIFSKLAGK KIKNLLISGL KG-CONH₂), ESC(1-21)-1C (GIFSKLAGK KIKNLLISGL KG-CONH₂)	poly(lactide-co-glycolide) (PLGA) NP	Emulsion/solvent diffusion method.	<i>Pseudomonas aeruginosa</i> PAO1	Kills and eradicates planktonic and sessile form of <i>Pseudomonas aeruginosa</i> . Cures lung infection	[62]
FLUPEP (WLFFVIFYFRRRRKK), FLUPEP LIGAND (CVVVTAAAWLVFFVIFYFFRRRKK)	AuNP & AgNP	A ligand shell matrix peptidol (CVVVT-ol) containing peptide solution was mixed to the AuNP/AgNP solution at a particular molar fraction and vortexed at room temperature.	Influenza virus (A/WSN/33 H1N1 subtype)	Inhibition of viral plaque formation and reduce the infectivity of virus particles outside the cells.	[75]
DAPTOMYCIN	CSNP	Daptomycin solution was either mixed with Chitosan solution at	methicillin-resistant <i>S. aureus</i> (MRSA) ATCC 43300,	Disruption of the membrane which subsequently leads	[76]

		different mass ratios, and tripolyphosphate (TPP) was added dropwise to form CSNP or the peptide was mixed to TPP solution and dropped into Chitosan solution.	methicillin-susceptible <i>S. aureus</i> (MSSA) ATCC 25923, <i>S. epidermidis</i> ATCC 14990, <i>Staphylococcus lugdunensis</i> ATCC 43809, <i>Staphylococcus haemolyticus</i> ATCC 29970, <i>Staphylococcus hominis</i> ATCC 27844, <i>Staphylococcus warneri</i> ATCC 27836, and <i>Enterococcus faecalis</i> ATCC 29212	to microbial cell death	
INDOLICIDIN (AC-CILPWKWPW WPWRR-CONH₂)	AuNP	Covalently conjugated with AuNP via thiol group of cysteine present at the N-terminus of the peptide sequence.	<i>Candida albicans</i> ATCC 90028, <i>Candida albicans</i> ATCC 14053, <i>Candida albicans</i> ATCC 10231, <i>Clinical isolates of Candida albicans</i> C1-C8, and <i>Candida tropicalis</i>	Fungicidal activity, Anti-biofilm activity. Suppression of biofilm-forming and transporter encoding genes	[77]
OH30 (KFFKCLKNS VKKRAKKFF KKPRVIGVSIP F)	Carboxymethyl chitosan nanoparticles	Mild ionic gelation method.	<i>Escherichia coli</i> ATCC 25922	Antibacterial activity and nonscar wound healing	[78]
BUFORIN II (BUF2) (TRSSRAGLQ	Magnetic NP	Firstly, Silanization was done using APTES to produce free amine	<i>Escherichia coli</i> ATCC 25922	Loss of antimicrobial activity due to	[79]

FPVGRVHRLLRK)		groups on the MNPs. Then The C-terminal group of the peptides was covalently conjugated with the MNPs		immobilization of the C-terminal but enhanced cell-penetrating ability and targeted drug delivery	
PEPTIDE K4 (KKKKPLFGLFFGLF)	poly (lactic-co-glycolic acid) (PLGA) NP	Peptide and PLGA NP was conjugated via carbodiimide chemistry (EDC/NHS coupling).	<i>Staphylococcus aureus</i> MTCC 9542 <i>Pseudomonas aeruginosa</i> MTCC 8076	Antimicrobial and wound healing activity	[80]
SHORT LIPOPEPTIDE (PALMITIC ACID/LAURIC ACID/OCTANOIC ACID LINKED WITH RWR/WRR)	AuNP	Self-assembly of 1-dodecanethiol-anchored gold nanoparticles (Au-DT NPs) with Lipopeptide via hydrophobic interactions	<i>Escherichia coli</i> (E. coli ATCC 25922) (<i>E. coli</i> DC2), <i>Staphylococcus aureus</i> (<i>S. aureus</i> ATCC 29213), <i>methicillin-resistant Staphylococcus aureus</i> (MRSA ATCC 43300), <i>Staphylococcus epidermidis</i> (<i>S. epidermidis</i> ATCC 14990), <i>Pseudomonas aeruginosa</i> (<i>P. aeruginosa</i> ATCC 27853), and <i>Candida albicans</i> (<i>C. albicans</i> ATCC 10231)	Disruption of the cytoplasmic membrane and cell lysis.	[81]
MELITTIN (MLT) (GIGAVLKVLTTGLPALISWIKRKRQQ)	Magnetic NP	Mixing of carboxylated MNPs with MLT solution at 0.5:1 mass ratio.	<i>Salmonella typhi</i> (ATCC 14028), <i>Staphylococcus aureus</i> (ATCC 27217), and <i>Escherichia coli</i> (ATCC 25922)	Screening of contaminated foods and water	[82]

NZX PEPTIDE	Mesoporous silica NP (MSNP)	Peptides were strongly adsorbed on the MSNP surface.	<i>Mycobacterium bovis</i> (BCG) Montreal strain	The killing of primary macrophage residing mycobacteria and enhanced targeted drug delivery	[83]
--------------------	-----------------------------	--	--	---	------

1.5. Application in Therapy and Diagnostics

1.5.1. Drug delivery

Delivery of a drug to its specific and particular target site in the human body system is still a significant challenge. Peptide-based drugs have an advantage over this problem, and it emerged as a potential candidate having modular selectivity and enhanced activity against a range of severe health problems, including cancer. Being composed of mainly natural amino acids, peptides can easily interact with different cellular and subcellular systems, which in turn allow them to be used against broad aspects to get effective results. Application of this peptide-based system as drug delivery vehicle, however, gets hindered due to several reasons, including short half-life, poor biodistribution, low diffusivity and partition coefficients against the biological barrier in the *in vivo* system and high production cost as discussed previously.

Conjugation of peptides with nanoparticle is the simplest way to solve these problems in case of drug delivery also. Nanoparticles can be tuned in ingenious ways for successful drug delivery at specific sites as well as protecting the drug from several enzymes via encapsulation and remarkably increases its plasma circulation time. The main advantage is that both the peptides and nanoparticles have a tuneable property, which renders a limitless opportunity to the researchers for designing more and more robust delivery system.

Involvement of nanotechnology in the delivery of AMPs follows two different ways. The passive or non-directed pathway refers to the NP-conjugated system, which mainly controlled by size or shape and possesses no surface modification to guide the molecule to a particular site [84]. The active or directed pathway involves the application of functional groups to the surface of the NPs for specific binding with the receptor sites which provides a successfully targeted delivery [85].

1.5.1.1. Non-directed pathway

Here we discussed a few selected AMPs that are well studied in terms of drug delivery via the passive way in both *in vitro* and *in vivo* systems.

Cyclosporine A is a non-ribosomal, highly lipophilic, fungus-derived cyclic AMP, comprised of 11 amino acid residues [86]. It has an excellent activity against a vast range of microbes and also includes immunosuppressive property. Romero *et. al.* made a stable amorphous nanoparticle of Cyclosporine A (CyA) by mixing 5% of CyA in water along with tocopherol polyethylene glycol succinate. They further incorporated the nano-system inside a hydrogel and applied it on a fresh pig ear skin and found 6.3 fold higher penetrating efficiency compared to its free particles [87]. To increase the bioavailability of CyA, chitosan and gelatin-based nanoparticles were used by El-Shabouri where he got 73% and 18% increment, respectively, in an *in-vivo* system [88].

Nisin is a polycyclic, broad-spectrum lantibiotic isolated from *Lactococcus lactis* and made of 34 amino acids residues including some unnatural amino acids like didehydroalanine (DHA) and didehydroaminobutyric acid (DHB). Nisin is extensively used as a food preservative and in food packaging but few groups have also explored its anti-cancerous properties in both *in-vitro* and *in-vivo* [89]. To obtain an alternative application of nisin in antifungal therapies with stable and prolonged release of drug at a particular infection site, de Abreu, *et. al.* encapsulated it using biodegradable polymeric nanoparticles. They demonstrated the permeation capacity of polycaprolactone (PCL) coated nisin by Franz diffusion cells in an *in vitro* model and concluded that the system could be used as a prophylactic agent against candidiasis [90]. Polyvinyl alcohol-based nanofiber encapsulated nisin has also shown promising activity against *S. aureus* for a prolonged time with controlled drug release [91].

Vancomycin is a highly potent, broad-spectrum, branched-chain tricyclic glycopeptide isolated from *Amycolatopsis orientalis*. The primary mode of action of this peptide is to prevent bacterial cell wall synthesis and reproduction. However, it has several severe side effects including ototoxicity and nephrotoxicity [92]. Conjugation and encapsulation of vancomycin by biodegradable polymeric nanoparticles like PLGA, EUDRAGIT or PCL showed reduced toxicity with prolonged drug release at high efficacy [93,94]. Yang *et. al.* reported that vancomycin loaded liposomes coated with chitosan nanoparticles prevents the uncontrolled release of the drug and increases its local

bioavailability in lungs, which in turn solves the nephrotoxicity problem and cures lung infection [95].

Polymyxins (B and E) are a non-ribosomal, branched-chain, cyclic peptides which have a broad range of activity against drug-resistant Gram-negative and Gram-positive bacteria. It is also known as colistin and isolated from *Paenibacillus polymyxa*. Despite having high potency, polymyxin also shows neuro and nephrotoxicity in patients. To overcome this limitation, Severino *et. al.* formulated a solid lipid nanoparticle (SLN) loaded with polymyxin and treated against resistant *P. aeruginosa* strains *in vitro* [96]. The results showed complete inhibition at very less concentration than its free form, which was active at 10 mg/ml. Liposome containing polymyxin B was developed by Alipour *et. al.*, showed lower MIC values than its unloaded counterpart and had higher penetrability against *P. aeruginosa* strains as obtained from immunohistochemistry and electron microscopy studies [97].

There are also several AMPs conjugated nanocarrier systems reported in various articles which follow the indirect pathway of drug delivery besides the list mentioned above. For example, Peng *et. al.* devised an integrated gold nanoparticle system that can carry DNA and AMPs simultaneously to inhibit cancer cells and pathogenic microbes, respectively [98].

1.5.1.2. Directed pathway

Modification of nano-carrier via attachment of a particular chemical moiety or peptide sequence onto the surface to achieve site-directed drug delivery is called targeted or active pathway [99]. There are several biological barriers that hinder specific drug release at intended sites. This includes low pH of the gastrointestinal tract, abundance proteases in serum, selective permeability of cell membranes and lysosomal pathway of cells for foreign molecules. Here also we have mentioned a few selected articles among hundreds of publications to understand the mechanism.

Cell-penetrating peptides (CPPs) have been used by several groups to deliver siRNA, plasmid DNA, and oligomers into different cell lines and *in vivo* system for targeted drug delivery. One of such CPP which has been widely used is Transactivated-transcription or TAT which is an arginine-rich peptide isolated from HIV [100]. Bi *et. al.* worked with a designed cationic AMP modified by combining TAT-sequence at C-terminus and palmitic acid at N-terminus [101]. The unique design helped individual monomers to form self-

assembled peptide nanoparticle of 150 nm diameter which was active against a series of gram-positive and gram-negative bacteria including drug-resistant strains. The TAT-sequence helped the nano-system to cross the blood-brain barrier and target infected sites in the rat brain to cure bacterial meningitis [101]. Therefore, modification of nanoparticles with CPP helps to mediate specific delivery. Our group also showed that a CPP, namely DK17, isolated from *Drosophila* can breach the tight endothelial network of BBB and can be used as a potential drug delivery vehicle in different neurodegenerative disorders [102].

In another study, mesoporous silica nanoparticles (pSiNPs) were used as a biodegradable carrier where Lactoferrin-dKK peptide was loaded inside the porous chamber of the vehicle via phosphonate surface chemistry [103]. The results showed remarkably reduced *P. aeruginosa* cells in the lungs of treated mice compared to untreated sets, which subsequently improved the survival rate. Thus, it showed an exciting way for specific treatment of a particular organ.

In a different study, PLGA nanoparticle was used for encapsulation of plectasin peptide, which is a member of defensin AMPs to target persistent *S. aureus* infection in host airway epithelium [104]. *S. aureus* resides inside the epithelial cells and thus blocks antibiotic actions. The PLGA encapsulated plectasin went into the Calu-3 and THP-1 cells and subsequently reduced the infection in a monolayer model while cell viability was unaffected at the treated concentration. A different approach was taken by Yeom *et. al.* to eliminate intracellular *Salmonella enterice* serovar *Typhimurium* in both *ex vivo* and mice infection model [105]. They designed an AuNP conjugated DNA aptamer system to precisely deliver A3-APO AMP into *S. typhi* infected HeLa cells and injected the same into mice model. The results showed complete elimination of *S. typhi* in the HeLa cell line and mice organ leading to 100% survival of the mice. These reports showed novel mechanisms to treat persistent intracellular organisms with high specificity.

1.5.2. Imaging and Diagnostics

Molecular or cellular imaging via different microscopic or computer-aided machinery enables us to visualize and analyse complex biological phenomena at high resolution. It gives quick and real-time access to researcher and clinicians to monitor and track a particular disease progression or output of a treated sample, which subsequently helps in diagnosis. There are different probes available in the market to mark a specific cellular or subcellular material or drug for tracking purposes. Though peptides have been successfully used as nanoprobe in different experimental setup for high-resolution

imaging, however, due to their several limitations in biological systems, peptides are often conjugated with varying types of nanoparticles to get a better signal to noise ratio and improved pharmacokinetics. This strategy not only provides good imaging quality but also helps in rapid diagnosis. This section highlights some recent reports where peptide and nanoparticle conjugated system has been used for imaging and diagnostic purposes in different infection systems.

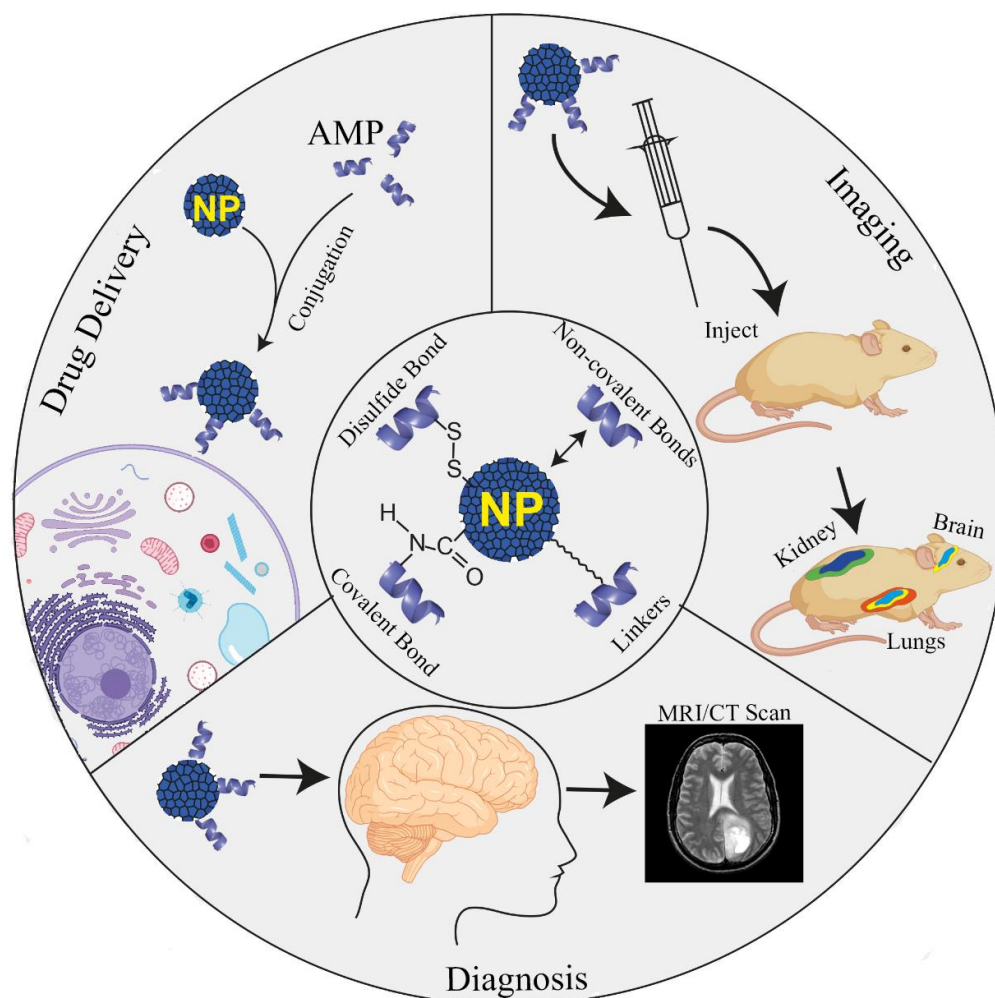


Figure 1.4. Application of NP-AMP conjugates in drug delivery, imaging and diagnostics.

Zhao *et. Al.* have uniquely designed a bacteria activated nanoprobe to monitor MRSA infection in the *in vivo* model [106]. The probe is composed of silicon oxide NP coated with vancomycin. The system was further modified with polyelectrolyte cytochrome complexes which are mainly responsible for the detection of bacteria via dissociation from silicon NP. The whole complex ($\text{SiO}_2\text{-Cy-Van}$) is nonfluorescent in aqueous solvents, but when it comes in contact with MRSA, then the Cy-Van complex gets attached to the bacterial

surface, leading to the change of the state of cypate from aggregation to free form and thus it produces near-infrared fluorescence (NIRF) in *in vitro* condition [106]. *In vivo* experiments in mice model also demonstrated that the complex enables rapid NIRF imaging after injecting it into the mice, and the MRSA colonies can be eliminated via photothermal therapy (PTT). One can monitor the infection site for long term (16 days) to check resurgence of the infections [106]. The whole idea is very novel, and the platform can be used in other detection or diagnosis model to combat MDR strains.

Porous silicon NP (PsiNps) with intrinsic photoluminescence (PL) property was used to monitor the release of an AMP D[KLAKLAK]₂ by Jin *et. Al.* in both *ex vivo* and *in vivo* mice model [107]. The PL lifetime of the NP-complex gets decreased as it dissolves in an aqueous environment, which also indicates the release of payload to the infection site. The PL signal can be used as a probe to track the PsiNP molecules inside the mice via Continuous-wave images (CWI) and time-gated images (TGI) after the injection with high resolution. Being biodegradable by its nature, PSiNPs also get cleared from the organs of the treated animals easily [107]. Thus, it can be used as a self-reporting, non-toxic, non-invasive drug carrier and molecular imaging probe with an accurate assessment of drug distribution.

Multifunctional superparamagnetic iron-oxide nanoparticles (SPION) have been used in different aspects like drug delivery vehicles, imaging probe, or in the diagnostic system used to detect cancer. SPIONs are non-toxic and show excellent biocompatibility in the mammalian system. However, it is non-specific towards a particular drug delivery site. Yu *et. al.* has designed a short linear peptide (3-Methylbutyryl-VV-Sta-A-Sta-C) namely Pepstatin A (PA), which has a high affinity towards multidrug transporter P-glycoprotein (P-gp) situated in the epileptic brain. Overexpression of P-gp protein on BBB is mainly responsible for reduced uptake of anti-epileptic drug in the brain, subsequently leading to drug-refractory epilepsy [108]. They conjugated the PA on SPIONs with near IR probe to target the P-gp proteins on the brain of epileptic mice model. The results showed that the nano-complex can specifically interact with P-gp proteins and can modulate the expression of it [108]. The near IR probe on SPION enabled to detect the signals from the nano-complex via both magnetic resonance imaging (MRI) and *ex vivo* optical imaging without applying any invasive procedure [108].

A recent trend of using luminescent semiconductor nanoparticle or quantum dots (QDs) in cellular or molecular imaging has attracted many researchers for their various tuneable properties. QDs are tiny size nanoparticles with high inherent fluorescence properties at a broad range of wavelengths along with chemical stabilities, which makes it a multidimensional useful nano-system. Conjugation of different peptides including CPP on QDs has shown promising results in cancer therapy and imaging. Walther *et. al.* designed a nanosystem using multicolour QDs and conjugated it with hCT CPP peptide to accurately deliver a siRNA cargo to a particular cell line. Fluorescence microscopic analysis have showed that the system could enter into the cells via an endosomal pathway and then get released from it via the action of chloroquine and thus get diffused into the cytoplasm [109] for targeted delivery. Our group has also reported two hybrid AMPs (KG18 – KNKSRVARGWGRKCPLFG and, VR18 – VARGWGRKCPLFGKNKSR) conjugated with tungsten disulfide (WS₂) QD nanoparticle that can attach to two AMPs (either KG18 or VR18) at a time via thiol group interaction [110]. Thus, it increases the local concentration of AMP on the QD surface which helps the peptide to target bacterial and fungal pathogens at a low micromolar level. At the same time, the inherent fluorescence property of WS₂ QD can be used to track the system inside a cell by using confocal microscopy [110]. These systems can further be used in different approaches for rapid detection and elimination of pathogenic microbes.

The application of NP-AMP conjugates, as discussed above, have been portrayed in Figure 1.4 where a schematic illustration has been given to provide a general idea about this novel theranostics tool.

1.6. Understanding and unveiling the de-novo designed AMP-membrane interactions by employing biophysical techniques

Antimicrobial peptides that occur naturally are an evolutionarily conserved component of the innate immune system. The primary disadvantages of such natural and powerful cationic AMPs like pardaxin, melittin, and gramicidin include their cytotoxicity against mammalian RBC, which limits their use to topical treatment, limited absorption, and high production cost. In light of this, *de-novo* designed and chemically synthesized peptides based on naturally occurring AMPs have received huge attention recently. They are rationally created with an antibacterial pharmacophore while providing a chemical structural flexibility to modify for desirable features such as enhanced activity, decreased cytotoxicity, and proteolysis. To circumvent the problems of producing non-canonical

amino acids and complicated structural motifs, synthetic mimics are utilized. Solid-phase peptide synthesis is utilized to generate a variety of antimicrobial peptides with the capacity of facile changes of certain moieties. Chemically produced peptide mimics are also more cost-effective than traditional approaches. These peptides have been shown to have similar or several folds higher broad-spectrum antibacterial activity and lower toxicity when compared to their native counterparts against drug-resistant pathogens and removal of preformed biofilms.

To understand the method of action of AMPs, we must first comprehend the structure and physical features of the bacterial membrane, which is the primary target of AMPs. Bacteria are categorised as Gram-positive or Gram-negative based on major changes in their cell envelopes. Both types of bacteria have comparable inner or cytoplasmic membranes; however, the outer cell envelopes differ greatly. A layer of crosslinked peptidoglycan adorned with negatively charged teichoic acid surrounds the cytoplasmic membrane in Gram-positive bacteria, providing a thick matrix that preserves the bacterial cell's stiffness. AMPs can diffuse through nano-sized holes that permeate the peptidoglycan layers. In Gram-negative bacteria, the peptidoglycan layer is substantially thinner and less cross-linked. Furthermore, Gram-negative bacteria have an extra outer membrane that exists outside of the peptidoglycan layer. The inner leaflet is entirely composed of phosphate lipids, whereas the outside leaflet is predominantly composed of a special type of glycolipid known as lipopolysaccharide (LPS). LPS molecules have a large number of negatively charged phosphate groups that form salt bridges with divalent cations (e.g., Ca^{2+} and Mg^{2+}), resulting in an electrostatic network. Most hydrophobic antibiotics are blocked by this electrostatic area, resulting in limited permeability. Therefore, the details as to how AMPs penetrate into Gram-positive and Gram-negative bacteria certainly vary in their atomistic interactions. The complexity of biological membrane makes it always difficult or impractical in a lot of case to study the membrane intact. A variety of membrane mimicking models such as vesicles (liposomes), micelles and bicelles have been developed over decades to overcome the obstacles. These mimics come in a variety of shapes and sizes, and they're made by combining existing synthetic lipids with or without detergents. A key concern here is the use of a model system that not only closely replicates the microbial membrane under research, but also depicts their natural environment while being compatible with the biophysical approaches used to investigate them.

Vesicles (liposomes) are the most often utilized biological membrane mimics because they are relatively easy to prepare, handle and, manipulate. The liposomal sphere is made up of self-assembled circular lipid-bilayers that imitate the plasma membrane. An enclosed aqueous compartment that replicates cytoplasm can be utilized to integrate a variety of interesting items (including drugs). A vesicle can be small unilamellar (SUV), large unilamellar (LUV), giant unilamellar (GUV) or multilamellar (MLV), depending on its size and shape. A wide range of biophysical techniques such as fluorescence dye leakage assay, phase contrast microscopic analysis and confocal laser scanning microscopy (CLSM) have been used to investigate the interaction between AMPs and membrane replicated by lipid vesicles. Micelles are liquid-dispersed clusters of surfactant molecules. The repulsive forces between hydrophobic surfactant tails and hydrophilic solvent molecules determined the stability of colloid solution. In structural research by employing solution or solid-state nuclear magnetic resonance (NMR) spectroscopy, lipid or detergent molecules can be utilized as a surfactant to produce micelles and study the micelle bound form of the AMPs. When bioactive peptides interact with detergent micelles, isotropic bicelles, unilamellar vesicles, and even living microbial cells, solution NMR methods are effectively employed to determine their three-dimensional structures. The distance constraints for structure computations are mainly determined using the transferred NOESY (*tr*NOESY) approach. The transferred NOESY (*tr*NOESY, also known as exchange-transferred NOE, *et*-NOE) experiment is a version of the NOESY experiment that is aimed to offer information on the structure of an excess receptor-bound ligand that is in quick exchange between free and bound states. It is often detected utilizing a NOESY experiment that incorporates a relaxation filter to eliminate interfering receptor signals. NOEs form on the bound ligand but appear on the spectrum of the free ligand after dissociation from the complex. Furthermore, the dynamics of interaction between any AMP and membrane mimic can be more precisely deduce from magnetization relaxation NMR (spin-lattice or T_1 and spin-spin or T_2) experiments. Additionally, solid-state NMR techniques help to probe the interaction between the AMPs in anisotropic micelles or bicelles or liposomes that are aligned spontaneously in magnetic fields.

Recent study from multiple groups has determined that AMPs are a specific class of molecules with diverse features. These peptides possess several ideal qualities for further drug development, such as the capacity to permeabilize and rupture the bacterial membrane, the ability to regulate the immune system, broad-spectrum antibiofilm action,

and reduced propensity to select for bacterial resistance. This means that AMPs can adopt a variety of conformations and topologies governed by their structural flexibility; each of which confers diverse biological functions. Such discoveries found to be extremely promising in the present race to produce better and more sophisticated peptide-based therapeutics to fight against infectious diseases like microbial keratitis.

With this context in mind, the work in this thesis aims to -

(A) Describe, investigate, and overcome the limits of peptide-based treatment by employing the approach of *de-novo* antimicrobial peptide design to create peptides that are effective against corneal keratitis-causing microorganisms. The structural insights gained from AMP interactions with bacterial outer and inner membrane components will also pave the path for the development of new antimicrobial peptides.

(B) Application of the *de-novo* designed peptide against real infection models in mice and human cadaveric corneas to check the therapeutic potential of the peptides.

(C) Additionally, potential nano-material has been employed and studied in conjunction with the designed AMP to be used as a drug-delivery system, tracking of biomolecule and potential anti-biofilm agent.

(D) Finally, the interaction of rationally designed and chemically synthesized small molecules to inhibit the amyloidogenic aggregation of lysozyme was deciphered by using biophysical studies.

Chapter II

2. *De-novo* Designing and Biophysical Characterization of Different Antimicrobial Peptides

2.1. *Design, Synthesis, Antibacterial Potential and Structural Characterization of N-acylated Derivatives of Human Autophagy 16 Polypeptide*

This chapter has been adapted from the following publication:

Varnava, K.G., Mohid, S.A., Calligari, P., Stella, L., Reynison, J., Bhunia, A. and Sarojini, V., 2019. Design, synthesis, antibacterial potential, and structural characterization of N-acylated derivatives of the human autophagy 16 polypeptide. *Bioconjugate chemistry*, 30(7), 1998-2010.

2.1.1. Introduction

Increased morbidity and mortality from bacterial infections and the ability of bacteria to mutate and become resistant to successive generations of antibiotics necessitates the development of novel antibacterial drugs [111]. Novel platforms that help to deepen our current understanding of antibacterial drug discovery and create drugs that can be used as weapons against lethal bacterial infections are urgently needed. *Pseudomonas aeruginosa*, *Staphylococcus aureus* and *Escherichia coli* are bacterial pathogens implicated in numerous severe health conditions and infections [112].

Antimicrobial peptides (AMPs) are widely distributed in humans, plants and animals and play crucial roles in protecting the host from bacterial infections [113]. AMPs primarily target the bacterial cell membrane and either create pores or cover the membrane like a carpet ultimately causing bacterial cell lysis [114]. Pore forming AMPs insert part of the peptide into bacterial phospholipid bilayer membranes, bind to a component of the membrane causing membrane lysis, or enter the cells and bind to intracellular targets such as DNA, enzymes or proteins [115]. The overall net positive charge possessed by many AMPs facilitates the interactions with the negatively charged bacterial membrane [115]. The design of a library of peptide antibiotics is usually done using a parent peptide (naturally occurring or designed in the laboratory) followed by structure-activity relationship (SAR) studies and fine tuning the activity of the peptide. Conjugation of fatty acids is often used to enhance the activity and serum stability of AMPs and is a strategy inspired from lipopeptide antibiotics such as polymyxin [116]. N-acylated derivatives of other AMPs have been reported in the literature and have generally led to enhancements in antibacterial

activity [117]. Our ongoing work in this area has led to fine tuning the structure and length of the fatty acid component of the antimicrobial lipopeptide battacin [118].

The work reported in this chapter continues on from a published report on the antibacterial activity of the human autophagy 16 polypeptide (Atg16, K5) [119]. The effect of different N-terminal fatty acids on the activity of a truncated analogue of the human Atg16 has been investigated in this study. An analogue with the best therapeutic index was selected for in-depth biophysical studies to further probe and prove the peptide's ability to insert into and interact with the bacterial membrane. The association between chain length and activity, as well as the accompanying chain length to hemolysis relationship, has been demonstrated through systematic studies. For structural studies Sodium dodecyl-d₂₅ sulfate (d₂₅-SDS) and Dioctanoyl phosphatidylglycerol (D8PG) were used to mimic the anionic environment of bacterial membranes. D8PG was used as an anionic membrane model because the bacterial membranes possess abundant phosphatidylglycerol (PGs) moieties which are mainly targeted by several membrane active proteins and peptides. Interestingly, the peptide shows drastic conformational change from random coil in aqueous solution to helix-loop-helix structure in D8PG micelles, which mimics the bacterial inner membrane. The helical hairpin or helix-loop-helix structure is stabilized through several side chain-side chain and side chain-backbone hydrogen bonds as well as compact hydrophobic interactions by aromatic and hydrophobic residues that play crucial roles in maintaining an amphipathic nature. More importantly, it was possible to delineate the atomistic information about the location of the peptide in the micelle bound form by analysing the intermolecular NOE contacts. The position of the peptide was further supported by paramagnetic relaxation enhancement (PRE) NMR experiments using two different paramagnetic probes, MnCl₂ and 16-doxyyl stearic acid (16-DSA). Collectively, all the information proves that this peptide interacts with bacterial membranes, subsequently leading to cell death by membrane disruption.

2.1.2. Materials and methods

2.1.2.1. Chemicals

All Fmoc-protected amino acids and coupling reagents were purchased from Protein Technologies Inc. 2-Nal (3-(2-naphthyl)-L-alanine) was purchased from ChemPep and OxymaPure, piperidine, trifluoroacetic acid (TFA), triisopropyl silane (TIS), 2,2'-(ethylenedioxy) - diethanethiol (EDDT), and N, N-diisopropylethylamine (DIPEA) were purchased from Sigma-Aldrich.

2.1.2.2. *Synthesis and Purification of Peptides*

All peptides were manually synthesized in University of Auckland, New Zealand by solid-phase peptide synthesis following standard Fmoc protocols using capping steps with acetic anhydride [120]. The peptides were assembled on 2-chlorotriyl chloride resin, on either a 0.1 or 0.2 mmol scale in N, N-dimethylformamide (DMF) as C-terminal acids. The C-terminal amide peptides were assembled on Tentagel S NH₂ resin (substitution level of 0.29 mmol/g) using the Rink amide linker on either the 0.1 or 0.2 mmol scale. A 4-fold excess of each amino acid, 3.9 equivalent of coupling reagent (HCTU), and OxymaPure (3.9 equivalent) as a suppressor of racemization were used. COMU (3.9 equivalent) was used as the coupling reagent for the conjugation of caprylic and palmitic acids only. N, N-Diisopropylethylamine (DIPEA) was used as the base for couplings. Fmoc deprotection was performed using 20% piperidine in DMF. Cleavage from the resin was accomplished using 10 ml of the trifluoroacetic acid (TFA) cocktail mixture (TFA–TIS–H₂O 95:2.5:2.5 v/v/v) per gram of the resin. Upon evaporation of TFA, diethyl ether was added to precipitate the crude peptides. The crude peptides were lyophilized and purified using reverse-phase high-performance liquid chromatography (RP-HPLC) on a GE Pharmacia ÄKTA purifier 10 system or a Thermo Scientific Dionex VWD 3x00 system using a Phenomenex Luna 5 µm C₁₈ 100 Å (250 mm × 10 mm) column. Solvent A was 0.1% TFA in water, and solvent B was 0.1% TFA and 0.09% water in 99% acetonitrile at a flow rate of 10 ml per min. Analytical RP-HPLC was performed using a Phenomenex Luna 5 µm C₁₈ 100 Å (250 mm × 4.6 mm) column with the same solvent system as above at a flow rate of 1 ml per min. Electrospray ionization mass spectrometry (ESI-MS) recorded on a Bruker micro-TOF-Q mass spectrometer and matrix-assisted laser desorption/ionization–time-of-flight mass spectrometry (MALDI-TOF MS) recorded on a Bruker UltrafleXtreme MALDI/TOF were used to characterize the peptides.

2.1.2.3. *Antibacterial Assays*

The minimal inhibitory concentration (MIC) and minimal bactericidal concentration (MBC) were performed in the University of Auckland, New Zealand, by following previously published protocols.[121] Briefly, bacterial strains (*P. aeruginosa*, *E. coli* DH5 α , and *S. aureus* 16207) were plated in Mueller Hinton (MH) plates and grown overnight. From the overnight cultures, single colonies were diluted in fresh MH broth and further incubated to grow to an OD₆₂₅ of 0.1 (approximately 1 × 10⁸ CFU/ml). To prepare the bacterial inoculum, further dilutions according to the above-mentioned protocol were made. The peptide stock solutions were dissolved in type 1 water and serially diluted in the

96-well plates. Then bacterial inoculum was added to each well, and the plates were incubated at 37 °C for 24 h and the absorbance at 625 nm was measured using an EnSpire Multimode Multiskan Go (Thermo). The MIC was considered to be the lowest concentration that showed growth inhibition after 24 h, as observed visually and through absorbance. For MBC determination, 20 µl from each well of the MIC experiment containing peptide K30 and bacteria were plated on Mueller Hinton agar plates in triplicate, and the plates were incubated at 37 °C for overnight. MBC was determined to be the concentration where no bacterial growth occurred on the plates after this overnight incubation.

2.1.2.4. Antifungal Assays

The antifungal activity of the designed peptides was determined in the University of Auckland, New Zealand, according to a standardized broth microdilution method (Clinical and Laboratory Standards Institute (CLSI) document M27-A2).[122] Briefly, the yeast colonies from 24 h cultures of *Candida albicans* were picked and resuspended in 5 ml of sterile 0.145 mol/l saline and adjusted to a cell density of 1×10^6 to 5×10^6 cells/ml. The yeast stock suspension was then diluted to obtain a starting inoculum of 5.0×10^2 to 2.5×10^3 cells/ml. Conventional antifungal drug amphotericin B (Sigma, USA) was included in this study as the control and to compare the antifungal activity with the designed peptides. Peptide and amphotericin B stock solutions were serially diluted in RPMI medium, which was further supplemented with glucose to a final volume of 50 µl per well, giving final concentrations ranging from 120 to 0.235 µM in sterile 96-well polypropylene microplates. Standardized yeast suspensions (50 µl) were then added to each well. Plates were incubated for 48 h at 37 °C. The minimal inhibitory concentration (MIC) was defined as the lowest concentration that inhibited the growth of the fungus as confirmed by visual inspection. The MICs were determined in triplicate, and results were taken at both 24 and 48 h. Hemolysis of Mouse Blood Cells. The Vernon Jensen Unit, Faculty of Medical and Health Sciences, University of Auckland provided us with mouse blood cell that were used fresh for this assay. Several washes of the cells with Tris buffer (10 mM Tris, 150 mM NaCl, pH 7.4) upon centrifugation at 1000g for 5 min were performed, and finally the cells were resuspended in 2% (v/v) Tris buffer. The same buffer was used to dissolve the peptides, which were then serially diluted in 96- well plates. The resuspended blood cells were added to each well, and the plates were left to incubate for 1 h at 37 °C without agitation. Neat buffer was used as the negative control, and 0.25% Triton X-100 was used

as the positive control. The assay was done in triplicate. After incubation, the plates were centrifuged (3500g for 10 min) and the supernatant from each well (100 μ l) was transferred to new 96-well plates and absorbance at 540 nm was measured (Enspire Plate Reader). The percentage of hemolysis, at each peptide concentration, was calculated using the following equation (1):

$$\% \text{ hemolysis} = \left(\frac{A_{\text{exp}} - A_{\text{Tris}}}{A_{100\%} - A_{\text{Tris}}} \right) \times 100 \quad (1)$$

A_{exp} is the experimental absorbance at 540 nm measurement, A_{Tris} is the absorbance of the negative control, where only Tris buffer was added to mouse blood cells, and $A_{100\%}$ is the absorbance of the positive control, where 0.25% Triton X-100 was used to cause the lysis of 100% mouse blood cells present.

2.1.2.5. Circular Dichroism (CD) in SDS, D8PG and DPC Micelles

CD spectra of K30 were recorded in negatively charged (SDS and D8PG) micelles following a previously reported protocol.[123] The spectra were recorded in a Jasco J-815 spectrophotometer (Jasco International Co., Ltd. Tokyo, Japan) equipped with a Peltier cell holder and temperature controller unit accessory. Stock solutions of the peptide and detergents were prepared in 10 mM phosphate buffer (pH 7.4). The CD data was obtained at 37 °C in a 0.2 cm quartz cuvette at a final peptide concentration set at 25 μ M and titrating with increasing concentration of SDS (2-50 mM) and D8PG (2-10 mM) micelles. The far UV spectral range was set at 190 to 260 nm with 1 nm data pitch and averaging 5 accumulations. The buffer subtracted spectral data obtained in millidegree was converted to molar ellipticity (θ) ($\text{deg cm}^2 \text{ dmol}^{-1}$), using equation (2), where m_0 is millidegrees, M is the molecular weight (g mol^{-1}), L is the path length of the cuvette (cm) and C is the concentration (g l^{-1}).

$$\text{Molar ellipticity } (\theta) = \frac{m_0 M}{10 \times L \times C} \quad (2)$$

2.1.2.6. Calcein Dye Leakage Assay

All fluorescence experiments were performed in Jasco FP-8500 spectrophotometer using path length of 0.1 cm quartz cuvette at 37 °C. The anionic bacterial membrane and zwitterionic mammalian membrane mimicking model was prepared by using 1,2-dioleoyl-sn-glycero-3-phosphoethanolamine (DOPE), 1,2-dioleoyl-sn-glycero-3-phospho-(1'-rac-

glycerol) (DOPG), 1,2-dioleoyl-sn-glycero-3-phosphocholine (DOPC) and cholesterol lipids in 3:1 DOPE/DOPG, 7:3 DOPE/DOPG and 6:4 DOPC/cholesterol, respectively, at a final concentration of 2 mg/ml. The lipid mixture was dissolved in chloroform and then a lipid film was prepared by passing N₂ gas over it and lyophilized overnight. The films were subsequently hydrated with 70 mM calcein prepared in 10 mM Tris-HCl buffer (pH 7.4) and then subjected to five freeze-thaw cycles by using liquid nitrogen for freezing and hot water (60 °C) for thawing. Large unilamellar vesicles (LUVs) were obtained by extruding the calcein containing solution for 27 times through a polycarbonate filter (Avanti Polar Lipids, Inc.) of 100 nm diameter. Free calcein was removed via gel filtration using a Sephadex G-50 column (GE Healthcare, Uppsala, Sweden) previously saturated with same buffer. Calcein leakage experiment was done by adding K30 peptide using a series of concentrations starting from 1 to 20 μM into the fixed concentration of LUVs (20 μM) suspended into 10 mM Tris-HCl buffer with 100 mM NaCl. Measurement was done using the emitted fluorescence of calcein (515 nm) that leaked from LUVs via the interaction of K30 peptide. 0.1% Triton X-100 (Sigma-Aldrich, St. Louis, USA) was added as positive control and only LUVs were added as negative control. Measurement of calcein leakage (C) was calculated using equation (3):

$$C = \left(\frac{F_{exp} - F_0}{F_T - F_0} \right) \times 100 \quad (3)$$

where F_0 is the initial calcein fluorescence intensity, F_{exp} is the final fluorescence intensity 5 min after addition of the peptide and F_T is the highest fluorescence intensity after addition of Triton X-100.

2.1.2.7. Isothermal Titration Calorimetry (ITC)

Isothermal Titration Calorimetry (ITC) was performed to determine the thermodynamic parameters of binding of K30 peptide with D8PG and DPC micelles using a VP-ITC microcalorimeter (Malvern PANalytical Inc, Westborough, MA, USA) and TA-affinity ITC (TA instruments, Lukens Drive, New Castle, DE, USA). All detergents and peptide were dissolved in 10 mM phosphate buffer at pH 7.4 and degassed. A sample cell (volume 200 μl) containing 0.5 mM K30 was titrated against D8PG and DPC from a stock solution of 25 mM at 308 K. A total of 20 injections were carried out at an interval of 3 min with 2 μl of detergent aliquots per injection. The raw data were plotted using Origin v9 software supplied with the instrument. The data was fitted using a single site binding model. The fitting was done in the same software which produced the dissociation

constant (K_D), change in heat of enthalpy of reaction (ΔH°), free energy of binding (ΔG°) and entropy (ΔS°). All these parameters were evaluated using the equations $\Delta G^\circ = -RT \ln K_D$ and $\Delta G^\circ = \Delta H^\circ - T\Delta S^\circ$, respectively. Binding affinity $K_A (M^{-1}) = 1/ K_D (M)$.

2.1.2.8. NMR Spectroscopic Analysis

All NMR experiments were performed at 310 K on a Bruker Avance III 500 MHz equipped with a 5 mm SMART probe spectrometer and 600 MHz equipped with RT probe. NMR samples were prepared in 10% deuterated water (pH 4.5) and 3-(Trimethylsilyl) propanoic acid (TSP) was used as an internal standard (0.00 ppm). Two-dimensional (2D) 1H - 1H total correlation spectroscopy (2D TOCSY), and 2D 1H - 1H Nuclear Overhauser effect spectroscopy (2D NOESY) was recorded for the peptide with a mixing time of 80 ms and 150 ms respectively keeping a spectral width of 12 ppm in both directions. Next, the interaction of the K30 / K22 / K22.2 peptide (1mM) upon successive titration with D8PG and predeuterated d_{25} -SDS (200 mM) was monitored by 1D proton NMR acquired using excitation-sculpting scheme for water suppression and the States-TPPI for quadrature detection in the t1 dimension. Consequently, 2D NOESY spectra of the peptide in the context of D8PG and d_{25} -SDS were acquired with 150 ms mixing time.

Paramagnetic relaxation enhancement (PRE) NMR experiments were performed to measure the depth of insertion of K30 peptide in D8PG/ d_{25} -SDS micelles. The experiment was done by titrating with surface paramagnetic quencher, manganese chloride ($MnCl_2$) dissolved in water and in-depth paramagnetic quencher 16-doxyl-stearic acid (16-DSA) dissolved in deuterated methanol (d_4 -MeOH), into the NMR samples containing peptide and micelles. The sample was allowed to equilibrate for few min before the acquisition of 2D TOCSY spectra with the same acquisition parameters as mentioned above. NMR data processing and analysis were carried out using TopspinTM v3.1 (Bruker Biospin, Switzerland) and SPARKY [124] (Goddard, T. D., and Kneller, D. G., University of California, San Francisco) programs, respectively.

2.1.2.9. NMR Derived Structure Calculations

The three-dimensional NMR derived structures were first calculated using the CYANA program (version 2.1) as reported previously[125] without the N- and C- terminal 4-methyl hexanoyl and 3- (2-naphthyl) -L- alanine residues, respectively. Briefly, on the basis of cross-peak intensities obtained from the NOESY spectra recorded in presence of D8PG and d_{25} -SDS micelles at a mixing time of 150 ms, the NOE intensities were qualitatively categorized into strong, medium and weak and then translated to upper bound

distance limits to 2.5, 3.5 and 5.0 Å, respectively. The lower bound distance constraint was fixed at 2.0 Å. The backbone dihedral angle phi (Φ) and psi (ψ) were restrained (-30° to -120° and 120° to -120° , respectively) for all non-glycine residues of the peptide to minimize the conformational space. No hydrogen bond constraints were used in the structure calculation. Several rounds of structure calculations were carried out and depending on NOE violations, the distance constraints were adjusted. Out of the 100 structures, 20 lowest energy structures were used for further analysis.

The peptide structure obtained from CYANA was completed with the N-terminal 4-methylhexanol and the C-terminal 3-(2-naphthyl)-L-alanine (2Nal). The resulting structure was then refined in the University of Rome, Italy, by all-atom molecular dynamics (MD) simulation with NOE-derived distance restraints. The AMBER03 force field was used to model all atomic interactions. Calculation of the partial atomic charges for the terminal groups was performed by calculating the electrostatic potential at the HF/6-31G(d) level of theory using R.E.D. Server Development. MD was performed with GROMACS software applying ensemble-averaged NOE distance restraints as flat-bottomed harmonic potential terms with a force constant of 2000 kJ/mol. The initial structure was first refined with energy minimization and a short-simulated annealing run (temperature range 300–500 K) of 500 ps in a periodic simulation box filled with 1600 explicit water molecules (modelled by the TIP3P force field). The particle mesh Ewald algorithm was applied to calculate electrostatic forces, while range-limited nonbonded interactions were calculated with a 10 Å cut-off. During these steps, only the terminal residues were free to move without additional position restraints. After equilibration, four replica production runs of 30 ns were performed and a set of 20 lowest-energy structures were extracted from the resulting trajectories. For comparison, the peptide structure was also modelled by in vacuo MD simulations; the resulting structures were very similar to the solvated ones (backbone RMSD ~ 1 Å between the lowest-energy conformers obtained by the two approaches).

2.1.3. Results and discussion

2.1.3.1. Design and Synthesis of the Peptide Library

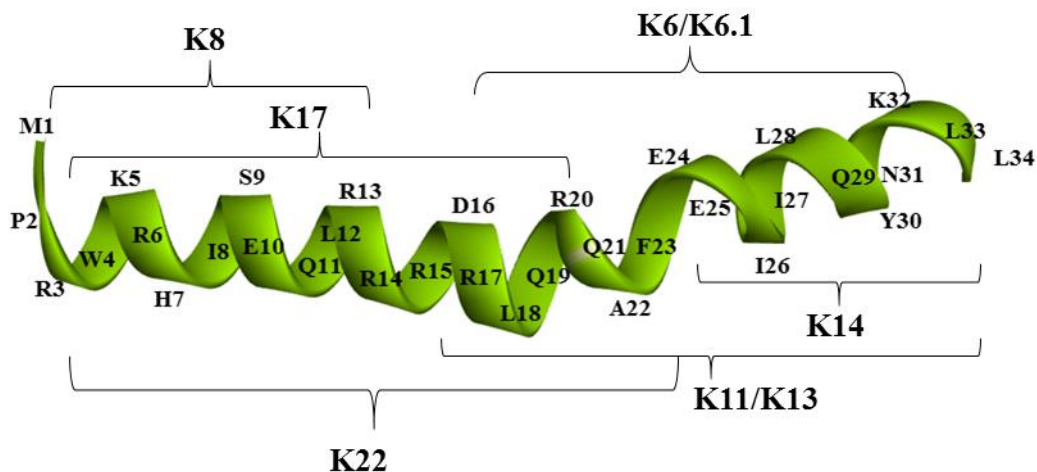


Figure 2.1.1. Sequence and motif of human Atg16 (K5). The position of the synthetic truncated peptides is indicated in the diagram.

The crystal structure of Atg16 bound to Atg5 shows that the peptide (Atg16, K5) adopts a helix-loop-helix motif when bound to its target protein (Atg5). A library of truncated forms corresponding to the two helices, the loop and several fragments of the helix-loop-helix motif of Atg16 has been synthesised. All peptides in this library have significantly lower positive charge than K5, two are neutral and one is anionic. (Figure 2.1.1 and Table 2.1.1).

Table 2.1.1. Library of Truncated Analogues of the Human Atg 16 (K5)

Peptide	Sequence	Net charge at pH=7
K5	MPRWKRHISEQLRRRDRLQRQAFEEIILQYNKLL	5
K6	DRLQRQAFEEIILQYNK	0
K6.1	DRLQRQAJEEIILQYNK	0
K7	ILQYNKLL	1
K8	MPRWKRHISEQLR	3
K11	RDRLQRQAFEEIILQYNKLL	1
K13	RDRLQRQAJEEIILQYNKLL	1
K14	EEIILQYNKLL	-1

All peptides in the current library have the Phe residue, where present, substituted with 2-naphthyl alanine (2-Nal), based on our previous observation that this substitution is

beneficial to the antibacterial activity of the peptide. Unfortunately, none of the peptides exhibited antibacterial or antifungal activity, which reiterates the charge-dependent mode of action of the Atg-16 peptide family, as has been recently reported by us.[126] Additionally, the length of the peptide chain can also be a determining factor for antimicrobial activity.

Therefore, peptide K17, which is the shortest possible fragment (residues 3-20) with the highest net positive charge, was synthesized. This peptide also showed only moderate activity against bacterial strains (Table 2.1.2). The sequence of K17 was also extended by three more residues in order to include Phe 23, resulting in K18. A further analogue of K17 substituting Phe to 2-Nal (K22) was also synthesised. As compared to K5, both K18 and K22 showed moderate enhancement in potency against bacterial strains, indicating that the aromatic residue at position 23 is also crucial for antibacterial activity in this peptide family.

Table 2.1.2. Antibacterial Activity of Peptides and Peptide Conjugates

No	Code	Sequence	<i>C. albicans</i>		<i>P. aeruginosa</i>	<i>E. coli</i>	<i>S. aureus</i>	Net charge at pH=7
			24hr	48 hr				
1	K17	RWKRHISEQLRRRDRLQR	>120.0	>120.0	>120.0	>120	45.5-91	6
2	K18	RWKRHISEQLRRRDRLQRQA F	>120.0	>120.0	60.0-120.0	60-120	28.8-57.6	6
3	K22	RWKRHISEQLRRRDRLQRQA J	60.0-120.0	>120.0	60.0-120.0	30-60	14.4-28.8	6
4	K24	R^1 - RWKRHISEQLRRRDRLQRQA J	60.0-120.0	>120.0	60.0-120.0	32-64	7.2-14.4	5
5	K28	R^2 - RWKRHISEQLRRRDRLQRQA J	3.7-7.5	7.5-15.0	4.5-9.5	6.4-12.8	1.8-3.2	5
6	K30	R^1 - RWKRHISEQLRRRDRLQRQA J-NH ₂	30.0-60.0	60.0-120.0	13.5-27	6.4-12.8	0.9-1.8	6
7	K31	R^2 - RWKRHISEQLRRRDRLQRQA J-NH ₂	3.2-6.4	7.5-15.0	3.2-6.4	3.2-6.4	1.8-3.2	6

8	K33	R^{3-} RWKRHISEQLRRRDRLQRQA J-NH ₂	1.8-3.7	3.7-7.5	6.4-12.8	3.2- 6.4	1.8-3.2	6
9	K34	R^{2-} RWKRHISEQLRRRDRLQRQA F-NH ₂	1.8-3.7	3.7-7.5	6.4-12.8	3.2- 6.4	1.8-3.2	6
10	K36	R^{5-} RWKRHISEQLRRRDRLQRQA J-NH ₂	15.0- 30.0	15.0- 30.0	6.4-12.8	3.2- 6.4	0.9-1.8	6
11	K46	R^{4-} RWKRHISEQLRRRDRLQRQA J-NH ₂	30.0- 60.0	30.0- 60.0	3.2-6.4	3.2- 6.4	1.8-3.2	6
11	Streptomycin		NT	NT	NT	NT	1.8-3.2	NA
12	Polymyxin		NT	NT	<0.9	<0.9	NT	5
13	Amphotericin		0.9-1.8	0.9-1.8	NT	NT	NT	NA

^aThe assays were carried out three times, in triplicate each time. J = 2-Nal. The MBC and MIC values for the lead peptide (K30) are identical.

2.1.3.2. Fatty Acid Conjugates

A small library of fatty acid conjugates of K22 was generated (K24-K34 and K46), where linear fatty acids ranging in length from 10-16 carbon atoms, as well as a branched chain fatty acid, were conjugated to the N-terminus of K22 (Figure 2.1.2). All these analogues carry C-terminal amidation, to retain the overall net positive charge of K22. Our previous studies on the battacin peptides showed that the presence of Fmoc protecting group may also increase the activity of the peptides. Therefore, the Fmoc protected analogue of K22 in the amidated form (K36) was also included in the library (Figure 2.1.2). Palmitic and caprylic acid precipitated out during the activation step when HCTU was used as the coupling reagent. However, use of COMU as the coupling reagent helped to address this issue. COMU, a morpholinium-uronium coupling reagent, can be found only in *O*-form, the most reactive uronium species, when coupling. In contrast HCTU, an ammonium uronium-based coupling reagent can be found in both *O*- and *N*-forms but the most predominant form is the less reactive *N*-form. The two active forms present during coupling may be the reason for the solubility issues of the fatty acids.

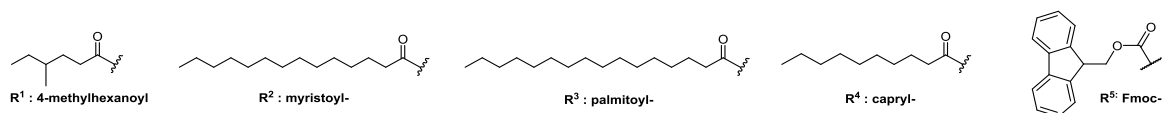


Figure 2.1.2. Chemical structures of the N-acyl chains used to synthesize the peptide conjugates.

2.1.3.3. Antimicrobial Assays

All of the fatty acid-conjugated peptides have shown a remarkable increase in activity against both bacterial and fungal strains as compared to the nonconjugated peptides (Table 2.1.2 and Figure 2.1.2). Even though fatty acid conjugation to peptides is known to increase their antimicrobial potential, in many cases the activity–toxicity relationship was not examined thoroughly or data were not presented. In the current Atg16 peptide library, this increase in activity coincided with an increase in hemolysis (Figure 2.1.3). The significant increase in the hemolysis of the fatty acid conjugates compared to K22 (Figure 2.1.3) can be attributed to the loss of selectivity against bacterial membranes upon fatty acid conjugation and an interaction of the fatty acid chain with bacterial and mammalian cell membranes in general. Interestingly, even though K30, the peptide conjugated to 4-methyl hexanoic acid, showed negligible activity against the tested fungal strain, to our delight it showed increased potency against all bacterial strains, particularly nanomolar activity against *S. aureus*, while retaining very low hemolysis even at high concentrations (5% at 1 mM) (Table 2.1.2 and Figure 2.1.3). The minimal bactericidal concentration (MBC) of K30 was the same as the minimal inhibitory concentration (MIC), indicating a bactericidal rather than a bacteriostatic effect of the peptide, further highlighting the importance of our findings. When taken together, the activity of the peptide against bacterial cells and the low hemolysis indicate that peptide K30 binds and interacts selectively with bacterial and not mammalian membranes. To investigate this hypothesis further, we have performed a series of biophysical experiments using bacterial and mammalian cell membrane mimics. It is not surprising that the peptide has comparatively higher potency against the Gram-positive strain (*S. aureus*) than against the two Gram-negative strains (*P. aeruginosa* and *E. coli*) tested. The presence of the lipopolysaccharide in Gram negative bacteria is known to create an additional barrier which minimizes the access of antibiotics to the outer membrane, which would necessitate a higher drug concentration to elicit antibacterial activity. Nevertheless, results from the dye-leakage experiments (showed later) prove that the peptide indeed does damage the membranes of both Gram-positive and Gram-negative bacteria, even though higher peptide concentrations were needed against the Gram-negative strains.

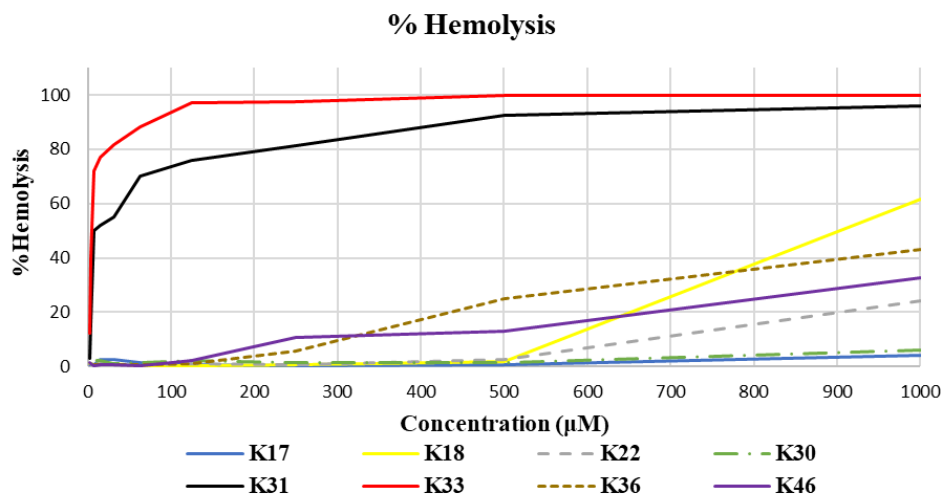


Figure 2.1.3. Percentage of hemolysis of mouse blood cells at various peptide concentrations. The experiment was done in triplicates and results averaged out.

2.1.3.4. Circular Dichroism (CD)

Figure 2.1.4 (A) shows the far UV region of the CD spectrum of K30 in phosphate buffer, SDS and D8PG micelles. The peptide adopted a random coil conformation in 10 mM phosphate buffer (pH 7.4), as evidenced from the characteristic single negative minimum at 201 nm in the CD spectrum. In the presence of SDS micelles (2 to 50 mM), K30 showed a weak positive band at ~190 nm and a weak negative band at 203 nm; no other peaks were observed, suggesting that the peptide does not adopt a well-defined secondary structure in SDS micelles. In contrast, for K30 in D8PG micelles, the positive band at 190 nm increased its intensity more than two-fold and the negative band shifted towards ~206 nm. Another negative shallow peak was also observed at ~220 nm, indicating a shift from random coil to folded conformations, with resemblance to alpha-helical conformation in the D8PG micellar environment.

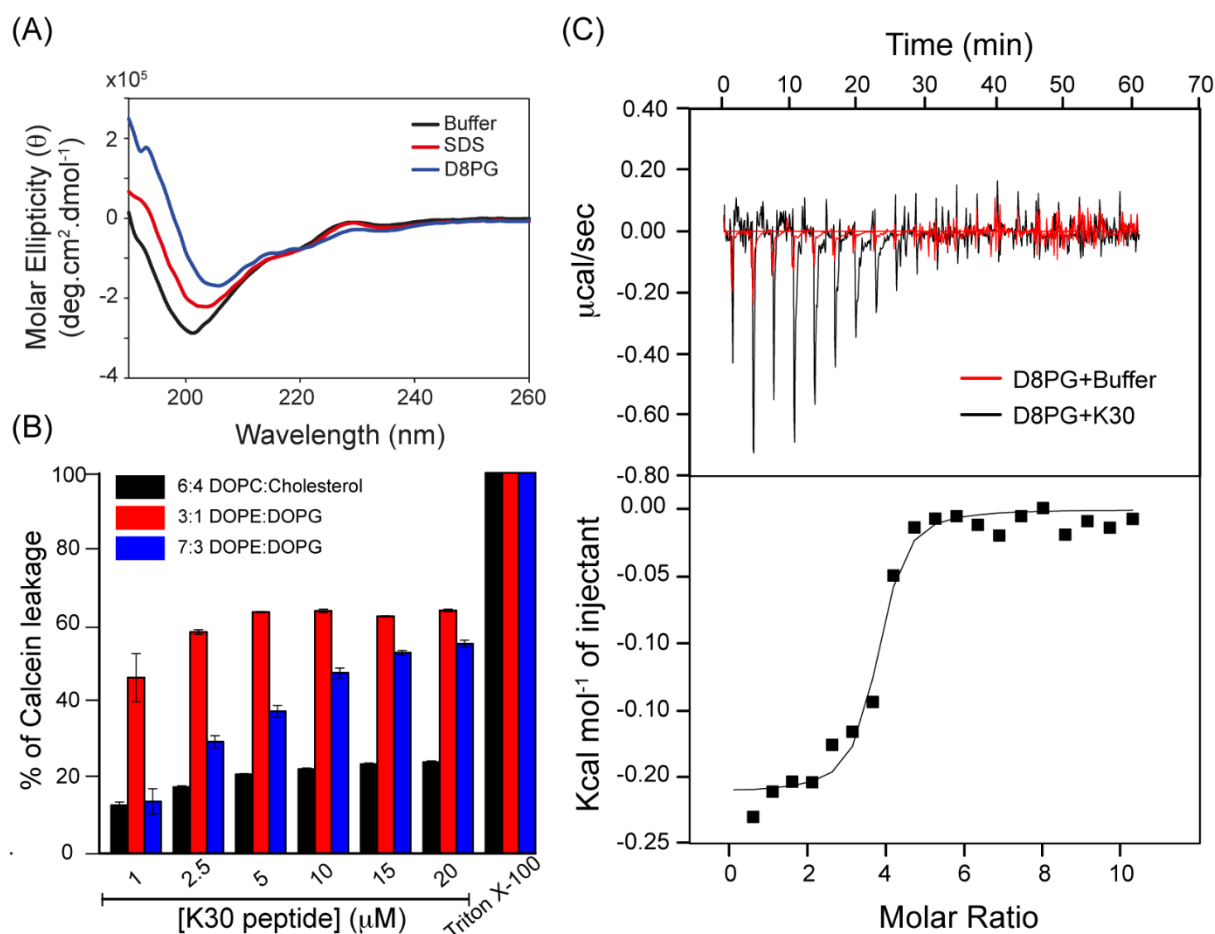


Figure 2.1.4. (A) CD spectra of K30 (25 μM) in 10 mM sodium phosphate buffer (pH 7.4) (black line), 5 mM SDS (red line) and 2 mM D8PG (blue line) micelles. The experiment was repeated twice. (B) Bar diagram showing the leakage, in percentage, of calcein entrapped in membrane vesicles, in the presence of increasing concentrations of K30. The experiment was performed in three different model systems viz. 7:3 DOPE/DOPG (blue bars), 3:1 DOPE/DOPG (red bars) and DOPC containing 40% cholesterol (black bars). All experiments were repeated three times and the data were averaged (\pm S. D). (C) Upper panel shows the heat of reaction (μcal) in time (sec) for K30 – D8PG (black) and D8PG-buffer (red) interaction. Lower panel shows the corresponding enthalpy change of the reaction per mole of K30 where the heat of dilution was subtracted. The experiment was performed by injecting 2 μl aliquots of D8PG from a 25 mM stock into the sample cell containing the 500 μM K30 peptide dissolved in 10 mM sodium phosphate buffer (pH-7.4).

2.1.3.5. Calcein Dye Leakage Assay

In order to assess the membrane perturbing potential and membrane specificity of K30, we evaluated the leakage of calcein dye entrapped in liposomes made of 3:1 DOPE/DOPG, 7:3 DOPE/DOPG and DOPC with 40% cholesterol as shown in Figure 2.1.4 (B). The DOPE/DOPG combination facilitates unilamellar, stable and perfect liposomes due to the presence of symmetric, long and unsaturated acyl chains of these phospholipids.

The fluorescence intensity of calcein is very low when it is entrapped in large unilamellar vesicles (LUV) at a self-quenching concentration of 70 mM. However, administration of a membrane perturbing peptide destabilizes the vesicles leading to concomitant calcein release, which gets diluted in the outer volume hence increasing its fluorescence intensity. K30 was tested at a concentration of 1-20 μM in 3:1 and 7:3 DOPE/DOPG liposomes, which mimics the inner membrane of all bacterial species and outer membrane of Gram-negative bacteria, respectively.[127] It is worth mentioning that the membrane composition of bacteria varies depending on the strain but the major lipids are phosphatidylethanolamine (PE) and phosphatidylglycerol (PG) and are identical for the plasma membrane of Gram positive and Gram-negative bacteria respectively. After addition to the anionic lipid vesicles, K30 gave rise to 46% leakage at 1 μM in case of 3:1 DOPE/DOPG LUVs and gradually increased to 58% and 63% at 2.5 and 5 μM , respectively, within 15 min; no further increase was observed till 20 μM . Additionally, time kinetics experiment was performed using the same LUVs at 1 μM and 10 μM concentration for 1 h to understand the effect of K30 peptides on the 3:1 DOPE/DOPG LUVs. Figure S2.1.1 showed that the peptide is capable to release the same amount of calcein at 1 μM concentration within approximately 15 min. In case of the LUVs made of 7:3 DOPE/DOPG, a concentration dependent calcein release was observed which started from 13% at 1 μM and finally reached up to 55% at 20 μM . Interestingly, in case of LUV composed of DOPC and 40% cholesterol, which mimics the eukaryotic cell membrane, only 12% leakage was observed at 1 μM concentration of K30 peptide with saturation observed at 15 μM showing maximum of 23% leakage. These results, taken together, indicate that the peptide is particularly selective to bacterial membranes but not toxic to eukaryotic cell membranes. This finding also correlates well with our MIC and hemolysis assays and further establishes the membrane specific activity of the peptide.

Table 2.1.3 Thermodynamic parameters of K30, K22 and, K22.2 binding to D8PG micelle. The experiment was performed in 10 mM sodium phosphate buffer (pH 7.4) and at 35°C.

Peptide	n (number of binding sites)	ΔH° (kcal/mol)
K30	4	-0.21 ± 0.006
K22	6	-2.31 ± 0.052
K22.2	7	-2.44 ± 0.040

2.1.3.6. Isothermal Titration Calorimetry (ITC) Analysis of K30 in D8PG and DPC Micelles

Isothermal titration calorimetry (ITC) provides thermodynamic parameters such as changes in enthalpy (ΔH°), entropy (ΔS°) and Gibbs free energy of binding (ΔG_b°) along with binding affinity (K_D) allowing to investigate the receptor-ligand binding phenomenon. The ITC experiments were performed to identify the crucial thermodynamic forces underlying the binding of K30 to the D8PG and DPC micelles. Figure 2.1.4 (C) shows the thermogram and the corresponding titration curve of the peptide in D8PG micelles. The integrated heat, shown in the thermogram indicates the total heat of each injection after subtracting the heat of dilution of the lipid in the same buffer. A single site binding model provided information such as the number of binding sites (n) and the change in standard enthalpy (ΔH°) (Table 2.1.3). The dissociation constant from the fitted curve was much lower than the concentration of peptide K30. The experiment was also repeated with a lower peptide concentration (24 μM); however, the signal followed an unphysical trend, which made it difficult to reliably determine the thermodynamic parameters (Appendix II, Figure S2.1.3A). It was interesting to observe from Table 2.1.3 that one K30 molecule interacts with three to four molecules of D8PG. Additionally, ΔH° for the K30–D8PG micellar interaction was found to be -0.21 ± 0.006 kcal/mol, suggesting that the reaction is mainly driven by entropy rather than enthalpy (Appendix II, Figure S2.1.2). Because the standard enthalpy (ΔH°) is fairly small for the K30–D8PG interaction, electrostatic forces do not play an important role in this reaction. In contrast, for the K30–DPC interaction no saturation was observed in the ITC thermogram (Appendix II, Figure S2.1.3 (B)), and the heat of dilution of DPC in the buffer was more intense than for the peptide, which indicates that the peptide does not interact with zwitterionic micelles. Furthermore, to understand the roles of acylation and amidation of the peptide sequence, we also performed the ITC experiments for K22–D8PG and K22.2–D8PG interactions (Appendix II, Figure S2.1.4). Apart from the fact that one peptide molecule interacts with six to seven molecules of D8PG (Table 2.1.3), the major difference we observed was that the ΔH° values for both K22–D8PG and K22.2–D8PG are 10 times higher than that for K30–D8PG, suggesting that the interactions of K22 and K22.2 with D8PG are mostly electrostatic.

2.1.3.7. Solution Structure of K30 peptide

A comparison of ^1H NMR spectra of the K30 in free and bound form with both D8PG and d_{25} -SDS micelles showed an overall change in chemical shifts as well as line broadening when bound to micelles, indicating that the peptide interacts with both micelles

(Appendix II, Figure S2.1.5). Two dimensional (2D) homonuclear ^1H - ^1H TOCSY and NOESY experiments were conducted in aqueous buffer and both d_{25} -SDS and D8PG micelles to gain insight into the three-dimensional structure of K30. The NOESY spectrum of K30 in aqueous solution showed only a limited number of intra- and inter-residue NOEs between backbone and side chain protons. Though the NOESY spectrum of K30 in d_{25} -SDS micelles was dispersed with distinct peptide signals, neither medium range αN ($i, i+2/3/4$) nor long-range side chain/side chain or side chain/aromatic NOEs were observed (Appendix II, Figure S2.1.6), correlating well with the CD spectrum that the peptide K30 did not adopt any particular folded conformation in the presence of SDS. Strikingly, K30 in the presence of D8PG micelles showed several intra, sequential and long range NOEs (Figure Figure 2.1.5 (A-B)) which primarily suggests that the peptide adopts some folded conformation upon interaction with D8PG. Additionally, a large number of medium range αN ($i, i+2/3/4$) NOEs were observed at the N-terminal region of K30 in D8PG micelles (Figure 2.1.5 (B)). The marked chemical shift deviation of C^αH resonances of K30 from the random coil values also supports a folded conformation of the peptide K30 in D8PG micelles (Figure 2.1.5 (C)). Generally, $\Delta\text{H}\alpha$ values for four continuous residues with upfield shifts indicate α -helical conformation. The NOE connectivity diagram for K30 in D8PG micelles is shown in Figure 2.1.5 (C). A combination of strong sequential (i to $i+1$), medium ($\text{H}^\alpha_i\text{-H}^{\text{N}}_{i+1}$, $\text{H}^\alpha_i\text{-H}^{\text{N}}_{i+3}$, $\text{H}^\alpha_i\text{-H}^\beta_{i+3}$), and weak ($\text{H}^\alpha_i\text{-H}^{\text{N}}_{i+4}$) NOE cross peaks indicate a helix-loop-helix structure where helical folding is evident for the stretch between R4 to R11 and L16 to A20. Figure 2.1.5 (A) shows the long-range NOEs between the aliphatic side chains of I6, L10, L16 and A20 with the aromatic ring protons of W2. Surprisingly, the indole ring proton ($\text{N}\epsilon\text{H}$) of W2 did not show any long-range NOEs with the aliphatic side chain of any amino acids (Appendix II, Figure S2.1.7). In contrast, we observed a larger number of NOEs between aromatic ring protons of W2 and aliphatic $\text{C}\beta\text{H}$ s of A20 and $\text{C}\gamma\text{H}$ s/ $\text{C}\delta\text{H}$ s of L16, depicting that these long-range NOEs could be instrumental in forming a hydrophobic hub at the central region to stabilize K30 in D8PG micelles. To further understand the role of acylation and amidation, two-dimensional TOCSY and NOESY experiment was also performed using K22 and K22.2 peptide in D8PG micelle. However, due to huge precipitation of the peptides in D8PG micelle we could not observe any NOEs and hence no structure could be determined (Appendix II, Figure S2.1.8 and S2.1.9).

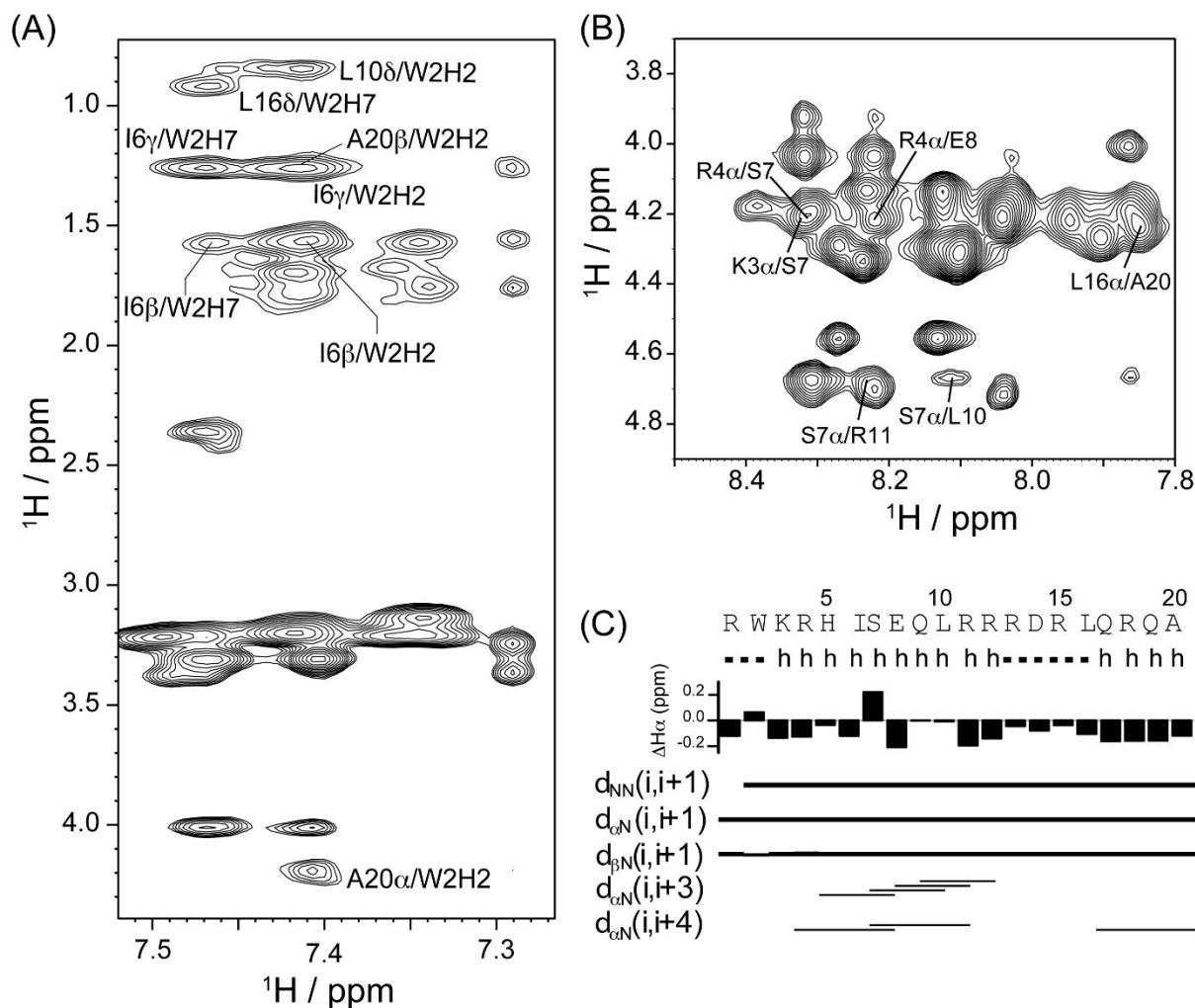


Figure 2.1.5. (A) Long range NOEs between the side chains of I6, L10, L16, A20 and aromatic protons of W2. (B) Medium range αN (i to $i+3/i+4$) NOEs of K30 in D8PG micelles. The experiment was performed at 310K on Bruker Avance III 500 MHz NMR spectrometer, equipped with a SMART probe. (C) The sequence of K30 where helical regions are denoted by 'h' and loop regions are denoted by '---'. Chemical shift index (CSI) showing upfield shifts for most of the amino acid residues. Bar diagram showing the sequential and medium range NOEs.

The three-dimensional solution structure of K30 bound to D8PG was first calculated using CYANA program using 132 NOE-derived distance restraints and 18 backbone angle restraints (see materials and method for details). Backbone angle restraints were derived from PREDITOR,⁴³ based on H^α protons of the amino acids. An ensemble of 20 backbone structures of D8PG bound to K30 peptide is shown in Figure 2.1.6 (A). The average backbone RMSD of the 20 lowest energy structures (excluding the N-terminal 4-methyl hexanoyl and C-terminal 2-Nal as they are very flexible in nature) is $0.74 \pm 0.22 \text{ \AA}$ whereas the RMSD values for heavy atoms are found to be $1.74 \pm 0.34 \text{ \AA}$ (Table 2.1.4).

PROCHECK analysis of the peptide shows that 95% of the residues are in favoured region of the Ramachandran plot. Table 2.1.4 shows a detailed statistic of the structures. Subsequently, an MD simulation in water was performed including 4-methylhexanoyl and 3-(2-naphthyl)-L-alanine) at the N- and C-termini of K30, respectively. The backbone RMSD is 0.89 Å in the absence and presence of capping at both terminals.

Table 2.1.4. Summary of statistical analysis of the 20 lowest energy structures of peptide K30 in D8PG micelles.

Distance restraints	
Intra residue ($i - j = 0$)	46
Sequential ($ i - j = 1$)	59
Medium range ($2 \leq i - j \leq 4$)	19
Long range ($ i - j \geq 5$)	8
Total	132
Angular restraints	
Φ	20
Ψ	20
Distance restraints from violation (≥ 0.4 Å)	0
Deviation from mean structure (Å)	
Average backbone to mean structure	0.74 ± 0.22
Average heavy atom to mean structure	1.74 ± 0.34
Ramachandran plot*	
% Residues in the most favoured regions	88.9%
% Residues in the additional allowed region	11.1%
% Residues in the generously allowed region	0%
% Residues in the disallowed region	0%

*Obtained from PROCHECK NMR.

The solution structure of K30, bound to D8PG was characterized by helical hairpin or helix-loop-helix conformation, resembling several other antimicrobial peptides such as MSI-594, paradaxin and KYE28. The architecture of the D8PG bound K30 is tuned by the N-terminal helix W2-R11 followed by a loop involving residues R12-R15 and then a short helix L16-A20 (Figure 2.1.6 (B)). Close inspection suggests that the peptide adopts an amphipathic structure. The folded conformation was stabilized by the hydrophobic interactions between W2, I6, L10, L16, A20 and 2-Nal residues, which created a compact hydrophobic hub opposite to the charged residues (Figure 2.1.6 (C)). The interesting feature of this peptide sequence is that it has only 25% hydrophobic/aromatic amino acid residues and all of them are involved in forming the hydrophobic hub, governing the structural stabilization. In addition, the N-terminal helix is stabilized either by salt bridge or hydrogen bond interactions between side chains of R4-E8 or E8-R11 or S7-R11 (Figure 2.1.6 (D)). The hydrophobicity and charge distribution on the surface of the peptide is also shown in Figure 2.1.6 (E) which clearly depicts that the cationic residues are present on one side and hydrophobic residues are present on the opposite side which makes the peptide amphipathic in nature. The amphipathic composition of K30 helps in stabilizing the loop region to a great extent. Since D14 is juxtaposed with R13 and R18, it can easily form a triad unit R13-D14-R18 by side chain-side chain electrostatic interactions (Figure 2.1.6 (D)). Additionally, the backbone-side chain hydrogen bond was also observed between L16-D14, which subsequently stabilizes the folded loop structure of the K30 (Appendix II, Figure S2.1.10). The presence of positively charged microenvironment throughout the peptide sequence, supported by potential electrostatic map (Figure 2.1.6 (E)), helps in the initial interaction with negatively charged bacterial membranes which, we believe, in turn helps the membranolytic property of the peptide towards microbial cells.

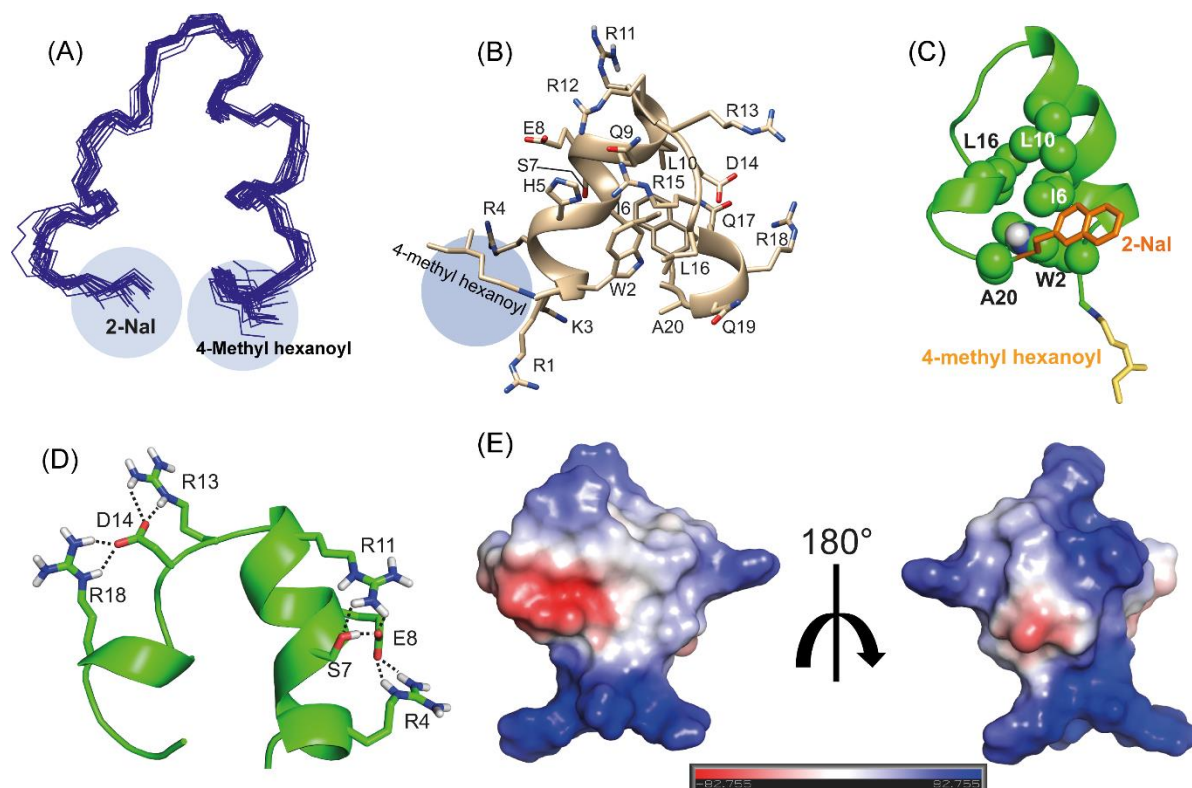


Figure 2.1.6. (A) An ensemble showing the superposition of twenty lowest energy backbone (N, C α and C') structures of K30 peptide in D8PG micelle. The PDB acquisition code is 5ZYX.pdb. (B) A representative structure of K30 peptide bound to D8PG, showing the orientation of the side chains. The peptide K30 adopts amphipathic structure in D8PG micelles. (C) Hydrophobic hub of K30 peptide comprising of aromatic (W2) and non-polar residues such as I6, L10, L16 and A20. (D) The black dotted line represents the plausible electrostatic interactions and/or hydrogen bonds for further stabilization of K30 in micelle bound form. (E) Electrostatic potential surface of K30 in D8PG micelles. Blue, white and red color denotes the positively charged, neutral and negatively charged amino acid residues (the average electrostatic surface potential energy is ± 82.76 Kcal/mol.e $_c$). The images were prepared by MOLMOL, PyMOL and Chimera software.

2.1.3.8. Orientation of K30 Peptide in D8PG Micelles

The orientation of K30 in D8PG micelles, was further established by investigation of the intermolecular NOEs between the peptide and lipid from the NOESY spectra. As the peptide K30 and D8PG possess unique chemical shifts, it is possible to probe the intermolecular NOEs between the two different molecules. Figure 2.1.7 (A) shows the chemical structure of the D8PG and Figure 2.1.7 (B-E) and S2.1.11 show several 1D slices taken from the 2D spectral regions, corresponding to D8PG signals e.g., 1.23 ppm (C3–C7 H), 2.34 ppm (C2H), and 5.25 ppm (H β). These unique chemical shifts of the D8PG lipid molecule do not mix with the peptide signals. They also cover the entire peptide signals

providing crucial intermolecular NOEs, which help us to map the location of the peptide in the lipid environment. The observed distinct sharp peaks shown in Figure 2.1.7 (C) reveal that majorly of hydrophobic and aromatic residues are interacting with the C3-C7 acyl chain of the lipid molecule. In contrast, charged and polar residues such as E8, Q9 and Q17/Q19 are in close proximity to C2 of D8PG (Figure 2.1.7 (D)), suggesting that the hydrophobic and aromatic residues are in close proximity to the hydrophobic acyl chain and the charged residues are in closer proximity towards more polar C2 carbon. Surprisingly, the aromatic ring protons of W2 did not show any intermolecular NOEs with the backbone glycerol C^βH proton of D8PG while the aliphatic side chain of I6 and L10/L16 showed strong peaks with C^βH proton. Taken together these data show that K30 binds and interacts at the interface of the lipid molecule.

This finding was further supported by the paramagnetic relaxation enhancement (PRE) experiment. To obtain atomistic information about the depth of insertion and to probe the position of the peptide within the D8PG lipid micelle, two different paramagnetic probes (MnCl₂ and 16-doxyl stearic acid (16-DSA)) were used. MnCl₂ was used as a surface quencher because Mn²⁺ ions possess paramagnetic properties and thus are able to quench the diamagnetic signals coming from the residues that are exposed at the surface of the peptide. The 2D TOCSY spectra of peptide K30 in the presence of D8PG micelles titrated with MnCl₂ (Figure 2.1.8 (A)) revealed a signal perturbation of the side chains of charged residues like R1, H5, S7, R11, R13, and D14. Additionally, significant resonance broadening was observed for all the charged residues including Q17 and Q19 in presence of 0.4 mM MnCl₂ (Appendix II, Figure S2.1.12). 16-doxyl stearic acid (16-DSA) was used as a transversal paramagnetic quencher. The paramagnetic doxyl moiety present at the 16th carbon position of 16-DSA, can perturb the signals either coming from those residues which are inserted deeply inside the micelle or the residues stays at the interfaces because it can flip the doxyl moiety towards the more polar region of the bicelle or micellar aggregates and thus can quench signals from both sides. In the presence of 0.2 mM 16-DSA only few residues of K30 were affected like H5^β and R18^{α/β} but these two are placed just opposite of each other as evidenced from the structure. Titration with 0.4 mM 16-DSA showed that the signals of I6^γ and L16^β were perturbed. According to the pdb structure it can be seen that the charged residues like R1, K3, H5, R11 and R13 are placed in the N-terminal helical portion and their signal get quenched by MnCl₂ which has already been discussed above. The R18 residue is just at the opposite side of this helical portion and only

get affected by 16DSA. Thus, it can be concluded that 16DSA affects both the interfacial and distant protons to some extent but the overall spectra do not get affected too much due to its longer fatty acyl chain (Appendix II, Figure S2.1.12). These titration data taken together (using MnCl_2 and 16-DNA) suggest that the peptide is oriented in a way that it is neither totally outside nor inside but rather inserted into the interface of the micelles, where the side chains of the charged residues are exposed towards the surface keeping the backbone and mostly H^α inaccessible to both the quencher molecules.

A diagrammatic representation of these observations is shown in the Figure 2.1.8 (B) where the residues affected by MnCl_2 and 16-DNA are coloured red and blue, respectively. Thus, we can hypothesize that the peptide initially anchors on the negatively charged membrane and then folds due to the interactions of hydrophobic residues. Subsequently the folded structure inserts into the non-polar acyl chain of the lipid molecules and destabilizes the integrity of the membrane.

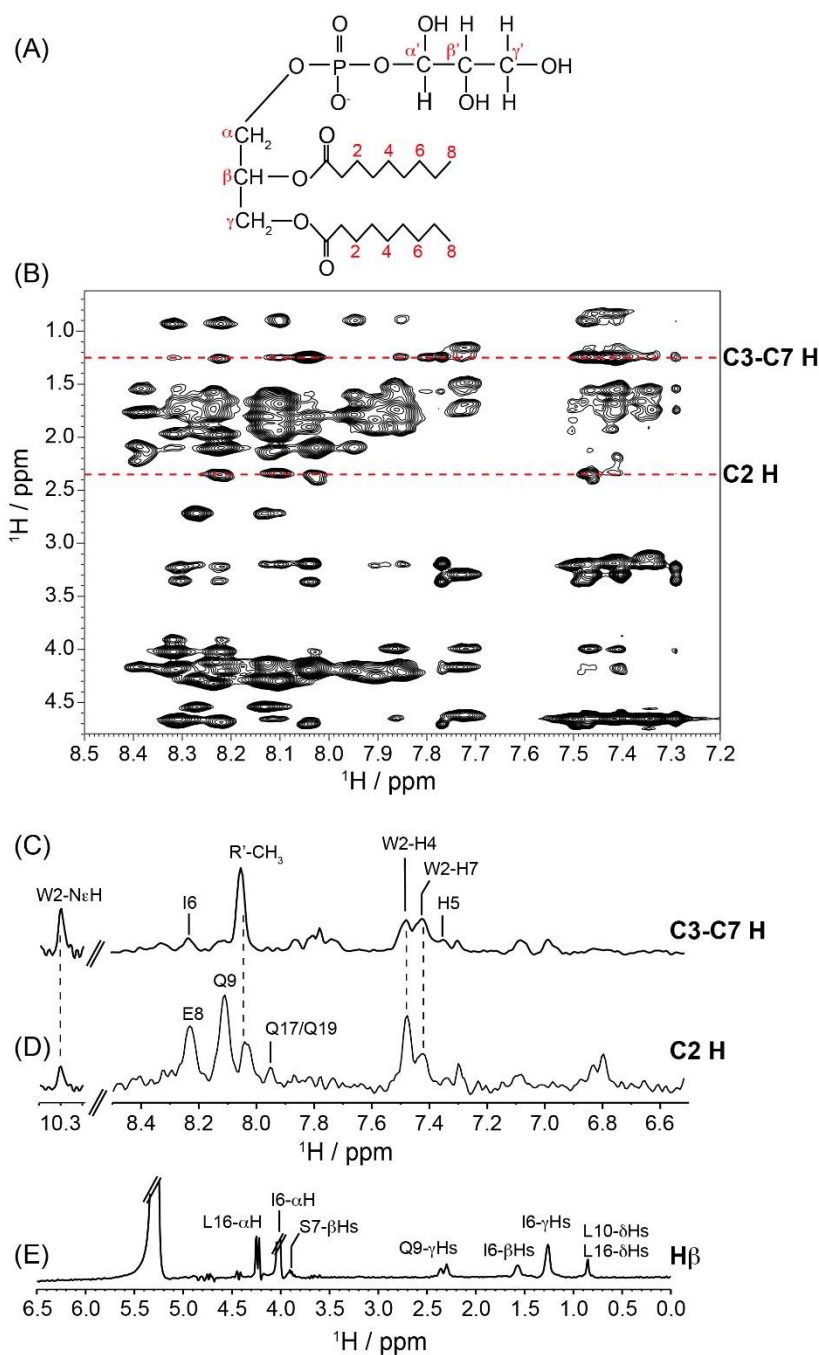


Figure 2.1.7 (A) Chemical structure of D8PG molecule. (B) A portion of the NOESY spectrum (mixing time 150 ms) of K30 in complex with D8PG. The dotted lines show the unique chemical shifts of D8PG where the 1D slice analysis was done. 1D slices taken at (C) 1.23, (D) 2.34, and (E) 5.25 ppm (well-resolved lipid signals) of the indirect dimension of the 2D NOESY spectrum. The residues that are in close proximity to micelles are shown (R'-CH $_3$ stands for 4-methyl hexanoyl). The experiment was performed at 310K on Bruker Avance III 600 MHz NMR spectrometer.

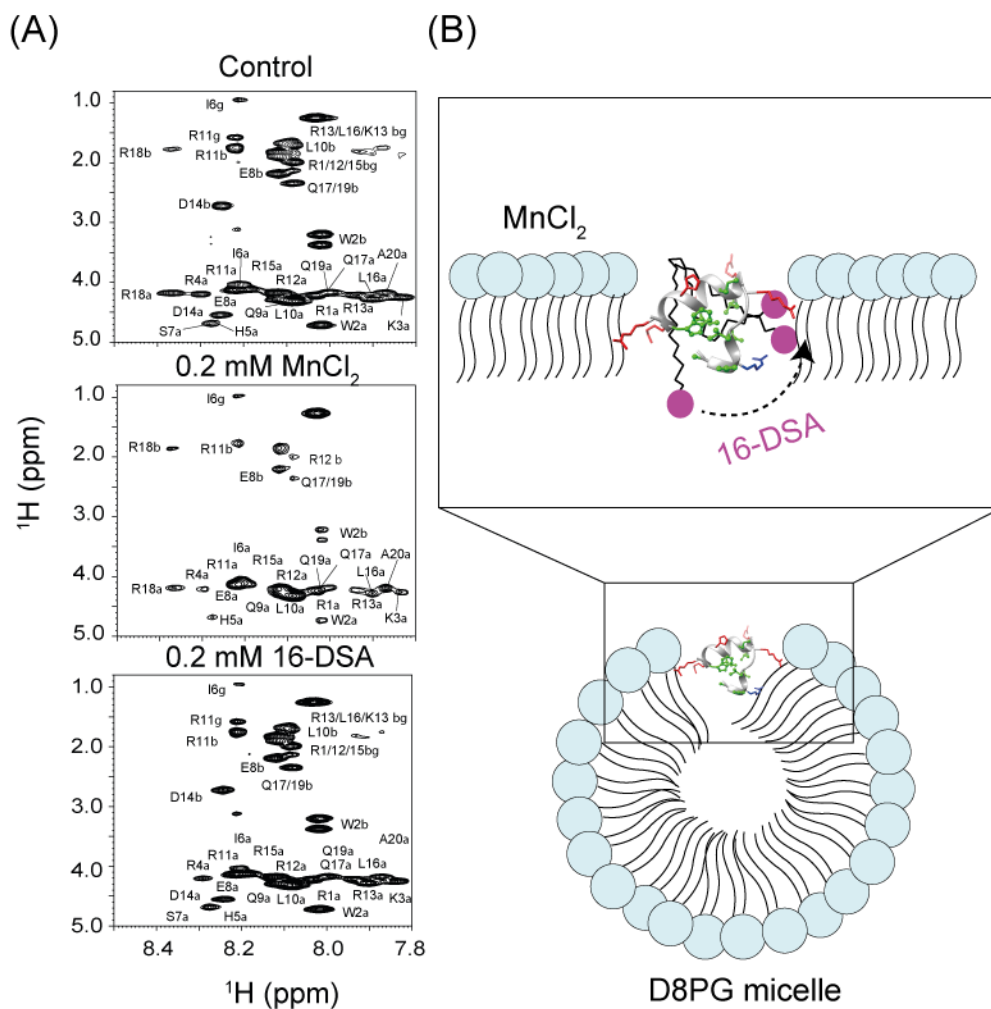
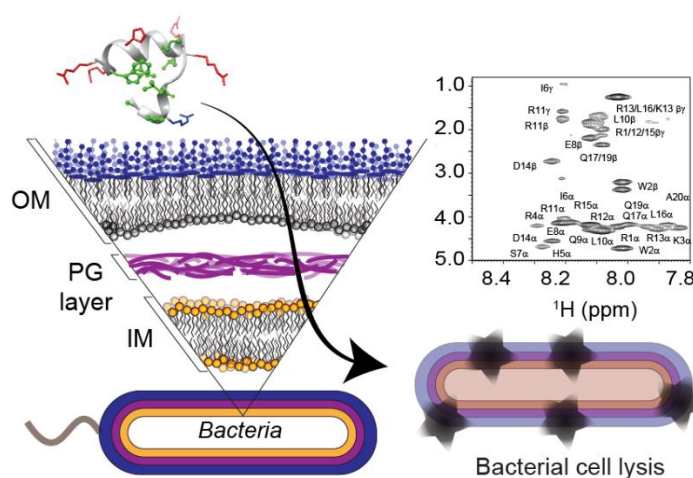


Figure 2.1.8. (A) Comparison of 2D TOCSY NMR profile of K30 peptide in D8PG. Control: without any paramagnetic quencher showing all the intra-residual peaks. Addition of 0.2 mM MnCl_2 and 16-DSA showing the immediate diamagnetic signal exchange of the residues that are present at the ‘solvent exposed region’ or ‘in depth’, respectively. (B) Schematic diagram of K30 in D8PG, showing the residues affected by MnCl_2 (red) and 16-DSA (blue). The residues that are not affected are marked green. The cartoon representation describes the location of the peptide in the D8PG micelle for a general audience and it has not been prepared according to lipid-peptide ratio. The area of action of the quencher molecules is shown in the box.

2.1.4. Conclusions

N-terminal acylation of a promising fragment from the autophagy 16 polypeptide (Atg 16) using 4-methyl hexanoic acid led to a lipopeptide that exhibited nanomolar activity against a *S. aureus* strain and low micromolar activity against the opportunistic pathogenic Gram-negative strains *P. aeruginosa* and *E. coli*. Biophysical studies indicate that the peptide adopts a random coil conformation in aqueous buffer, but folds into an α helix in the presence of D8PG micelles. The ability of the peptide to insert into and destabilize the

membrane has been established using dye leakage experiments as well. The ITC experiments identified the crucial thermodynamic forces underlying the binding of K30 to the D8PG and DPC micelles. Data from the ITC experiment showed that the binding of the peptide is stronger in D8PG micelles (and therefore negatively charged membranes) rather than DPC micelles (zwitterionic membranes). The standard enthalpy and entropy values also suggest that the K30-D8PG interaction is mainly electrostatically driven, which further gets stabilized by hydrophobic and Vander Waal interactions. The solution NMR structure of K30 in D8PG micelles shows that the peptide adopts a helix-loop-helix structure and maintains the crucial amphipathicity in the PG rich membrane. The probing of the localization of K30 in the micelles by 1D slice analysis from NOESY spectrum as well as PRE NMR experiment proves that the peptide fits into the interface area of the membrane. Moreover, 2D TOCSY experiment using two different paramagnetic probes ($MnCl_2$ and 16-DSA) in the presence of D8PG lipid revealed the exact orientation of the peptide upon interaction with the lipid and showed the side chains of the charged residues exposed to the surface. These findings are helpful in correlating the membrane active property of K30 peptide towards the bacterial membranes. Based on these observations we envision that the negatively charged membrane becomes an anchor point for the peptide. The subsequent interactions with the hydrophobic residues of the peptide force the peptide to fold. The folded structure is able to penetrate into the non-polar acyl chain of the lipid molecules where it subsequently causes membrane disintegration leading to cell lysis.



2.1.5. Appendix II

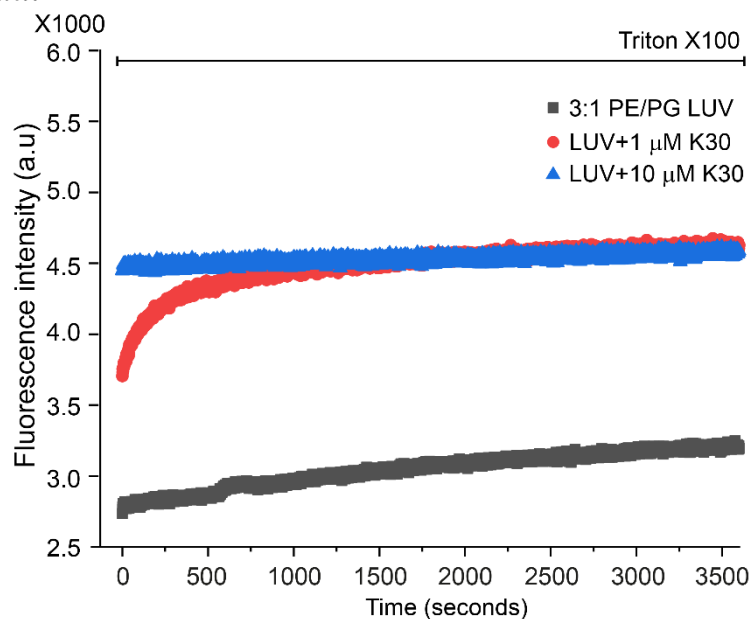


Figure S2.1.1. Time kinetics experiment of calcein dye leakage assay using K30 peptide in presence of 3:1 PE/PG LUVs.

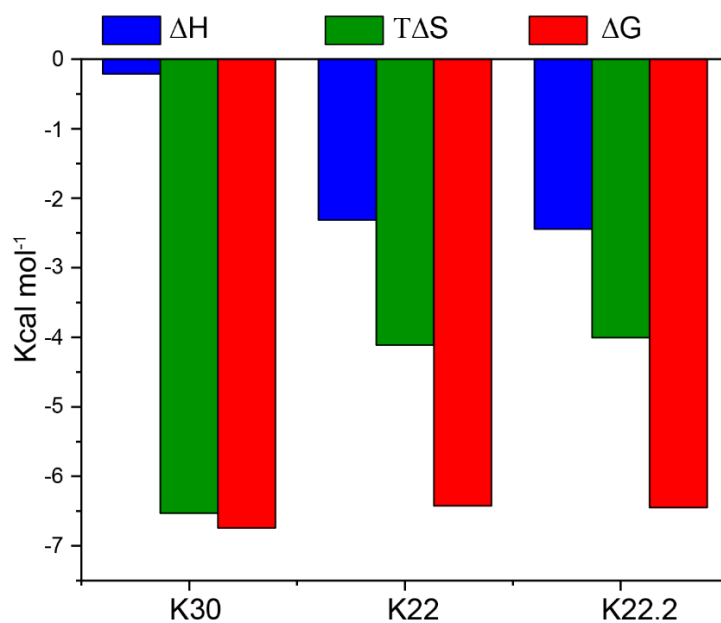


Figure S2.1.2. The binding signature (binding enthalpy, entropy factor and free energy) of all the three peptides in D8PG.

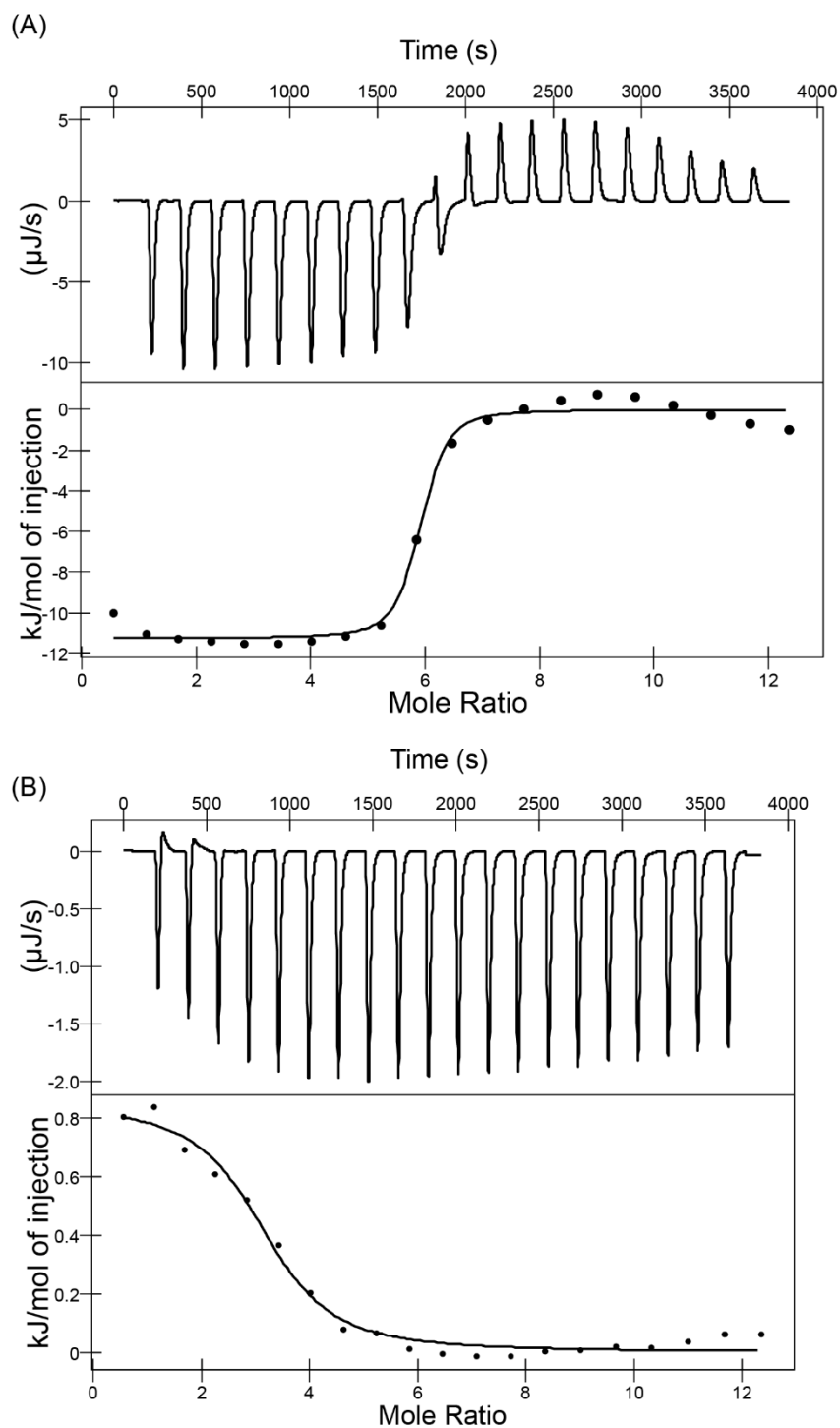


Figure S2.1.3. This figure shows binding isotherm of K30 in presence of D8PG (A) and DPC (B), where the heat of dilution of D8PG or DPC was subtracted. The experiment was performed in 10 mM sodium phosphate buffer (pH-7.4). Data acquisition was done in a TA affinity ITC calorimeter.

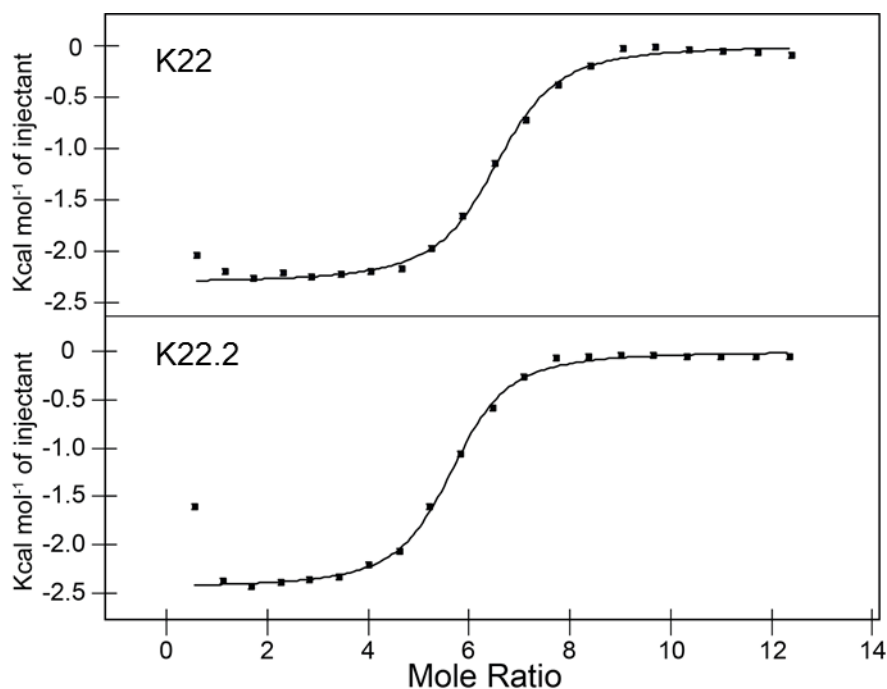


Figure S2.1.4. This figure shows binding isotherm of K22 and K22.2 in presence of D8PG, where the heat of dilution of D8PG was subtracted. The experiment was performed by injecting 2 μL aliquots of D8PG from a 25 mM stock into the sample cell containing the 500 μM of either K22 or K22.2 peptide dissolved in 10 mM sodium phosphate buffer (pH-7.4). Data acquisition was done in a TA affinity ITC calorimeter.

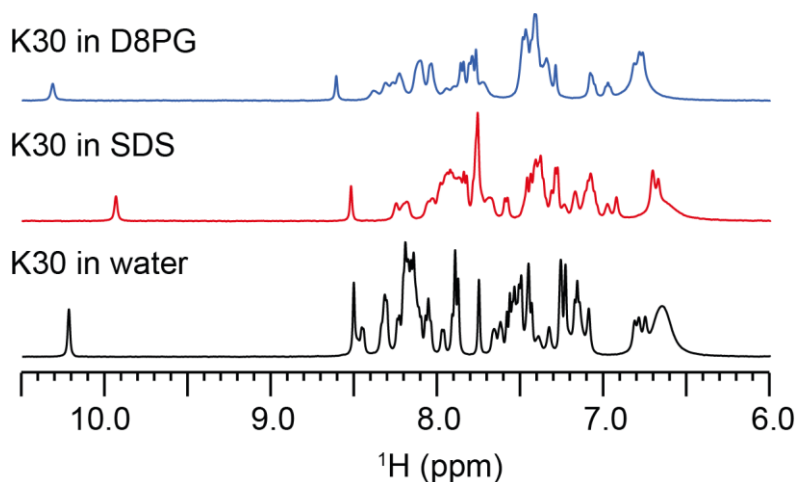


Figure S2.1.5. One-dimensional ^1H NMR spectra of K30 in aqueous solution, d_2 -SDS or D8PG micelles. All experiments were performed at 37 $^\circ\text{C}$ and at Bruker Avance III 500 MHz NMR spectrometer, equipped with SMART probe.

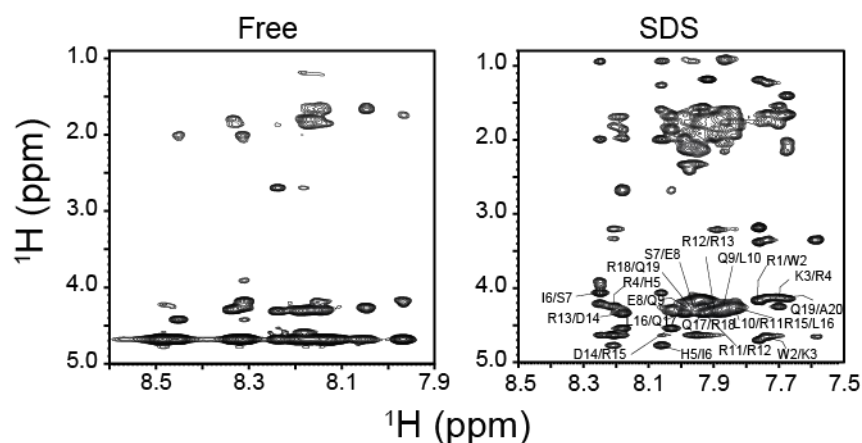


Figure S2.1.6. The NOEs of the signature region of K30 in aqueous solution and d_{25} -SDS bound state. In free solution there are very few intra residue NOEs indicating a very flexible conformation. When bound to d_{25} -SDS only intra and sequential NOEs but no medium and long-range NOEs were observed. All experiments were performed at 37 °C on Bruker Avance III 500 MHz NMR spectrometer, equipped with a SMART probe.

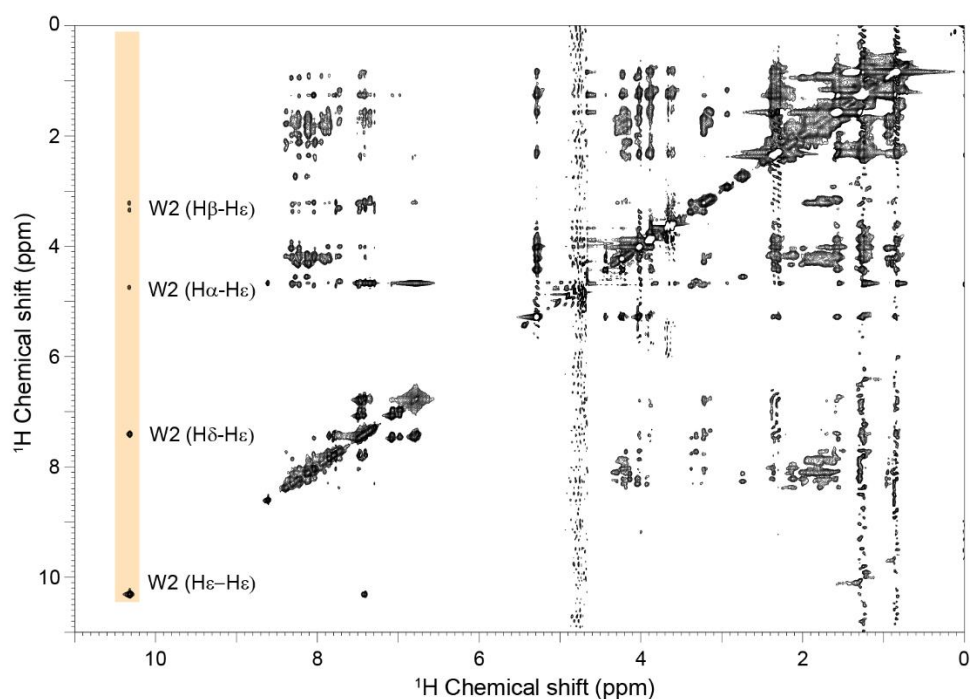


Figure S2.1.7. NOESY spectrum of K30 peptide in D8PG micelle. The W2 indole ring proton showed only intramolecular NOE cross peaks and no other intermolecular or long-range NOEs were observed with any other aliphatic proton of the peptide.

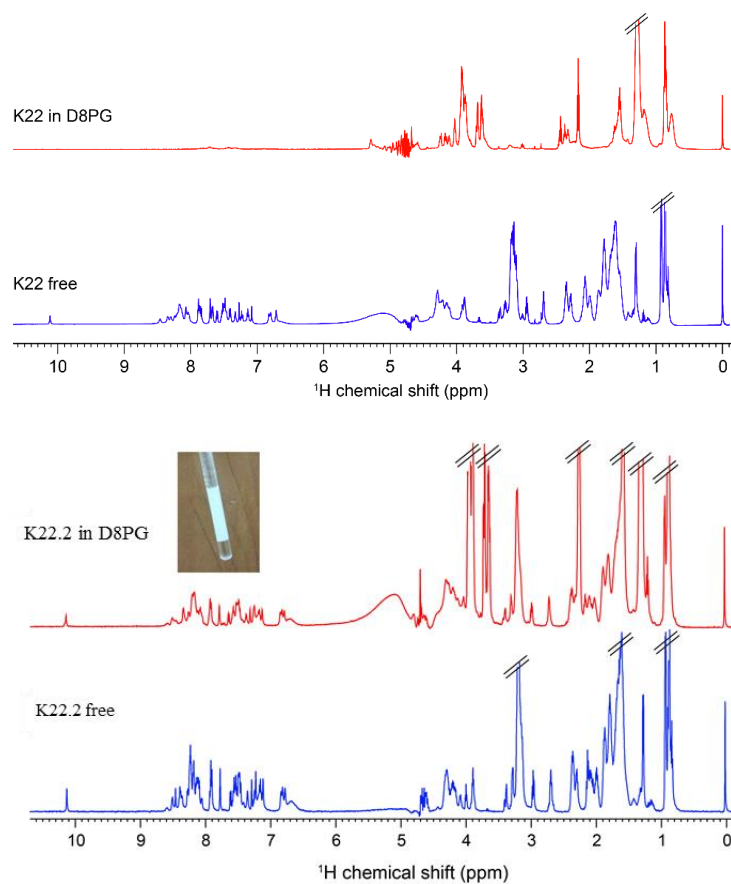


Figure S2.1.8. One-dimensional ^1H NMR spectra of K22 and K22.2 in aqueous solution and D8PG micelles. White opaque solution was found upon addition of 10mM D8PG in the peptide solution (inset). All experiments were performed at 37 °C and at Bruker Avance III 600 MHz NMR spectrometer, equipped with RT probe.

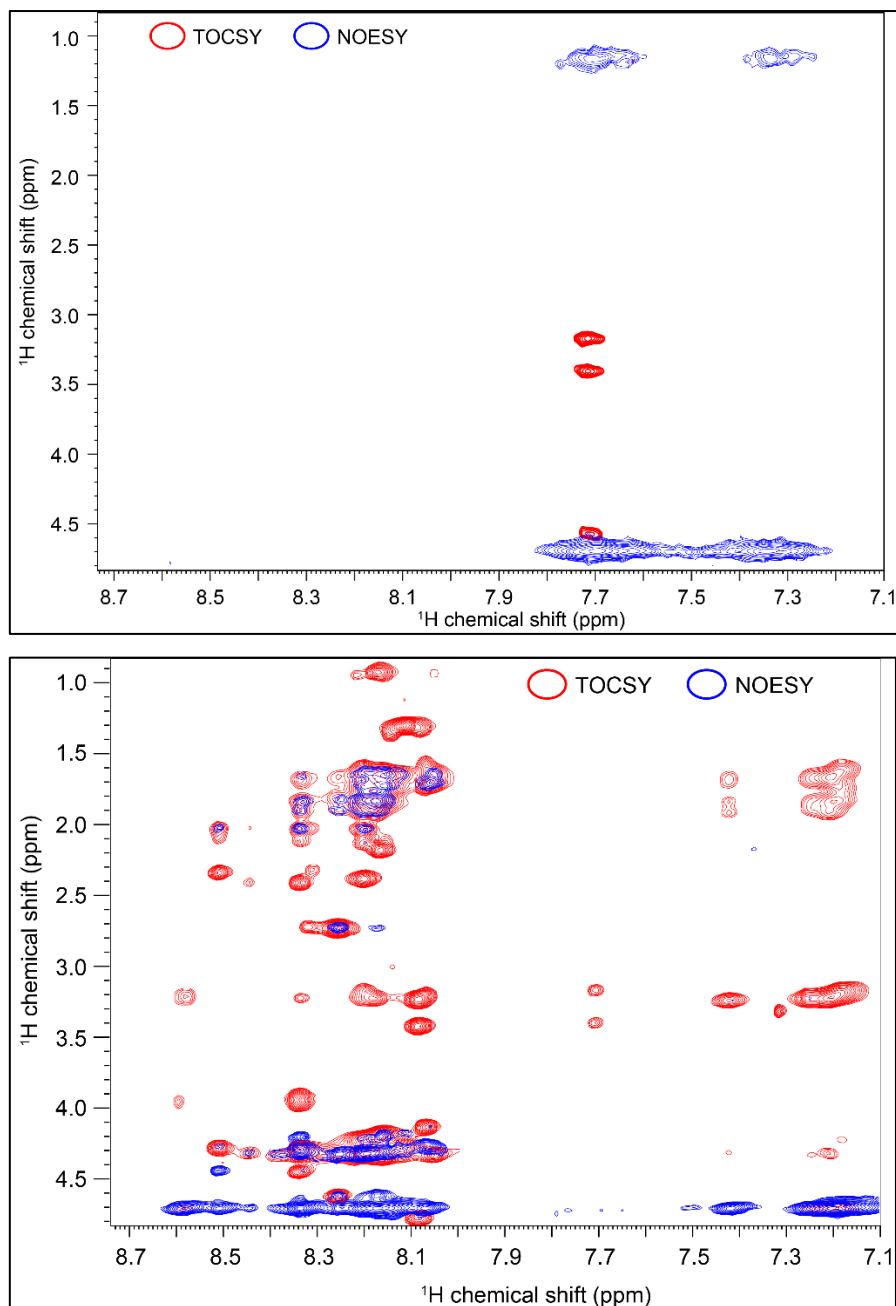


Figure S2.1.9. Two-dimensional ^1H - ^1H TOCSY and NOESY NMR spectra overlay of K22 (above) and K22.2 (below) in D8PG micelles. All experiments were performed at 37 °C and at Bruker Avance III 600 MHz NMR spectrometer, equipped with RT probe.

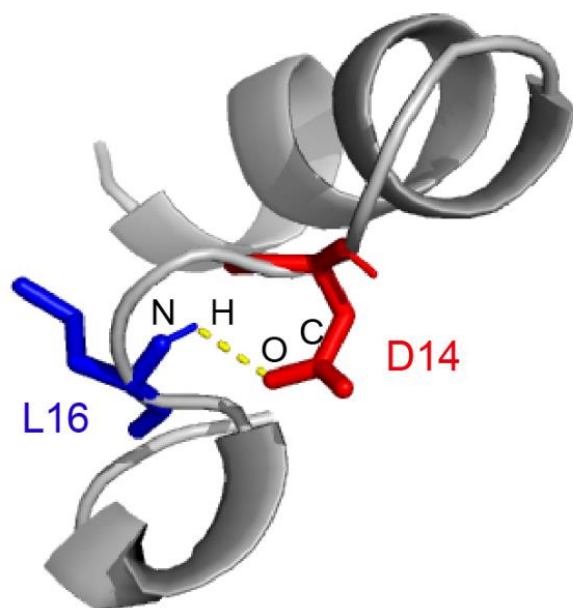


Figure S2.1.10. Backbone (L16)-side chain (D14) H-bond in the K30 peptide in presence of D8PG micelle.

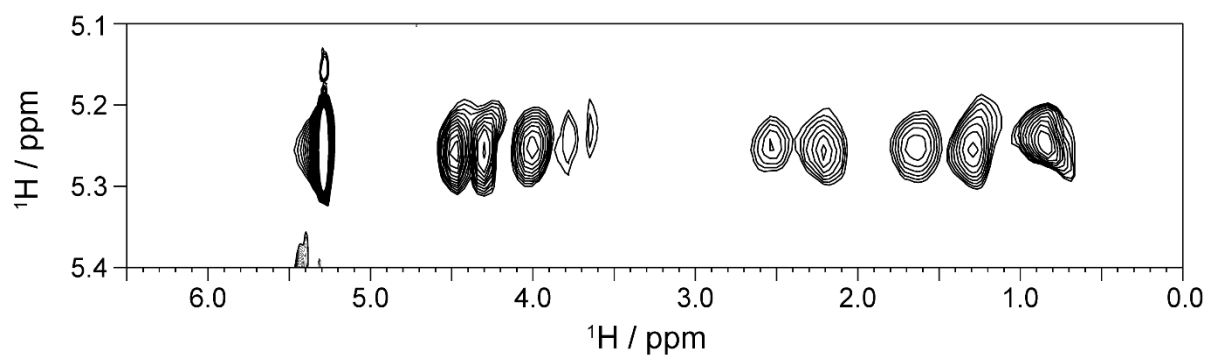


Figure S2.1.11 Partial 2D NOESY spectrum (150 ms mixing time) of K30 peptide in D8PG. The experiment was performed using Bruker Avance III 500 MHz NMR spectrometer and at 310K.

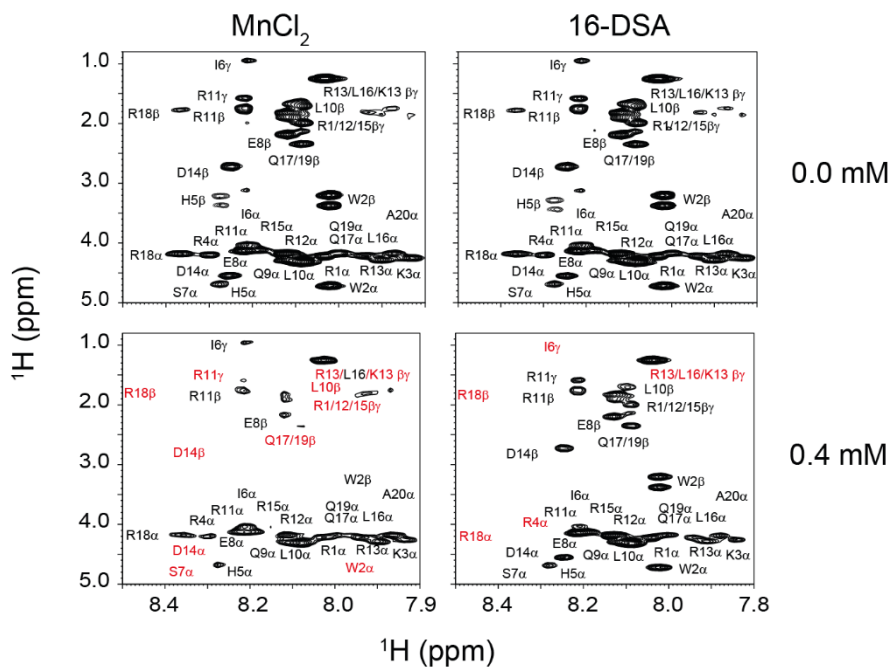


Figure S2.1.12. 2D TOCSY profile of PRE NMR of D8PG bound K30 peptide in 0.4 mM MnCl₂ and 16-DSA respectively compared with control (no quencher molecule). All the experiments were performed at 37 °C and at Bruker Avance III 600 MHz NMR spectrometer.

2.2. Synthesis and antibacterial study of cell-penetrating peptide conjugated trifluoroacetyl and thioacetyl lysine modified peptides

This chapter has been adapted from the following publication:

Patel, K.D., **Mohid, S.A.**, Dutta, A., Arichthota, S., Bhunia, A., Haldar, D. and Sarojini, V., **2021**. Synthesis and antibacterial study of cell-penetrating peptide conjugated trifluoroacetyl and thioacetyl lysine modified peptides. *European Journal of Medicinal Chemistry*, 219, p.113447.

2.2.1. Introduction

Antimicrobial peptides (AMPs), also known as host defence peptides (HDPs) hold a prominent place as current and future broad-spectrum antibiotics in light of the emergence of multidrug resistance of pathogens towards conventional antibiotics [128]. AMPs have found use against various infections caused by Gram-positive and Gram-negative bacteria, viruses and fungal pathogens [129]. AMPs acts either by forming pores in membranes, causing membrane lysis or by acting on intracellular targets like enzymes or nucleic acids [130,131]. However, after the emergence of methicillin-resistant *S. aureus* (MRSA), the peptide antibiotics vancomycin and polymyxin B are used only for serious infections as the last line of defence [129,132]. Innovative research ideas can help develop new AMPs which act on novel targets that could also help address bacterial resistance issues.

Histone deacetylases (HDACs) identified in eukaryotes are broadly classified into four classes. Classes 1, 2, and 4 are called zinc-dependent HDACs. Class 3 also called as sirtuins (Sirt1-Sirt7) are NAD⁺ dependent enzymes. The intracellular target of these enzymes are histone proteins [133,134]. These positively charged proteins play a role in imparting compactness and rigidity to negatively charged DNA. The negatively charged DNA wraps around histone proteins resulting in transcription silencing. Acetylation of the lysine residues by histone acetyltransferases (HATs) neutralise the positively charged histone protein and thus results in the unwrapping of DNA from histone resulting in chromatin and gene transcription activation. HDACs catalyse the reverse reaction instigated by HATs, removal of acetate from histones, increasing the overall positive charge of histones and reinstating their interactions with DNA, thereby arresting transcription and cell division [135,136].

Sirtuins are HDACs that regulate metabolic homeostasis, genomic integrity, longevity and, are highly conserved among various forms of life. Thus, substrate-based sirtuin inhibitors hold promise as potential anti-bacterial agents with the potential to interact with bacterial genome and RNA. There is evidence of presence of these enzymes in procaryotes [137-140]. In *Staphylococcus aureus* and *Streptococcus pyogenes*, sirtuins possess ADP-ribosyl transferase activity [141], and in *E. coli*, sirtuin CobB deacetylates acetyl-CoA synthetase (AcS) at the active site lysine to stimulate its enzymatic activity [142]. Cob is a bacterial sirtuin that deacetylates lysine residues of acetyl CoA synthetase to stimulate its enzyme activity [143]. Studies also showed that sirtuins exhibit robust protein ADP-ribosylation activity in *Staphylococcus aureus* and *Streptococcus pyogenes* [143,144].

In this context, the anti-bacterial properties of trifluoroacetyl and thioacetyl lysine modified peptides KP 13, KP 15 and KP 24 has been investigated (Figure 2.2.1). The sequences of these inhibitors are based on the structures of the substrates recognised by mammalian and bacterial sirtuins. These linear peptides showed anti-bacterial activity at low micromolar concentrations against Gram-positive *S. aureus*. Cell-penetrating peptide conjugated derivatives TAT KP 13, TAT KP 15 and TAT KP 23 are more potent in killing *S. aureus* and *E. coli* compared to their non-conjugated derivatives. These peptides showed promising signs of DNA binding by their ability to inhibit transcription in *in vitro*, could be possible mechanism of bacterial cell death. Advanced biophysical studies like fluorine (¹⁹F) NMR and fluorescence-based dye leakage assay in presence of bacterial and eukaryotic model membranes also exhibited the membrane specificity and activity of the peptides towards bacterial membranes.

2.2.2. Materials and methods

2.2.2.1. Chemicals and reagents

Fmoc-protected amino acids, 2-chlorotrityl chloride resin, and Fmoc-rink amide linker were purchased from GL Biochem. Fmoc Lys-OH-HCl was purchased from ChemPep Inc. Ethyl dithioacetate was purchased from Sigma Aldrich. Tentagel S NH₂ was purchased from Peptide International.

2.2.2.2. Synthesis and purification of peptides

All peptides were synthesized and characterized in University of Auckland, New Zealand using conventional Fmoc/ tBu SPPS methodology and mass spectrometry, respectively. The amino acids were attached to Tentagel S NH₂ resin. Rink amide linker

(0.1 mmol scale) was used at the C-terminus resulting in peptide amides upon cleavage. Amino acids were coupled to Rink amide linked resin in DMF using HCTU as the coupling reagent, HOAt as additive and DIPEA as the base. The N-terminal was acetylated using acetic anhydride/pyridine/DMF (1:2:3). The final peptides were cleaved from the resin using 10 ml of the TFA cocktail mixture (TFA/TIS/H₂O 9.5/0.25/0.25). The cleavage solution was filtered and concentrated under nitrogen and the crude peptides were precipitated using an excess of cold diethyl ether. The solid was centrifuged and the pellet obtained was dissolved in water and lyophilized to obtain the crude peptide. The crude peptides were purified using RP-HPLC on C₁₈ 100 Å column, following gradient elution using 0.1% TFA in water as solvent A and acetonitrile/water/TFA mixture (99/1/0.1) as solvent B. Linear gradient of 10-60% of solvent B over a period of 35 min was followed. The identity of the peptides was confirmed using Bruker MALDI-TOF and ESI-MS.

2.2.2.3. Determination of minimal inhibitory concentration (MIC)

S. aureus, *E. coli* and *P. aeruginosa* strains were obtained from School of Biological Sciences, microbial culture collection, University of Auckland, New Zealand. The strains were stored at 80 and 20 °C. For routine use, bacteria were plated on agar plates containing Mueller Hinton Broth (MHB). The assays were also done in the University of Auckland, New Zealand, using 96 well polypropylene plates following standard literature procedures. Overnight grown cultures of *S. aureus*, *E. coli* and *P. aeruginosa* were cultured at 37 °C in MHB media until the turbidity of 0.08-0.13 at 625 nm (1×10^8 CFU/ml) was obtained. Peptide stock solution was prepared in MHB media and was then further diluted to get a range of concentrations (1000 - 1.9 µM) in polypropylene coated 96-well plates. The antimicrobial assay was performed by adding 50 µl of diluted *S. aureus*, *E. coli* and *P. aeruginosa* to 50 µl of peptide solution and 50 µl of the media in each well of the plates. The plates, also with wells containing suitable growth and sterility controls, were then incubated at 35 °C for 24 h to determine MIC. Streptomycin and polymyxin were used as positive control for Gram positive and Gram-negative bacteria respectively. Optical density measurements at 600 nm (O.D₆₀₀) for determination of MIC was done using EnSpire multimode plate reader. Three concordant experiments each with three replicates were used to determine the average MIC values.

2.2.2.4. Fluorescence-Based in vitro Transcription Assay

Purified *E. coli* RNA Polymerase at 400 nM concentration and $\sigma 70$ (determinants interacting with DNA) at 800 nM were incubated in 4 µl of transcription buffer consisting

of 50 mM Tris-HCl (pH 8.0), 100 mM KCL, 10 mM MgCl₂, 1 ml DTT, 50 nM BSA and 5% glycerol at 25°C for 20 min. This incubation essentially forms holoenzyme. Peptides in the concentration range from 0 μM to 50 μM in 6 μl transcription buffer were incubated with 500 ng Puc 19-lacCONS plasmid DNA samples at 25 °C for 20 min to allow the interactions between peptides and RNA, followed by a further incubation at 37 °C for 15 min to allow the formation of an open complex. Initiation of transcription reaction was done by adding 250 μM of NTP. After incubation for about 30 min, the reaction was stopped by adding 0.5 U RNase-free DNase. Samples were then diluted 10-fold with TE buffer (10 mM Tris-HCl, pH 7.4, 1 mM EDTA). Fluorescence at excitation/emission wavelength 495/535 nm was measured using a spectrofluorometer (Photon Technology International, HORIBA Scientific, Edison, NJ) after adding 100 μl of RiboGreen (Invitrogen, Carlsbad, CA) dye and incubating for 5 min for each sample.

2.2.2.5. Calcein dye leakage assay using model membrane LUVs

Membrane liposome model prepared by different composition of lipids depending on target membrane are widely used in medicine and pharmaceutical research to understand the interaction between lipid membrane and molecule of interest. In this study, the bacterial and mammalian membrane mimicking model was prepared by using 1,2-dioleoyl-sn-glycero-3-phosphoethanolamine (DOPE) and 1,2-dioleoyl-sn-glycero-3-phospho-(1'-rac-glycerol) (DOPG) lipids at 3:1 ratio and 1,2-dioleoyl-sn-glycero-3-phosphocholine (DOPC) with 40% Cholesterol, respectively.[126] The lipid mixtures were dissolved in chloroform, and a lipid film was prepared by passing Nitrogen gas over it and then subjected to freeze-drying for overnight to remove residual solvents. Next day, the films were subsequently hydrated with 70 mM calcein prepared in 10 mM Phosphate buffer (pH 7.4) and then subjected to five freeze-thaw cycles by using liquid nitrogen for freezing and hot water (60 °C) for thawing. Large Unilamellar vesicles (LUVs) were obtained by extruding the calcein containing solution 21 times through a polycarbonate filter (Avanti Polar Lipids, Inc.) of 100 nm diameter. Free calcein was removed via gel filtration using a Sephadex G-50 column (GE Healthcare, Uppsala, Sweden) previously saturated with the same buffer. The final concentrations of the vesicles were 2mg/ml. The concentration-dependent experiments were performed by increasing the peptide concentrations from 1 to 20 μM while keeping the fixed concentration of LUVs (20 μM) suspended in 10 mM Tris-HCl buffer with 100 mM NaCl. The emitted fluorescence of free calcein (515 nm) that got released from the compromised LUVs via the interaction of peptides was measured by

using a Hitachi F-7000 fluorometer (Hitachi, Ltd, Tokyo, Japan) at 37°C in a 0.1 cm quartz cuvette. 0.1% Triton X-100 (Sigma-Aldrich, St. Louis, USA) was added as positive control and only LUVs were treated as a negative control. The percentage of calcein leakage was calculated by following equation (3) as previously described.

2.2.2.6. ¹⁹F NMR with bacterial model membrane

The ¹⁹F NMR data was collected by using a Bruker 500MHz NMR spectrometer equipped with 5 mm RT probe at 298 K. The large unilamellar vesicles (LUVs) mimicking the bacterial inner membrane system was made following the same protocol as described in the dye leakage analysis without filling the vesicles with the calcein dye. A series of one dimensional (1D) ¹⁹F NMR spectra were obtained by using the ¹H-decoupled ¹⁹F pulse program (zgfhigqn.2). The number of scans for each spectrum was 32, and the size of the FID was set to 131072. Trifluoroacetic acid (TFA) was added as an external standard, with chemical shift set at -75.48 ppm.

2.2.2.7. Hemolytic and cytotoxicity assay

Hemolysis assays were conducted according to our previously reported protocols in the University of Auckland, New Zealand.[126] Mouse blood cells were centrifuged at 1000 g for 5 min to remove the buffy coat. The cells were then washed thrice in Tris buffer (10 mM Tris, 150 mM NaCl, pH 7.4) and resuspended in 2% (V/V) of Tris biffer. A stock solution of the peptide inhibitors at 1 mM concentration was prepared in Tris buffer. A 2-fold dilution series of the peptide solution was made in the 12- well plate. To 100 ml of the inhibitor solutions in wells 1 to 10, 100 ml of the resuspended blood cells were added. Triton X (100 ml of 0.5%) was used as positive control. Plates were incubated for 1 h at 37 °C without shaking. Plates were centrifuged at 3500 g for 10 min. Supernatant from each well (100 ml) was transferred to new plates and absorbance at 540 nm was measured. Percentage of hemolysis was calculated by using the equation (1) as previously described.

Cytotoxicity studies were done in the Centre for DNA Fingerprinting and Diagnostics (CDFD), Hyderabad, India, on human cervical carcinoma (HeLa) cells and human neuroblastoma cells (BE(2)-C) cells. HeLa cells were cultured in DMEM media. (BE(2)-C) cells were cultured in DMEM media with the addition of Ham's F12 nutrient mixture for neuroblastoma cells. Media was supplemented with PSG mixture (100 units/ml penicillin, 100 mg/ml streptomycin, 2 mg/ml L-glutamine, and 10% fetal bovine serum (FBS). Cells were maintained at 37 °C in a 5% CO₂ incubator in T-25 flasks. IC₅₀ values were determined using standard MTT assays. Briefly, the cells were seeded at the seeding

density of 5×10^4 cells/ml in 96- well tissue culture plates for 24 h at 37 °C/5% CO₂ after which time, the media was carefully pipetted out, and the cells treated with a range of concentrations of the peptides, each at 2-fold dilution from the previous concentration, for 48 h at 37 °C/5% CO₂. At the end of the incubation period, 20 ml of MTT (0.5 mg/ml in each well) was added and the samples incubated for 2-4 h. MTT was then removed carefully and 100 ml of DMSO was added to solubilize formazan crystals. The absorbance was then measured at 570 nm, and IC₅₀ values were calculated with Sigma Plot 11.0.

2.2.3. Results and discussion

2.2.3.1. Peptide design

Deacetylase proteins like HDAC8 and sirtuins like Sirt1, Sirt2 and Sirt3 act on H4 histone's acetyl lysine. In particular, amino acid residues corresponding to positions 8-19 of H4 and having the KRHR sequence (residues 16-19) are important for substrate recognition by deacetylase enzymes. CobB is a Sirt2 homolog protein deacetylase found in *E. coli* and studies have shown interaction of CobB with the histone H4 peptide (12-KGGAK_{Ac}RHRKIL-22), pointing to the importance of KRHR sequence in recognition by prokaryotic and eukaryotic deacetylase enzymes. Similar enzymes (SAV0325) are found in *S. aureus* and also in *Candida* called as Sirt2 and Hst proteins. Previously, trifluoromethyl ketone based eukaryotic HDAC inhibitors have shown interactions with bacterial class 2 histone deacetylases. Based on the above understanding, peptides with the sequence KGLRKFGAKRHRC were designed (Figure 2.2.1). Lysine residues marked in red were modified as thioacetyl (TAC) and trifluoroacetyl (TFA) derivatives (Figure 2.2.1). Considering the potential applications of such inhibitors against bacterial species, TFA and TAC modified peptides were tested for their antibacterial properties.

Because of its membrane permeability properties, conjugation to TAT (YGRKKRRQRRR) is generally used to enhance the cell penetrating properties of intracellular inhibitors. A triglycine linker is often made use of in such cases as simple amino acids like glycine do not affect peptide secondary structure and can additionally impart flexibility to the overall peptide chain.

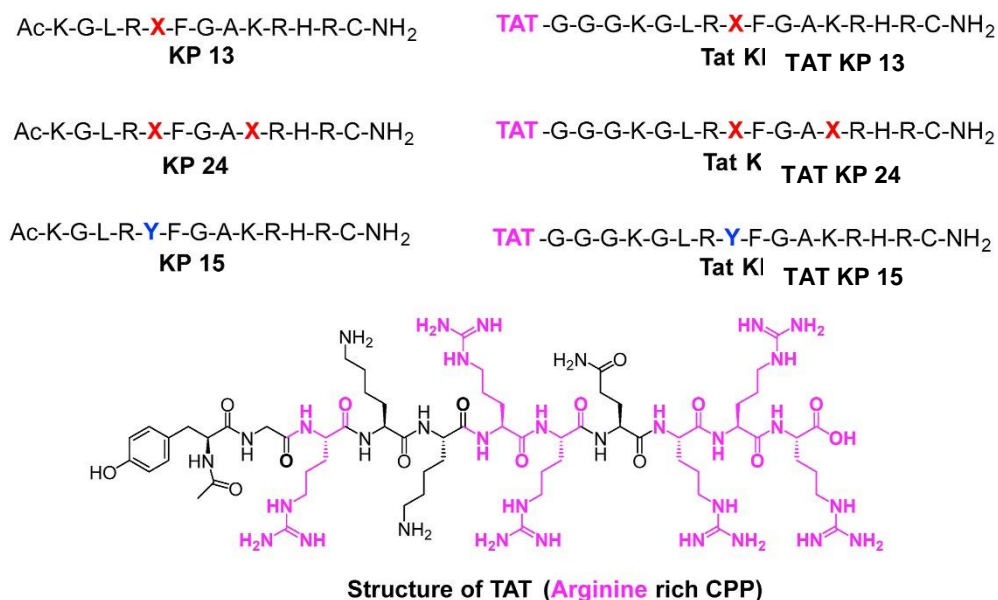


Figure 2.2.1. Sequence of KP 13, KP 24 and KP 15 and their TAT conjugated derivatives. X represents TFA-Lys and Y represents TAC-Lys. Chemical structure of TAT is also shown.

Table 2.2.1. Anti-bacterial activity of the peptides and antibiotic controls.

Peptides	MIC (μM)		
	<i>S. aureus</i>	<i>E. coli</i>	<i>P. aeruginosa</i>
KP 13	1.5-3	125-250	>250
TAT KP 13	0.2-0.4	1.5-3	25-50
KP 24	1.5-3	125-250	>250
TAT KP 24	0.2-0.4	1.5-3	25-50
KP 15	1.5-3	125-250	>250
TAT KP 15	0.2-0.4	1.5-3	25-50
TAT	1.5-3.1	50-100	>100
Streptomycin	2.2-4.3	-	-
Polymyxin B	-	0.09-0.19	0.15-0.3

*MIC was done in triplicate repeated on three individual days.

2.2.3.2. Antibacterial activity against *S. aureus* and *E. coli*

The antimicrobial potency of all the synthesized peptides against Gram-positive bacteria *S. aureus* and Gram-negative bacteria *E. coli* and *P. aeruginosa* was studied by determining the minimal inhibitory concentration (MIC) following standard protocols (Table 2.2.1). Compared to non-conjugated sequences KP 13, KP 24 and KP 15, TAT

conjugated peptides TAT KP 13, TAT KP24 and TAT KP 15 were approximately 8-times more active against *S. aureus* with MICs in the range of 0.2 - 0.4 μM and more than 40 times potent against *E. coli* with MICs in the range of 1.5 - 3 μM (Table 2.2.1). TAT on its own showed same potency as the non-conjugated peptides against *S. aureus* and was about 3 times more potent than the nonconjugated peptides against *E. coli*. Both TFA and TAC derivatives showed similar potency against all bacteria tested. TAT KP 13, TAT KP 24 and TAT KP 15 peptides showed moderate activity against *P. aeruginosa*. Even though TAT conjugation significantly enhanced activity against *S. aureus* and *E. coli*, the effect of conjugation was slightly less pronounced against *P. aeruginosa*.

2.2.3.3. Fluorescence-based *in vitro* Transcription Assay

Drugs targeting protein synthesis and the bacterial genome [145] such as streptomycin and rifampicin provide alternatives to membrane lytic drugs [146]. The possibility of peptides to interact with RNA was investigated through an *in vitro* transcription assay using the bacterial model of transcription. Transcription inhibition assay using *E. coli* RNAP-sigma 70 holoenzyme and TAT conjugated peptides TAT KP 13 and TAT KP 24 showed complete inhibition of transcription at 10 μM concentration. However, non-conjugated peptides were unable to completely inhibit transcription, even at 40 μM concentration (Figure 2.2.2). These observations suggest that the TAT conjugated peptides have a secondary mode of actions to kill the bacterial cells via intracellular targeting pathways, specifically by inhibiting the DNA transcription machinery. Thus, it supports that the conjugation of TAT with the trifluoroacetyl and thioacetyl lysine modified peptides enhances the potencies to kill bacterial cells via several mechanisms.

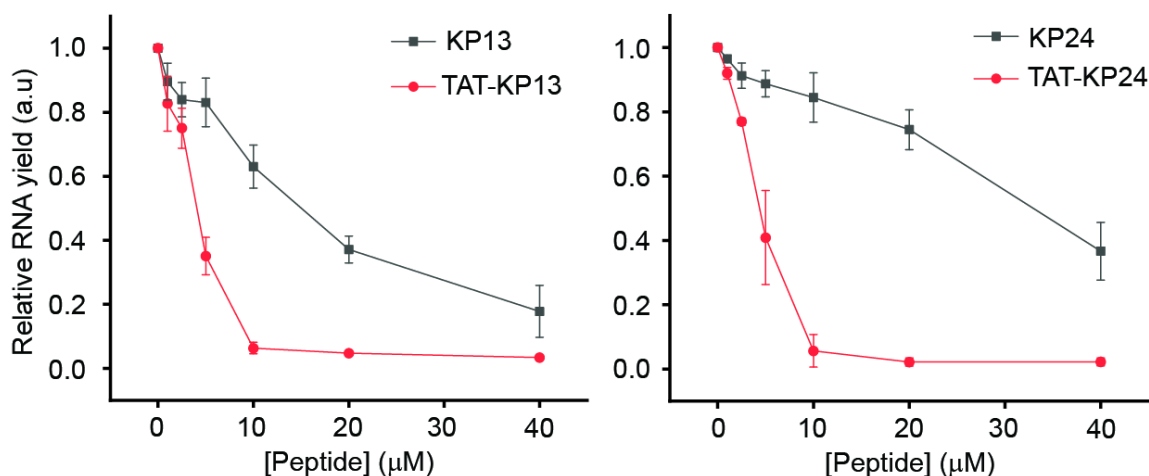


Figure 2.2.2. Plot of fluorescence intensity of ribogreen showing RNA yield versus peptides KP 13, TAT KP 13, KP 24 and AT KP 24 up to 40 μM concentration. Error bars represent standard deviation.

2.2.3.4. ^{19}F NMR with Bacterial Model Membrane

The one-dimensional ^{19}F NMR spectra of each peptide showed distinct interactions with the bacterial inner membrane mimicking liposomes. The initial intensities of the free peptides were almost the same in the absence of the 3:1 PE/PG LUVs, as shown in Figure 2.2.3. Addition of the vesicles from 30 $\mu\text{g}/\text{ml}$ to 180 $\mu\text{g}/\text{ml}$ resulted in broadening of the peaks in the case KP 13 and KP 24 although the KP 13 showed a slight increase in intensity after 90 $\mu\text{g}/\text{ml}$ all the way to 180 $\mu\text{g}/\text{ml}$. On the other hand, the TAT KP 13 and TAT KP 24 showed completely different behaviour in the presence of LUVs (Figure 2.2.3). TAT KP 13 showed a stepwise increment of its intensity with increasing concentrations of the LUVs. On the other hand, TAT KP 24 showed a broad peak in its free form and then after addition of 30 $\mu\text{g}/\text{ml}$ LUV it showed maximum intensity which later started decreasing with increasing concentrations.

The results suggest that the ^{19}F nucleus attached to the lysine residues of the unconjugated peptides (KP 13 and KP 24) showed a sharp peak because its T_2 relaxation was slow as we know that the nuclear spin of a small molecule rotates at higher speed compared to a bigger molecule, which results in a longer decay time for transverse magnetization. Addition of LUVs with increasing concentration resulted in the broadening of the peaks which suggests that the lysine residues interact with the negatively charged head groups of phosphatidylglycerol (PG) lipids, that is bulk in size as a part of vesicle, which resulted in faster T_2 relaxations because the rate of transverse relaxation rate of a LUV is faster. On the contrary, the TAT conjugated peptides might have been self-assembled as previously reported by Zhang, *P et al* [147] because the amphipathic nature of the peptide and the TAT assembly probably promoted a micellar type of aggregation, which caused broader peaks in their free forms because of the bulkier size. Addition of negatively charged lipid vesicles caused immediate isolation/separation of the peptide assemblies via electrostatic interactions, which caused sharp intensities. Increasing the concentration of the vesicles caused an increase in the T_2 relaxation of the lysine residues resulting from the firm binding with the model membrane mimics.

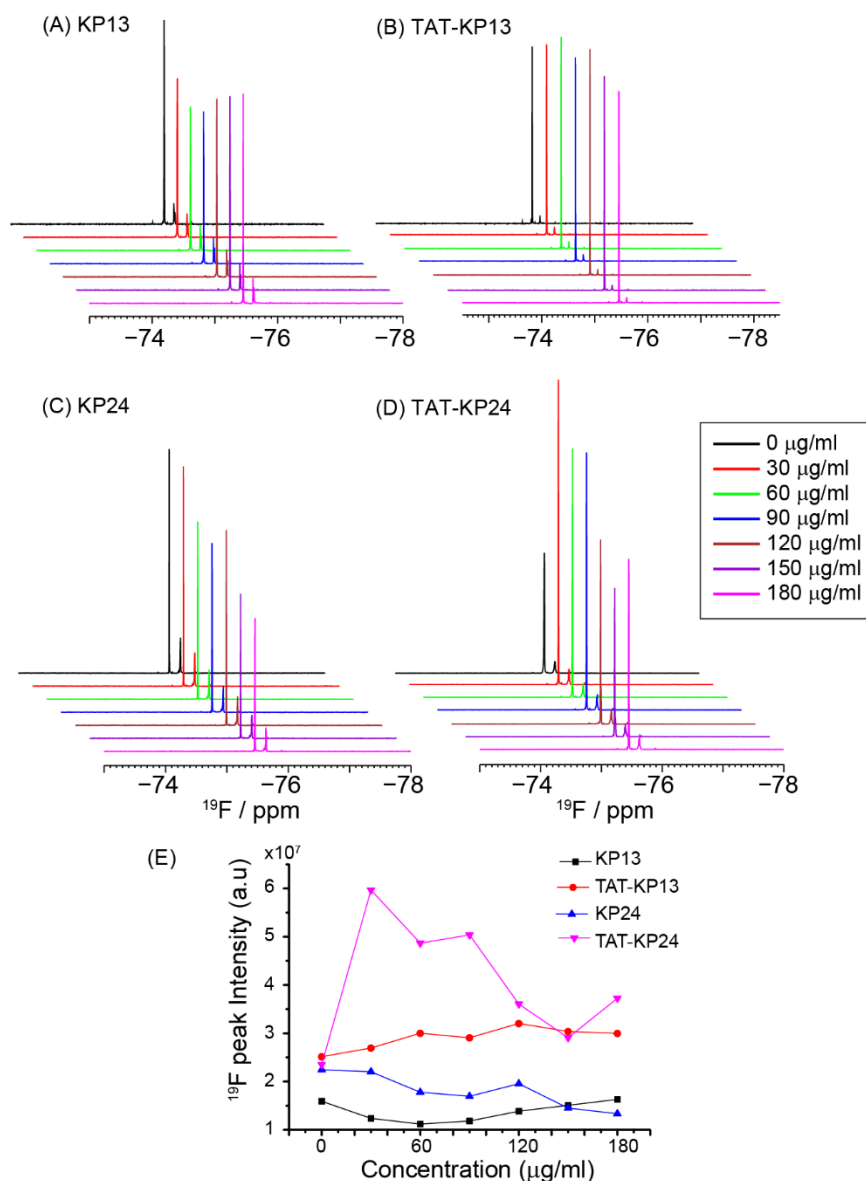


Figure 2.2.3. The ^{19}F NMR spectra of the trifluoroacetyl lysine and thioacetyl lysine peptides (A-D) in the absence and presence of 3:1 POPE/POPG LUVs at different concentrations. The relative intensities of the peptides were plotted with the respective concentration of the LUVs to show the stepwise change of the spectra (E). The experiments were done in a Bruker 500 MHz spectrometer at 298 K.

2.2.3.5. Calcein dye leakage assay

Calcein, a slightly water-soluble green fluorescent dye that gets self-quenched above 70 mM concentration. Synthetic liposomes filled with calcein above self-quenched concentration shows lower fluorescence, but the release of the entrapped calcein is a signature of vesicle disruption, transient pore formation or vesicle fusion which subsequently increases the fluorescence intensity. The calcein leakage assay using the lipid vesicles of 3:1 DOPE/DOPG LUV, mimicking the bacterial inner membrane showed a 90%

leakage at 2.5 μM and showed little change till 20 μM concentration by TAT conjugated peptides. On the contrary, the non-conjugated peptides showed a stepwise increment at each concentration and showed a maximum 70% leakage at 20 μM concentration which is depicted in Figure 2.2.4 (A). However, when treated on vesicles composed of DOPC and 40% cholesterol, that mimics mammalian membranes, less than 20% leakage was observed until 20 μM concentration for all TAT conjugated and non-conjugated peptides (Figure 2.2.4 (B)). The overall leakage fashion was almost similar for mammalian membrane mimetics which indicates that the peptides are highly selective and interacts strongly with negatively charged phosphate head groups where the TAT conjugated peptides have more efficient interaction with those vesicles than the non-conjugated peptides.

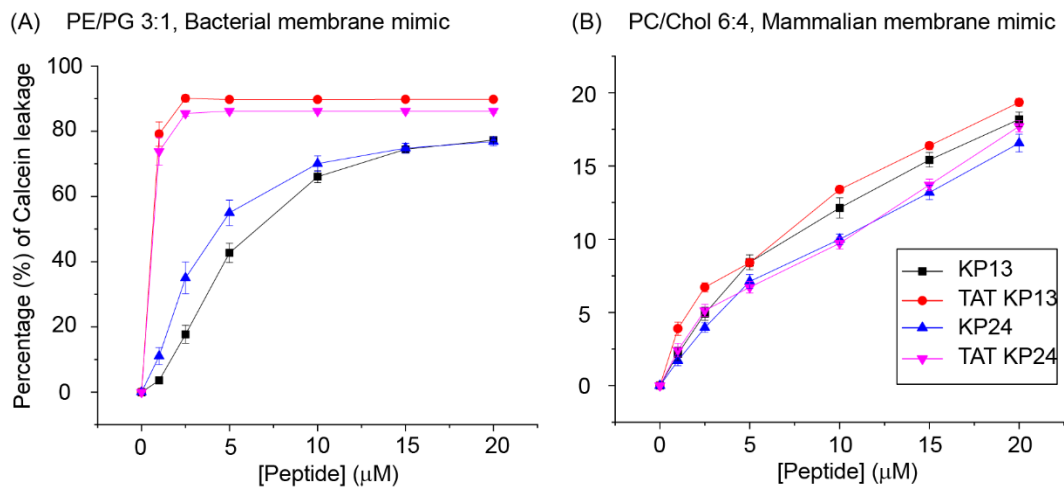


Figure 2.2.4. Percentage (%) of calcein leakage (A) in the presence of DOPE: DOPG 3:1 LUVs, which mimics bacterial inner membrane and (B) The vesicles made of DOPC with 40% cholesterol which mimics mammalian membrane.

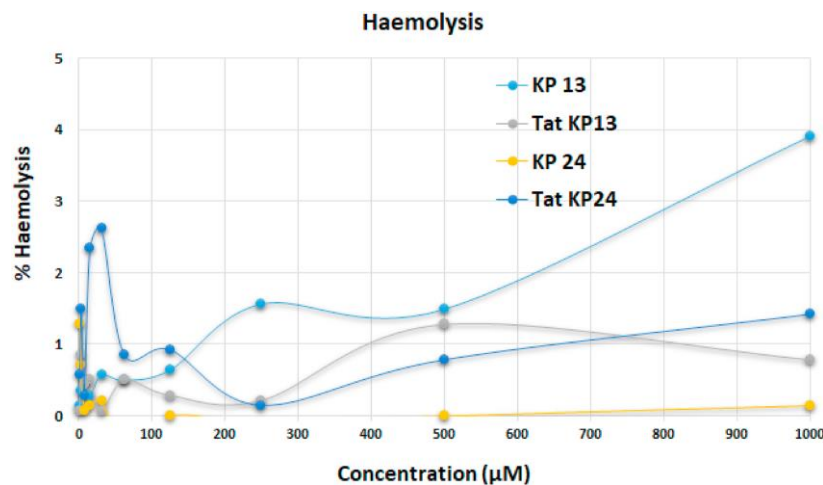


Figure 2.2.5. Effect of peptides KP 13, TAT KP 13, KP 24 and TAT KP 24 on the mouse blood cells. The experiment was done in triplicate and the results averaged out.

These results prove the higher susceptibility of these peptides towards microbial membranes compared to the mammalian membranes. All experiments were performed at least three times, and the data were averaged (\pm SD).

2.2.3.6. Hemolysis and cytotoxicity study

Zwitterionic phospholipids such as phosphatidyl choline and sphingomyelin in red blood cell (RBC) membranes causes an increase in the affinity of cationic and hydrophobic peptides towards RBC. Hemolysis assays provide insight into a compound's toxicity profile. For a compound to be a suitable drug candidate, it is necessary to have a high potency without significant toxicity. The inhibitors KP 13, TAT KP 13, KP 24 and TAT KP 24 which showed high potency against both Gram-positive and Gram-negative pathogens were tested for hemolytic activity against mouse red blood cells. All peptides showed less than 5% hemolysis at 1000 μ M concentration (Figure 2.2.5). The designed peptides were also tested for cytotoxicity against HeLa and BE (2)-C cells (Figure 2.2.6 (A-B)). Peptides KP 13 and KP 15 were non-cytotoxic toward these cell lines (IC_{50} 94.6 μ M, and 84.4 μ M against HeLa cells, IC_{50} 77.9 μ M and 81.6 μ M against BE (2)-C cells). The TAT conjugated derivatives TAT KP 13 and TAT KP 24 were cytotoxic against HeLa cells at IC_{50} 20.2 μ M and 31.6 μ M respectively and against BE (2)-C cells at IC_{50} of 17.4 μ M and 23.4 μ M respectively. The significantly lower concentrations of the TAT conjugates to induce cytotoxicity can be attributed to increased absorption and cell permeability by TAT because of its cationic nature. Comparison of the IC_{50} values to MICs in Table 2.2.1 clearly show that the peptides by themselves as well as the TAT-conjugates are much more potent against and selective towards *S. aureus* and *E. coli*. However, their IC_{50} values are not significantly different to the MICs observed against *P. aeruginosa*. These results thus prove that these peptides have the potential to be developed as antibacterial agents.

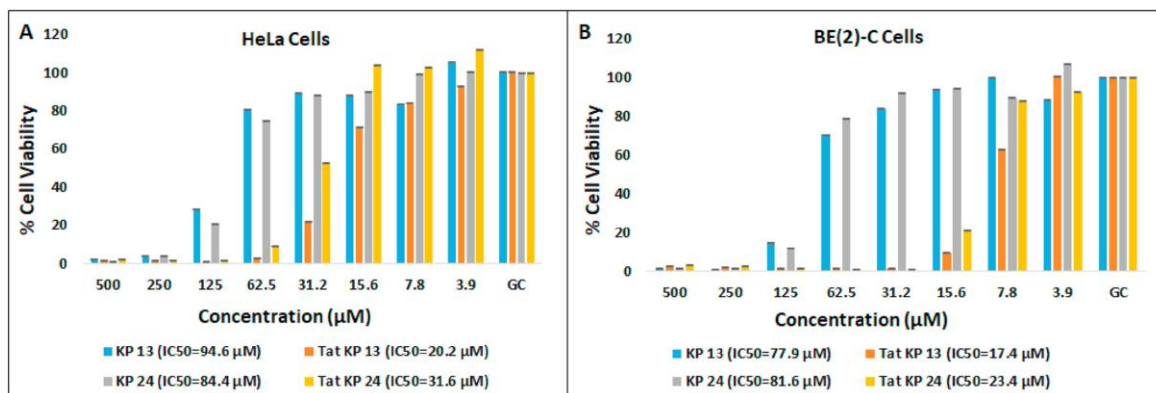


Figure 2.2.6. IC₅₀ of TAT conjugated and non-conjugated derivatives against (A) HeLa and (B) BE (2)-C cell lines. Experiments were done in triplicates.

2.2.4. Conclusions

The designed peptides reported here exert potent antimicrobial activity via membrane lysis and via acting on internal targets such as RNA. This is the first report of TAT conjugated trifluoro acetyl lysine and thioacetyl lysine modified peptides designed to inhibit eukaryotic histone deacetylase enzymes. Evidence of N^ε-lysine acetylation in bacteria, prokaryotic origin of histone proteins and sirtuins acting on them were the main inspiration to test these peptides on model Gram-positive and Gram-negative bacterial strains such as *S. aureus*, *E. coli* and *P. aeruginosa*. The antibacterial properties of non-conjugated peptides KP 13, KP 15 and KP 24 were significantly improved upon conjugation to the cell penetrating peptide, TAT. Overall results show that conjugation to TAT facilitates selective and more efficient internalisation of the peptides resulting in transcription inhibition. Thus, we concluded that the TAT-conjugated peptides can be used as a potent therapeutic agent against Gram-positive and Gram-negative bacterial infections.

Chapter III

3. Structural Insights into the Interaction of Antifungal peptides and Fungal Membrane-specific Ergosterol

This chapter has been adapted from the following publication:

Mohid, S.A.; Biswas, K.; Won, TJ; Mallela, L.S.; Gucchait, A.; Butzke, L.; Sarkar, R.; Barkham, T.; Reif, B.; Leipold, E.; Roy, S.; Misra, A.K.; Lakshminarayanan, R.; Lee, D. K.; Bhunia, A.; **2022**, Structural insights into the interaction of antifungal peptides and ergosterol containing fungal membrane; *BBA - Biomembranes* (doi: 10.1016/j.bbamem.2022.183996).

3.1. Introduction

Membrane-active antimicrobial peptides (AMPs), which selectively disrupt the structural integrity of microbial membranes, are considered a new generation of antibiotics to combat multidrug-resistant pathogenic fungi [148-150]. A precise understanding of the interaction between membrane-active drugs with the components of biomembranes is a prerequisite to unravel their molecular mechanisms on one hand and to optimise their target specificity and thus reduce potential side effects on the other [40]. In a bilayer structure, membrane-active medicines or toxins may target the membrane lipids directly [151]. Naturally occurring and *de novo* designed AMPs are predominantly cationic, but also contain hydrophobic residues [152]. Hence, they interact via electrostatic and hydrophobic interactions with negatively charged lipid headgroups and the hydrophobic acyl chains of their target membranes, respectively [153-156].

Microbial membranes are inherently anionic in composition and spatial geometry, making them structurally and functionally distinct from the host membranes [157-159]. On the other hand, fungal and mammalian cells share a similar membrane surface chemistry, which complicates the development of effective membrane-targeted antimicrobial therapeutics [158,159]. The need to develop new antimicrobial therapeutics is particularly evident in the global increase in antibiotic-resistant fungal infections. Apart from this, most antifungals available today show only limited target specificity and thus are associated with severe systemic toxicity in humans, which is observed especially in deep fungal infections that require prolonged pharmacotherapy [160-163].

One major difference between mammalian and fungal cell membranes lies in the presence of membrane sterols: while cholesterol (CHL) is the principal sterol component

in the membranes of higher mammals, fungi utilize ergosterol (ERG) instead. Both CHL and ERG modulate the physicochemical properties of biomembranes such as the fluidity, the packing density or the lipid ordering states differently [164]. Polyene macrolide antibiotics such as amphotericin B (AMB) induce fungal cell death by forming cation selective pores in fungal membranes in a process that requires the presence of ERG [165,166]. Although substances such as AMB represent the gold standard in the treatment of severe systemic fungal infections, they are considered last resort therapeutics, because their application is associated with severe side effects, including neuro- and nephrotoxicity, particularly in cases that require prolonged treatment periods [167]. However, considering the importance of CHL and ERG for the selectivity and efficacy of available antifungal therapies, it appears plausible to exploit their structural and chemical differences to develop new ERG-selective antibiotics such as AMPs that combine broad antifungal activity with reduced host toxicity[168].

Previously, we reported the design of the broad-spectrum AMP VG16KRKP (VARGWKRKCPLFGKGG), targets bacterial membranes with greater affinity than mammalian plasma membranes.[169-171] In this work, we probe in detail the antifungal properties of VG16KRKP and determine its membrane sterol specificity in mammalian and fungal model membranes. By combining *in vitro* activity assays with low- and high-resolution spectroscopic techniques and microscopic analysis, we demonstrate that the antifungal activity of VG16KRKP is based on its selective interaction with the sterol moiety as well as the phosphatidylethanolamine (PE) lipid in fungal membranes.

3.2. Materials and methods

3.2.1. Strains and media.

A total of 24 fungal strains were used, of which only one type strain was obtained from ATCC. *Candida albicans* ATCC 24433 was purchased from HiMedia Laboratories Pvt. Ltd (India). *Candida albicans* SC5314 as well as *Cryptococcus neoformans* var. *grubii* were a humble gift from Prof. Kaustav Sanyal, JNCASR, Bangalore. Clinical strains were obtained from Tan Tock Seng Hospital, Singapore. The fungal strains were grown and maintained in yeast extract peptone dextrose (YPD) media containing 1% yeast extract, 2% peptone, 2% dextrose, and 1.5% agar.

3.2.2. Peptide synthesis, purification and characterization

VG16KRKP was purchased from Genscript, USA while VG16PA, VG16CA, VG16WA, VG16FA, VG16WFA were purchased from GL Biochem (Shanghai) Ltd.,

China. VG16WLFA and VG16KRKA were synthesized using a conventional F-moc chemistry-based solid-phase peptide synthesis[172] protocol and MBHA-Rink amide resin (0.1 mmol scale) was used for this purpose. After washing the resin in dry Dimethylformamide (DMF), sequential coupling of F-moc protected amino acids followed by subsequent F-moc deprotection using 20% piperidine solution was performed for 1 h and 40 min, respectively. N, N-Diisopropylethylamine (DIPEA) and benzotriazole-1-yloxytripyrrolidinophosphonium-hexafluorophosphate (PyBOP) served as base and peptide coupling reagent, respectively. The peptides attached to the resin were cleaved using standard resin cleavage cocktail containing a mixture of Trifluoroacetic acid (82.5 %, v/v), milli-Q water (5 %, v/v), 1,1-Ethanedithiol (2.5 %, v/v), anisole (5 %, v/v), and phenol (5%, v/v). The filtrate containing the cleaved peptide was precipitated in chilled diethyl ether and subsequently collected by centrifugation. After removing the residual ether from the filtrate, reverse-phase HPLC was carried out on a Phenomenix C₁₈ column using dual UV detection at 220 nm and 280 nm and a binary acetonitrile (1–100 % gradient) solvent system at a flow rate of 3.8 ml/min. The purified peptides were finally analyzed using MALDI-TOF mass spectroscopy.

3.2.3. Peptide susceptibility assay

Fungal cells were grown in YPD medium at 28 °C under shaking conditions for 24-48 h. Conventional micro-broth dilution assay with a single-step modification [171] was performed to assess the anti-fungal activity of the designed peptides. Briefly, the fungal cultures were centrifuged and pellets were washed with and resuspended in 10 mM Phosphate buffered saline (PBS) (pH 7.4). Subsequently, cell suspensions containing 10⁴ CFU/ml were supplemented with the designed peptides. Negative controls containing cells only and positive controls containing cells treated with Amphotericin B were maintained simultaneously. After overnight incubation of both the control as well as the treated samples, OD₆₃₀ was recorded to monitor viability of *Candida spp.* All experiments were performed in triplicates. The viability of *Pythium insidiosum* was detected by MTT assay [173]. Part of this experiment was done in the Singapore Eye Research Institute, Singapore and LV Prasad Eye Institute, Hyderabad, India.

3.2.4. In vitro treatment of human corneal epithelial cells (HCEC) infected with *C. albicans*.

HCECs (1×10⁴ cells/well) were cultured overnight in 96-well plates at 37 °C in presence of 5% CO₂. Cells were infected with *C. albicans* at a multiplicity of infection (MOI) of 10 (HCECs: fungal cells, 1:10). Viability of *C. albicans* was determined 24 h post

infection by measuring the optical density of the fungus-occupied medium at 630 nm (OD_{630}). Subsequently, fungus-containing medium was removed, centrifuged and supernatant was used to determine the cytotoxicity by lactate dehydrogenase (LDH) assay [174]. This experiment was performed in the LV Prasad Eye Institute, Hyderabad, India.

3.2.5. Chemical modification of ergosterol

The ergosterol was modified by hydrogenolysis of the unsaturated bonds present in it using a modified catalytic transfer hydrogenation condition avoiding direct use of hydrogen gas [175]. To a solution of ergosterol (200 mg, 0.504 mmol) in CH_3OH (7 ml) was added 10% Pd/C (40 mg) followed by drop wise addition of Et_3SiH (240 μ l, 1.51 mmol) over a period of 5 min. The reaction mixture was allowed to stir at room temperature for 3 h, filtered through a Celite bed and washed with methanol (CH_3OH) (2×15 ml). The filtrate was concentrated under reduced pressure to give the crude product, which was purified over SiO_2 using hexane-EtOAc (2:1) as eluant to give pure hydrogenated ergosterol (hERG) (176 mg, 87%). [176]

3.2.6. Liposome preparation.

1,2-dioleoyl-sn-glycero-3-phosphocholine (DOPC), 1,2-dioleoyl-sn-glycero-3-phosphoethanolamine (DOPE) cholesterol (CHL) and ergosterol (ERG) were purchased from Avanti Polar Lipids Inc. (AL, U.S.A). Stock solution of all the lipids were prepared in chloroform to obtain a concentration of 25 mg/ml. Model membrane mimics were created following standard protocol wherein fungal membrane was mimicked composing 5:4:3 DOPC/DOPE/ERG and mammalian membrane mimic was formed using 6:4 DOPC/CHL. Other model membrane mimics containing 100% DOPC, 5:4:3 DOPC/DOPE/hERG, 5:4:3 DOPC/DOPE/CHL, 5:4 DOPC/DOPE and 5:3 DOPC/ERG were also prepared. These model mimics were dried in a stream of nitrogen gas and lyophilized overnight to create lipid films. Next day, the lipid film was hydrated with 70 mM calcein dissolved in 10 mM Tris buffer (pH 7.4), vortexed for 30 min, followed by five freeze-thaw cycles in liquid nitrogen and lukewarm water to obtain the dye entrapped vesicles. The vesicles were then passed through a 100-nm polycarbonate membrane filter stacked in a mini extruder (Avanti Polar Lipids, Alabaster, AL) set up to obtain unilamellar vesicles (LUVs) [170]. The free calcein dye was removed by passing the extruded samples through a gel-filtration based hydrated Centriscp-Spin Column (Thermo Fisher Scientific, Waltham, MA) which was centrifuged at 3000 rpm for 2 min. The suspensions obtained after the centrifugation were used for subsequent experiments.

3.2.7. Fluorescence spectroscopy: Calcein dye leakage assay

Dye-encapsulated liposome representing model fungal and mammalian membrane mimics were suspended in extra vesicular buffer containing 10 mM Tris buffer, 100 mM NaCl (pH 7.4). The leakage of calcein caused by liposome rupture was analyzed by fluorescence emission at 519 nm using a JASCO F-8500 fluorescence spectrophotometer (Easton, MD). The slit width for both excitation and emission were kept at 2.5 nm. Test peptides were added at various concentrations and enhancement in fluorescence was measured. 0.1% Triton X-100 served as a positive control, completely disrupting the calcein-encapsulated unilamellar vesicles. Percentage leakage was calculated using the equation (3) as described in chapter 2. In case of temperature dependent dye leakage assays, a water bath with temperature control connected to the fluorimeter was used to keep the temperature constant from 25 – 45 °C, at an interval of 5 °C during the experiments.

3.2.8. Preparation of giant liposomes (GLs) for microscopy

Unlabeled and fluorescently labelled GLs were prepared by following the gel-assisted method as described by Weinberger *et al.* and modified as per requirement.[177] Briefly, a solution of 5 % (w/w) poly-vinyl alcohol (PVA) was prepared by dissolving into Millipore water and heated at 90 °C with constant stirring until the suspension formed a clear solution. 300 µL of the solution was then dropped in a small 30 mm Petri dish to make a thin even layer. The plates were then transferred into a hot air oven and kept for drying at 50 °C for 30 min. For phase contrast microscopy, stock solutions of 2 mg/ml DOPC, DOPE, CHL and ERG were prepared in chloroform and 20 µl of the lipid mixture (prepared by maintaining the particular ratios) were spread on the PVA film in a non-overlapping way. Then, the plates were placed in a Lyophilizer for 45 min to remove the trace amount of the solvents. Before using the lipid films, the plates were subjected to UV treatment for 15 min to prevent dewetting and cleaning. To create a phase difference while observing the GLs under the microscope, 800 µl of 100 mM sucrose solution was added into the lipid film to swell and kept for 10-15 min [178]. Then the plates were gently swirled to dislodge the liposomes from the PVA layer and thereafter, the GLs were collected in a centrifuge tube within 45 min. Next, the vesicles were added into a well where a 105 mM glucose solution was already added with or without the peptide solution. The correct formation of GUVs were verified using a Nikon Microscope (model Ts2FL, Nikon, Japan) [178].

For Confocal microscopy, *C. albicans* cells were grown in YPD broth and washed with 10 mM PBS. Then the cells were incubated in presence of 10 µM FITC-VG16KRKP

and 8 $\mu\text{g/ml}$ propidium iodide for 15 min at 28 °C at 160 rpm. The cells were washed again, followed by 2 μl of the suspension was placed on a glass slide, covered with a coverslip and sealed to observe under the microscope. For the liposomal systems, the lipid mixtures were doped with 1 mol% rhodamine-DOPE and then the films were prepared by following the same protocol as detailed above. This time, the lipid films were swelled by adding 10 mM phosphate buffer (pH 7.4) and the GLs were seen under a TCS SP8 Confocal Laser scanning microscope (Leica, Wetzlar, Germany) against an extra vesicular solution containing 10 μM FITC-VG16KRKP. The images were collected with a 488 nm band-pass filter for FITC excitation and a 543 nm band-pass filter for propidium iodide or rhodamine excitation at a magnification of 63 \times (oil immersion) with a numerical aperture of 1.4. Acquisition Suite X software (Leica) was used for capturing images and data processing.

3.2.9. Dynamic light scattering (DLS) analysis

The 5:4:3 PC/PE/ERG LUV was prepared as described in liposome preparation section without the calcein dye. The experiment was performed by using a Malvern Zetasizer Nano S (Malvern Instruments) device came with a 4-mW He-Ne laser ($\lambda = 633$ nm) and a backscattering angle of 173° [171]. The LUVs were taken in a disposable cuvette and titrated with the VG16KRKP peptide from 5 mM to 30 mM and the spectra were recorded for 1 h. The temperature was set to 25 °C. The refractive index and viscosity of the Tris buffer (pH 7.4) was set to 1.35 and 0.89, respectively. The particle size distribution, polydispersity index (PDI) and autocorrelation data were obtained from the Zetasizer Software v.7.11 (Malvern Instruments) that was provided with the instrument.

3.2.10. Preparation of NMR sample

For ^{31}P solid-state NMR, 5 mg/ml and for solution state NMR, 2 mg/ml of the lipids from specified ratios were used as previously described [170]. The lipid samples were dried under a stream of nitrogen and then subjected to lyophilize for overnight to eliminate any residual solvent. For Solid state NMR, the lipid films were prepared in the NMR tubes but for solution state, the films were prepared in a small glass vial. The lipid films were then hydrated by adding 50 μl (solid state) or 600 μl (solution state) Tris buffer (pH 7.4 and 6.5, respectively) and were vortexed for 5 min at ambient temperature and freeze-thawed using liquid nitrogen at least five times to ensure the uniform size of the vesicles. The analogs of the VG16KRKP peptide solution were added to the buffered lipid solution at appropriate concentrations and the final volume was adjusted to 100 μl for each solid-state NMR experiment. For solution state NMR, the freeze-thawed samples were extruded through a

100 nm polycarbonate filter (Avanti Polar Lipid, AL, USA) for 21 times and a uniform sized LUVs were prepared for further assessment. In case of *C. albicans* live cell experiments; the cells were grown overnight in a modified YPD broth where the dextrose (Carbon source) was replaced with 2% ^{13}C -labelled glucose (Sigma-Aldrich, Merck KGaA, Darmstadt, Germany). Overnight stationary phase *C. albicans* cells were sub-cultured to get log phase cells of *C. albicans*. The cells were then collected by centrifuging at 5500 rpm for 5 min and washed twice with the same buffer and finally $\text{O.D}_{630} = 1$ (i.e., 1×10^7 CFU/ml), cell concentration in 600 μl volume was taken for the experiment.

3.2.11. Solid-state NMR spectroscopy

NMR experiments were performed on an Agilent NMR spectrometer (DD2) operating at the resonance frequency of 699.88 MHz for ^1H and 283.31 MHz for ^{31}P and equipped with a 4 mm MAS HXY Solid Probe (Agilent). ^{31}P NMR experiments were performed using a single 90° pulse and 24 kHz TPPM proton decoupling. The $\pi/2$ pulse lengths were 7.5 μs for ^{31}P nucleus. MLVs were kept in a 4 mm Pyrex glass tube, which was cut to fit into the MAS probe, and sealed with parafilm. An Agilent temperature control unit was used to maintain the sample temperature at 25 $^\circ\text{C}$. After collecting spectra, the sealed samples were kept on the lab bench for the subsequent experiments. For 5:4:3 DOPC/DOPE/ergosterol or cholesterol or hydrogenated ergosterol MLV samples, ^{31}P spectra were collected with 256 scans and a recycle delay of 2 s was applied. ^{31}P spectra were referenced externally to 85% phosphoric acid (0 ppm). All the spectra were processed with MestReNova software (Ver 8.1) with 250 Hz line broadening.

3.2.12. Solution-state NMR spectroscopy

All NMR experiments were done at 298 K on a Bruker Avance III 700 MHz NMR spectrometer equipped with a 5 mm RT probe. 10% deuterated water and 3-(trimethylsilyl)-2,2,3,3-tetradeuteriopropionic acid (TSP) was used for locking and internal standard (0.00 ppm), respectively. First a free one-dimensional (1D) ^1H NMR spectrum of the free peptide was recorded and next a series of 1D ^1H (water suppression using excitation sculpting) and ^1H coupled ^{13}C -NMR (zgpg30, 1D sequence with gated decoupling using 30° flip angle) spectra were recorded after addition of the 1×10^7 CFU/ml cells. Appearance of new peaks were observed in the 1D ^{13}C as a result of the efflux of metabolites from the cells. Two-dimensional (2D) ^1H - ^1H total correlation spectroscopy (2D TOCSY, mlevesgpph), and two-dimensional ^1H - ^1H nuclear Overhauser effect spectroscopy (2D NOESY, noesyegpph) was recorded after a series of titration using live cell and 1D ^1H spectra were

observed to obtain a significant line broadening which indicates sufficient free to bound peptide ratio in presence of cells. The mixing time of 80 ms for TOCSY and 150 ms for NOESY was used, respectively with a spectral width of 12 ppm in both directions. Number of scans for TOCSY and NOESY was set to 8 and 16, respectively with 16 numbers of dummy scans in both the cases. $256 (t_1) \times 2048 (t_2)$ for TOCSY and $456 (t_1) \times 2048 (t_2)$ for NOESY experiments were performed in order to complete the data collection within 4 h using a Bruker Avance III 700 MHz spectrometer. Data processing and analysis were carried out using TopspinTM v3.1 software (Bruker Biospin, Switzerland) and Sparky software, respectively.[124] Live cell 1D ¹H and 2D NMR experiments were done by suspending the cells in 10 mM phosphate buffer (pH 5.25) and ¹³C NMR was done using 10 mM phosphate buffer of pH 7.4. The SWH (Hz) parameters for all the solution NMR experiments are as follows: 1D ¹H experiment (pulse program: zgesgp): 8417.509 Hz; 1D ¹³C coupled/fully decoupled (pulse program: zggd30 and/or zgpg30): 42613.637 Hz; 2D TOCSY/NOESY: 7002.801 (F2), 7001.853 (F1) Hz, respectively.

3.2.13. NMR derived structure calculation

For calculation of the three-dimensional *C. albicans*-bound structure of the peptides, the volume integrals of their respective NOE cross-peaks were qualitatively differentiated into strong, medium and weak, depending on their intensities in the *tr*NOESY spectra. This information was further transformed to inter-proton upper bound distances of 3.0, 4.0 and 5.0 Å for strong, medium and weak peaks, respectively, while the lower bound distance was fixed to 2.0 Å. The backbone dihedral angles of the peptides, phi (ϕ) and psi (ψ) were kept flexible (-30° to 120° and -120° to 120° , respectively) for all non-glycine residues to limit the conformational space. CYANA program v2.1 was used for all structure calculations with iterative refinement of the structure based on distance violation [179]. Hydrogen bonding constraints were excluded from structure calculation. The NMR-derived ensemble structures were analyzed using PyMol and UCSF Chimera [180].

3.2.14. Electrophysiology

HEK293 cells (CAMR, Porton Down, Salisbury, UK) were maintained in Modified Eagle's Medium (MEM), supplemented with 9.5 % fetal calf serum and 1% penicillin-streptomycin (Thermo Fisher Scientific, USA) in a 5% CO₂ incubator at 37 °C. Cells were transiently transfected with a 5:1 ratio of a plasmid containing the coding sequence of Kv3.4 (NP_001116248) and a construct coding for the enhanced green fluorescent protein (EGFP) using the Metafectene Pro transfection reagent (Biontex Laboratories GmbH,

München, Germany). Individual transfected cells were identified visually by their green fluorescence using a LED light source (CoolLED Ltd., NY, USA) and an EGFP filter set. Whole-cell voltage-clamp recordings were obtained using an EPC-10 patch-clamp amplifier operated by PatchMaster software (HEKA Elektronik, Reutlingen, Germany). Data were low-pass filtered at 4 kHz and sampled at an interval of 50 μ s. Patch pipettes with a resistance of 1.5–2 M Ω were fabricated from borosilicate glass and coated with silicone adhesive (Dow Corning GmbH, Wiesbaden, Germany) to reduce tip capacitance. This experiment was performed in the University of Lubeck, Germany.

Table 3.1. MIC_{90%} values of VG16KRRP for antagonizing various fungal strains.

FUNGAL CELLS	STRAINS	MIC_{90%} (μM)
<i>CANDIDA ALBICANS</i>	SC5314	10
	2672R	128
	ATCC 24433	10
<i>CRYPTOCOCCUS</i>	H99	10
<i>NEOFORMANS SER. GRUBII</i>		
<i>CANDIDA TROPICALIS</i>	CT 1001	8
	CT 1002	2
	CT 1003	32
	CT 1004	2
	CT 1005	2
	CT 1006	2
	CT 1007	64
	CT 1008	4
	CT 1009	16
	CT 1010	16
<i>CANDIDA PARAPSILOSIS</i>	CP 1001	64
	CP 1002	64
	CP 1003	32
	CP 1004	32
	CP 1005	32
	CP 1006	32

<i>CANDIDA GLABRATA</i>	CP 1007	32
	CP 1008	32
	CP 1009	32
	CP 1010	32
	CG 1008	128

Series resistance was corrected electronically up to 80 %. The bath solution contained 120 mM NaCl, 3 mM KCl, 2.5 mM CaCl₂, 1 MgCl₂, 30 HEPES, 15 glucose (pH 7.4 with NaOH), and the patch pipettes 140 mM KCl, 1 mM MgCl₂, 10 mM EGTA, 10 mM HEPES (pH 7.4 with KOH). VG16KRKP was diluted in bath solution to a final concentration of 100 μM and locally applied using a fine-tipped glass pipette as described previously.[181] All recordings were performed at room temperature (22 ± 1 °C) between 24–48 h after transfection. Activation of Kv3.4 channels was assayed with repetitive voltage pulses of 100 ms duration, ranging from –80 to 80 mV, delivered at an interval of 4 s. Modulation of Kv 3.4-mediated peak current amplitudes by VG16KRKP was measured with repetitive 30 ms pulses to 50 mV, applied at an interval of 3 s. Leak currents were subtracted online using a p/n procedure provided by PatchMaster software. The holding potential was –80 mV throughout. Data analysis was performed with FitMaster (HEKA Elektronik, Reutlingen, Germany) and IgorPro (WaveMetrics, Lake Oswego, OR, USA) Software.

3.3. Results and discussion

3.3.1. Evaluation of the antifungal property of the peptide

To determine the antifungal spectrum of VG16KRKP, we assessed the impact of the peptide on the growth of a set of clinically relevant and widely used laboratory strains of the *Cryptococcus neoformans* and *Candida* family [182], including *C. albicans*, *C. tropicalis*, *C. parapsilosis* and *C. glabrata*. The minimum inhibitory concentration of VG16KRKP required to reduce fungal growth by 90% (MIC₉₀) ranged from 2–128 μM among the strains tested (Table 3.1), demonstrating a broad-spectrum antifungal activity of the peptide against these fungal strains. Despite the observed variability in MIC₉₀ values, which is most likely due to the differences in the chemical composition of the cell membranes of the different strains, VG16KRKP yielded a promising mean MIC₉₀ (± SEM) of 32.7 ± 6.9 μM ($P < 0.0001$). To analyze the impact of VG16KRKP on fungal cell viability in more detail, *C. albicans* cells were exposed to Fluorescein isothiocyanate (FITC)-labelled VG16KRKP and propidium iodide (PI), a non-specific nucleic acid stain

that exclusively enters non-viable cells with ruptured cell membranes to generate red fluorescence. As revealed by confocal laser scanning microscopy, FITC-VG16KRKP stained the fungal plasma membranes and triggered entry of PI into the cells (Figure 3.1 (A)). By contrast, PI-mediated fluorescence was absent in control *C. albicans* cells not exposed to the peptide confirming that VG16KRKP destabilized the fungal membranes.

3.3.2. Selective activity of the peptide

Since *Candida spp.* is one of the leading causes of corneal infections, often associated with severe and permanent visual impairment [183,184], we analyzed the mammalian-specific cytotoxicity of VG16KRKP and its clinical potential as antimycotics using immortalized human corneal epithelial cells (HCECs) as a model [185,186]. To mimic corneal infection, *in vitro* HCECs (Figure 3.1 (B)) were infected with *C. albicans* (Figure 3.1 (C)) in the absence or presence of the peptide (Figure 3.1 (D)). As shown in Figure 3.1 (D), infected HCEC treated with VG16KRKP had less fungal load compared to cells not treated with the peptide (Figure 3.1 (C)). LDH assay was done to determine the cytotoxicity of the peptide towards HCEC, and significantly reduced cytotoxicity was observed in infected cells treated with the peptide (Appendix III, Figure S3.1). Subsequently, the viability of HCECs and *Candida* was assessed for 24 h post infection. As shown in Figure 3.1 (C), exposure of the co-culture to increasing concentrations of VG16KRKP gradually reduced the fungal population by $50 \pm 0.9\%$ ($P < 0.05$) while viability of the HCECs was largely unaffected by the presence of the peptide, indicating that VG16KRKP targets preferentially fungal cells.

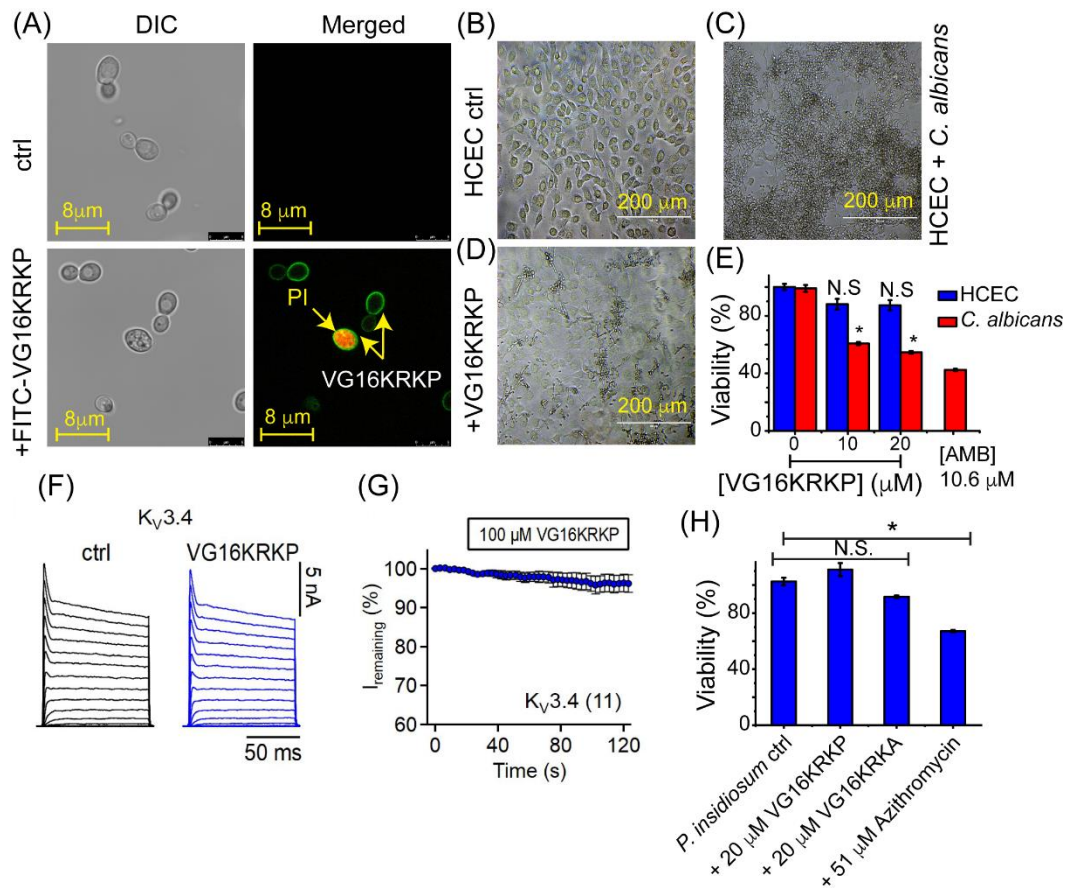


Figure 3.1. (A) Confocal laser scanning microscopic (CLSM) images of FITC-VG16KRKP-untreated (ctrl, upper row) and -treated (10 μ M, lower row) *C. albicans* cells. Propidium iodide (PI) was present in both conditions to monitor cell viability. FITC-VG16KRKP (green) associated with cell membranes disrupted membrane integrity within 15 min, leading to cell death, which triggered prominent PI signals (red). Phase contrast microscopic images of peptide-untreated HCECs before (B) and after (C) infection with *C. albicans*. (D) HCECs infected with *C. albicans* after addition of 20 μ M VG16KRKP (2 \times MIC). (E) Percent viability of HCECs co-cultured with *C. albicans* in presence of different concentrations of VG16KRKP demonstrating the antifungal activity of the peptide. Amphotericin B (AMB) was used as positive control. (F) Representative whole-cell current traces of a HEK293 cell transiently expressing *K_v3.4* channels before (ctrl) and after (blue) equilibration with 100 μ M VG16KRKP (10 \times MIC) for 100 s. Test depolarizations ranged from -80 to 80 mV in steps of 10 mV. (G) Time course of *K_v3.4* peak currents at 50 mV upon application of 100 μ M VG16KRKP. Data points are means \pm Sem. With the number of experimental replicates, *n*, indicated in parentheses. (H) Percent viability of *P. insidiosum* cells (ctrl) treated with either VG16KRKP, VG16KRKA or azithromycin. While azithromycin was used as positive control, VG16KRKA was used as a negative control. Bars in E, F are means \pm Sem. Obtained from three independent experimental replicates. Asterisks indicate statistical significance between pairs of data according to a two-sided Student's *t*-test: **P* < 0.05, N.S. not significant.

3.3.3. Interaction with ion channels

VG16KRKP is very similar in size and positive net charge to neurotoxic cone snail peptides (conopeptides), which specifically target ion channels in the membranes of vertebrates [187,188], also raising the possibility of functional interactions between VG16KRKP and mammalian ion channels. Most ion channels in cornea epithelial cells are K⁺-selective, of which the voltage-gated potassium channel Kv3.4 is the most abundant subtype.[189] These channels participate in a variety of different signaling pathways, including osmoregulation, cellular stress responses, control of cell cycle progression, and are involved in maintaining the cells resting membrane potential. To probe if Kv3.4 channels are functionally modulated by VG16KRKP, the channels were transiently expressed in HEK293 cells and their current responses were analyzed in absence and presence of VG16KRKP during single-cell patch-clamp recordings. Application of 100 μM VG16KRKP did not affect the shape of Kv3.4-mediated current responses (Figure 3.1 (F)) and reduced the peak current amplitudes only marginally by $3.7 \pm 2.2\%$ ($P > 0.05$) (Figure 3.1 (G)), demonstrating that Kv3.4 channels are not a target of VG16KRKP.

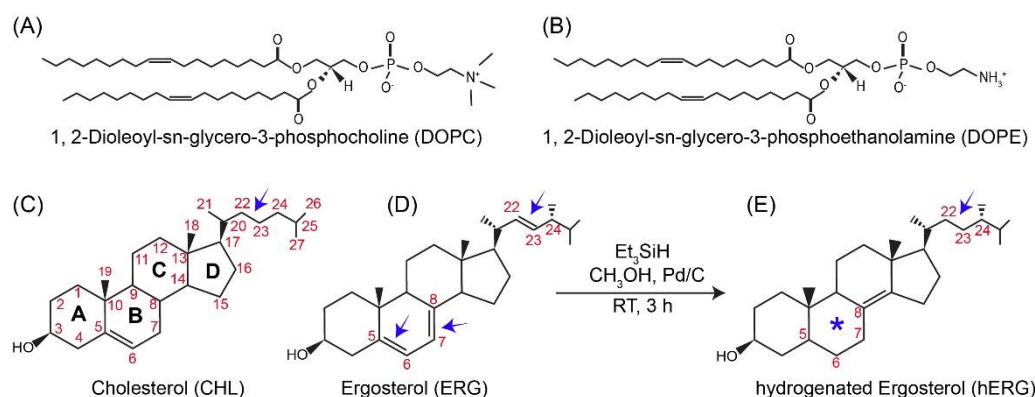
3.3.4. Ergosterol specific activity

The data presented so far confirm that VG16KRKP specifically targets fungal cell membranes, while mammalian cell membranes are largely unaffected by the peptide. The chemical compositions of mammalian and fungal cell membranes are very similar; however, they differ considerably with respect to their sterol moieties. While mammalian membranes employ cholesterol, fungal membranes instead contain the chemically distinct ergosterol (Scheme 3.1). Since ergosterol is the only fungus-specific membrane component, we wondered if the antimycotic activity of VG16KRKP is ergosterol-dependent. To test this hypothesis, we evaluated the effect of VG16KRKP and its analog VG16KRKA with reduced positive charge, on the growth of *Pythium insidiosum*, an oomycete lacking ergosterol in its membrane. As depicted in Figure 3.1 (H), neither VG16KRKP nor VG16KRKA inhibited the growth of *P. insidiosum*, whereas azithromycin, used as positive control, significantly suppressed *P. insidiosum* ($P < 0.05$) (Figure 3.1 (H)).

3.3.5. Probing the sterol selectivity of the peptide

To determine the mechanism underlying the susceptibility of fungal and ergosterol-deficient cells to VG16KRKP, we generated calcein-filled large unilamellar vesicles and giant liposomes (LUVs and GLs, respectively) that mimic the membrane composition of fungal or mammalian cells. While the fungal membrane model mimic was composed of

DOPC/DOPE/ERG at a molar ratio of 5:4:3, the mammalian membrane model contained DOPC/CHL at a molar ratio of 6:4. As reported earlier, VG16KRKP is non-toxic against eukaryotic model membrane composed of 6:4 PC/CHL [170]. In this present study, therefore, we have used 5:4:3 PC/PE/CHL to draw closer resemblance to the fungal mimic 5:4:3 PC/PE/ERG and also probe the role of PE, if any in the interaction. Compared to CHL, ERG contains two additional unsaturated bonds at positions C7 and C22 as well as an additional methyl group (-CH₃) at C24 (Scheme 3.1 (C-D)).



Scheme 3.1: Chemical structures of DOPC (A), DOPE (B), Cholesterol (C) and Ergosterol (D). (E) A modified catalytic transfer hydrogenation condition avoiding direct use of hydrogen gas was used to synthesize hydrogenated ergosterol (hERG).

These differences led us to hypothesize that the packing of the acyl chain of ERG might affect the interaction with VG16KRKP. To test this hypothesis, we removed the unsaturated bonds in ERG by hydrogenation (Scheme 3.1) to generate another class of sterol molecule named hERG as described in the materials and methods section. As revealed by NMR (Appendix III, Figures S3.2 and S3.3) and mass spectroscopy (Appendix III, Figure S3.4), hERG contained only a single unsaturated bond at C8 (Scheme 3.1 (E)), indicating successful hydrogenation [175,190]. Since the peptide contains one cysteine residue (Cys9), a MALDI TOF/TOF analysis was further performed to ensure that the peptide does not form any dimeric structure. The MALDI analysis showed one single peak at *m/z* ratio of ~1760 (Appendix III, Figure S3.5), which confirms that the peptide used in all the experiments are in monomeric form. Next, a model vesicle containing 5:4:3 DOPC/DOPE/hERG was prepared for further assays to test our hypothesis. The vesicles were subjected to increasing concentrations of VG16KRKP, while monitoring the release of calcein at 25 °C by means of its intense fluorescence signal. As shown in Figure 3.2 (A),

VG16KRKP caused the release of calcein from 5:4:3 DOPC/DOPE/ERG vesicles in a concentration-dependent manner. Thus, the dye leakage increased almost linearly with peptide concentrations up to 20 μM showing a maximum of 60 % leakage. Titrating with higher concentrations of peptide did not cause any further increase in the leakage percentage depicting saturation. By contrast, LUVs containing CHL or hERG showed a rather weak response upon titration with VG16KRKP. At a concentration of 30 μM only 15 % of the fluorescent probe was released from 5:4:3 DOPC/DOPE/CHL and < 10% from LUV containing 5:4:3 DOPC/DOPE/hERG (Figure 3.2 (A)), further confirming the preference of VG16KRKP for ergosterol over cholesterol.

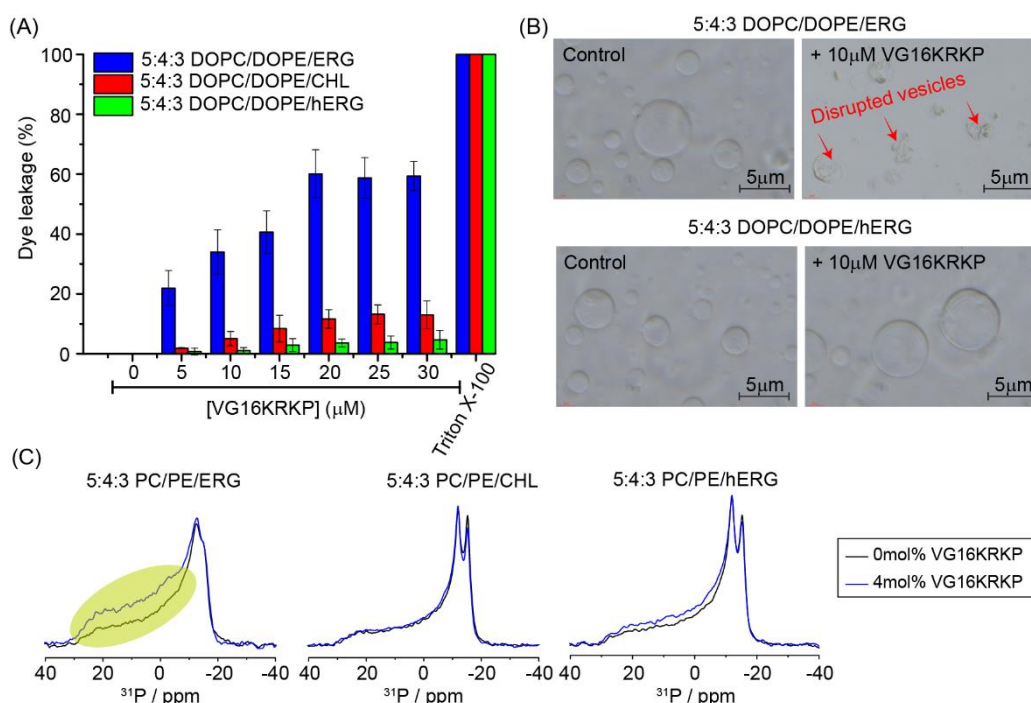


Figure 3.2. (A) Calcein dye leakage assay using either 5:4:3 DOPC/DOPE/ERG-, DOPC/DOPE/CHL-, or DOPC/DOPE/hERG-containing LUVs with increasing concentrations of VG16KRKP. For all conditions, Triton X-100 was used as positive control. (B) Phase contrast microscopic analysis of GUVs consisting of either 5:4:3 DOPC/DOPE/ERG or DOPC/DOPE/hERG result in distinguishable peptide activity. Arrows mark disrupted vesicles. (C) ^{31}P NMR spectra of the three model membrane vesicles as detailed above in the absence and presence of 4 mol% VG16KRKP.

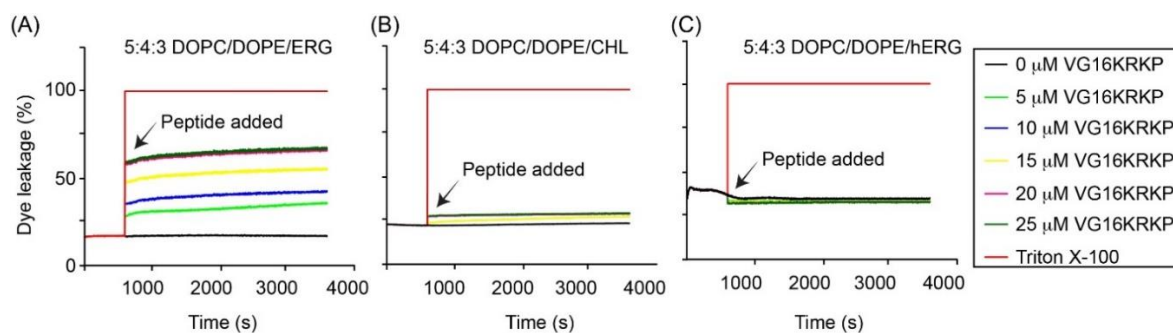


Figure 3.3. Time dependent calcein dye leakage assay with 5:4:3 DOPC/DOPE/ERG (A), DOPC/DOPE/CHL (B) and DOPC/DOPE/hERG (C) LUVs for 1 h. The addition of peptide (arrows) at various concentrations triggered dye leakage exclusively in LUVs containing DOPC/DOPE/ERG. In all conditions, 0.1 vol% Triton X-100 was used as a positive control.

3.3.6. Kinetics of dye release

It is noteworthy to mention that the release of calcein from vesicles occurred almost instantaneously with the addition of the peptide (Figure 3.3 (A-C)) in all the three liposomes. However, the 5:4:3 DOPC/DOPE/ERG vesicles showed increasing intensities of calcein fluorescence as obtained in the dye leakage assay shown in Figure 3.2 (A). To confirm these findings further, we carried out phase contrast microscopy in the absence and presence of VG16KRKP. Addition of 10 μM peptide to GLs composed of 5:4:3 DOPC/DOPE/ERG caused immediate membrane disruption as shown Figure 3.2 (B), whereas no changes in vesicular morphology were observed for hERG-containing GLs exposed to the same concentration of the peptide (Figure 3.2 (A-B) and 3.3 (C)).

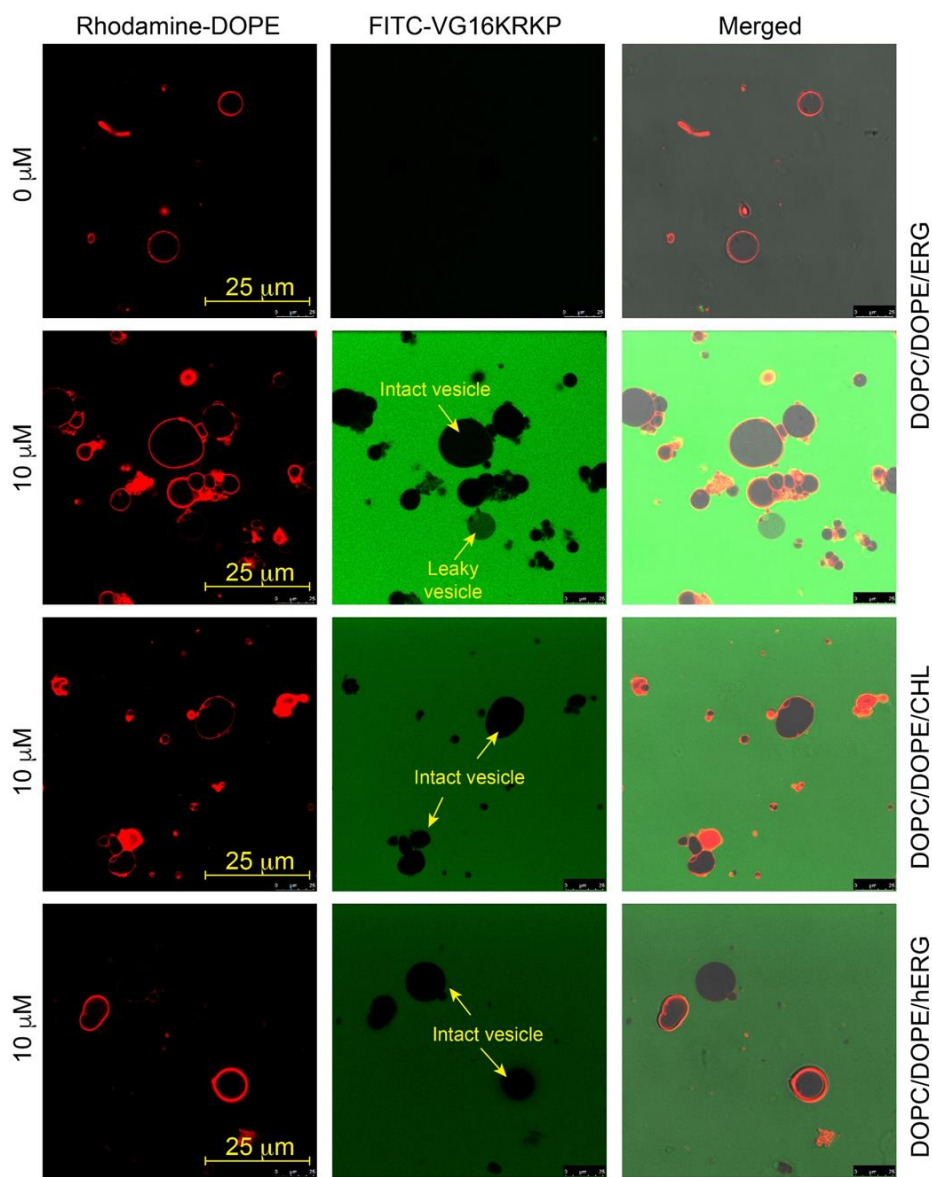


Figure 3.4. Confocal laser scanning microscopy (CLSM) of the GLs composed of 5:4:3 DOPC/DOPE/ERG, 5:4:3 DOPC/DOPE/CHL and 5:4:3 DOPC/DOPE/hERG. Vesicles were prepared in presence of 1% Rhodamine-DOPE (red). Subsequently, rhodamine-DOPE-labeled vesicles were exposed to 10 μM FITC-VG16KRKP (green).

3.3.7. Microscopic and ^{31}P NMR analysis

Furthermore, confocal laser scanning microscopy (CLSM) was carried out using 1% rhodamine-DOPE as a fluorescence probe, in the absence and presence of 10 μM FITC-VG16KRKP (Figure 3.4). The images revealed that all control GLs are perfectly sphere-shaped and were stable for more than 4 h. Addition of VG16KRKP into GL buffer caused membrane perturbation within 5-10 min only for 5:4:3 DOPC/DOPE/ERG GLs. In the presence of VG16KRKP, GLs became 'leaky', which was evident by increased green fluorescence inside the vesicle (Figure 3.4). Since the $\text{MIC}_{99\%}$ of FITC-VG16KRKP is 30

μM (Appendix III, Figure S3.6), the vesicles did not show any leakage in the presence of $10 \mu\text{M}$ concentration, rather than showing passive incorporation inside the vesicles.

The morphology of vesicles containing hERG or CHL remained unaltered after the addition of the peptide FITC-VG16KRKP and no FITC fluorescence signal was found inside the vesicles. To investigate the effects of VG16KRKP on membrane rigidity, we performed ^{31}P solid-state NMR experiments (Figure 3.2 (C)). The one-dimensional static ^{31}P NMR of the vesicles yielded a typical powder pattern spectrum with characteristic frequencies at ~ 30 ppm (parallel edge) and -15 ppm (perpendicular edge), suggesting that the lipids were distributed almost homogeneously in the multi-lamellar vesicles (MLVs). Addition of 4 mol% VG16KRKP into the three vesicle preparations showed no isotropic peak. However, vesicles composed of 5:4:3 DOPC/DOPE/ERG showed an increase of intensity of the parallel edge, which might resemble membrane disordering or an increased population of flattened vesicles (Figure 3.2 (C)). On the contrary, 5:4:3 DOPC/DOPE/CHL and/or DOPC/DOPE/hERG MLVs showed almost similar spectra in the absence and presence of the peptide (Figure 3.2 (C)), suggesting no change of liposome integrity in the presence of the peptide. These results further corroborate the selectivity of VG16KRKP for fungal membranes or mimetic fungal membranes.

3.3.8. Temperature Dependent Dye Release Assay

In order to understand the membrane destabilizing property of the peptide with increasing temperature towards the vesicles composed of 5:4:3 DOPC/DOPE/ERG, DOPC/DOPE/CHL and DOPC/DOPE/hERG, a series of calcein leakage assays were performed in a range of 30°C to 45°C temperature, at an interval of 5°C . Although the temperature range was higher than the phase transition temperatures of the vesicles containing CHL or ERG or hERG [from the liquid ordered (L_o) to liquid disordered (L_d) state] [191,192], the percent of dye leakage for the vesicles containing ERG showed more destabilization compared to the CHL and hERG vesicles (Figure 3.5 (A)). Interestingly, a dramatic increment of dye leakage from 49 % at 30°C to 95 % at 45°C was observed at $20 \mu\text{M}$ concentration of VG16KRKP in case of ERG-containing 5:4:3 DOPC/DOPE/ERG vesicles, whereas the 5:4:3 DOPC/DOPE/CHL or DOPC/DOPE/hERG vesicles showed only ~ 20 -25 % leakage at same concentration ($30 \mu\text{M}$) of VG16KRKP and at the same temperature. This data suggests that the peptide maintains selectivity for DOPC/DOPE/ERG LUVs over DOPC/DOPE/CHL or DOPC/DOPE/hERG LUVs at higher temperatures as well (Figure 3.5 (A)).

3.3.9. Determination of vesicle size after peptide treatment

In order to show the lytic action of the peptide upon the ERG containing vesicles, time lapse dynamic light scattering (DLS) experiment was performed (Figure 3.5 (B)) [193,194]. The DLS experiment was carried out by incubating the 5:4:3 DOPC/DOPE/ERG LUVs in the absence and presence of 5, 10 and 20 μM VG16KRKP for 1 h. The control vesicles were monodispersed with a hydrodynamic diameter of around 90 ± 10 nm. By contrast, the LUVs that were incubated with 5, 10 and 20 μM peptide showed a decreased hydrodynamic diameter of approximately 74 nm, 47 nm, and 30 nm, respectively, after 20 min. The polydispersity index (PDI) of the solutions was also increased after the addition of VG16KRKP, suggesting that addition of the peptide to the originally homogenous vesicles generated deformed lipid-peptide complex, which corroborates well with the phase contrast microscopic analysis.

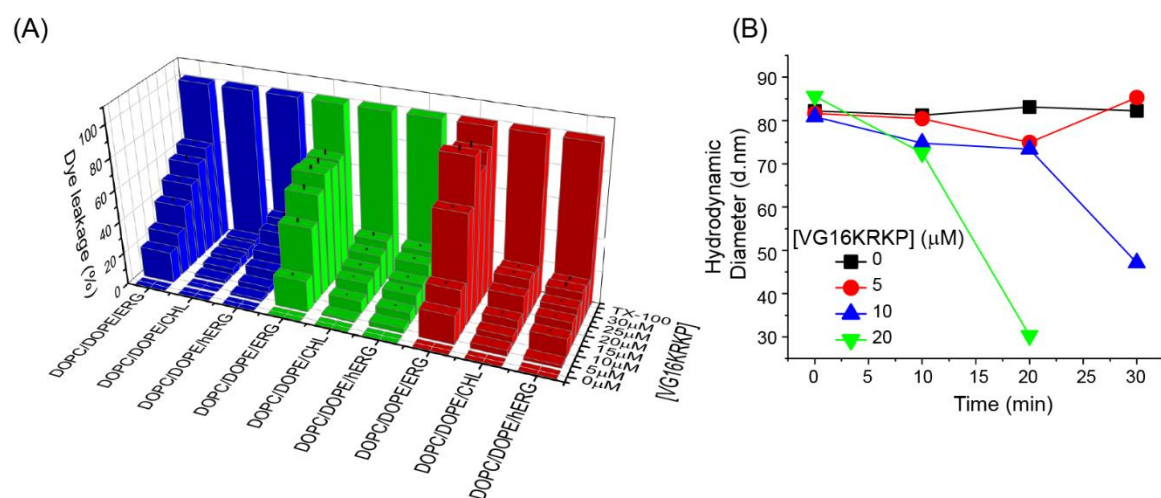


Figure 3.5. (A) Three-dimensional bar plot showing the percent of temperature-dependent calcein dye leakage of ERG- CHL- and hERG-containing vesicles. Different colour codes indicates 30 °C (blue), 40 °C (green) and 45 °C (red) temperatures, respectively. (B) Time-lapse dynamic light scattering experiment showing the decrease in size of the vesicles with time upon exposure to various concentrations of VG16KRKP.

3.3.10. Comparison of other membrane systems with fungal model membranes

As a control, we prepared other model membranes using the following ratios viz. 100 % DOPC, 5:3 DOPC/ERG (DOPE was removed) and 5:4 DOPC/DOPE (no sterol was used). Surprisingly, VG16KRKP showed negligible activity against these lipid membranes,

as shown in Figure 3.6. Though ERG is an important component in fungal membranes, 5:3 DOPC/ERG LUVs were still not affected by VG16KRKP. The data indicates that the membrane composition constituting of 5:4:3 DOPC/DOPE/ERG, corresponding to the more realistic fungal membrane composition, provides the optimum conditions as well as interface to VG16KRKP to interact with the membrane model [35,170]. Interestingly, the role of phosphatidylethanolamine in governing the interaction was also noteworthy (Figure 3.6). Other membrane mimics, on the other hand, were unable to drive the interactions of VG16KRKP at the lipid-peptide interface. These results are in agreement/consistent with our previous structural studies in LPS, demonstrating the selectivity of VG16KRKP toward fungal membranes.

3.3.11. Elucidation of the three-dimensional structure

To understand the lipid-peptide interaction at atomic level, we determined the three-dimensional solution NMR structure of VG16KRKP in the presence of live *Candida spp.* using transferred NOESY [195-197] (Table 3.2, Figures 3.7 (A) and S3.7, S3.8, Appendix III) before the cells released the metabolites (~ 4 h). During this time period, we observed only three long-range NOE cross peaks Val1H α /Trp5H2, Phe12 β /Trp5H2 and Leu11 β /Trp5H2, in addition to \odot to $i+1$ NOEs, indicating that the 3D structure of VG16KRKP is loosely bound to the cells (Figure 3.7 (A)) with an average RMSD value of the backbone (N, C α , C') 2.42 ± 0.62 Å and heavy atoms 3.44 ± 0.73 Å of 15 ensemble structures (Figure 3.7 (B)).

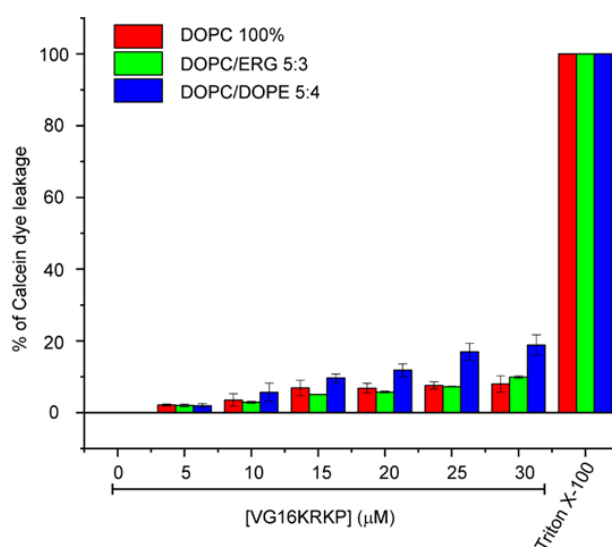


Figure 3.6. Concentration dependencies of calcein dye leakage using vesicles consisting of 100% DOPC, 5:3 DOPC/ERG, or 5:4 DOPC/DOPE. Under all conditions, vesicles showed less than 20% leakage compared to 0.1% Triton X-100, which served as positive control.

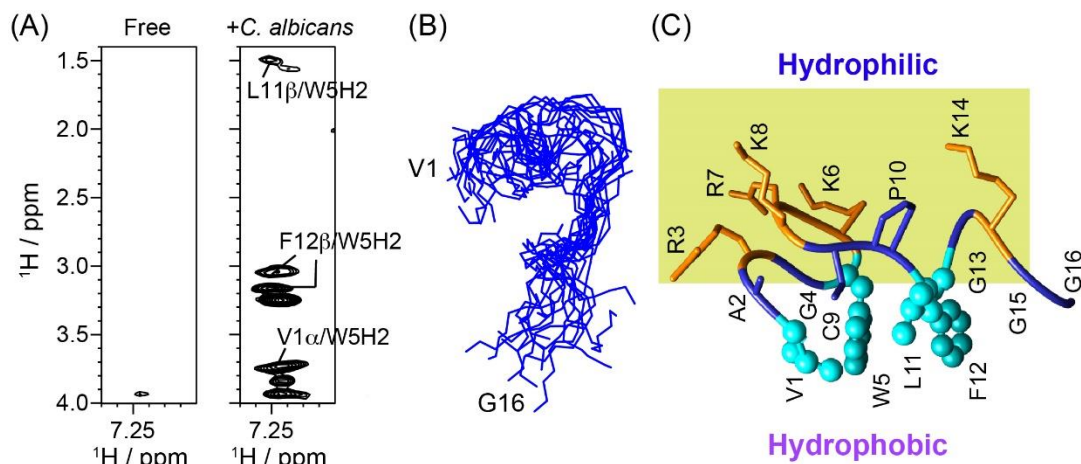


Figure 3.7. (A) Long-range ($i, \geq i+5$) NOEs of VG16KRKP obtained in presence of *C. albicans* cells (right) compared with the free peptide (left) in the same spectral region. (B) 15 lowest energy ensemble structures (N, C α , C') of VG16KRKP; (C) Cartoon representation of the lowest energy structure of the peptide showing clear separation between hydrophilic and hydrophobic residues (right).

This provides a highly dynamic *C. albicans* bound solution NMR structure within the NMR time frame. Further, close inspection suggested that the hydrophobic triad consists of Trp5-Leu11-Phe12 of *C. albicans*-bound VG16KRKP structure (Figure 3.7 (B) and, 3.7 (C)) was similar to that of peptide-lipopolysaccharide (LPS) complexes reported before (Figure 3.8 (A)) [169]; however, the RMSD of overlaid structure was very high (Figure 3.8 (B)), confirms that the overall structural arrangement differs depending on the membrane environment. Of note, LPS is the major component of the outer-membrane of Gram-negative bacteria. Though VG16KRKP is loosely bound to *C. albicans* at initial time period (before disruption of the live fungus cells), the “structural functional motif”, consisting of Trp5-Leu11-Phe12 supports the hydrophobic hub could be the driving force playing an important role for stabilizing the peptide into cells, followed by disruption of cells (Figure 3.8 (C-D)). In the structural model, “membrane anchoring motif” consisting of Arg and Lys residues (Arg3, Lys6, Arg7 and Lys8) is segregated from the hydrophobic face. The Cys9-Pro10 peptide bond adopts a ‘trans-’ conformation, as judged by the presence of the Cys9H α /Pro10H δ s NOE. The proline induces a kink in the peptide structure that assists to pull the hydrophobic residues together to form a better “structural functional motif”. This finding is consistent with a previous study.[35] In addition, the positively charged residues Arg3, Lys6, Arg7, Lys8 and Lys14 are highly dynamic

Table 3.2. Summary of structural statistics for the 15 lowest energy ensemble structures of VG16KRKP in presence of *C. albicans* cells.

VG16KRKP	<i>Candida albicans</i>
Distance restraints (Å)	
Intra residue ($i - j = 0$)	28
Sequential ($ i - j = 1$)	32
Medium range ($2 \leq i - j \leq 4$)	0
Long range ($ i - j \geq 5$)	3
Total	63
Angular restraints	
Φ	13
Ψ	13
Distance restraints from violation (≥ 0.4 Å)	0
Deviation from mean structure (Å)	
Average backbone to mean structure	2.42 ± 0.62
Average heavy atom to mean structure	3.44 ± 0.73
% Residues in Ramachandran plot*	
most favored region	20
additionally allowed region	80
generously allowed region	0.0
disallowed region	0.0

* Procheck NMR based analysis (<https://services.mbi.ucla.edu/PROCHECK/>).

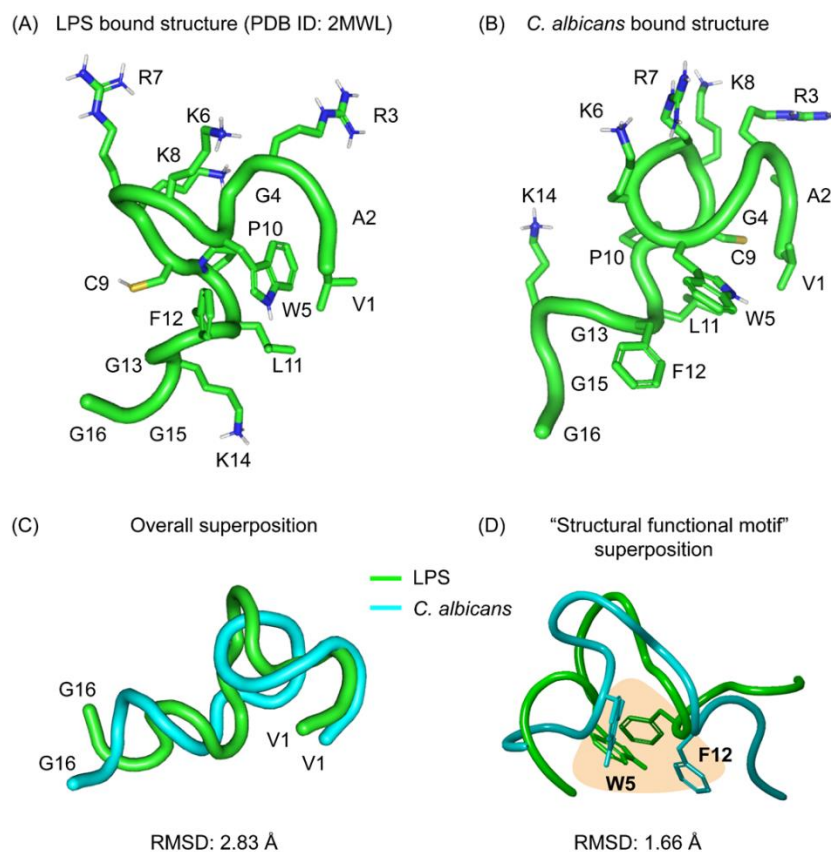


Figure 3.8. Cartoon representation of average structure of VG16KRKP conformations bound to either LPS (A) (PDB ID: 2MWL) or in presence of *C. albicans* cells (B). Positively charged residues are facing one side and the hydrophobic residues formed a cluster, which confers an amphipathicity to the peptide. (C) Superposition of backbones of both the structures. (D) Superposition of “structural functional motif” consisting of Trp5-Leu11-Phe12 of both the structures.

in the bound conformation, and are responsible for recognizing or anchoring the negatively charged membrane surface. These residues help in docking the peptides on the fungal cell surface and then the hydrophobic residues interact with the acyl chain moieties of the lipid membranes, which eventually causes membrane lysis. Such membranolytic mechanisms are well depicted in case of other naturally occurring α -helical amphipathic peptides like LL-37, magainin, melittin etc [198-200]. It is noteworthy to mention that a 12-residue long synthetic peptide namely YW12 also showed an amphipathic structure by adopting a β -sheet-loop fold in presence of LPS micelle [201]. The four central cationic residues (KRKR) played the initial docking interaction and the N- and C-terminal hydrophobic residues interacted with the acyl chain of LPS micelles [201]. Other modified β -boomerang peptides (YI12F, YI12WW, YI12WY, YI12FF and GG8WF) also showed similar kind of conformation along with aromatic/aromatic packing interaction in presence of LPS [202].

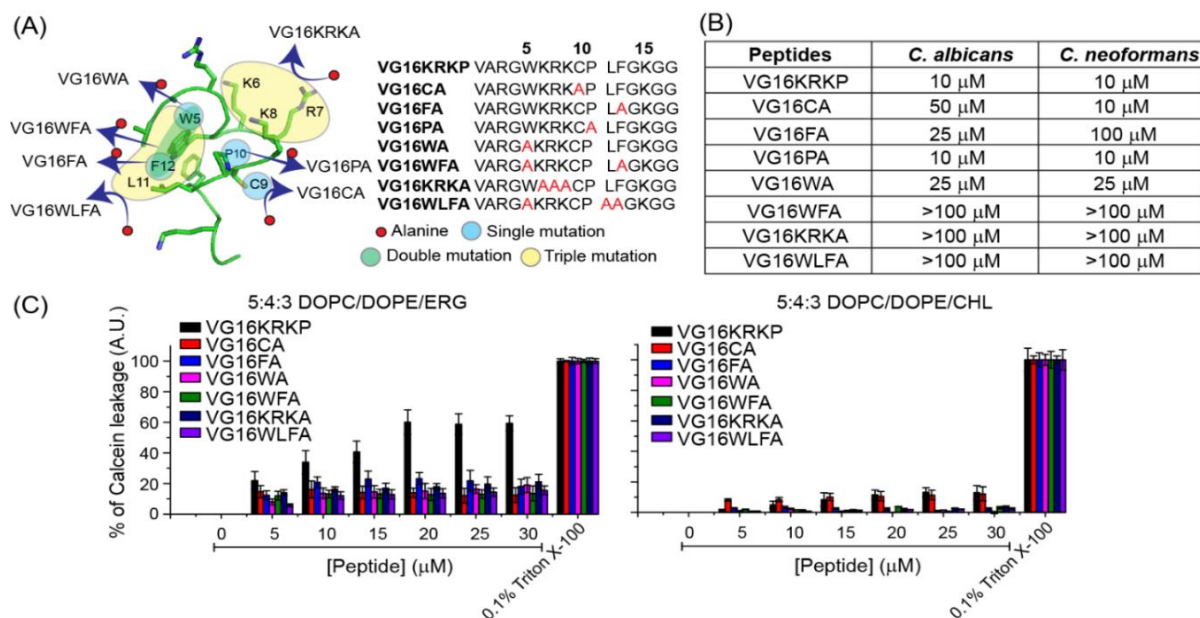


Figure 3.9. (A) Schematic representation of the VG16KRKP mutant analogs designed by alanine scanning. Amino acid sequences of single, double and triple mutant analogs are provided. (B) MIC (μM) of VG16KRKP and its mutant analogs to antagonize *C. albicans* and *C. neoformans* var. *grubii*. (C) Calcein dye leakage assay using either 5:4:3 DOPC/DOPE/ERG (left) or DOPC/DOPE/CHL (right) LUVs in presence of the indicated concentrations of VG16KRKP (black) and various mutant analogs.

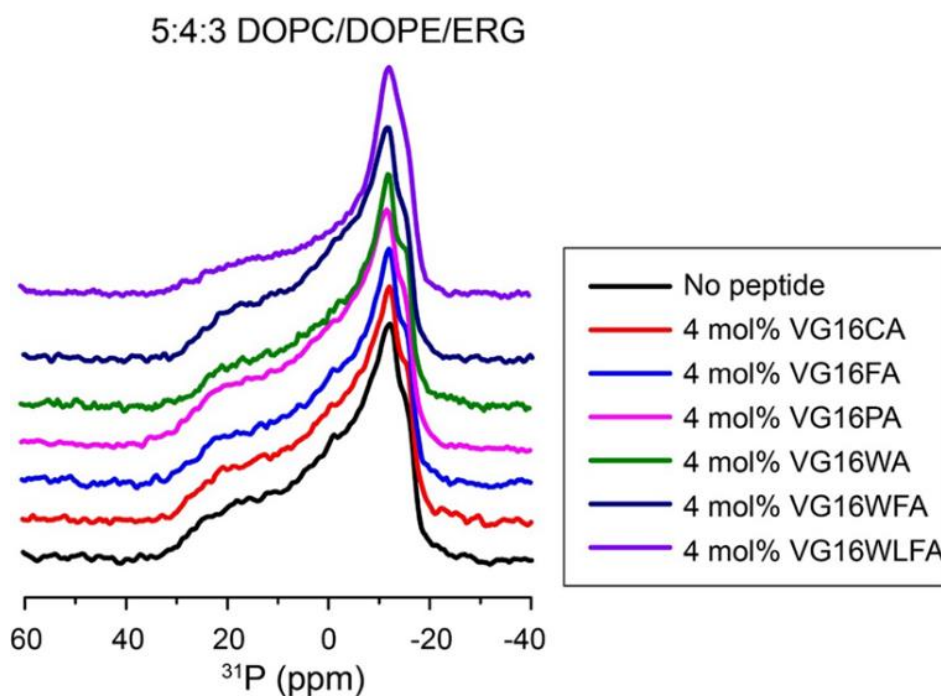


Figure 3.10. ^{31}P solid-state NMR of 5:4:3 DOPC/DOPE/ERG MLVs in presence of 4 mol% of the indicated VG16KRKP mutant analogs revealed characteristic powder patterns that were practically indistinguishable from the spectrum of control vesicles (black) in the absence of peptides.

3.3.12. Characterization of the mutant analogs

Finally, to understand the role of individual amino acid residues as well as “membrane anchoring motif” and/or “structural functional motif” in driving the antifungal activity of VG16KRKP, we generated a peptide library consisting of mutants of VG16KRKP as shown in Figure 3.9 (A). Single-, double-, or triple-mutations of the significant residues into alanine (Figure 3.9 (A)) either resulted in partial or complete loss of antifungal activity (Figure 3.9 (B)) as tested against *C. albicans* and *C. neoformans*.

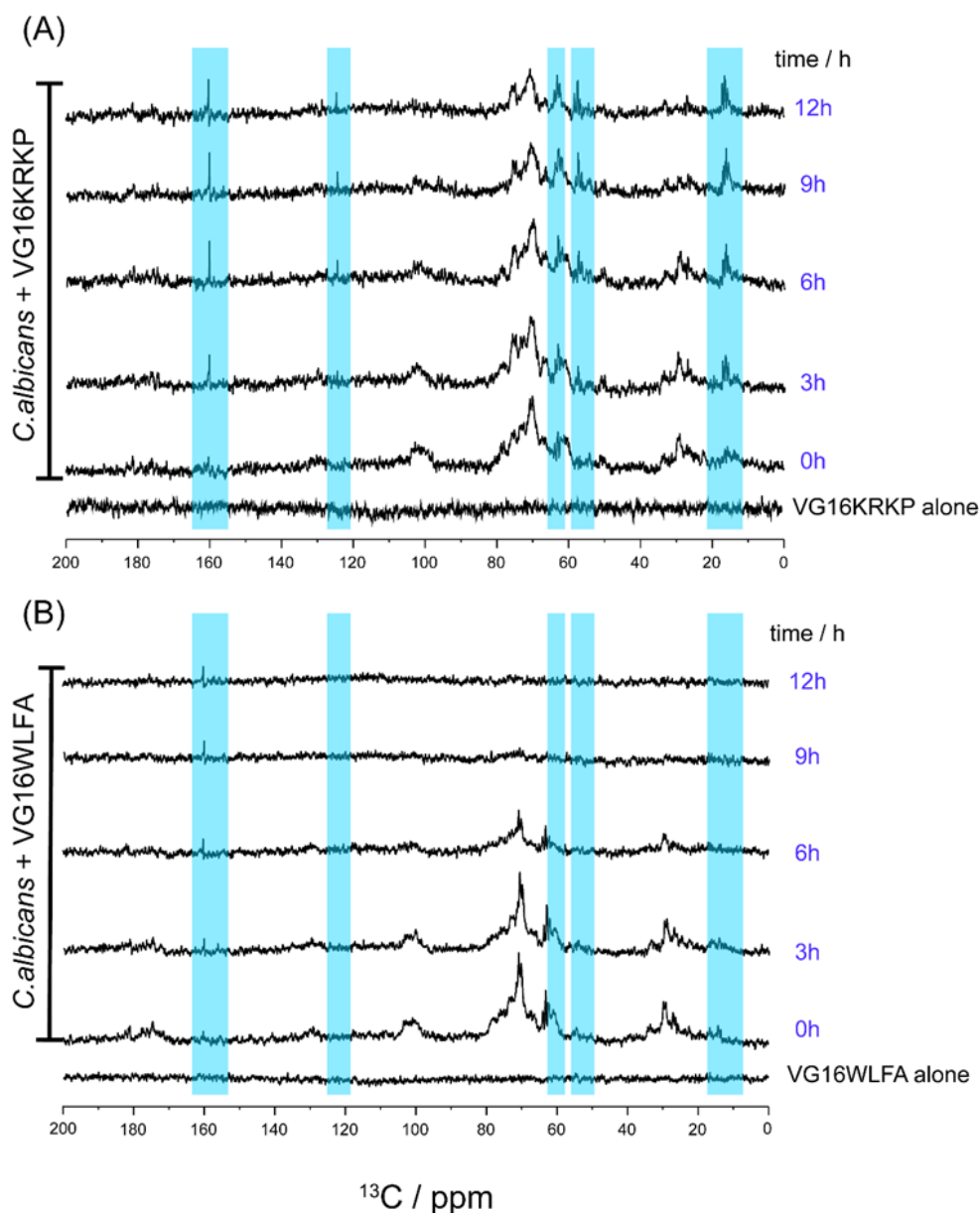


Figure 3.11. 1D ^1H coupled ^{13}C NMR (pulse program: zgpg30) spectra of *C. albicans* cells (1×10^7 cells/ml) grown in YPD broth where the Dextrose (carbon source) was replaced with ^{13}C -glucose to probe the metabolites that came out from the cells as a result of the peptide action. VG16KRKP treated cells showed several metabolite peaks which got increased with time (A) but the VG16WLF

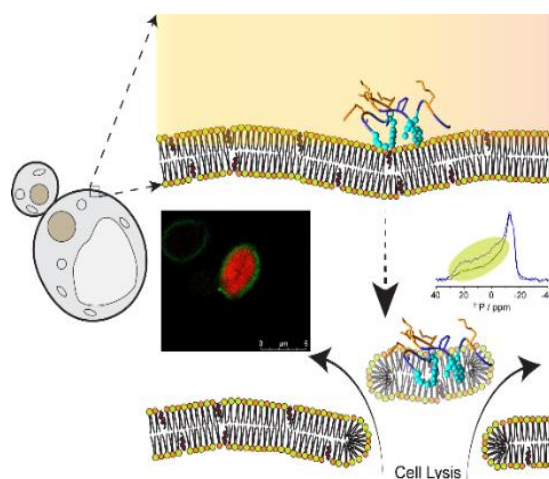
showed only one peak at 160 ppm whether other peaks got broaden with time due to the precipitation of the *C. albicans* cells (B).

Trp5 plays an important role for the activity of VG16KRKP. While VG16WA displayed >2-fold diminished activity compared to the original peptide; the other substitutions resulted in a complete loss of antifungal activity. These results suggest that the “structural functional motif” consisting of Trp5, Leu11 and Phe12 is quintessential for its interaction with membrane-bound sterols. Mutation of the “membrane anchoring motif” such as Lys6, Arg7 and Lys8 (i.e., VG16KRKA) also abrogated antifungal activity. This might be due to the loss of surface recognition in an early stage of binding, as well as hindered docking of VG16KRKP by electrostatic interaction with the phosphate head groups of the fungal cells. To further support the above findings, the dye leakage assay was performed using the mutant analogs. Interestingly, all mutant peptides failed to cause significant changes in dye leakage (Figure 3.9 (C)). Similar, ³¹P solid-state NMR spectra of 5:4:3 PC/PE/ERG MLV (Figure 3.10) in presence of 4 mol% VG16KRKP mutant analogs showed no significant changes as well, corroborating the antifungal activity and dye leakage assays. A series of one-dimensional ¹H coupled ¹³C NMR spectra (Figure 3.11 (A-B)) were recorded to probe the metabolites released from the disrupted fungal cells. The fungal cells grown in ¹³C labeled glucose media, released ¹³C labeled metabolites on interaction with VG16KRKP over time, reflecting cell lysis (Figure 3.11(A)). Using VG16WLFA, an inactive analog of VG16KRKP, as a negative control, similar experiments were performed (Figure 3.11(B)); no release of metabolite confirmed the specificity of VG16KRKP towards *C. albicans*. This observation also supports the importance of “structural functional motif”. Collectively, these results establish the importance of the sequence of the peptide in imparting its antifungal activity. To the best of our knowledge, this is the first report that unveils the development of an ergosterol-specific antifungal peptide.

3.4. Conclusion

In summary, we established a relationship between the primary sequence, structure and antifungal activity of VG16KRKP using *C. albicans* as a model system for fungal infections. Our data demonstrate that VG16KRKP specifically interacts with the ergosterol moiety of the fungal membrane. Phosphatidylethanolamine also showed to play a significant role in driving this interaction. The complexity of the fungal membrane due to its diverse lipid composition makes detailed studies extremely complicated. Studies are ongoing to further unravel the role of the varied lipid components of the fungal membrane

in interacting with VG16KRP and imparting its activity. However, the optimised ergosterol specificity of VG16KRP suggests fewer side effects in mammals as compared to established but largely cytotoxic antifungals, such as Amphotericin B, making VG16KRP particularly interesting for clinical applications. Overall, this study provides a *proof-of-principle* that rationally designed peptides with high affinity for membrane-associated ergosterol can be developed into effective antifungal agents with reduced side effects.



3.5. Appendix III

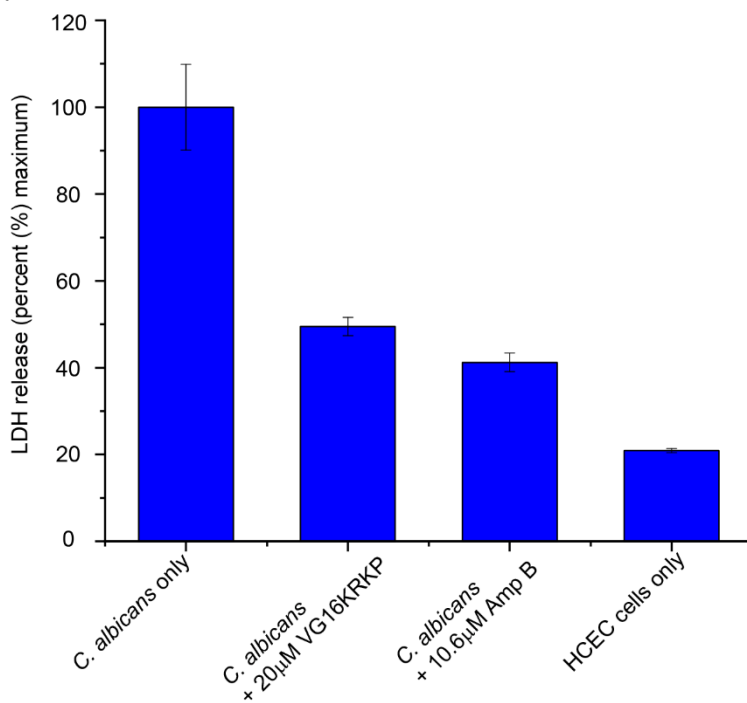


Figure S3.1. Percent release of LDH after addition of 20µM VG16KRKP to the co-culture infection setup.

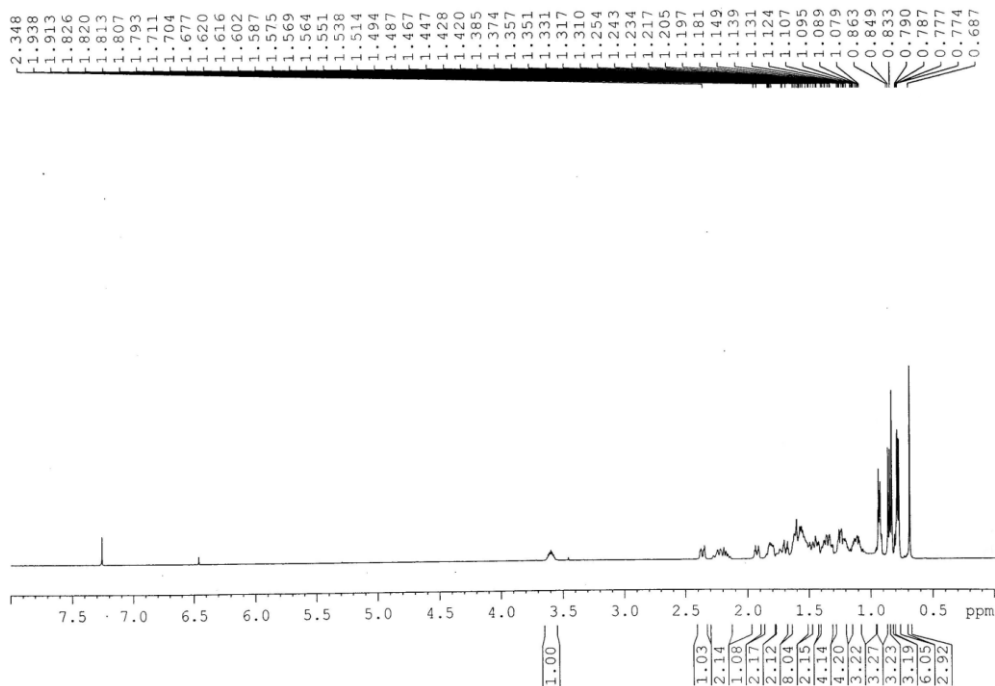


Figure S3.2. One dimensional ¹H NMR spectra of hydrogenated ergosterol (hERG) (500 MHz, CDCl₃).

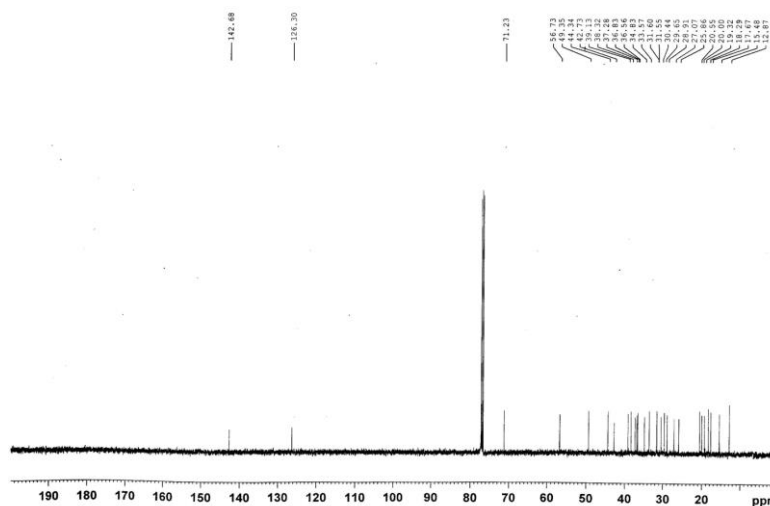


Figure S3.3. One dimensional ^{13}C NMR spectra of hydrogenated ergosterol (hERG) (500 MHz, CDCl_3).

Analytical data of hydrogenated ergosterol. ^1H NMR (500 MHz, CDCl_3): δ 3.63-3.58 (m, 1 H), 2.40 (m, 1 H), 2.29-2.12 (m, 2 H), 1.95-1.90 (m, 1 H), 1.83-1.80 (m, 2 H), 1.79-1.69 (m, 2 H), 1.67-1.50 (m, 8 H), 1.49-1.42 (m, 2 H), 1.40-1.30 (m, 4 H), 1.28-1.20 (m, 4 H), 1.24-0.9 (m, 3 H), 0.93-0.912 (d, $J = 6.5$ Hz, 3 H), 0.86-0.83 (m, 6 H), 0.79-0.77 (m, 6 H), 0.68 (s, 3 H); ^{13}C NMR (125 MHz, CDCl_3): δ 142.7 (1C), 126.3 (1C), 71.2 (1C), 56.7 (1 C), 49.3 (1 C), 44.3 (1 C), 42.7 (1 C), 39.1 (1 C), 38.3 (1 C), 37.2 (1 C), 36.8 (1 C), 36.5 (1 C), 34.8 (1 C), 33.5 (1 C), 31.6 (1 C), 31.5 (1 C), 30.4 (1 C), 29.6 (1 C), 28.9 (1 C), 27.0 (1 C), 25.8 (1 C), 20.5 (1 C), 20.0 (1 C), 19.3 (1 C), 18.3 (1 C), 17.7 (1 C), 15.5 (1 C), 12.9 (1 C); HRMS (ESI) calcd. for $\text{C}_{28}\text{H}_{48}\text{O}$ (547.1842): $[\text{M}+\text{H}]^+$ 401.3778; found: 401.3754.

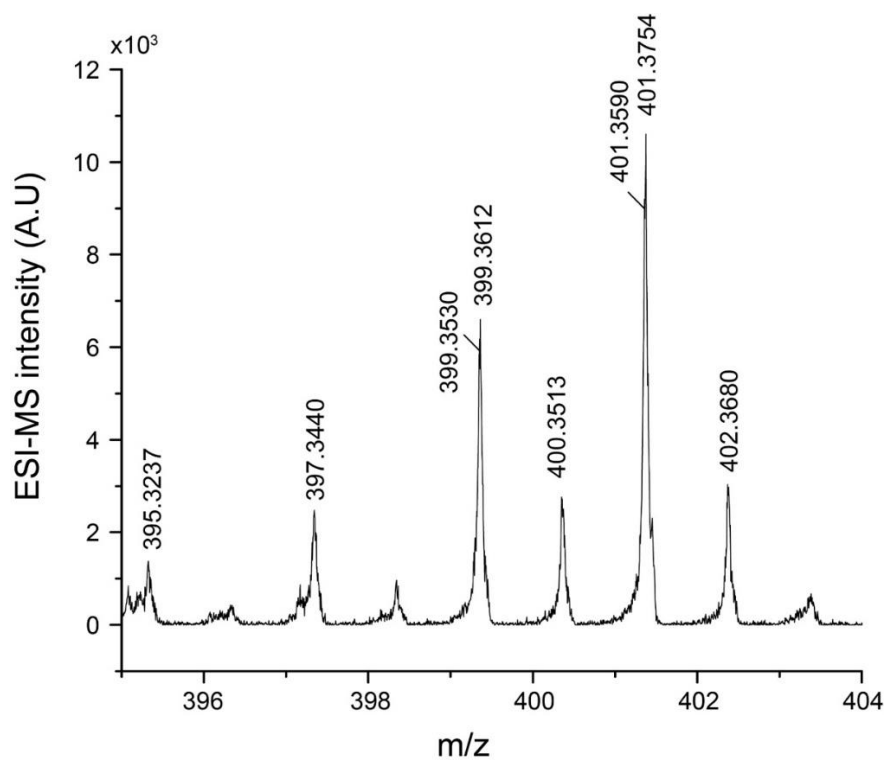


Figure S3.4. Mass spectrum of hydrogenated ergosterol (hERG) (ESI-MS, Waters Inc.).

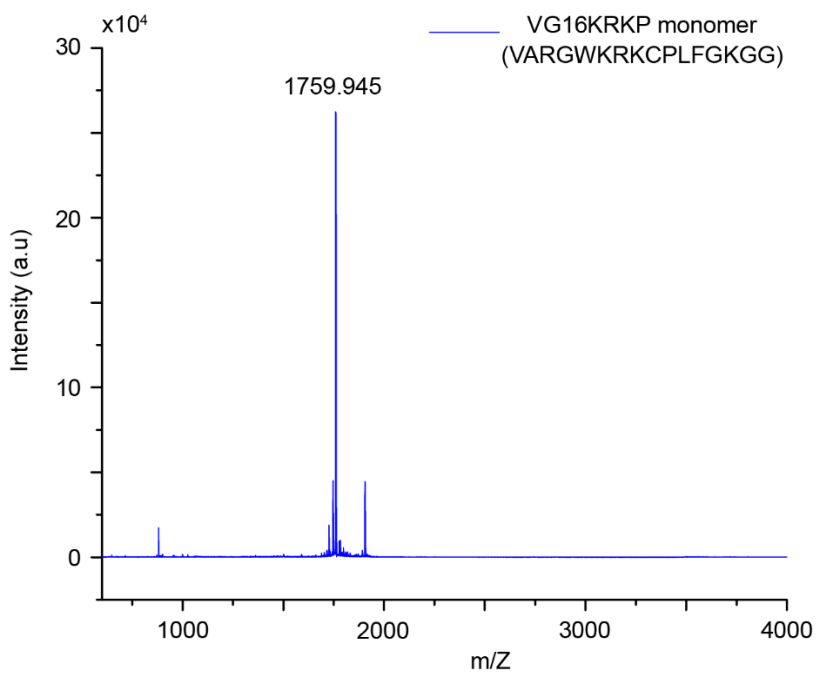


Figure S3.5. MALDI analysis of VG16KRKP peptide (Bruker ATS-00699, autoflex TOF/TOF).

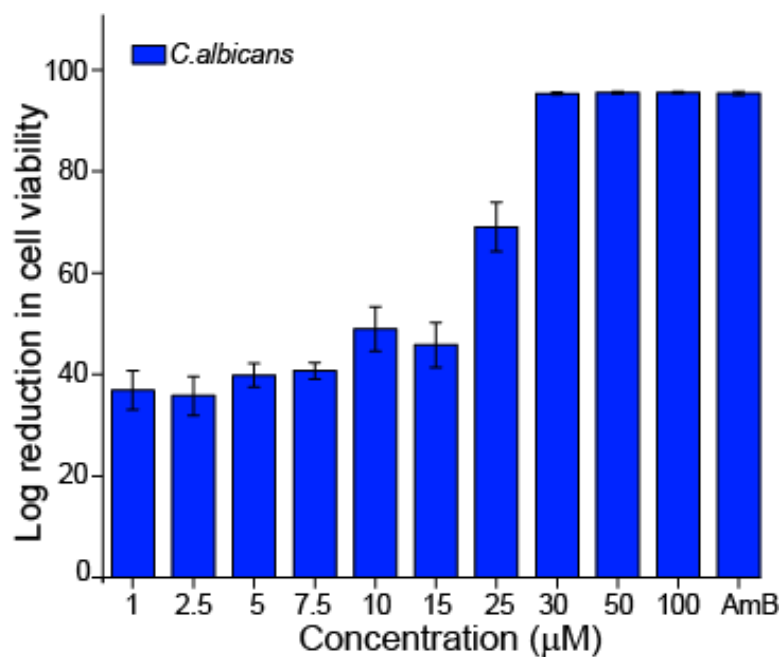


Figure S3.6. Micro broth dilution assay showing MIC_{99%} at 30µM concentration of FITC-VG16KRKP against *C. albicans* cells.

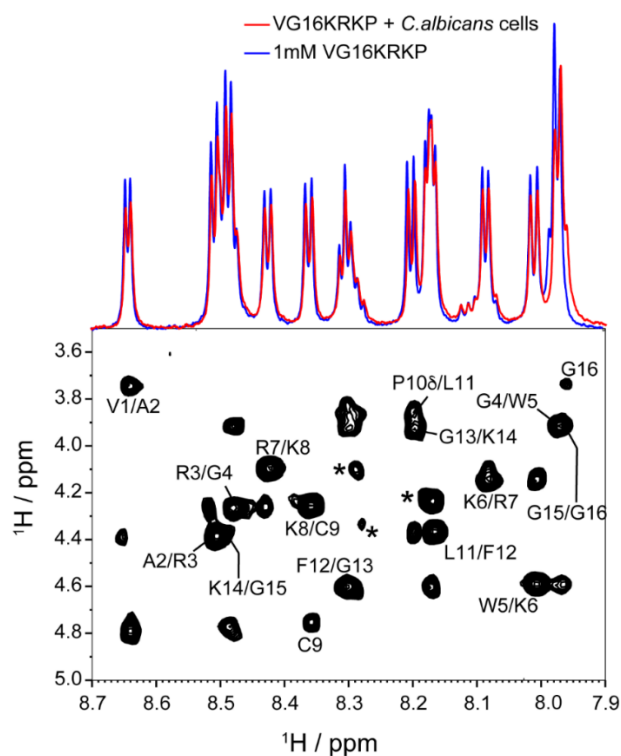


Figure S3.7. Representative 1D ¹H NMR profiles of VG16KRKP (1 mM) in the absence (blue, top) and presence (red, top) of *C. albicans* cells. Presence of fungal cells (red) caused line broadening and intensity changes of spectral components. The lower panel shows sequential (*i*, *i*+1) NOESY cross peaks of VG16KRKP, obtained within 4 h of data acquisition in presence of *C. albicans* cells (lower panel).

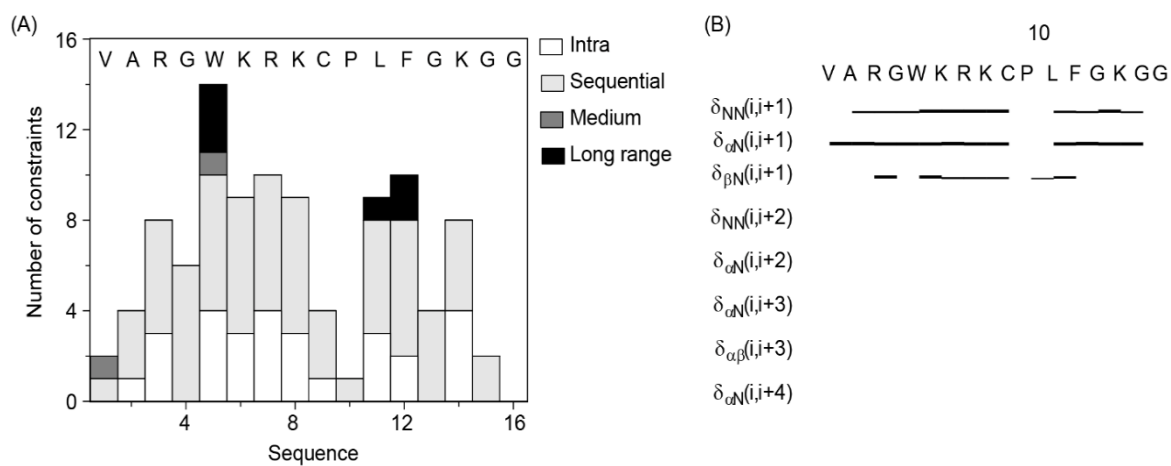


Figure S3.8. (A) Bar diagram showing sequential NOEs of VG16KRKP in presence of *C. albicans* cells. The bar thickness indicates the peak intensity assigned as strong, medium, and weak. (B) histogram depicting the number of trNOEs of VG16KRKP in presence of *C. albicans* cells with respect to residue numbers.

Chapter IV

4. A rationally designed synthetic antimicrobial peptide to treat Bacterial Ocular Infections

This chapter has been adapted from the following publication:

Mohid, S.A., Sharma, P., Alghalayini, A., Saini, T., Datta, D., Willcox, M.D., Ali, H., Raha, S., Singha, A., Lee, D. and Sahoo, N., **2022**. A rationally designed synthetic antimicrobial peptide against *Pseudomonas*-associated corneal keratitis: Structure-function correlation. *Biophysical Chemistry*, 286, p.106802.

4.1. Introduction

Corneal opacity is the fifth leading cause of blindness globally, accounting for ~3.2% of all cases [203] [204]. The recent World Health Organisation (WHO) report highlighted that ~6 million of the world's population are affected by cornea-related blindness or moderate/ severe visual impairment, including 2 million of those who are affected by trachoma [205]. Infectious keratitis is considered a “silent epidemic” in the western world, with an annual incidence on the order of 25,000-30,000 in the US alone [206,207]. Being more abundant in developing countries, infectious keratitis has been designated as a “neglected tropical disease”. To date, antibiotics like vancomycin, tobramycin and amphotericin B (AmB) are the best choices for treating microbial keratitis [208,209]. These drugs, however, are toxic to mammalian cells and cause membrane disruption, interruption of physiological ion transport, neurotoxicity and nephrotoxicity [167,210]. On the other hand, the emergence of several multidrug-resistant bacteria is causing all new antibiotics to fail [64,211].

The last few decades have seen the rise of antimicrobial peptides (AMPs) as potent alternatives to the available therapeutic agents, owing to their species specificity [28]. The predilection for the lipid environment is a common trait of membrane-active peptides [115]. They are mostly unstructured in solution and, in the presence of lipid membranes, it is thought they will adsorb onto the surface via electrostatic interactions, alter secondary structure, then intrude into the hydrophobic core of the membrane bilayer and destroy bilayer stability [115,212,213]. The molecular process by which these membrane-active peptides lyse membranes is defined by several models like barrel-stave, toroidal pore, carpet or detergent mechanisms [28,154,214]. In previous studies, we have demonstrated the

feasibility of engineering short peptides that specifically disrupt the structural integrity of bacterial and fungal cell membranes but do not interact with mammalian cell membrane components [171]. The VR18 peptide is a chimera consisting of a portion of the dengue viral fusion peptide and a portion of the lactoferrampin peptide that includes a lipopolysaccharide KNKSR binding motif. Thus, VR18 was explicitly designed to interact with lipopolysaccharides (LPS) and then to disrupt the lipid outer membrane of bacteria leading to cytoplasm leakage and bacterial death [110].

Here, using live-cell NMR, high-end microscopy, interactions with sparsely tethered lipid bilayer membranes and live-cell Raman spectroscopy, we confirm that VR18's actions are membrane-mediated. We then further show that VR18 reduced *Pseudomonas*-associated keratitis in mice and in *ex vivo* human corneal infection models. Finally, we conclude that the topical application of VR18 could be used as an effective therapeutic agent for combating *Pseudomonas*-associated corneal infections.

4.2. Materials and methods

4.2.1. Reagents

The *P. aeruginosa* serotype 10 lipopolysaccharide (LPS), polymyxin B, calcein, and propidium iodide (PI) were purchased from *Sigma Aldrich Co.* (St. Louis, USA). Deuterium oxide was purchased from *Cambridge Isotope Laboratories, Inc.* (Tewksbury, USA). The bacterial media was purchased from *Himedia Laboratories Pvt. Ltd.*, Mumbai, India. 1-palmitoyl, 2-oleoyl-phosphatidylethanolamine (POPE) and 1-palmitoyl, 2-oleoyl-phosphatidylglycerol (POPG), 3-(cholamido-propyl) dimethylammonio-2-hydroxy-1-propane-sulfonate (CHAPSO) and *Escherichia coli* total lipid extract (*E. coli* TLE) were obtained from *Avanti Polar Lipids* (Alabaster, AL).

4.2.2. Peptide synthesis

¹⁵N labeled VR18 was synthesized by Fmoc solid-phase peptide synthesis chemistry, as described previously, using an automated peptide synthesizer (Aapptec Endeavor 90, Louisville, KY, USA) [110,215]. The Val-1, Ala-2, Gly-4, Gly-6, Leu-11 and Gly-13 residues were selectively labeled with ¹⁵N by using the ¹⁵N labeled Fmoc-amino acids, respectively. N-terminal Val-1 residue was subjected to acetylation in order to provide protection during the peptide cleavage step. The crude peptide was purified by a reverse-phase high performance liquid chromatographic system (RP-HPLC) (LC-20AT, SHIMADZU, Kyoto, Japan) using a Phenomenix C₁₈ column. The peptide fraction was collected from the RP-HPLC elution and subjected to lyophilization to obtain the powder

form. The calculated and actual molecular weight obtained for the peptides was 2107.49 and 2107.26, respectively. The purified peptide (>95% purity) was stored at -20°C.

4.2.3. Determination of minimal inhibitory concentration

To determine the MIC_{99%}, a modified micro broth dilution assay was done, as previously described [171]. In brief, the mid-log phase cultures of *P. aeruginosa* 6294 was pelleted down by centrifuging at 8000 rpm for 10 min, washed twice with 10 mM sodium phosphate buffer, pH 7.4 and re-suspended in the same buffer to get a final cell suspension containing 10⁶ CFU/ml. The exposure to the peptide was set with 50 µl of this cell suspension (i.e., 5×10⁵ CFU/ml) being added to a series of concentrations of the VR18 peptide (ranging from 1 to 100 µM diluted from a 1 mM stock solution) in a sterile 96-well micro titter polypropylene plate and incubated for 3 h at 37 °C. A positive control containing only cells and a negative control containing 10 µM Polymyxin B treated cells were also maintained. Following peptide exposure, 200 µl of nutrient broth was added to each well and incubated overnight at 37 °C. Absorbance of each well was measured at 630 nm to estimate MIC_{99%} of each peptide. The MIC_{99%} was defined as the lowest concentration that inhibited 99% growth of the microorganisms from initial microbial cell density. All experiments were set in triplicates.

4.2.4. Zeta potential analysis

Overnight grown log phase cultures of *P. aeruginosa* 6294 in nutrient broth, were washed twice and resuspended in 10 mM phosphate buffer of pH 7.4. 1 ml cell suspension of 10⁵ cells per ml and were subsequently incubated with 1-15 µM VR18 peptide for 90 min. The same microbial suspension without the peptide was used as the negative control set and a 10 µM Polymyxin B treated cell suspension was used as a positive control. All of these suspensions were placed in disposable zeta cells and read at 25 °C using a Nano S ZEN3690 (Malvern Instruments, Westborough, MA). The zeta potential for each sample was calculated using the Zetasizer software [216].

4.2.5. Propidium iodide uptake assay

Mid-log phase of *P. aeruginosa* 6294 cells (O.D₆₃₀ 0.5) obtained from an overnight culture nutrient broth were pelleted by centrifugation at 8000 rpm for 10 min at 25 °C, washed twice with 10 mM phosphate buffer (pH 7.4) and resuspended in the same buffer. propidium iodide (PI), a nucleic acid binding dye, was added to 50 µl of the cells with a concentration of 10 µM and allowed to stabilize for 30 min. The intensity of the PI bound with intact cells was measured using the time kinetics mode of the spectrometer. An

increasing concentration of the VR18 peptide was added to the cell after 10 min and the increase in PI fluorescence due to outer and inner membrane permeabilization was measured using a Hitachi F-7000FL spectrophotometer. The excitation wavelength was set at 580 nm and the emission was recorded at 620 nm with a slit width of 5 nm.

4.2.6. Raman spectroscopy

The *P. aeruginosa* 6294 cells were processed in a similar way to the zeta potential sample preparation and treated with the peptide at 1x and 2x MIC concentrations. The cell suspensions were then drop-casted onto clean aluminum foil mounted on the glass slide.[217] Raman spectra were obtained in backscattering geometry using a LabRAM HR - Jobin Yvon (Horiba, Kyoto, Japan) spectrometer equipped with a Peltier-cooled CCD [217]. A diode laser of wavelength 785 nm was used as an excitation source, and the light was focused on the sample using a 50× objective. All data were recorded within a wavenumber range from 800 to 1800 cm^{-1} .

For curve fitting, the *Origin* program was used. First, the baseline of the Raman spectra was processed by asymmetric least squares (ALS) method. The parameter for the asymmetric factor was kept 0.001, while keeping the threshold, smoothing factor and number of iterations at 0.05, 4 and 10, respectively. To reduce the noise and to get a clearer picture of the Raman shifts, further smoothening of the data was done by using Savitzky-Golay methods where the points of window were kept to 25 and the polynomial order was set at 5 without any boundary condition. The specific and significant Raman shifts of the different chemical groups and bonds were matched with a previously reported article by GB Jung et al [218].

4.2.7. Preparation of unilamellar vesicles

Approximately 2 mg each of 1-palmitoyl, 2-oleoylphosphatidylethanolamine (POPE) and 1-palmitoyl, 2-oleoylphosphatidylglycerol (POPG) were dissolved in chloroform with molar ratio of 3:1 (mimicking the bacterial inner membrane composition). The solvent was then evaporated by passing N_2 gas and then lyophilized overnight. Thereafter, the film was hydrated with 10 mM Tris buffer (pH-7.4) containing 70 mM calcein (Sigma, St. Louis, USA). Then the mixture was subjected to five freeze-thaw cycles in liquid N_2 and heated to 60 °C along with vigorous vortexing. Large Unilamellar vesicles (LUV) of 100 nm were created by passing the mixture 25 times through a polycarbonate filter (pore size 100 nm) attached with an extruder (Avanti Polar Lipids, Alabaster,

Alabama) at 25 °C. Free calcein was separated by passing the solution through a Sephadex G-50 column (GE Healthcare, Uppsala, Sweden) at 25 °C with Tris buffer as eluent.

4.2.8. Calcein dye leakage assay

The leakage of calcein was monitored on a Hitachi F – 7000FL spectrophotometer by setting the excitation wavelength at 495 nm, and the wavelength scan showed the emission maxima at 517 nm from the LUV dispersion (20 µM lipid in 10 mM Tris with 100 mM NaCl, pH 7.4) as described previously [219]. 1 % Triton X-100 was used as a positive control and the percentage of leakage was calculated using the equation (3) as mentioned in chapter 2. Each experiment was done in triplicate at 37 °C.

4.2.9. Phase contrast microscopic analysis

Unlabeled giant unilamellar vesicles (GUVs) were prepared by following the gel-assisted method as described by Weinberger et al. and modified as per requirements [177]. Briefly, a solution of 5% (w/w) poly-vinyl alcohol (PVA) was prepared by dissolving into Millipore water and heated at 90 °C with constant stirring until the suspension become a clear solution. 300 µl of the solution was then dropped in a small 30 mm petri dish to make a thin even layer. The plates were then transferred into a hot air oven and kept for drying at 50 °C for 30 min.

For phase contrast microscopy, stock solutions of 2 mg/ml POPE, and POPG were prepared in chloroform and 20 µl of the lipid mixture (prepared by maintaining the particular ratios) were spread on the PVA film in a non-overlapping way. Then, the plates were placed in a Lyophilizer for 45 min to remove the trace amount of the solvents. Before using the lipid films, the plates were subjected to UV treatment for 15 min to prevent dewetting and cleaning. To create a phase difference while observing the GUVs under the microscope, 800 µl of 100 mM sucrose solution was added into the lipid film to swell the GUVs for 10-15 min [178]. Then the plates were gently swirled to dislodge the vesicles from the PVA layer and thereafter, the GUVs were collected in a polypropylene microcentrifuge tube within 45 min. Next, the vesicles were added into a well where a 105 mM glucose solution was already added, with or without the peptide solution. The GUVs were imaged using a Nikon model Ts2FL microscope (Nikon, Japan) [178].

4.2.10. Sparsely tethered bilayer lipid membranes (stBLMs).

To measure how the VR18 peptide interacts with lipid bilayers, sparsely tethered bilayer lipid membranes (stBLMs) in conjunction with swept frequency electrical impedance spectroscopy (EIS) was used [220,221]. Changes in membrane conduction and

dissolved in 10 mM phosphate buffer at pH 7.4 and degassed. A sample cell (volume 182 μ l) containing 0.5 mM VR18 peptide was titrated against *P. aeruginosa* LPS from a stock solution of 0.025 mM at 298 K. A total of 20 injections were carried out at an interval of 2 min with 1 μ l of LPS aliquots per injection. The raw data was plotted using NanoAnalyze 3.7.5 software supplied with the instrument. An independent model was used to analyze the dissociation constant (K_d), and the change in the heat of enthalpy of interaction (ΔH), free energy of binding (ΔG) and entropy (ΔS) were evaluated using the equations $\Delta G = -RT \ln K_d$ and $\Delta G = \Delta H - T\Delta S$, respectively.

4.2.12. Circular dichroism analysis

Circular Dichroism (CD) of VR18 peptide was done in *P. aeruginosa* LPS. The spectra were recorded in a Jasco J-815 spectrophotometer (Jasco International Co., Ltd. Tokyo, Japan) equipped with a Peltier cell holder and temperature controller unit accessory. Stock solutions of peptide and LPS were prepared in 10 mM phosphate buffer (pH 7.4). The CD data was obtained at 28 °C in a 0.5 cm Quartz cuvette using the final concentration of peptide set at 25 μ M and titrating with increasing concentration of LPS (12.5-50 μ M) micelles. The spectral range was set at 190 to 260 nm with 1 nm data pitch and averaging 3 accumulations. The buffer subtracted spectral data obtained in milli degrees were converted to molar ellipticity (θ) ($\text{deg cm}^2 \text{dmol}^{-1}$), using equation (2) as described in chapter 2.

4.2.13. NMR experiments

All solution NMR experiments were done at 298 K on a Bruker Avance III 500 MHz equipped with a 5 mm SMART probe and 700 MHz NMR spectrometer equipped with a 5 mm RT probe. NMR samples were prepared in 10% deuterated water (pH 4.5) and 3-(Trimethylsilyl) propionic-2,2,3,3-d₄ acid (TSP) sodium salt was used as an internal standard (0.00 ppm). Two-dimensional ¹H-¹H total correlation spectroscopy (2D TOCSY), and two-dimensional ¹H-¹H Nuclear Overhauser effect spectroscopy (2D NOESY) was recorded for the VR18 peptide with a mixing time of 80 ms and 150 ms, respectively and spectral width of 12 ppm in both directions. The number of scans were fixed to 20 and 40 for TOCSY and NOESY experiments, respectively. The recycle delay (D1) for both the experiments was set to 1.5 sec with 456 increments in the t_1 , and 2048 data points in the t_2 , dimensions along with states time-proportional phase incrementation (TPPI) for quadrature detection in t_1 dimension and excitation-sculpting scheme for water suppression were used to record both the experiments [171]. Next, the interaction of the peptides upon successive

titration with *P. aeruginosa* LPS bicelles or *E. coli* total lipid extract (TLE) bicelles were monitored by 1D proton NMR acquired using an excitation-sculpting scheme for water suppression and the States-TPPI for quadrature detection in the t1 dimension [223]. Consequently, 2D TOCSY and *transferred* NOESY (*tr*NOESY) spectra of the peptide in the context of LPS or *E. coli* TLE bicelles were acquired with 80 ms and 150 ms mixing time, respectively. Data processing and analysis were carried out using Topspin™ v3.1 software (Bruker Biospin, Switzerland) and Sparky[124] software, respectively. LPS and *E. coli* TLE bicelles were made as described previously [171,224]. Briefly, 2 mg of *P. aeruginosa* serotype 10 LPS or *E. coli* TLE were measured and mixed separately with 1.5 mg of CHAPSO. 10 mM phosphate buffer (pH 7.4) with 150 mM NaCl was used for hydration and the lipid/detergent ratio (q-ratio) was kept between 0.25 to 0.3. After 3 h of hydration, the mixed solution was subjected to five freeze-thaw cycles and used for further assays.

4.2.14. Sample preparation for solid-state NMR

For ³¹P solid-state NMR, 5 mg/ml of the lipids from the specified ratio were used as previously described.[170] The lipid samples were dried under a stream of nitrogen and then subjected to lyophilization overnight to eliminate any residual solvent. The films were prepared in a small glass vial. The lipid films were hydrated by adding 50 µl Tris buffer (pH 7.4) and were vortexed for 5 min at ambient temperature and freeze-thawed using liquid nitrogen at least five times to ensure the uniform size of the vesicles. The VR18 peptide was added to the buffered vesicle solution at appropriate weight (for either 2 or 4 mol %), and the final volume was adjusted to 100 µl for each solid-state NMR experiment.

4.2.15. Live cell NMR

Live cell 1D ¹H NMR experiments were done with 0.5 mM VR18 peptide dissolved in 90% 10 mM Phosphate Buffer (pH 6.5) and 10 % D₂O. Overnight stationary phase *P. aeruginosa* 6294 cells were sub-cultured to get log phase cells. The cells were then collected by centrifuging at 5500 rpm for 5 min and washed twice with the same buffer and a final 600 µl of 1 O.D₆₃₀ cell concentration I was taken for the experiment. First, a free 1D ¹H NMR spectrum of the VR18 peptide was obtained in a Bruker Avance III 500 MHz NMR spectrophotometer (equipped with smart probe). Then the peptide was added to the cell. A series of 1D ¹H NMR spectra were obtained over 4 h. Cells in the NMR tube were monitored every 15 min and mixed thoroughly to stop the sedimentation. New peaks were

observed after 5-10 min as a result of the efflux of metabolites. The number of scans was 48 and the recycle delay was 2 sec for every 1D spectra.

4.2.16. ^{31}P solid state NMR

NMR experiments were performed on an Agilent NMR spectrometer (DD2) operating at the resonance frequency of 699.88 MHz for ^1H and 283.31 MHz for ^{31}P and equipped with a 4 mm MAS HXY Solid Probe (Agilent). ^{31}P NMR experiments were performed using a single 90° pulse and 24 kHz TPPM proton decoupling. The $\pi/2$ pulse lengths were 6.8 μs for the ^{31}P nucleus. MLVs were kept in a 4 mm Pyrex glass tube, which was cut to fit into the MAS probe, and sealed with parafilm. An Agilent temperature control unit was used to maintain the sample temperature at 298K. ^{31}P spectra were collected with 256 scans and a recycle delay of 2 s and referenced externally to 85% phosphoric acid (0 ppm) [170]. All the spectra were processed with MestReNova software (Ver 8.1) with 250 Hz line broadening.

4.2.17. NMR derived structure calculation

For calculation of the LPS bicelle-bound three-dimensional structure of the peptide, the volume integrals of the respective nuclear Overhauser effect (NOE) cross-peaks were qualitatively differentiated into strong, medium and weak, depending on their intensities in the *tr*NOESY spectra. This information was further transformed to inter-proton upper bound distances of 3.0, 4.0 and 5.0 Å for strong, medium and weak, respectively, while the lower bound distance was fixed to 2.0 Å. The backbone dihedral angles of the peptides, phi (ϕ) and psi (ψ) were kept flexible (-30° to 120° and 120° to -120° , respectively) for all non-glycine residues to limit the conformational space. CYANA program v2.1 was used for all structure calculations with iterative refinement of the structure based on distance violation [179]. Hydrogen bonding constraints were excluded from structure calculation. The NMR-derived ensemble structures were analyzed using PyMOL and their stereochemistry was checked using Procheck [225].

4.2.18. Calculation of dynamics of the NMR derived structure

The ^{15}N relaxation parameters R_1 , R_2 and $[^1\text{H}]-^{15}\text{N}$ steady-state heteronuclear NOE (hetNOE) were measured on the Bruker Avance III 700 MHz NMR spectrometer using 1.0 mM solution of the selectively ^{15}N -labelled VR18 peptide prepared in 90% H_2O and 10% D_2O solution (pH 4.5) [215]. Following this, the relaxation experiments were carried out using the $^1\text{H}-^{15}\text{N}$ two-dimensional sensitivity-enhanced heteronuclear single quantum correlation (HSQC) based pulse sequences. The complete set of R_1 , R_2 and hetNOE data

sets were recorded at 298 K with 1024 (t₂) and 256 (t₁) complex data points, respectively, along the ¹H (SW = 12 ppm, offset = 4.701 ppm) and ¹⁵N (SW = 22 ppm, offset = 117.5 ppm) dimensions. All these spectra were processed and analyzed using Topspin™ software suite. Each R₁ and R₂ data sets were collected using 8 scans and a recycle delay of 2.5 sec. For R₁ measurements, the following relaxation delays were used: 10, 50, 90, 150, 250, 350, 550, 770, 990 and 1100 ms. For R₂ measurements the following relaxation delays were used: 0.00, 16.96, 33.92, 50.88, 67.84, 101.76, 135.68, 169.60, and 237.44 ms. The R₁ and R₂ values with their errors were extracted using MATLAB program “*Relaxation Decay*” developed in MathWorks Inc. Steady-state [¹H]-¹⁵N hetNOE measurements were carried out with a proton saturation time of 3 s and a relaxation delay of 3 s. For the experiment without proton saturation, the relaxation delay was set to 6 s. The NOE intensities for every residue were calculated as I_{sat}/I_{ref}, where I_{sat} and I_{ref} are intensities of the peaks in the HSQC spectra, with and without proton saturation, respectively.

4.2.19. *In vitro* treatment of human corneal epithelial cells infected with *P. aeruginosa* PAO1.

Human corneal epithelial cells (HCECs) (1x10⁴ cells/well) were cultured overnight in 96-well plates at 37 °C and in the presence of 5% CO₂. Cells were infected with *P. aeruginosa* PAO1 at a multiplicity of infection of 10 (Cells: bacteria, 1:10) and incubated in presence or absence of VR18 for 4 h. The viability of *P. aeruginosa* PAO1 was determined by measuring the absorbance at OD₆₀₀. The bacterial supernatant was then removed, cells were washed twice with 1x PBS and the viability of HCECs were determined by MTT assay [226]. This assay was done in LV Prasad Eye Institute, Hyderabad, India

4.2.20. *Ex vivo* treatment of human cornea infected with *P. aeruginosa* PAO1.

Ex vivo corneas were cleaned and kept in antibiotic-free media for 24 h. Corneas were scratched with a scalpel and infected with 10⁵ CFU/ml of PAO1 (n = 3). 50 μM VR18 peptide was added at the time of infection in 3 other corneas. 24 h post-infection, corneas were washed with PBS and homogenized and plated by serial dilutions and colonies were counted after overnight incubation. This experiment was performed in the LV Prasad Eye Institute, Hyderabad, India.

4.2.21. *Murine models of corneal infection.*

The Institutional Animal Ethics Committee approved this study, which was carried out at the LV Prasad Eye Institute in Hyderabad (Institutional Animal Ethics Committee, Vivo Bio Tech Ltd.; Study Number: 18/0077). C57BL/6 mice (6-8 weeks old) were

anesthetized by intraperitoneal injection of ketamine (8.7 mg/ml) and xylazine (0.5 mg/ml) at a dose of 0.01 ml/g body weight and the corneal epithelium was abraded with three parallel 1 mm scratches using a 26-gauge needle and separated in two random groups. An aliquot of 3 μ l containing approximately 1×10^5 PAO1 was added topically to one eye, and 1x PBS was added to the fellow eye of one group. To the second group, 5 μ l of 50 μ M of VR18 was added immediately after the addition of PAO1. The second dose of VR18 was added topically 6 h post-infection to the second group. Mice were euthanized and examined for corneal opacification, ulceration, or perforation 24 h post-infection. Clinical scores for the opacity were determined in a blinded fashion according to a scale earlier reported.[185] To measure colony forming units (CFUs), whole eyes were homogenized in sterile 1x PBS using a tissue homogenizer (Genetix Biotech, Hyderabad, India) and serial dilutions were plated on LB agar plates, and cfu was counted manually. All animals were housed in pathogen-free conditions in microisolator cages and were treated in accordance with the guidelines provided in the ARVO Statement for the Use of Animals in Ophthalmic and Vision research.

4.2.22. Reactive oxygen species (ROS) measurements from VR18 treated *P. aeruginosa*. *Bacteria and reagents:* *P. aeruginosa* 15692GFP strain was grown aerobically in Luria-Bertani (LB) broth at 37 °C overnight. ROS-sensing dye, *CM-H2DCFDA* (2',7'-dichlorodihydrofluorescein diacetate) was obtained from Invitrogen™ Molecular Probes™, oxidant, tertbutyl hydrogen peroxide (tbH₂O₂) was obtained from Fischer scientific, and VR18 peptide was obtained from Genscript [227].

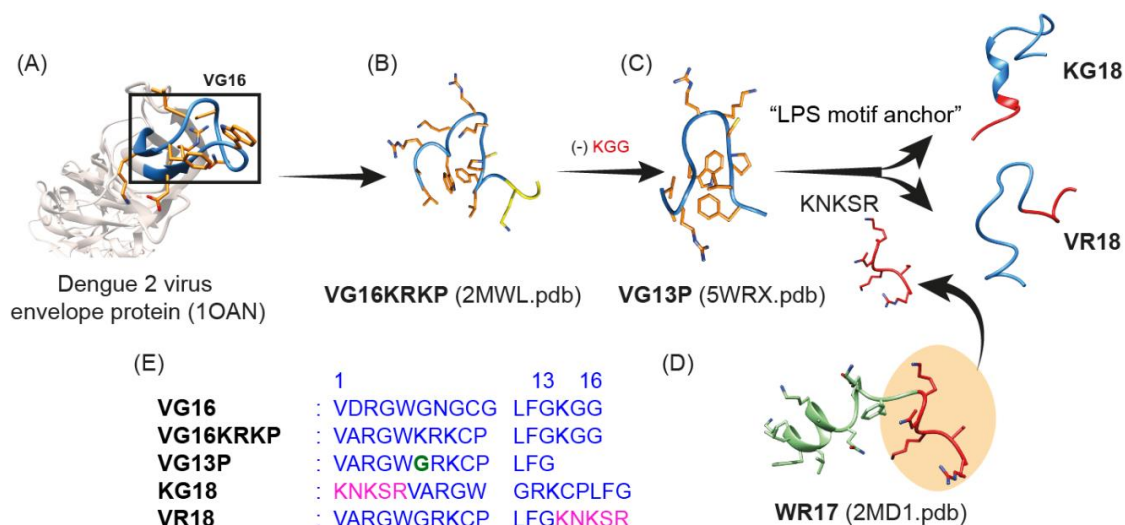
Measurement method: ROS measurement was performed in the University of Texas Rio Grande Valley, TX, USA, at room temperature with the PTI EasyRatioPro system (HORIBA Scientific). Log-phase cultures of *P. aeruginosa* were incubated with 10 μ M ROS-sensing dye, *CM-H2DCFDA* in Tyrode's solution (145 mM NaCl, 5 mM KCl, 2 mM CaCl₂, 1 mM MgCl₂, 10 mM Glucose, and 20 mM HEPES, pH 7.4) for 1 h in the dark. Following incubation, the bacteria were washed twice to remove the excess dye. A small drop of ~30 μ l of the bacterial suspension was placed on a glass coverslip and 0.5% agarose pad of 0.7 x 0.7 cm was placed on top of the bacteria. The imaging was performed on an Olympus IX71 inverted microscope attached to PTI EasyRatioPro system. A change in fluorescence was recorded with EasyRatioPro software with an excitation wavelength at 494 nm and an emission wavelength at 520 nm. All the chemicals such as VR18, tbH₂O₂

(1 M) of 5 μ l were dropped into the side of the agarose pad during the live measurements to test their effect on the intracellular ROS generation [228].

4.3. Results and discussion

4.3.1. Peptide designing

Previous studies on a dengue viral fusion peptide, VG16 (VDRGWGNGCGLFGKGG), chiefly responsible for host endosomal membrane fusion with viral envelope and subsequent progress of infection, led to the identification of VG16KRKP (VARGWKRKCPLFGKGG) as a potent antimicrobial peptide [169]. Structural insights into the three-dimensional LPS-bound structure of VG16KRKP revealed a hydrophobic triad formed by Trp5, Leu11, and Phe12, stabilizing a loop or turn-type structure with a fairly flexible C-terminal end that was not seen to participate in the stabilizing interactions. Based on this, a second-generation peptide, VG13P (VARGWGRKCPLFG) [215] was subsequently designed by removing the last three residues. In addition, Lys6 was replaced with a Gly to enhance the hydrophobic interactions stabilizing the structure. Simultaneously, previous reports of structural studies on Bovine Lactoferrin-derived AMP (residues 265 to 284), named WR17 (WKLLSKAQEKFGKNKSR), revealed that its N-terminal ‘KNKSR’ motif was chiefly responsible for anchoring to LPS [229]. The detailed structural information depicting the incorporation of this peptide into LPS was chiefly driven by the K13xK15xR17 motif at the N-terminus that acted as an anchor. This novel anchoring “K¹³NK¹⁵SR¹⁷” motif was fused with VG13P at the N- or C-terminal end to give rise to two peptides, namely KG18 (KNKSRVARGWGRKCPLFG) and VR18 (VARGWGRKCPLFGKNKSR) respectively, with a view to achieve enhanced antimicrobial properties (Scheme 4.1). The MIC analysis with *P. aeruginosa* (ATCC 27853) and *C. albicans* (SC5314) showed that both the peptides have similar activity (Table 4.1).



Scheme 4.1. (A) The virus fusion peptide VG16 (highlighted by box) from in the X-ray crystal structure of Dengue virus envelope protein (10AN.pdb). (B) VG16 was further modified by the addition of ‘KRK’ stretch in the loop region to generate 16-residues VG16KRKP that had an overall amphipathic structure and showed potent antimicrobial activities. In order to generate a shorter and more potent analogue, the C-terminal ‘KGG’ residues were removed to give (C) 13-residues VG13P peptide, which showed higher endotoxin effects compared to its precursors. A parallel study on a second 17-residues peptide, WR17 (D), led to the identification of a key motif form by the ‘KNKSR’ stretch, which was responsible for its potent activity. Therefore, this KNKSR stretch was incorporated at the N- and C- terminal of VG13P, giving rise to two highly potent 18-residues peptide, namely KG18 and VR18. (E) The amino acid sequences of the respective peptides are shown.

Table 4.1. MIC_{99%} (μM) values against *P. aeruginosa* (ATCC 27853) and *C. albicans* (SC5314).

Organism	VG16KRKP	VG13P	WR17	KG18	WS2-KG18	VR18	WS2-VR18
<i>P. aeruginosa</i>	> 100 μM	>100 μM	9.5 μM	5 μM	2.5 μM	5 μM	2.5 μM
<i>C. albicans</i>	2 μM	5 μM	25 μM	5 μM	2.5 μM	5 μM	2.5 μM

4.3.2. Interaction of VR18 with invasive *Pseudomonas aeruginosa*

Since both KG18 and VR18 peptides showed similar activity (5 μM) against *P. aeruginosa* (ATCC 27853), we continued with only VR18 in the subsequent experiments for this chapter. We explored the efficiency of VR18 against two invasive *P. aeruginosa* strains (6294 and PAO1) which are widely used for the model organisms for bacterial

keratitis studies [230,231]. In the next chapter, the complete biophysical analysis is done using *P. aeruginosa* (ATCC 27853) and *C. albicans* (SC5314).

In order to check the *in vitro* activity of VR18, a micro broth dilution assay was prepared by using *P. aeruginosa* 6294. This showed that the VR18 killed the pathogen in a dose-dependent manner with ~80% and 99% bacterial cell death at 5 μM and 10 μM concentrations, respectively (Figure 4.1 (A)).

Next, to understand the interaction between the peptide with the *P. aeruginosa* 6294 strain, several biophysical approaches were taken to understand the mechanism of action of VR18. Firstly, the zeta potential of the bacterial membrane was checked in the absence and presence of the peptide to observe any alterations on the bacterial cell surface. Zeta potential is defined by the electrical potential difference between solid surfaces that are submerged in a colloidal suspension [216]. The surface potential of the bacterial cells play a significant role in the maintenance of the cellular function and also provides useful information about cell surface characteristics [232]. It has been reported that the membrane targeting agents that alter the membrane integrity also changes the zeta potential of the cell surface [232]. This technique can identify the microbial surface targeting agents that act via neutralizing the membrane potential. Previous studies have shown that the Gram-negative microbial cells have a higher negative zeta potential value due to the presence of LPS molecules on their outer membrane [216]. Figure 4.1 (B) showed the live-cell zeta potential analysis of the *P. aeruginosa* 6294 cells at different concentrations of the VR18 peptide. The average surface charge of the bacterial cells in phosphate buffer was around -32 mV in the absence of the peptide. This negativity of the surface potential was decreased sequentially with increasing concentration of the VR18 peptide and became -17.2 mV at 15 μM (1.5x MIC) concentration, which suggests that the peptide actually neutralizes the negatively charged LPS molecules via electrostatic interactions between positively charged Lys and Arg residues.

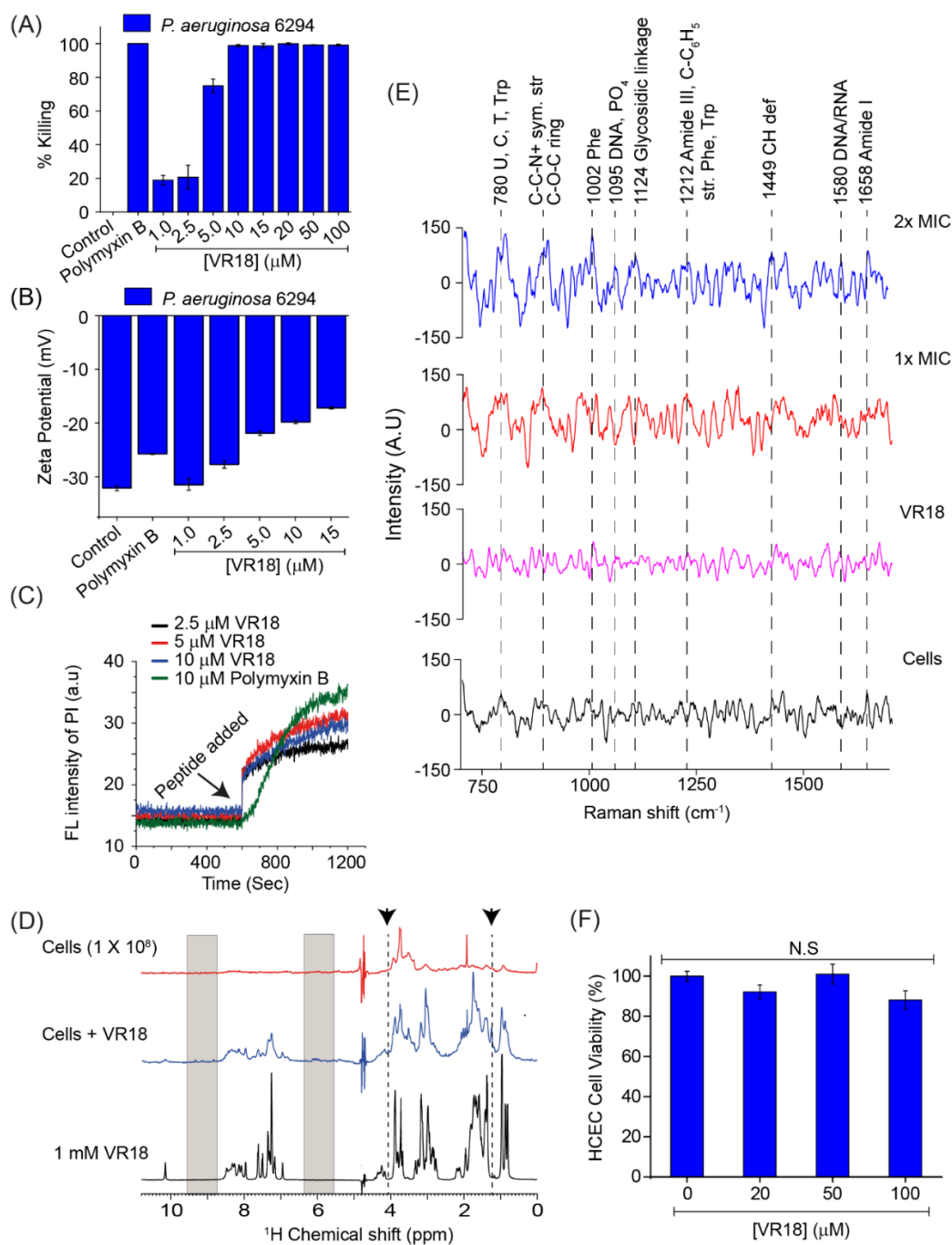


Figure 4.1. (A) Micro broth dilution assay showing MIC_{99%} at 10 μM concentration of VR18 against *P. aeruginosa* 6294. (B) Measurement of zeta potential of the bacterial cells in presence of different concentration of VR18. (C) Cell membrane permeabilization assay by using propidium iodide (PI) as a probe. The fluorescence spectra showed immediate increment after the addition of VR18 at 2.5 μM, 5 μM and 10 μM concentrations. 10 μM polymyxin B was used as a positive control. (D) Live cell NMR analysis of the *P. aeruginosa* 6294 cells in absence and presence of 1 mM VR18 peptide. (E) the averaged Raman spectra of the free bacteria, free VR18 and the bacteria treated with 1x and 2x MIC of VR18, respectively, showing several peaks which originated from the lysed bacterial

cell after the treatment of the peptide. (F) MTT assay of HCEC cells at 2x, 5x and 10x MIC of VR18. The error bars represent the \pm SD. N.S- Not significant.

This finding also suggests that the initial binding of the peptide occurs on the bacterial cell surface and not via any passive insertion or ion-channel mediated incorporation into the microbial cells. Of note, 10 μ M polymyxin B was used as a positive control because it kills 99% of the microbial cells at this concentration, but it showed -25.8 mV zeta potential, which is less compared to the zeta potential value (-19.8 mV) of VR18 at its 1x MIC concentration. This suggests that the mode of action of polymyxin B and the VR18 peptide are different in the presence of Gram-negative bacterial cells.

To probe the target of the VR18 on the microbial cell surface and to understand the mode of action, propidium iodide (PI) uptake assay was performed [233]. PI, a membrane-impermeable nucleic acid (DNA/RNA) binding fluorescent dye, generally used to differentiate between apoptotic, necrotic, and healthy cells based on membrane integrity [234]. The time-dependent PI uptake assay with live *P. aeruginosa* 6294 cells treated with different concentrations of VR18 (0.25x, 0.5x and 1x MIC) showed a stepwise increment of PI fluorescence intensity which was compared with a positive control, 10 μ M polymyxin B (Figure 4.1 (C)). These data indicate that the outer and inner cell membranes of the bacterial cells were compromised. The polymyxin B, showed a sigmoidal increment of the graph, whereas the peptide exhibited an exponential graph pattern which indicates that the rate of activity of the VR18 peptide is instant and much faster compared to the polymyxin B.

In order to correlate this data, live-cell one dimensional proton (^1H) NMR experiment was done by using a 1 mM peptide solution against 1×10^8 number of *P. aeruginosa* 6294 cells in 10 mM phosphate buffer (pH 6.5) at 25 °C. The high concentration of the peptide (1 mM) caused immediate lysis of the bacterial cells, as shown previously [169], which results in an increasing concentration of cellular metabolite release into the peptide solution. The metabolite peaks of the compromised cells have been observed within 5-10 min as compared to the control spectrum of bacterial cell suspension as well as the spectrum of the free peptide, as shown in Figure 4.1 (D). The new peaks from the lysed bacterial cells increased gradually with time (Figure 4.1 (D)). The above observations indicate that the microbial cell membrane is the primary target for the peptide.

Table 4.2. The peaks developed in the Raman spectra after the treatment of VR18 on *P. aeruginosa* cells.

Peak (cm ⁻¹)	Assignment*				
	DNA/RNA	Proteins	Lipids	Carbohydrates	Carotenoids
780	U, C, T ring br.	Ring br. Trp			
878			C-C-N ⁺ sym. str.	C-O-C ring	
933		C-C bk. Str. α-helix		C-O-C glycos	
1002		Sym. Ring br. Phe			C-CH ₃ def
1039		C-H in plane Phe			
1095	DNA PO ₂ ⁻ back				
1104	PO ₂ ⁻ str. Sym.			C-C str. C-O-C skeletal str. Glycosidic link of saccharides	
1124				C-C str. C-O-C skeletal str. Glycosidic link of saccharides	
1212		Amide III, C- C ₆ H ₅ str. Phe, Trp			
1313			CH def.	CH def.	
1449	G, A	CH def.	CH def.	CH def.	
1530					C=C str.
1580	DNA	Amide II		COO ⁻ str. Asym.	
1658		Amide I			

Since the one dimensional NMR experiments suggested that the *P. aeruginosa* cells are getting disrupted in the presence of a higher concentration (1 mM) of VR18 peptide, we further showed that the lytic effect of the VR18 peptide also occurs at its MIC concentration (10 μ M). Live cell Raman spectroscopy was utilized in this case to understand this phenomena. Raman spectroscopy identifies changes in the vibrational and rotational spectra of large molecules [235]. In this study, the effect of the VR18 peptide was investigated against the *P. aeruginosa* 6294 strain.

Figure 4.1 (E) showed the averaged Raman spectra of the free cells, VR18 and the cells treated with 1x and 2x MIC of VR18, respectively. The vibrational bands typical for nucleic acids, proteins, lipids, and carbohydrates are detailed in Table 4 [218]. The spectrum of the free peptide did not overlap with the spectrum of the untreated bacterial cells, and peaks of the treated sets were independent of the individual peptide peaks. Several prominent peaks in the VR18 treated cells matched with the vibrational modes of phenylalanine (1002 cm^{-1}) and amide I (1658 cm^{-1}) in proteins. The sharp band at 1449 cm^{-1} which shows CH deformations can be assigned to polysaccharides, lipids as well as proteins, which are all components of bacterial cell membranes. The Raman spectrum obtained from the nucleus of *P. aeruginosa* 6294 cells is characterized by bands at 780 cm^{-1} (uracil, cytosine and thymine), 1095 cm^{-1} (DNA, PO_4^{3-} stretching), and 1574 cm^{-1} (guanine and adenine). The peak at 1124 cm^{-1} could be associated with the stretching vibration from symmetric glycosidic linkages (C-O-C) and the ring breathing mode of polysaccharides or C-C stretching vibrations. The increment of the above-mentioned peak intensities with increasing concentration of the peptide further suggest that the cellular compartment of the bacterial cells is compromised, and the molecules have been released from the microbial cells.

The subsequent concern was to check any adverse effect of the peptide against human corneal epithelial cells (HCEC). An MTT dye reduction assay[44] was done to check the toxicity of the peptide on HCEC in the presence of 2x, 5x and 10x MIC of the VR18 [226]. The results show there are 90% viable HCEC cells at 10x MIC after 4 h exposure, which indicates that the peptide acts selectively on bacterial cells but is not active against human corneal epithelial cells (Figure 4.1 (F)).

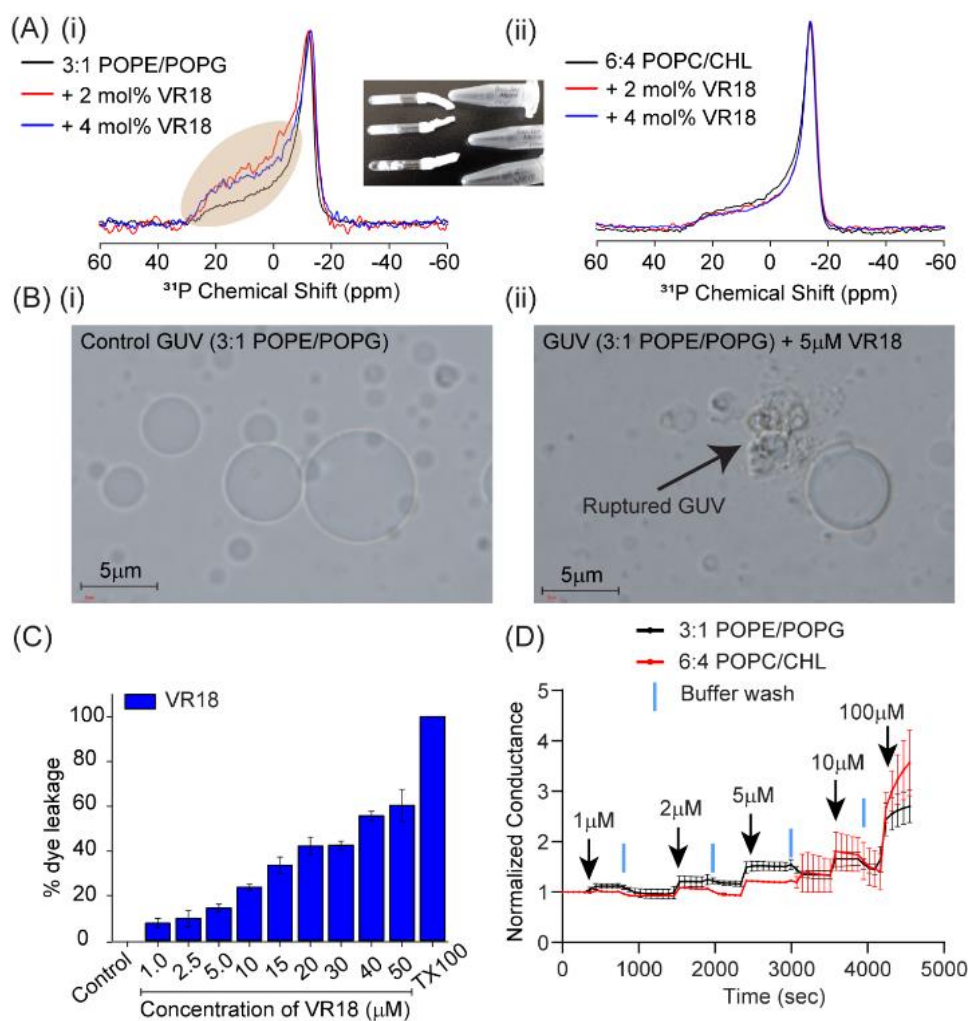


Figure 4.2. (A) (i) Solid state ^{31}P NMR of the 3:1 POPE/POPG LUVs show immediate thickening of the spectrum at around 0 ppm (marked area). All the ^{31}P NMR spectra were normalized to 1 for the highest peak intensity. (ii) On the contrary, LUVs made of POPC with 40% Cholesterol mimicking the eukaryotic membrane showed no changes. (B) (i-ii) Phase contrast microscopy of GUVs in absence and presence of the VR18 showed bursting of the vesicles with time. (C) Bar graph showing calcein dye leakage assay using the bacterial inner membrane mimicking vesicles. (D) Time-dependent ionic conduction responses in sparsely tethered bilayer lipid membranes composed of 3:1 POPE/POPG and 6:4 POPC/Cholesterol membranes in presence of VR18 peptide. The error bars represent the $\pm\text{SD}$ of $n=3$ membranes.

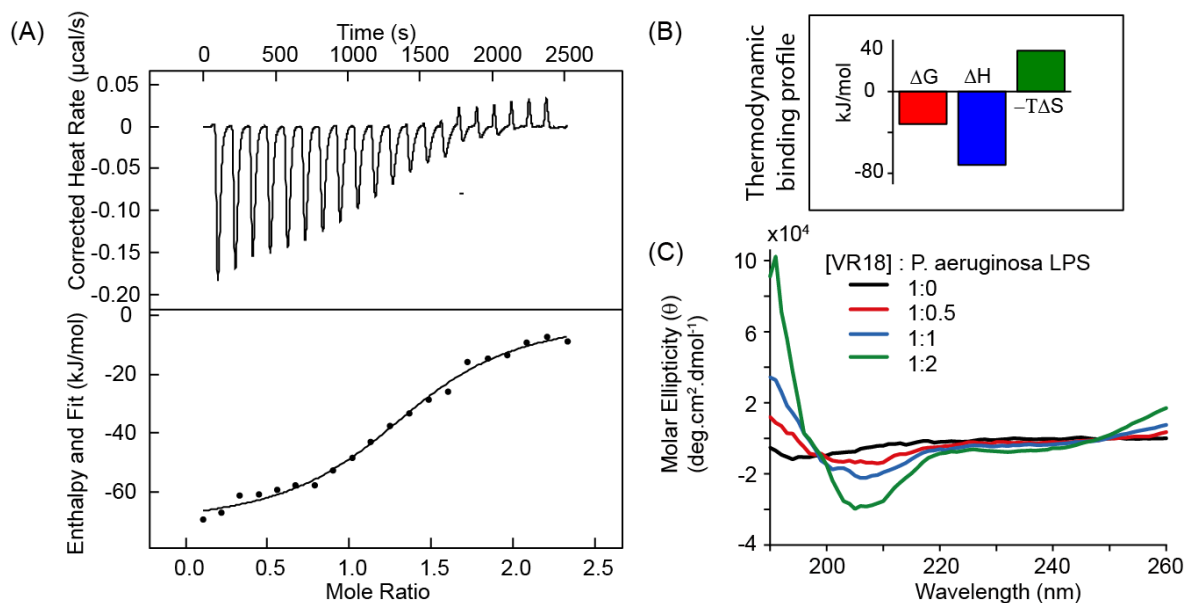


Figure 4.3. (A) ITC analysis of VR18 peptide in the presence of *P. aeruginosa* LPS. ITC thermogram obtained at 25°C. A total of 20 injections of *P. aeruginosa* LPS were made, at an interval of 2 min, into VR18 solution and the heat exchange was measured. The data were fitted by the non-linear least-squares minimization method subsequent to the correction for the heats of dilution for *P. aeruginosa* LPS. (B) CD analysis of VR18 in the presence of the *P. aeruginosa* LPS showed the change of the spectra from random coil to a folded conformation.

4.3.3. Probing the membrane specificity of the VR18 peptide

To further demonstrate the selective membranolytic nature of the VR18 peptide, model bacterial and eukaryotic membranes were prepared by using 3:1 POPE/POPG and 6:4 POPC/Cholesterol (CHL), respectively (described in the experimental section).[126] Solid-state NMR spectroscopy was employed to monitor the interactions between lipid bilayers and the VR18 peptide by using the ³¹P nucleus on the phospholipid headgroup. Solid-state ³¹P NMR spectroscopy is an important technique for studying the different phases formed by model phospholipid membranes [170]. The form of ³¹P NMR spectrum has different characteristics for different lipid phases, such as gel and liquid crystal lamellar phase, inverted hexagonal phase and isotropic phase (such as small vesicles or micelles) [236]. The vesicles composed of 3:1 POPE/POPG and POPC with 40% cholesterol (6:4 POPC/CHL) showed a typical powder pattern of liquid crystal lamellar phase (parallel edge at ~30 ppm and perpendicular edge around -15 ppm) of ³¹P spectra, as shown in Figure 4.2 (A) (i-ii) in black line. There was no liquid domain separation, suggesting that the lipids are distributed almost homogeneously in the vesicles of liquid-crystalline L α phase. Compared to the peptide free spectrum, the spectra of the 3:1 POPE/POPG vesicles with

VR18 showed changes in the relative intensities at the parallel edges (~30 ppm) and perpendicular edges (~-15 ppm). This indicates that the peptide interacted with lipids and changed the shape of the vesicles to flattened shape, having an increased number of the lipid molecules of parallel orientation relative to the external magnetic field (Figure 4.2 (A- (i))). However, no disruption of the vesicle into small vesicles or micelles was observed as there was no isotropic peak obtained at this concentration of the peptide. Surprisingly, the addition of the peptide caused immediate precipitation of the vesicles in the NMR tube as shown in the inset image (Figure 4.2(A)), which resulted from increased electrostatic interaction between the peptide and the POPG lipid molecules. This might be the reason to change the ^{31}P spectral shape. On the other hand, the vesicles containing 40% cholesterol showed negligible changes with 2 and 4 mol% peptide as shown in Figure 4.2 (A- (ii)), since the zwitterionic POPC lipid does not interact with the charged peptide. It is noteworthy that the presence of cholesterol molecules also increases the acyl chain order of the vesicles, which subsequently increases its endurance against different AMPs [158]. These observations suggest that the peptide selectively interacted between POPE and POPG lipids due to the electrostatic interaction with oppositely charged headgroups of PG lipids.

The activity of VR18 peptide towards the bacterial model membrane was further examined by the dye release assay and the phase contrast microscopy using large unilamellar vesicles (LUVs) and giant unilamellar vesicles (GUVs), respectively, while keeping the same lipid composition as described above. To visualize the lytic action, GUVs filled with 100 mM sucrose solution were employed inside of 105 mM glucose solution to create the phase difference of the incident light in the phase contrast microscope that helps to visualize the vesicles [178]. The addition of VR18 peptide results in a time-dependent burst of the GUVs within 15 min of the treatment as compared to the control GUVs (Figure 4.2 (B) (i-ii)). Likewise, LUVs filled with calcein dye were used to check the dye leakage by using fluorometric analysis. Figure 4.2 (C) showed a concentration-dependent intensity increment of the calcein dye with 10% to 60% leakage at 1 μM and 50 μM , respectively. This indicates that the peptide is capable of interacting with negatively charged membranes and subsequent disruption increases the free calcein molecules outside the vesicles that increases the intensity of the spectrum. These biophysical studies using model lipid vesicles suggests that the VR18 peptide specifically interacts with the lipid bilayer that mimics the microbial membrane.

Table 4.3. The thermodynamic parameters obtained in the ITC analysis of VR18 in presence of LPS.

Thermodynamic parameters	VR18 – <i>P. aeruginosa</i> LPS
K_D (M)	$2.65 \times 10^{-6} \pm 6.46 \times 10^{-7}$
K_A (M^{-1})	3.77×10^5
n (number of binding sites)	1.36 ± 0.037
ΔH (kJ/mol)	-71.89 ± 2.97
ΔS (J/mol. K)	-134.3
ΔG (kJ/mol)	-31.83

In order to gain insight of the lipid-peptide interaction from the electrical properties of the two different membrane models with the VR18, a further analysis was done using sparsely tethered bilayer lipid membranes (stBLMs) in conjunction with electrical impedance spectroscopy [221,222]. Figure 4.2 (D) shows a time-course of membrane interactions of the VR18 peptide at increasing concentrations, with subsequent wash steps between each increasing dose. Relatively small increases in membrane conduction, typical of an alteration in membrane packing, can be seen in both 3:1 POPE/POPG and 6:4 POPC/CHL model membranes in response to the peptide. The membrane conduction does not return to a baseline following each wash step which suggests that the peptide has a slow off-rate – a sign that it has the potential to accumulate at lipid membrane surfaces. It is feasible that this accumulation could be responsible for the lytic activity of the peptide seen in the GUV experiments. At lower concentrations of the peptide (2 – 5 μM), relative conductance changes are greater in the bacterial membrane mimic (3:1 POPE/POPG), suggesting an attraction to these negatively charged lipid headgroups which correlate with the previous findings.

As a Gram-negative bacterium, *P. aeruginosa* has a cytoplasmic membrane with a symmetric phospholipid bilayer and an asymmetric outer membrane with an inner surface of phospholipids and an outer layer that incorporates lipopolysaccharide (LPS), creating a permeation barrier. Since the peptide first interacts with this macromolecule on the microbial cell, isothermal titration calorimetry was done at room temperature to gain insight about the thermodynamic parameters of the interaction between the VR18 and the *P. aeruginosa* LPS. The results shown in Figure 4.3 (A) and Table 4.3 suggests that the binding of the peptide with LPS molecules is at micromolar concentration ($K_D = 2.65 \times 10^{-6}$

$6 \pm 6.46 \times 10^{-7}$ mol/L) and the process is an enthalpy (ΔH) driven mechanism, favouring a spontaneous interaction ($-\Delta G$) (Figure 4.3 (B)).

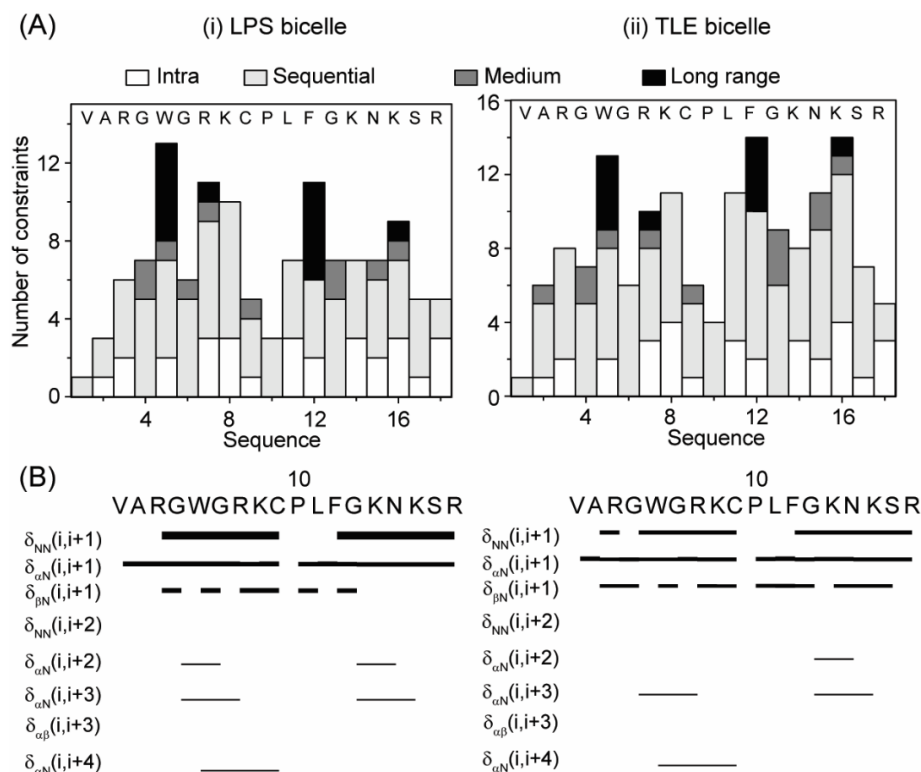


Figure 4.4. (A-B) Bar and histogram plot of VR18 showing intra, sequential, medium- and long-range NOEs in *P. aeruginosa* LPS (i) and *E. Coli* TLE bicelle (ii) bound form of the peptide.

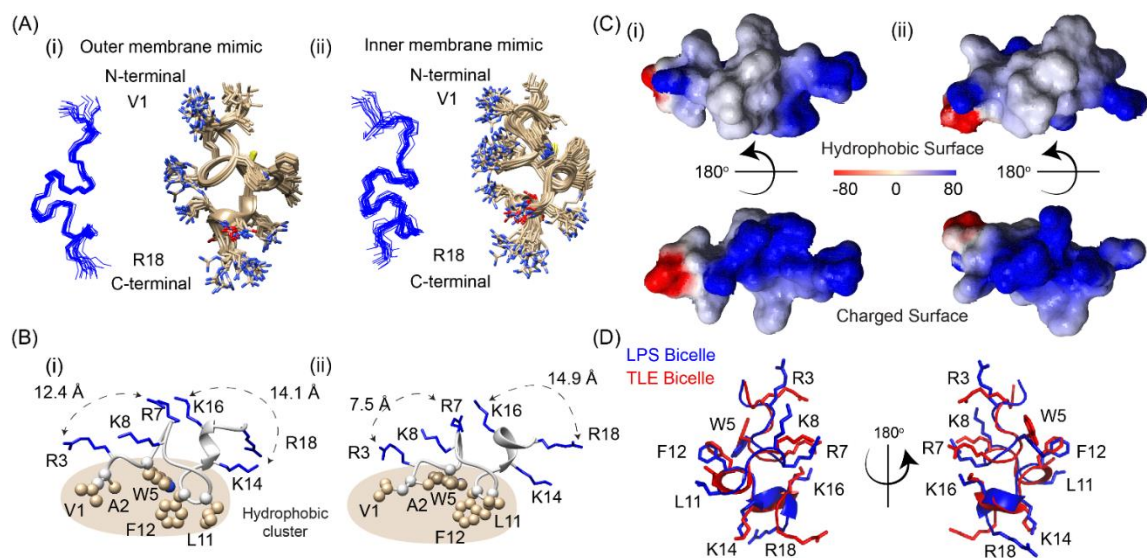


Figure 4.5. (A-C) Left and right panel shows the LPS bicelle or TLE bicelle bound solution NMR structures of VR18 (PDB IDs: 7VQI and 7VQH). (A) Backbone (Blue) and all states of the 20 ensemble lowest energy structures showing rigid structure with tight backbone packing. (B) Cartoon representation of the single structures showing the separation between charged (blue lines) and hydrophobic (grey) surfaces. (C) Surface representations of the peptide showing hydrophobic (grey) and charged (blue/red) surfaces. (D) Comparison of LPS Bicelle (blue) and TLE Bicelle (red) bound structures.

and hydrophobic (ball and stick model) residues. The positively charged residues maintained a clear separation of 12-15 Å or <10 Å between their hydrophilic head groups, which was comparable to the distance between LPS phosphate head group or PG headgroups (TLE). (C) the electrostatic surface potential of the complex bound to LPS or TLE at an angle of 180° also showed the clear delineation of the surface charge distribution, which was generated with *MOLMOL* software. (D) Overlaid structures of LPS bicelle and TLE bicelle bound VR18 peptide.

4.3.4. Deciphering the atomistic information of the peptide-membrane interaction

To gain insight into structural aspects of the VR18 peptide, high-resolution NMR spectroscopies were performed [237,238]. Since the K_D value obtained from the ITC experiment was in the micromolar range ($K_D \sim 2.65 \mu\text{M}$), transferred NOESY (*tr*NOESY) experiments were performed in the presence of bicelles made of *P. aeruginosa* LPS and *E. coli* total lipid extract (TLE). *tr*NOESY is a widely used experiment to determine the conformation and orientation of a ligand bound to a macromolecule [239]. Although the methodology applied may be used to determine the three-dimensional structure of the peptide in the context of a live cell, the release of metabolites within a few min of treatment restricted us from employing it in the presence of live *P. aeruginosa* 6294 cells. Instead, bicelles made of *P. aeruginosa* LPS and *E. coli* TLE (Appendix IV, composition shown in Table S4.1) were used to mimic the outer and inner membrane of the bacterial cell, respectively. The NOESY spectra of the free peptide did not exhibit pronounced NOEs except for certain intra- (i, i) or sequential (i, i+1) NOEs, indicating that the free peptide remains highly dynamic (Appendix IV, Figure S4.1 (A)). This was also confirmed by CD spectroscopy (Figure 4.3 (C)). Addition of 1-15 μl bicelles to the peptide resulted in concentration-dependent line broadening, without affecting the chemical shift in its one dimensional (1D) proton NMR spectra (Appendix IV, Figure S4.1 (B)). Similarly, the CD spectra also showed changes in the far UV absorbance, indicating adaptation of the secondary structure in presence of LPS (Figure 4.3 (C)). Thus, when the free peptide interacts with macromolecules (here bicelles), they undergo a fast to intermediate exchange with the bicelle-bound form under the NMR time-scale. Such a situation is ideal for *tr*NOESY experiments to determine the three-dimensional structure of the peptide in the presence of the bicelles. The *tr*NOESY spectra of the VR18 peptide in presence of the bicelles are summarized in Table 4.4 and Figure 4.4. A large number of intra- and sequential (i, i+1) NOEs were observed in both the cases. Several unambiguous medium range (i, i+2/i+3/i+4) NOEs were also observed in between Gly-4/Arg-7, Trp-5/Cys-9, Gly-13/Asn-15 and Gly-13/Lys-16 in the presence of both bicellar systems, except the NOEs between

Gly-4 α /Gly-6 was observed in case of *P. aeruginosa* LPS bicelle (Figure 4.4 and S4.2, Appendix IV) and Ala-2 β /Gly-4 was observed in case of *E. Coli* TLE bicelles (Figure 4.4). This indicates that the peptide gets a folded conformation from random coil structures in presence of the bacterial outer- and inner-membrane environment. Moreover, several long-range NOEs ($i, \geq i+5$) between Trp-5/Phe-12 and Arg-7/Lys-16 also suggests that the peptide VR18 adopts an amphiphilic structure in the presence of negatively charged membranes (Figure 4.4 and S4.2, Appendix IV).

Table 4.4. The *E. coli* Total Extract Phospholipid Profile derived from the website of Avanti polar Lipids.

VR18	<i>P. aeruginosa</i> LPS	<i>E. coli</i> TLE
Distance restraints		
Intra residue ($i - j = 0$)	29	31
Sequential ($ i - j = 1$)	36	50
Medium range ($2 \leq i - j \leq 4$)	5	5
Long range ($ i - j \geq 5$)	6	5
Total	76	91
Angular restraints		
Φ	15	15
Ψ	15	15
Distance restraints from violation ($\geq 0.4 \text{ \AA}$)	0	0
Deviation from mean structure (\AA)		
Average backbone to mean structure	0.48 ± 0.14	0.80 ± 0.19
Average heavy atom to mean structure	1.23 ± 0.23	1.51 ± 0.13
% residues in Ramachandran plot*		
most favored and additionally allowed region	83.3	58.3
generously allowed region	16.7	41.7
disallowed region	0.0	0.0

Using NOE-based distance constraints, we generated 20 ensemble structures of VR18 in *P. aeruginosa* LPS bicelle and *E. coli* TLE bicelle (Figure 4.5 (A) (i-ii)), demonstrating that the peptide adopts an amphipathic structure by clearly separating positively charged Lys and Arg residues from hydrophobic residues such as Val, Leu, and Phe (Figure 4.4). Closer inspection between the structures highlighted a marked difference between the position of the positively charged residues. The N-terminal Arg-3, Arg-7 and Lys-8 and the C-terminal K14xK16xR18 moiety of the LPS bound structure maintained a distance of 10-15 Å which closely correlates with the distance between two terminal phosphate groups of LPS (Figure 4.5 (B) (i)). On the other hand, the C-terminal K14xK16xR18 moiety only maintained a certain distance while the N-terminal Arg-3, Arg-7 and Lys-8 residues stayed closely within 10 Å (Figure 4.5 (B) (ii)). The *E. coli* TLE is mainly composed of PE (57.5 wt/wt %) and PG (15.1 wt/wt %) lipids which is why the positively charged residues rearranged themselves in such a way that facilitates the initial electrostatic interaction between the oppositely charged head groups on the bicelle. Of note, two aromatic residues, Trp-5 and Phe-12, maintained a distance of 4.5 - 7 Å while adopting an energetically favourable T-shaped geometry that stabilized both the structures in the bound form.[171] Apart from that, the non-polar residues consisting of Val-1, Ala-2, Trp-5, Leu-11 and Phe-12 formed a hydrophobic cluster, which is further stabilized by interacting with the acyl chain moieties of the LPS or the lipid molecules in the bicelles. A similar structural propensity was found in presence of LPS micelles in the case of the synthetically designed β -boomerang peptide YI12 and the MSI-594 peptide, which is an α -helical peptide designed from magainin and melittin [202,240]. The three active analogs of YI12 peptides (YI12WF, YI12WY, and YI12WW) formed a hydrophobic hub between Trp4 and Phe9/Tyr9/Trp9, but the inactive YI12AA peptide showed a deficiency in hydrophobic-aromatic packing in the presence of LPS [202]. The importance of amphipathic structure and hydrophobic packing via the phenylalanine residue was also reported in case of MSI-594 and its mutant analog MSI-594F5A peptide where the F5A mutation completely disturbed the helical hairpin structure of MSI-594 in LPS micelles [240,241]. The electrostatic potential map shown in Figure 4.5(C) supported both the amphipathicity as well as the compact bioactive conformation of the peptide. It is evident from the above two structures that how the peptide changes its random coil conformation to a defined amphipathic shape in the presence of bacterial outer and inner membrane environments as depicted by the overlaid structures shown in Figure

4.5 (D), that subsequently destabilizes the whole plasma membrane of this unicellular organism.

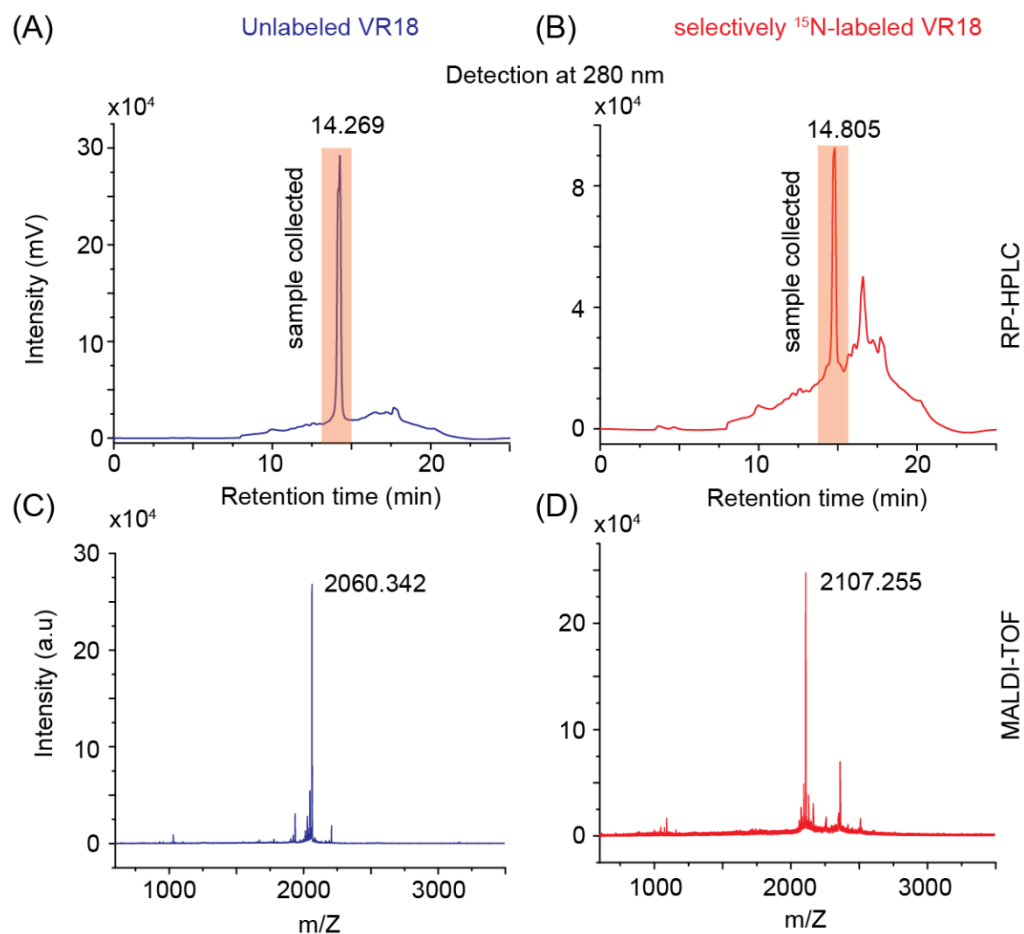


Figure 4.6. RP-HPLC profile of unlabeled (A) and selectively ^{15}N -labeled VR18 (B) shows a retention time of 14.269 and 14.805 min, respectively. The peak that was collected to analyze the mass is highlighted with saffron box. The MALDI-TOF analysis of unlabeled (C) and selectively ^{15}N -labeled VR18 (D) shows single major peak intensity at m/Z ratio of 2060.342 and 2107.255, respectively. Since the selectively ^{15}N -labeled VR18 was acetylated at the N-terminus and amidated at the C-terminus, it showed higher mass compared to the purchased unlabeled VR18.

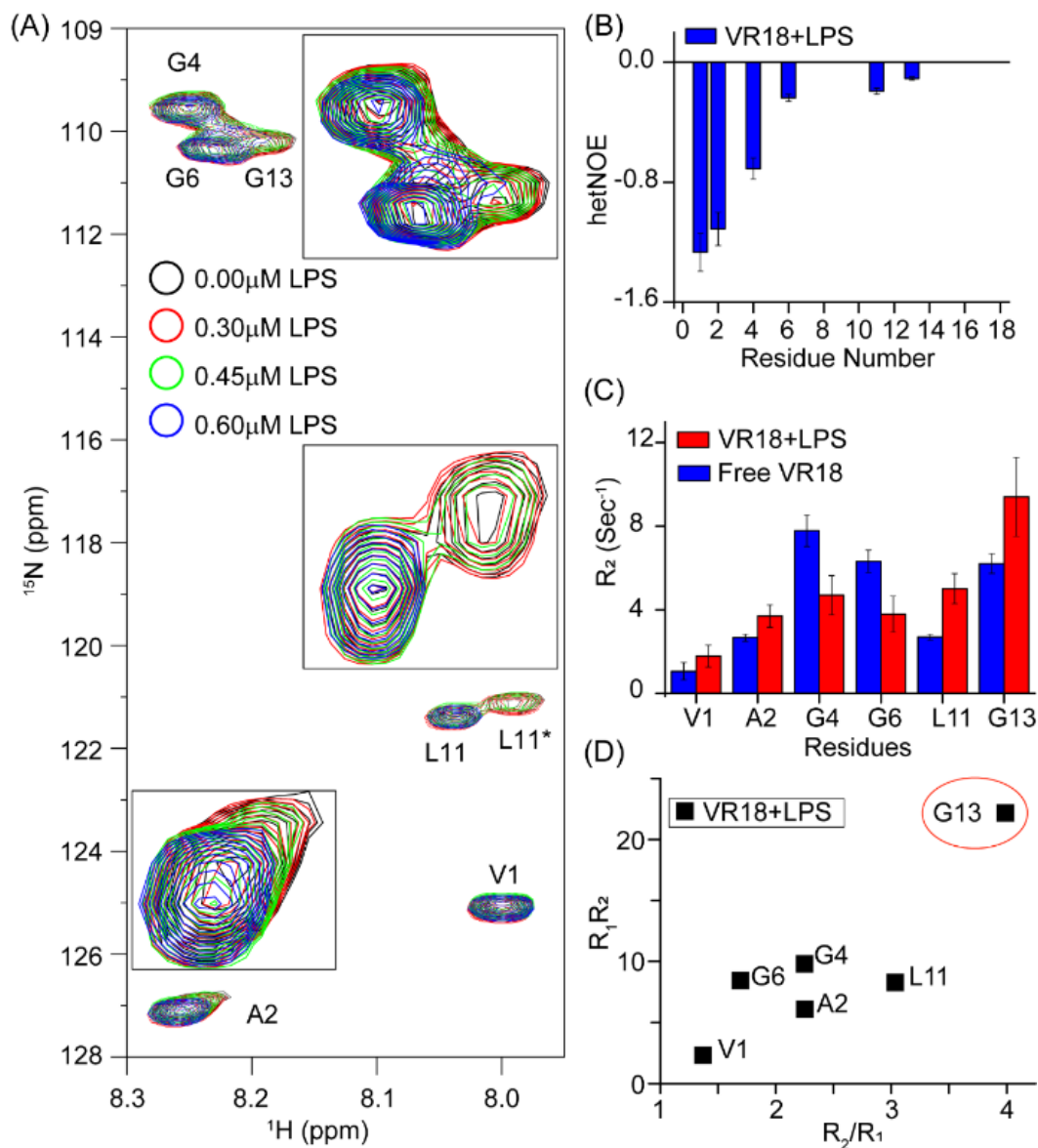


Figure 4.7. (A) Overlay of 2D ^1H - ^{15}N -HSQC spectra of 1.0 mM ^{15}N -labelled VR18 peptide (at 298 K, pH 4.5) recorded upon titration with increasing concentrations of LPS (ranging from 0 to 0.6 μM). Residue specific assignment for each peak is marked on the spectrum. The amino acid sequence of the peptide is shown at the top of the HSQC spectrum with selectively ^{15}N -labelled residues (Val-1, Ala-2, Gly-4, Gly-6, Leu-11 and Gly-13) highlighted in blue. Except for Leu-11 residue, the exchange peaks for all other ^{15}N labelled residues were broadened and overlapping with the major conformational peak, whereas Leu11 clearly showed two cross peaks signifying largely different conformations exchanging slowly. The HSQC cross-peak of Leu-11 corresponding to minor conformational state have been highlighted in the spectrum by an asterisk (*). (B) The heteronuclear NOE plot of LPS bound VR18. (C) The R_2 values of free and LPS bound VR18 peptide is shown in the bar plot. (D) The R_2/R_1 vs R_1R_2 plot of LPS bound VR18 depicting the level of molecular anisotropy and chemical exchange of each residue. The Gly-13 marked in the red circle is going through chemical exchange with LPS molecule. The error bars represent the $\pm\text{SD}$.

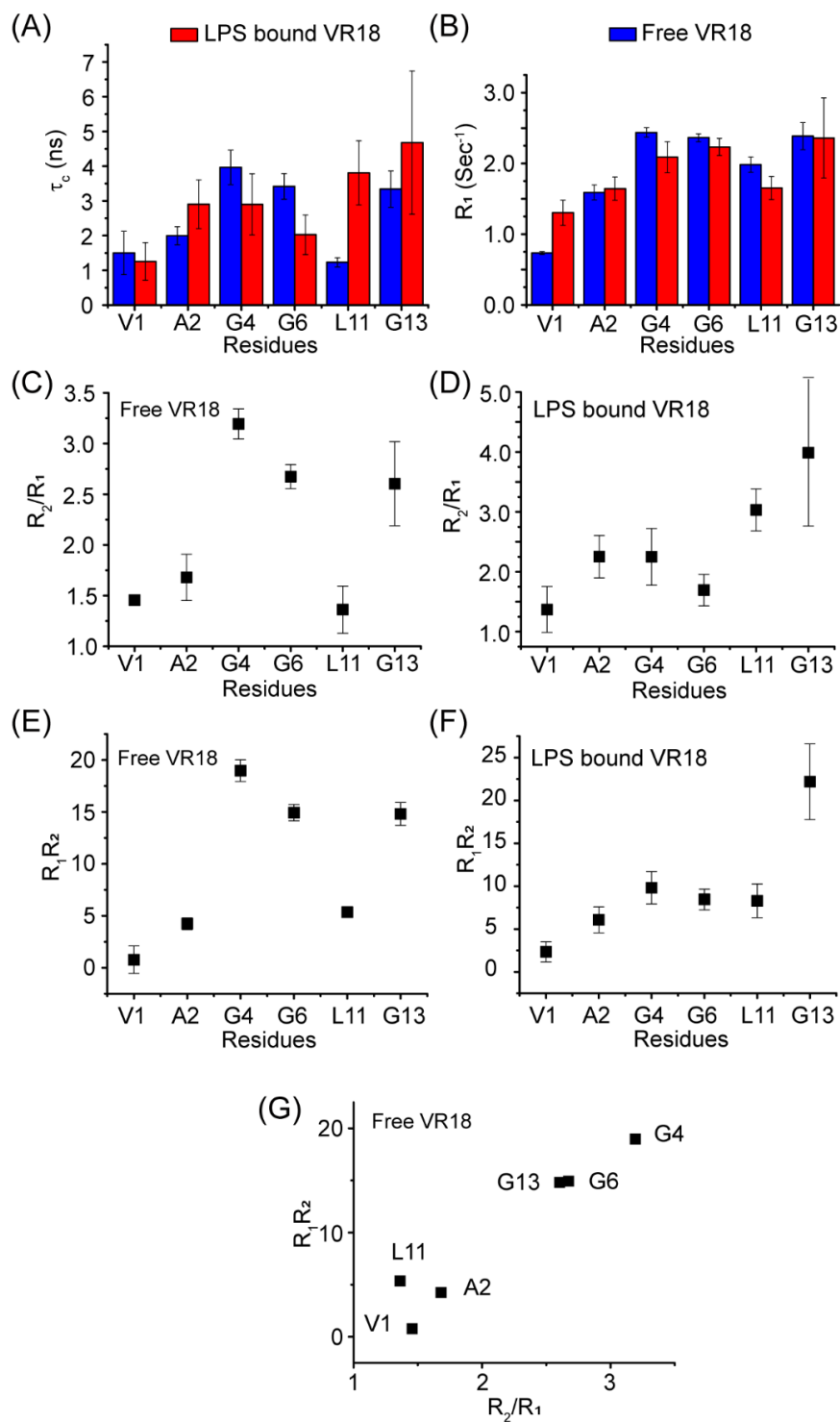


Figure 4.8. The residue-specific correlation time (A) and R_1 relaxation rates (B) of VR18 has been shown in the bar plot. (C-D) The residue-specific R_2/R_1 plot of free and LPS bound VR18. (E-F) The R_1R_2 vs residue plot of free and LPS bound VR18, respectively. (G) The R_2/R_1 vs R_1R_2 plot of free VR18 showing high dynamic and anisotropic values of the Glycine residues.

Heteronuclear spin relaxation rates have been shown to be powerful probes of the general and internal dynamics of macromolecules [242,243]. To gain insight into the

backbone dynamics of the LPS micelle bound VR18, the measurement of ^1H - ^{15}N heteronuclear NOE (hetNOE), ^{15}N longitudinal ($R_1 = 1/T_1$) and transverse ($R_2 = 1/T_2$) relaxation rates were studied at 298 K. Out of 18 amino acid residues, six residues (Val-1, Ala-2, Gly-4, Gly-6, Leu-11, and Gly-13) were selectively labelled with ^{15}N via Fmoc chemistry and subsequent purification and mass was observed and compared with unlabeled VR18 via RP-HPLC and MALDI TOF analysis as shown in Figure 4.6 (A-D) [120]. The peptide-LPS interaction was observed by titrating 1 mM VR18 aqueous solution with increasing concentration of LPS (0.3, 0.45, 0.6 μM) from 1 mM stock solution, which resulted in a concentration-dependent broadening to the amide signals as shown in Figure 4.7 (A). Close inspection revealed that Leu-11 exhibited multiple amide cross-peaks in the HSQC spectrum (shown in inset of Figure 4.7 (A)), suggesting that there is a slow conformational exchange ($\ll 10^3 \text{ sec}^{-1}$) between multiple conformations at the NMR time scale. This is probably due to the presence of Pro-10. The overlaid HSQC spectra of VR18 in the free state (black) and at increasing concentrations of LPS (red, green, and blue) (Figure 4.7 (A)) revealed no significant chemical shift perturbation, implying that the peptide binding to LPS involves a rapid conformational exchange between the free and bound states on the NMR time scale. The intensity vs LPS concentration plot in Figure S4.3 (Appendix IV) revealed that the amide peak broadening of Gly-4 and Gly-13 is maximum, followed by Ala-2, Val-1, Gly-6, and Leu-11. The bulky LPS molecule interacts with the positively charged C-terminal KNKSR moiety and other Arg, Lys residues, so the close proximity of Gly-13 to KNKSR moiety and the Ala-2 and Gly-4 to Arg-3 resulted in an increased T_2 relaxation similar to LPS. Leu-11 might not be involved in an immediate association with LPS compared to the Gly-13/Gly-4/Ala-2. In other words, Leu-11 comes close to LPS after the peptide adopts a folded conformation in LPS. Collectively, these results represent the systematic folding of VR18 in LPS micelles at an atomic resolution.

The flexibility of folded VR18 was estimated by measuring the hetNOE. The NOE value determined for each residue is plotted in Figure 4.7 (B). All the residues showed negative NOE with gradually increasing value from Val-1 (-1.27) to Gly-13 (-0.1). It suggests that the N-terminal end is more flexible than the C-terminal end in an overall dynamic structure. In parallel with the hetNOE, conformational flexibility of the individual residues is indicated by R_2 values. The non-polar residues (Val-1, Ala-2, and Leu-11) that took part in the hydrophobic cluster formation, and interacted with the acyl chains of the lipids, showed higher R_2 values than the free peptide as depicted in Figure 4.7 (C). The

rotational correlation time of the individual residues corroborates with this finding, as shown in Figure 4.8 (A). Notwithstanding, the R_1 relaxation rates for most of the residues do not show significant changes (Figure 4.8 (B)). Thus, to differentiate between the effects of residue-specific chemical exchange from the motional anisotropy in the complex formation, we plotted the product of the longitudinal and transverse relaxation rates that helped to accentuate the effect of the chemical exchange alone (Figure 4.8 (E-G)). This difference with the R_2/R_1 plots (Figure 4.8 (C-D)) corresponding to the rotational correlation time is particularly noteworthy in the free form with a high degree of molecular anisotropy. This, however, is largely abolished in the LPS-bound values. A significant difference was observed for Gly-13 in the LPS-bound complex [215,244]. This suggests the contribution of chemical exchange over the rotational anisotropy. Thus, the plot of $R_2.R_1$ vs R_2/R_1 (Figure 4.7 (D)) helps represent the partitioning between residues directly affected by chemical exchange at the interaction interface. The data reinstates the direct involvement of the C-terminal KNKSR moiety in binding firmly to the LPS phosphate head groups.

4.3.5. Evaluation of the in vitro, ex vivo and in vivo efficacy of VR18 peptide

In order to find the structure-function correlation, and study the protective effect of the peptide against *P. aeruginosa*, HCEC were infected with PAO1 for 4 h in presence or absence of the peptide. Microscopic images in Figure 4.9 (A) showed that the VR18-treated HCEC cells were more viable than the untreated cells in presence of PAO1, which was correlated with the bacterial viability as obtained from optical density measurement (OD_{600}) (Figure 4.9 (B)). The reduced cell death of HCEC was evident from the lowered LDH release in presence of increasing concentration of VR18 (Figure 4.9 (C)) which suggests that VR18 renders protection to the HCEC cells infected with PAO1.

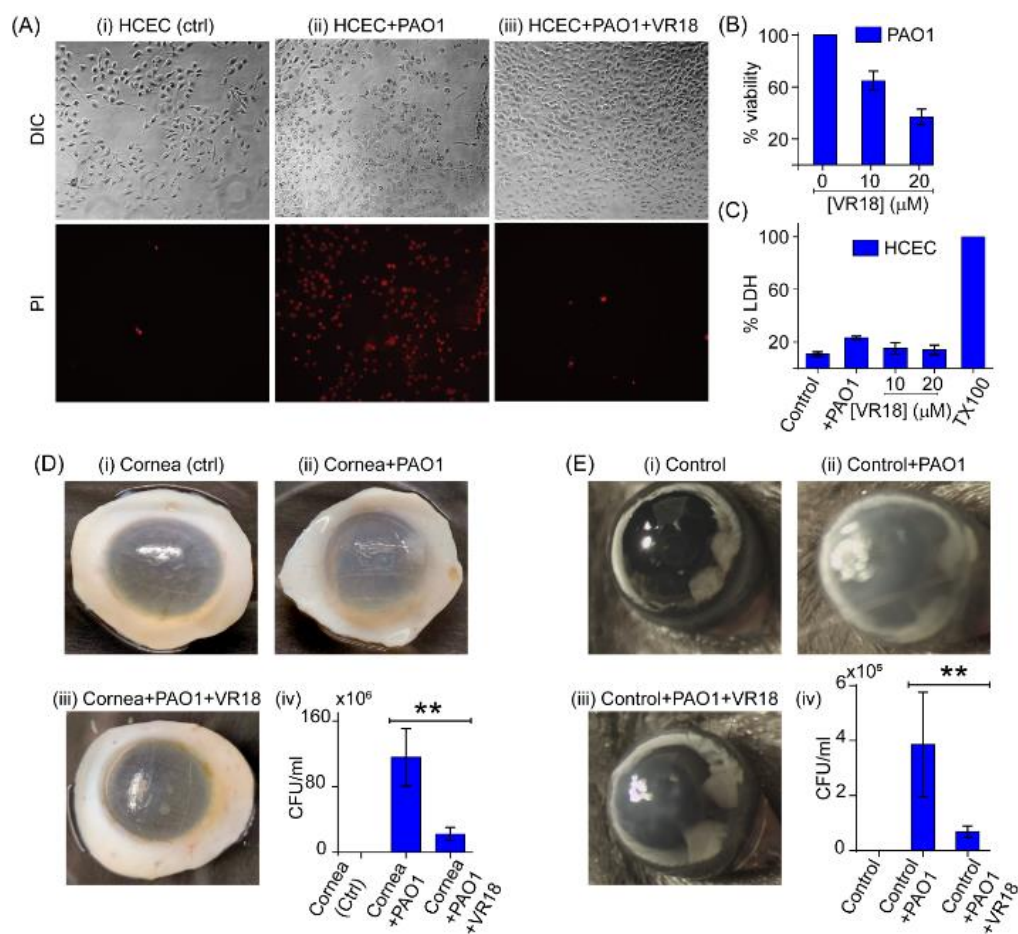


Figure 4.9. (A) The microscopic study showed that the Control HCEC cells along with PAO1 infected cells in DIC and PI channel. The addition of 10 and 20 μM VR18 had little impact on the viability of the HCEC cells. (B) The percentage of the viable PAO1 population was decreased with increasing concentration of VR18. (C) Percentage release of LDH enzyme from PAO1 infected and VR18 treated cells compared with positive control. (D) (i-iii) The *ex vivo* infection model of PAO1 was performed using the human corneas where the infected cornea showed an opaque condition but the VR18 treated cornea showed quite transparent appearance similar to the control set. (D) (iv) The CFU/ml count showed a drastic change in presence of VR18. (E) (i-iii) *in vivo* keratitis infection model where *P. aeruginosa* PAO1 was used as the causative agent. The control untreated eye showed clear cornea (i), the PAO1 infected eye showed severely opaque cornea (ii), The iris and lens and the VR18 (50 μM) treated eye showed moderately opaque cornea where iris and lens are still detectable (iii). (E) (iv) The CFU of PAO1 cells obtained after the treatment. (* $P < 0.01$. ** $P < 0.001$. N.S- Not significant).

The efficacy of the peptide was further determined using our *ex vivo* infection model [226,245] using human cadaveric corneas. The corneas were scratched and infected with 10^5 CFU/ml of PAO1 in presence or absence of 50 μM VR18 peptide (n=3). 24 h post infection, corneas were washed with PBS, imaged and homogenized and bacterial load was

determined by serial dilutions. There were reduced corneal opacity in corneas treated with the peptide along with significantly reduced bacterial colony forming units (CFU) (Figure 4.9 (D) (i-iv)).

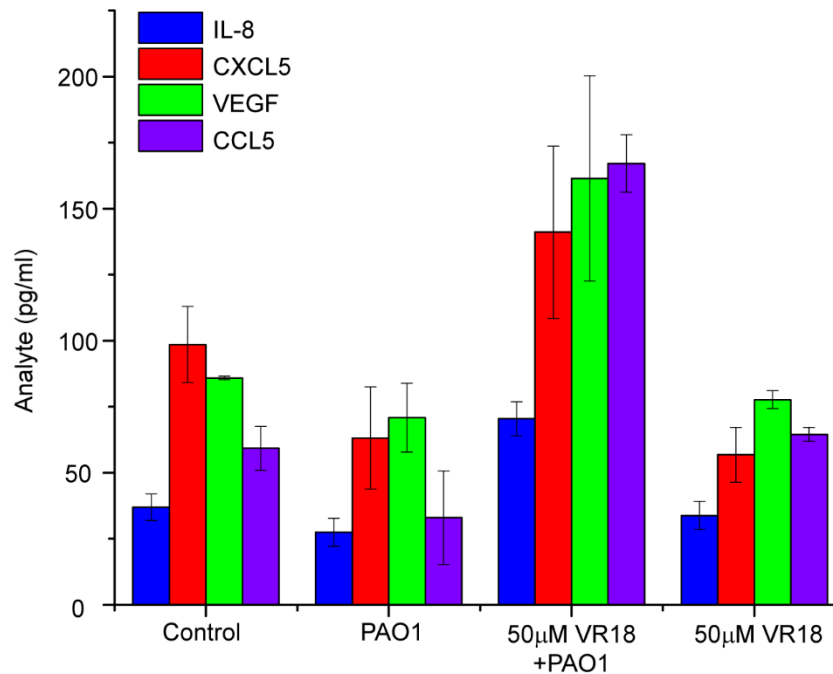


Figure 4.10. The multiplex ELISA profile of the cells infected with PAO1. The chemokines and signaling markers (IL-8, CXCL5, VEGF and CCL5) show downregulation of expression after PAO1 infection which were upregulated in presence of the VR18 peptide.

The effect of VR18 was further determined in *in vivo* using the established murine model of keratitis [226,245] in which corneas of C57BL/6 mice were scratched and infected with PAO1 and treated topically with VR18 (50 µM) at 0, and 6 h post-infection. Animals were euthanized after 24 h and corneas were imaged for opacification, and viable *P. aeruginosa* in whole eyes were quantified by CFU after enucleation. Increased corneal opacity was detected in mice infected with PAO1 (Figure 4.9 (E) (ii)), but significantly less opacity was observed in infected mice treated with VR18 (Figure 4.9 (E) (iii)). Consistent with this data, CFU per eye obtained from VR18 treated corneas were lower than the ones infected with PAO1 (Figure 4.9 (E) (iv)). The efficacy of the peptide was also tested against *P. aeruginosa* 6294 strain *in vivo*, and similar results were obtained (Appendix IV, Figure S4.4.). In the next step, a multiplex ELISA assay was performed to check the effect of the peptide on the inflammatory cytokines or chemokines. Increased secretion of IL-8, CXCL5, CCL5 and VEGF were observed in cells infected with PAO1 in the presence of VR18, indicating its immunomodulatory role (Figure 4.10). This is an interesting finding which

needs to be explored further to reveal the role of the peptide with expression of cell signalling factors in HCEC.

4.3.6. VR18 induces generation of reactive oxygen species (ROS)

The results, thus far, indicate that VR18 interacts with *P. aeruginosa* cells which induces bacterial cell death. However, little is known about how VR18 induces toxicity in *P. aeruginosa*. Previous studies have shown that antimicrobial stress in the presence of antibiotics or AMPs stimulates the generation of intracellular reactive oxygen species (ROS), resulting in bacterial cell death. Hydroxyl radicals, superoxide, hydrogen peroxide, which make up the majority of reactive oxygen species (ROS), cause intracellular damage by oxidizing GTP and CTP pools, as well as causing double-stranded DNA breaks. ROS-induced damage is secondary to the main stress-mediated injury, and this could activate subsequent ROS deposition rounds, resulting in stress-induced bacterial cell death.[228,246] Based on these studies, we hypothesized that VR18 induced toxic effects on *P. aeruginosa* trigger oxidative stress and ROS generation in bacterial cells. To test this hypothesis, we measured the ROS generation in *P. aeruginosa* in the presence of VR18. Interestingly, we found that the application of the VR18 to *P. aeruginosa* loaded with the ROS-sensing dye, CM-H2DCFDA produced a drastic increase in ROS production (Figure 4.11 (A-D)). To further validate this finding, as a control, the membrane-permeable oxidant “tertbutyl hydrogen peroxide (tbH₂O₂)” was applied. This showed an increase in intracellular ROS levels in *P. aeruginosa* while the application of buffer alone did not display any sensitivity towards ROS generation (Appendix IV, Figure S4.5). This observation suggests that the generation of ROS may be the secondary mechanism by which VR18 contributes to the VR18 mediated killing of *P. aeruginosa*. Further, our study showed that topical application of VR18 can significantly reduce keratitis in *in vivo* animal model. This applies that the *in vitro* observations are in direct agreement with clinical observations. Thus, VR18 can be considered as a highly potent therapeutic agent for treatment and management for *Pseudomonas* associated keratitis.

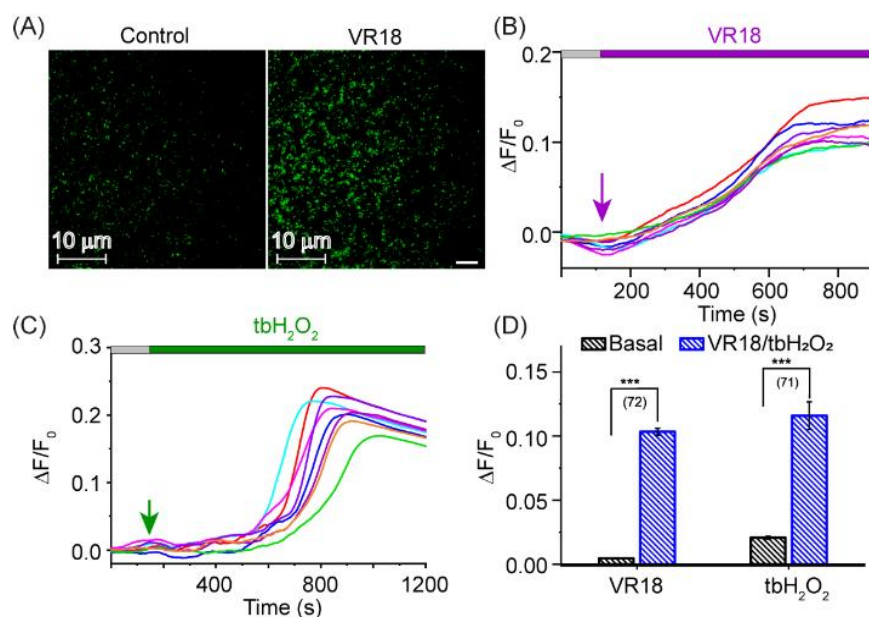
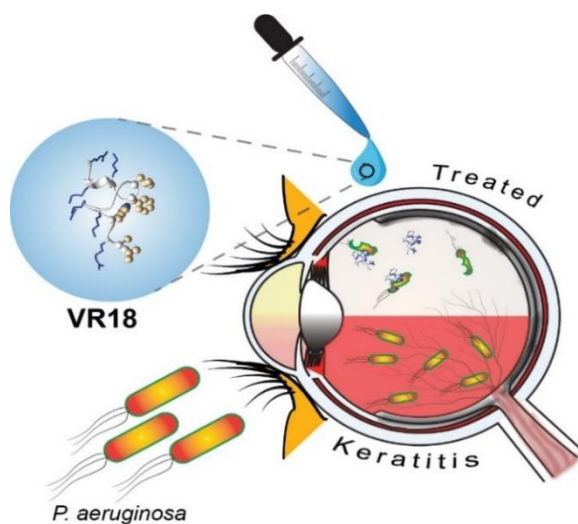


Figure 4.11. VR18 induces ROS generation in *Pseudomonas aeruginosa*. (A) Representative fluorescence microscopy image of *P. aeruginosa* at 100x magnification. *P. aeruginosa* was loaded with ROS sensing dye CM-H₂DCFDA before (left) and after 450 s of VR18 application. (B-C) Representative ROS imaging trace showing an increase in ROS level upon application of VR18 (B) and tbH₂O₂ (C). Each ROS imaging trace shown in (B, C) represents average fluorescence intensity of ~20-50 *P. aeruginosa* bacteria (D) Bar graph analysis of data shown in (B) and (C) depicting the maximum ROS generation after VR18 and tbH₂O₂ application. Statistical indicators reflect the t-test, measuring for an effect of VR18 and tbH₂O₂ on ROS production: ***P < 0.0001. The parentheses number in (D) represents the ROS imaging trace obtained from 2-3 independent measurements. Scale bar: 10 μm.

4.4. Conclusion

In summary, the hybrid antimicrobial peptide VR18 has high potency against *Pseudomonas aeruginosa* clinical isolates supported by *in vitro* experiments. The results of the *in vivo* studies are in agreement with the *in vitro* measurements. The biophysical analysis and the dynamics of the VR18 peptide indicate membrane specificity towards the microbial membrane over the mammalian membrane. Together with our previous report, it can be concluded that the mode of action of the VR18 peptide is through membrane lysis via an electrostatic interaction with negatively charged lipids and subsequent hydrophobic interactions. This mediates pore formation in the microbial cells as observed in the dye leakage assay and vesicle disruption in phase contrast microscopic analysis. We further tested its modes of action using live-cell NMR, Raman spectroscopy and sparsely tethered bilayer lipid membranes. We have also shown that VR18 has little toxicity against human

corneal epithelial cells. As VR18 has high potency against *Pseudomonas aeruginosa*, as shown by *in vitro*, *ex vivo* and *in vivo* experiments, we conclude it has the potential to be used clinically for the treatment and prevention of corneal keratitis.



4.5. Appendix IV

Table S4.1. The *E. coli* Total Extract Phospholipid Profile derived from the website of Avanti polar Lipids.

<https://avantilipids.com/product/100500>

<i>E. coli</i> Total Extract Phospholipid Profile	
Component	wt/wt %
PE	57.5
PG	15.1
CA	9.8
Unknown	17.6
Total	100.0

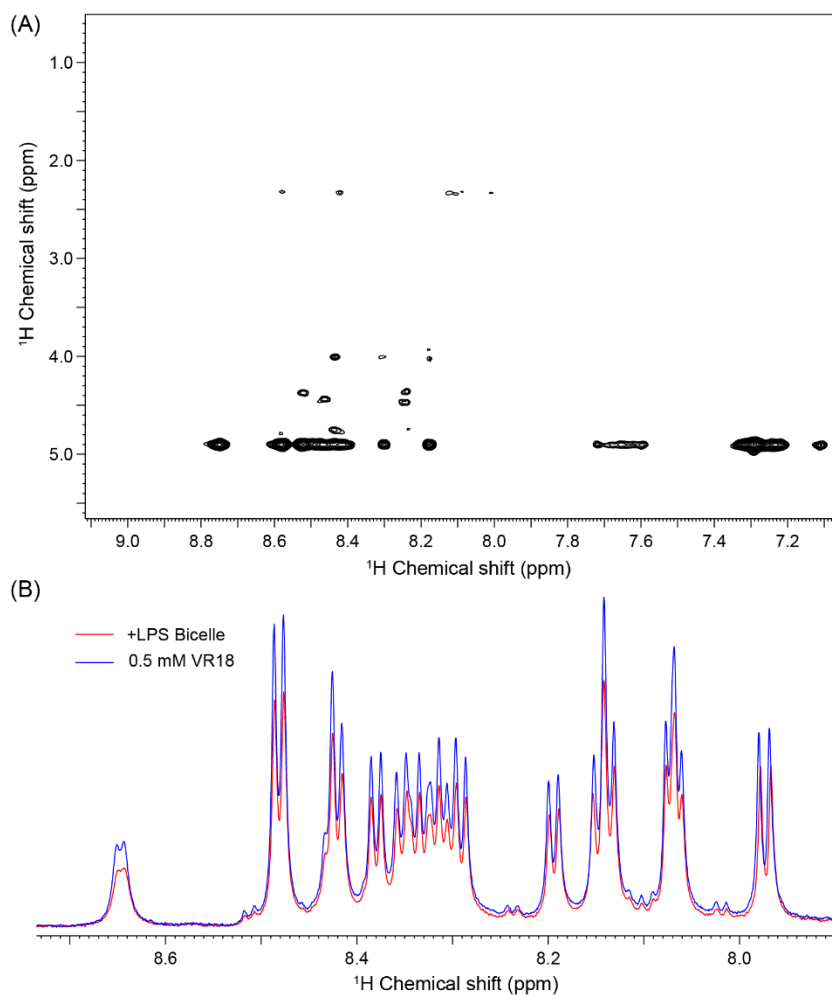


Figure S4.1. Free NOESY spectrum of VR18 peptide (A). The one-dimensional proton NMR (^1H) spectrum of 0.5 mM free VR18 (blue) peptide and the final peak broadening (red) of the spectrum after addition of *P. aeruginosa* LPS bicelle.

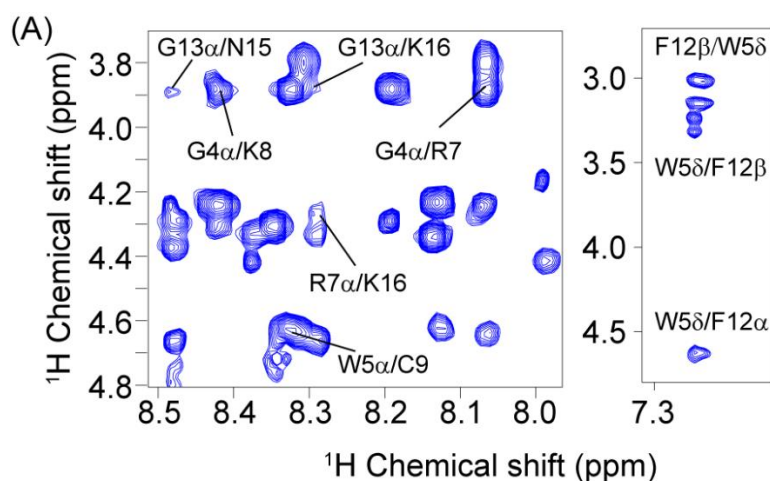


Figure S4.2. Two-dimensional medium range cross peaks in the *tr*NOESY spectrum of VR18 in presence of the LPS bicelles.

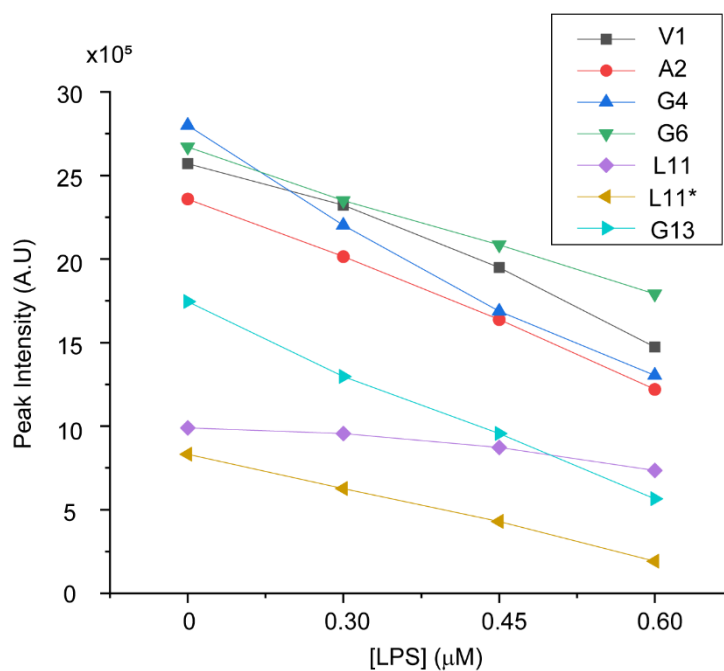


Figure S4.3. 2D ^1H - ^{15}N sofast-HSQC amide peak intensities of ^{15}N labeled amino acids vs concentration of LPS plot showing concentration-dependent broadening of the cross-peaks. Leu-11* indicates the minor HSQC cross-peak of Leu-11.

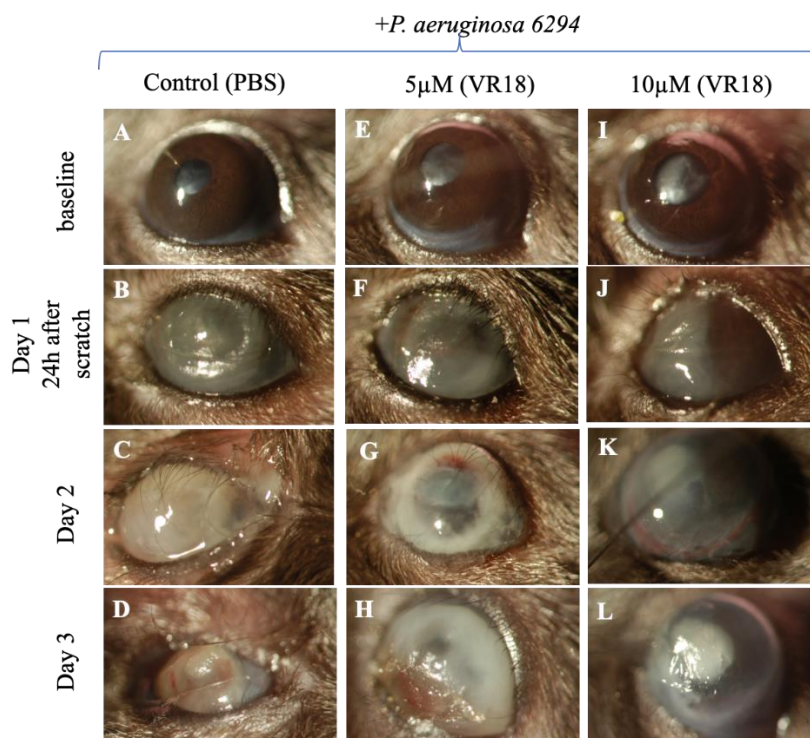


Figure S4.4. *in vivo* keratitis infection model where *P. aeruginosa* 6294 was used as the causative agent. The control untreated eye showed clear cornea (A), the 6294 infected eye showed severely opaque cornea (B-D), The iris and lens of the VR18 (10 μ M) treated eye showed mild improved and opaque cornea where iris and lens are still detectable (F-L).

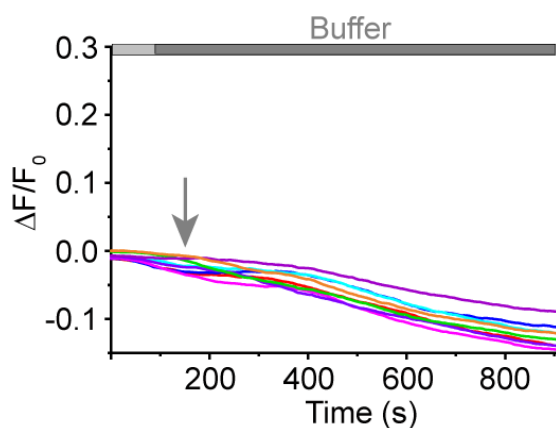


Figure S4.5. Tyrode's solution did not induce ROS generation in *Pseudomonas aeruginosa*. Representative ROS imaging trace showing no change in ROS level upon application of buffer (Tyrode's solution).

Chapter V

5. Application of Tungsten Disulfide Quantum Dot-Conjugated Antimicrobial Peptides in Bio-Imaging and Antimicrobial Therapy

This chapter has been adapted from the following publication:

Mohid, S.A., Ghorai, A., Ilyas, H., Mroue, K.H., Narayanan, G., Sarkar, A., Ray, S.K., Biswas, K., Bera, A.K., Malmsten, M. and Midya, A., **2019**. Application of tungsten disulfide quantum dot-conjugated antimicrobial peptides in bio-imaging and antimicrobial therapy. *Colloids and Surfaces B: Biointerfaces*, 176, pp.360-370.

5.1. Introduction

Fluorescence and photoluminescence are powerful techniques, widely used in biological and biochemical experiments via microscopy and spectroscopy [247-249]. Key advantages of these techniques include typically high sensitivity, as well as compatibility with non-invasive and non-destructive protocols, the latter key for live cell and *in vivo* imaging [250]. Unfortunately, numerous fluorophores are prone to photobleaching [251], while others have quantum yields sensitive to quenching [252,253], and/or to ambient dielectric properties [254,255]. Fluorescent proteins, such as Green Fluorescence Protein (GFP), on the other hand, suffer from disadvantages related to their bulky size [256,257]. Considering advantages relating to high sensitivity and photostability, optical nanomaterials have received considerable attention in material science and nanomedicine, e.g., in diagnostics and drug delivery, as well as in their theranostic combinations [258-260]. Among such nanomaterials, quantum dots (QDs) prepared from II/VI and IIIA/V semiconductors have received particular recent attention [261]. In this context, low-dimensional inorganic transition metal dichalcogenides (TMDC), consisting of triatomic building blocks (MX_2 , where $\text{M} = \text{Mo}$ or W , and $\text{X} = \text{S}$ or Se), represent a new and promising class of semiconducting materials, which are environmentally benign, highly fluorescent, and optically stable [262]. MoS_2 and WS_2 QDs are two members of TMDCs, sharing key properties such as small size (1-6 nm), high fluorescence intensity (20-30 times higher than organic dyes), and size-tunable emission. The broad range of excitation wavelength and the narrow emission of these QDs permit large Stokes shifts, which are advantageous in tissue imaging and for increased signal-to-noise ratio [263].

The aim of the present study was to investigate the use of such QDs as microbe-targeting fluorescent probes in conjugation with rationally designed antimicrobial peptides (AMPs) for potential use in antimicrobial therapy and diagnostics. The upsurge in multidrug resistance (MDR) against conventional antibiotics, during the last few decades in particular, has considerably enhanced the interest in AMPs [24,264-268], as well as in the use of various inorganic nanomaterials as antimicrobial agents [258]. As a result of this, efforts have been undertaken to design AMPs with enhanced potency, improved selectivity, and increased chemical and proteolytic stability [269-272]. Extending on such previous studies, we designed two hybrid AMPs, KG18 (KNKSRVARGWGRKCPLFG) and VR18 (VARGWGRKCPLFGKNKSR) from the parent peptides VG13P (VARGWGRKCPLFG) and WR17 (WKLLSKAQEKFGKNKSR) (Scheme 4.1), respectively, as previously described in the chapter 4. These chimeric third generation peptides display increased and broad-spectrum activity compared to their parents [215,229]. Conjugation of ultra-small WS₂ QD to these peptides was here performed in an effort to further increase their potency. The conformational arrangement of the conjugated peptides was investigated in detail by solution NMR, and linked to the interaction of the conjugates with both model lipid and bacterial membranes. Studies further addressed biological consequences of such interactions in terms of cell toxicity, as well as antimicrobial effects against both planktonic and biofilm pathogens, *Pseudomonas aeruginosa* (*P. aeruginosa*) and *Candida albicans* (*C. Albicans*). These two opportunistic pathogens are responsible for causing deadly infections, e.g., at intensive care units, for surgical patients, and for immunocompromised individuals suffering from AIDS, cancer, and cystic fibrosis [273,274]. From these combines studies, atomistics details were elucidated, which correlate with the functional attributes of the conjugated peptides. Furthermore, localization of the conjugates inside microbial cells was demonstrated, allowing imaging of the same.

5.2. Materials and methods

5.2.1. Reagents

P. aeruginosa serotype-10 lipopolysaccharide (LPS), Polymyxin B (95% pure) and Triton X-100 (95% pure), were obtained from Sigma Aldrich Co. (St. Louis, USA), while deuterium oxide (D, 99.9% with 99.5% purity) was from Cambridge Isotope Laboratories, Inc. (Tewksbury, USA). All bacterial and fungal media were obtained from Himedia Laboratories Pvt. Ltd., Mumbai, India.

5.2.2. Microbial Strains

P. aeruginosa (ATCC 27853) was obtained from ATCC (USA), while the fungus *Candida albicans* (*C. albicans*) SC5314 was provided by Prof. Kaustuv Sanyal, JNCASR, India.

5.2.3. Media Composition and Culture Condition

P. aeruginosa was grown and maintained in nutrient broth by incubating overnight at 37 °C under gentle shaking conditions (180 rpm). *C. albicans* was grown and maintained in YPD broth (1% yeast extract, 1% peptone, and 2% dextrose) by incubating overnight at 28 °C under gentle shaking. M63 minimal media (2.0 g (NH₄)₂SO₄, 13.6 g KH₂PO₄, 0.5 mg FeSO₄·7H₂O, 1 ml 1 M MgSO₄, and 10 ml 20% glycerol in 1.0 liter of MilliQ H₂O, to which 5 ml 20% Casamino acid was added) was used to produce *P. aeruginosa* biofilm, while RPMI 1640 media, without fetal bovine serum (FBS), and antibiotic was used for the formation of *C. albicans* biofilm, following the same culture condition and temperature [275,276].

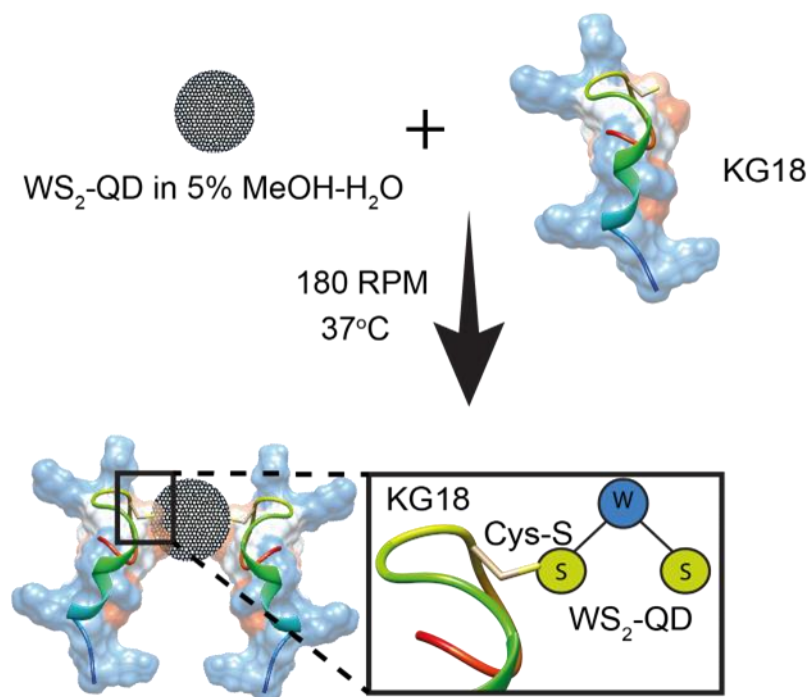
5.2.4. Synthesis Protocol

5.2.4.1. Antimicrobial peptides synthesis

KG18 (KNKSRVARGWGRKCPLFG) and VR18 (VARGWGRKCPLFGKNKSR) peptides were initially obtained from GL Biochem (Shanghai, China) with 95% purity. Later they were synthesized by Fmoc solid-phase peptide synthesis chemistry [120] using an automated peptide synthesizer (Aapptec Endeavor 90, Louisville, KY, USA). The crude peptides were purified by reverse phase HPLC system (LC-20AT, SHIMADZU, Kyoto, Japan) using Phenomenix C₁₈ column. The respective peptide fractions were collected and lyophilized. The molecular weight and purity of the peptides were confirmed by MALDI-TOF and NMR analysis, respectively. The calculated and actual molecular weight obtained for both the peptides was 2060.44 and 2060.47, respectively. The purified peptides (>98% purity) were dissolved either in sterilized Millipore water or in phosphate buffer (pH 7.4) and filter sterilized.

5.2.4.2. Synthesis of tungsten disulfide (WS₂) quantum dots

WS₂ quantum dots were synthesized in IIT Kharagpur, India, using lithium intercalated WS₂ nanosheet in dimethylformamide (DMF) solution, as described in detail elsewhere [277]. After bath sonication for 6 h, WS₂ nanosheet samples were centrifuged at 14,000 rpm for 10 min at 25 °C and the supernatant containing WS₂ quantum dots was collected. The WS₂ quantum dots thus obtained were of 2-3 nm in average size.



Scheme 5.1: Schematic illustration showing WS_2 interaction with KG18 through sulfhydryl group, confirmed by 2D 1H - ^{13}C HSQC or mass spectrometry (Figure 5.1). VR18 interacts with WS_2 -QD in a similar manner via the sulfhydryl group of Cys9 residue.

5.2.4.3. Conjugation of WS_2 with AMPs

WS_2 QD was dissolved in DMF and then exchanged with water by centrifugation at 20,000 rpm for 10 min and at 25 °C. The precipitate containing WS_2 QD was collected and re-dispersed in 5% methanol-water. This process was repeated several times until DMF was removed completely, followed by filter sterilization using 0.2 μm filter to obtain particles of uniform size. Finally, a 2 mM solution of the respective AMP (KG18 / VR18) was incubated with filter sterilized WS_2 QD (0.2 mg/ml) in a 1:1 vol/vol ratio and incubated at 37 °C for overnight under mild shaking to give a 1 mM stock solution of WS_2 -peptide conjugate (Scheme 5.1). The final concentration of the mixture was calculated by the following equation:

$$\text{Final concentration (mg/ml)} = (M_A V_A + M_B V_B) / (V_A + V_B)$$

Where, M stands for concentration and V stands for volume.

5.2.5. Physical Characterization of WS_2

5.2.5.1. Dynamic Light Scattering (DLS) Analysis

DLS analysis was performed using a Malvern Zetasizer, series-Nano S (Malvern Instruments, Malvern, UK) equipped with 4 mW He-Ne laser of 633 nm wavelength and a

fixed back scattering angle of 173°. 100 µM of the respective WS₂-AMP conjugated sample was dissolved either in filtered degassed water (Refractive Index: 1.33, Viscosity (cP): 0.88) or in 10 mM Tris-HCl buffer with 150 mM NaCl. The DLS experiment was performed for 10 scans after 120 sec equilibration time. The refractive index and absorption were set to 1.45 and 0.001, respectively.

5.2.5.2. Matrix-Assisted Laser Desorption Ionization (MALDI) analysis

MALDI analysis was performed on a Bruker MALDI TOF instrument (Model–Autoflex speed, Bruker Daltonics GmbH, MA, USA) equipped with Smart beam II laser technology (2 KHz solid state laser). 100 µM solution of the respective WS₂-AMP conjugate was mixed with α-Cyano-4-hydroxycinnamic acid (α-HCCA) in 1:1 (vol/vol) ratio and air dried. The data was collected and analyzed with POLYTOOLS v2.0 software (Bruker Daltonics GmbH, MA, USA).

5.2.5.3. High-Resolution Transmission Electron Microscopy (HR-TEM)

Samples containing 100 µM solution of the respective free AMPs, WS₂-AMP conjugates, or 0.2 mg/ml WS₂ QD were placed on a carbon coated copper TEM grid (TED PELLA Incorporation, Redding, CA, USA) and air dried overnight in a laminar airflow workstation. Samples were then observed under a high-resolution TEM (HR-TEM) instrument (JEOL Inc., MA, USA) at 200kV voltage.

5.2.5.4. Photoluminescence (PL) and PL Decay

Photoluminescence (PL) spectroscopy of WS₂ QD and WS₂-AMP conjugates were performed under the illumination of 376.6 nm laser light. For WS₂ quantum dot solution, a single strong peak at 478 nm was observed due to strong quantum confinement, whereas the peak intensity was lower for WS₂-AMP conjugates. Additionally, a slight blue shift was observed, indicating a charge transfer from WS₂ QD to the peptides, also supporting conjugate formation. Further, for better understanding the charge transfer mechanism, we performed time-resolved PL decay of the samples at 470 nm. The experimental data were fitted exponentially, and decay times calculated for both free WS₂ QD and WS₂-conjugated AMPs using Origin software (Origin Pro. V8.0, MA, USA).

5.2.5.5. Fluorescence quantum yield calculation

The photoluminescence quantum yield (PLQY) of WS₂, WS₂-KG18 and, WS₂-VR18 was calculated using the following equation:

$$\Phi_x = \Phi_{ST} \left(\frac{Grad_x}{Grad_{ST}} \right) \left(\frac{\eta_x^2}{\eta_{ST}^2} \right)$$

Where, Φ_x is the PLQY of the sample and Φ_{ST} is the PLQY of Rhodamine B (RhB; 31% in water). Grad_x and Grad_{ST} are the gradient of the absorbance versus area under the curve of PL measurement of all the samples and RhB, respectively. H_x and η_{ST} are the surface tension of the solvent, where WS_2 QDs, WS_2 -AMPs and RhB (standard) are dissolved, respectively.

5.2.5.6. Thermal analysis

Composition of the WS_2 -conjugated peptides were calculated using Thermo-Gravimetric and Differential Thermal Analyzer (TG-DTA) equipment (Perkin Elmer Pyris Diamond TG-DTA, US). The analysis was done using alumina pans under inert N_2 atmosphere (flow rate 50 ml/min). The analyses were performed from 30 to 700 °C with a heating rate of 10 °C/ min.

5.2.6. Biological Assays

5.2.6.1. Broth microdilution assay with AMPs, WS_2 QD and WS_2 -AMP conjugates

To determine the minimum inhibitory concentration ($\text{MIC}_{99\%}$), a modified broth microdilution assay was employed, as previously described [215]. In brief, mid-log phase cultures of the respective strains were pelleted down by centrifuging at 8,000 rpm for 10 min, washed twice with 10 mM sodium phosphate buffer, pH 7.4, and re-suspended in the same to obtain a final cell suspension of 10^6 cells/ml. 50 μl of this cell suspension (5×10^5 CFU/ml) was added to a series of dilutions of the respective free and WS_2 -conjugated peptides (ranging from 1 to 100 μM) in a sterile 96-well micro titer polypropylene plate (Tarsons Products Pvt. Ltd., Kolkata, India) and incubated for 3 h at 37°C and 28°C for *P. aeruginosa* for *C. albicans*, respectively. A negative control containing only cells and a positive control containing 100 μM Polymyxin B, were also included. After incubation, 200 μl of the respective media was added to each well and incubated overnight to allow cell growth. Absorbance at 630 nm was used to estimate the $\text{MIC}_{99\%}$, defined as the lowest concentration of peptide that inhibits 99% growth of the microorganisms from initial microbial cell density. $\text{MIC}_{99\%}$ of free WS_2 QD was also determined against *C. albicans* and *P. aeruginosa* cells for 24 h and 48 h. All reactions were performed in triplicate.

5.2.6.2. Minimal Hemolytic Concentration Assay

Fresh human blood was collected in an EDTA vial and centrifuged at 8000 $\times g$ for 10 min at 25°C to obtain red blood cell (RBC) pellets. The Bose Institute Research Ethics Committee approved this study and a certified medical professional was present during the blood collection. The pellets were washed thrice with 10 mM phosphate buffer saline (PBS,

pH 7.4) and serially diluted to obtain a final suspension containing 2×10^8 RBC/ml. 50 μ l of the cell suspension was incubated with equal volume of increasing concentrations of either free peptides, WS₂-AMP conjugates, or free WS₂ QD (up to 100 μ M) and incubated at 37 °C for 1 h under shaking. The samples were then centrifuged at 8000 \times g for 10 min at 25°C and the absorbance of the supernatant read at 414 nm to quantify RBC lysis and heme release. A positive control containing RBC treated with 2% Triton X-100 was also included, against which data from all other samples were normalized. All experiments were performed in triplicate.

5.2.6.3. Cytotoxicity Assay

Cell cytotoxicity was measured in the Division of Molecular Medicine, Bose Institute, India, using the MTT cell proliferation assay reagent (Himedia Laboratories Pvt. Ltd., Mumbai, India) according to the manufacturer's protocol. Briefly, WI38 cells (5×10^4 cells per well) were treated for 24 h with varying concentrations of the respective peptides in serum-free media, following which cells were processed for MTT assay and incubated for 3 h with 0.5 mg/ml of MTT at 37 °C. Cells were then washed with 1 \times PBS, followed by addition of 1ml DMSO to dissolve the formazan crystal, and absorbance was measured at 570 nm. Doxorubicin was used a positive control for all the experiments, which were all performed in triplicate.

5.2.6.4. Scanning Electron Microscopy (SEM)

Cultures of *P. aeruginosa* and *C. albicans* cells, grown overnight, were used to obtain mid-log phase cultures. The cell suspension was pelleted at 8000 rpm for 10 min. Cell pellets were washed twice with 10 mM phosphate buffer, pH 7.4, and re-suspended in the same buffer to a final O.D₆₃₀ of 0.01. The cell suspensions were treated with KG18 and WS₂-KG18 peptide at their MIC_{99%} concentration determined for different time periods between 5 min and 60 min at 37 °C. Next, the cells were fixed with 4% (v/v) glutaraldehyde, and 15 μ l of the respective cell suspension spotted on 0.1% (v/v) poly L-lysine-coated glass slides and kept overnight at 4 °C. The smears were washed twice with phosphate buffer and dehydrated by washing with a graded ethanol series (30%, 50%, 70%, 90% and 100%) for 15 min each. The slides were subsequently air dried, followed by gold coating, and observed by SEM (FEI, QUANTA 200, Oregon, USA).

5.2.6.5. Confocal Microscopic Analysis

Overnight cultures of *C. albicans* SC5314 were harvested by centrifugation, washed twice with 10 mM phosphate buffer, pH 7.4, and re-suspended in the same buffer to obtain

a suspension of 10^6 cells/ml. 100 μ l of this suspension was incubated with a sub-lethal dose (2 μ M) of FITC-KG18 and WS₂-KG18 at 37 °C for 1 h. At different time points, 20 μ l of the treated cells were removed, processed by washing, loaded on a glass slide, and mounted with DPX (Sigma-Aldrich, St. Louis, MO). Samples containing only WS₂ suspension were included as control. Fluorescent and differential interference contrast images were captured with a 488 nm band-pass filter corresponding to the excitation wavelength of FITC and a 405 nm band-pass filter for excitation of WS₂ QD using a TCS SP8 confocal microscope (Leica, Wetzlar, Germany) at a magnification of 63 \times (oil immersion). Acquisition Suite X software (Leica, Wetzlar, Germany) was used for capturing and analysis of images.

5.2.6.6. Time-kill kinetics assay by spread plate method

To determine the time required for killing the fungal cells, a kinetic assay using spread plate technique was employed [278]. Mid-log phase cultures of *C. albicans* cells were pelleted down by centrifuging at 8000 rpm for 10 min, washed twice with 10 mM sodium phosphate buffer, pH 7.4, and re-suspended to obtain a final cell suspension of 10^5 CFU/ml. 100 μ l of total reaction volume was set in a 96 well plate where cells were treated with MIC concentration at different time points with 5 min interval (starting from 0 min to 60 min). After every time point, all cells were centrifuged at same rpm mentioned above. The supernatant was removed, and the pellet was re-suspended in 5 μ l buffer. Subsequently, the whole volume was taken and spread plating was done on YPD agar containing petri dishes (Tarsons Products Pvt. Ltd., Kolkata, India). All plates were incubated for overnight at 28 °C. Next day the number of single colonies was counted to calculate the kinetics. Measurements were performed in triplicate.

5.2.6.7. Minimum Biofilm Eradication Concentration (MBEC) Assay

5.2.6.7.1. MBEC for *P. aeruginosa* biofilm

MBEC assay for *P. aeruginosa* biofilms was carried out as previously reported [279,280]. Briefly, mid-log phase culture of *P. aeruginosa* cells ($O. D_{630} = 0.5$), obtained from an overnight culture of stationary phase cells were used in this assay. Cells were pelleted down by centrifuging at 8000 rpm for 10 min, washed twice with 10 mM phosphate buffer, pH 7.4, and re-suspended in the same buffer to obtain a final concentration of 10^5 CFU/ml. 2 ml M63 minimal media was added to each well of a sterile 6-well plate, covered by grease-free coverslips. Next, the cells were added in each well and left overnight at 37 °C under mild shaking to allow biofilm formation. After mature biofilm formation, the coverslips were washed thoroughly with 10 mM sodium phosphate buffer, pH 7.4, to

remove the planktonic cells and placed in a new sterilized 6-well plate. Free peptide and their WS₂-AMP conjugates were added with increasing concentration up to 200 μ M and incubated for 4 h at 37 °C under shaking condition. Next, the cells were allowed to regenerate in presence of 1 \times M63 media, subsequently maintaining them under the same culture conditions. Positive and negative controls were prepared by adding 200 μ M Polymyxin B and 10 mM Phosphate buffer (pH 7.4), respectively to same concentrated cells. The experiments were performed in triplicate.

5.2.6.7.2. MBEC for *C. albicans* biofilm

Minimum biofilm eradication concentration (MBEC) assay for *C. albicans* biofilms was carried out as described in the literature [276]. Briefly, mid-log phase *C. albicans* cells (O.D₆₃₀= 0.5) obtained from an overnight culture of stationary phase cells in YPD media were pellet down by centrifuging at 8000 rpm for 10 min, washed twice with 10 mM sodium phosphate buffer, pH 7.4, and re-suspended in the same buffer to obtain a final concentration of 10⁷ cells/ml. 400 μ l total reaction volume was set in a sterile 24-well plate. After treatment, equal volume of RPMI 1640 was added to each well and incubated at 28 °C under shaking condition for 96 h to obtain mature *C. albicans* biofilm. The mature biofilm was treated with increasing concentration of WS₂-AMP conjugates and incubated for 4 h at 28 °C. Positive and negative controls were prepared by adding 200 μ M Polymyxin B and 10 mM phosphate buffer, pH 7.4, respectively. The experiments were performed in triplicate.

Coverslips with both biofilms were washed gently for five times to remove any non-adherent cells. The cells were then stained using 0.1% crystal violet solution for 10 min and washed thoroughly with water before observing under an optical microscope (Leica Microsystems, Wetzlar, Germany) at 400 \times magnifications. Quantification of both *P. aeruginosa* and *C. albicans* biofilms was performed in sterile 96-well plates. Matured biofilms were obtained using the above-mentioned protocol. A series of dilution (25-400 μ M) of peptides and WS₂ QD was evaluated, using 200 μ M Polymyxin B as positive control. The Conjugate-treated biofilms were then quantified using crystal violet staining [281] to measure the biofilm biomass. Crystal violet stain taken up by the mature biofilm was solubilized using 30% acetic acid and its absorbance measured at 550 nm. To evaluate the viability of *C. albicans* biofilm, MTT-based cell proliferation assay was performed as described earlier [282]. Measurements were performed in triplicate.

5.2.7. Circular Dichroism (CD) Analysis

Circular dichroism (CD) analysis of the free peptides and their WS₂ conjugates (final concentration of 25 μ M) in *P. aeruginosa* LPS (at 1:1, 1:2, and 1:3 ratios) was performed with a JASCO 815 spectrophotometer (Jasco, MD, USA) by dissolving the samples in 10 mM phosphate buffer (pH 7.4). Spectra were scanned from 190 to 260 nm, recorded thrice at 25 °C for each experiment in a cuvette of 0.1 cm path length.

5.2.8. NMR Spectroscopy

5.2.8.1. Sample Preparation and Data Acquisition

All NMR experiments were carried out at 298K either on a Bruker Avance III 500 MHz NMR spectrometer (equipped with a 5 mm SMART probe) or Bruker Avance III 700 MHz NMR spectrometer (equipped with a 5 mm cryoprobe). NMR samples were prepared in 10% deuterated water, pH 4.5, using 3-(trimethylsilyl)-2,2,3,3-tetradeuteriopropionic acid (TSP) as an internal standard (0.00 ppm). Two-dimensional ¹H-¹H total correlation spectroscopy (2D TOCSY) and two-dimensional ¹H-¹H Nuclear Over Hauser Spectroscopy (2D NOESY) were recorded for the free peptides and their WS₂ conjugates, with a mixing time of 80 ms and 150ms, respectively, and a spectral width of 11 ppm in both dimensions. Next, the interaction of the peptides upon successive titration with *P. aeruginosa* LPS was monitored by 1D proton NMR, acquired using excitation-sculpting scheme for water suppression and the States-TPPI for quadrature detection in the t1 dimension [283]. Consequently, 2D *transferred* NOESY (*tr*NOESY) spectra of the peptides in the context of LPS were acquired with two different mixing times 100 and 150 ms. Data processing and analysis were carried out using TopspinTM v3.1 software (Bruker Biospin GmbH) and Sparky software, respectively [124].

One-dimensional (1D) live cell ¹H NMR experiments were performed with 1 mM WS₂-conjugate peptides dissolved in 10 mM phosphate buffer, pH 6.5, containing 10% D₂O. Overnight stationary phase *C. albicans* cells were sub-cultured to obtain log-phase cells of *C. albicans*. The cells were collected by pelleting at 5500 rpm for 5 min and then washed twice with the same buffer to obtain a final cell concentration of O.D₆₃₀ =1. For these, 1D ¹H NMR spectra of the WS₂ peptide conjugates and the cell suspension in phosphate buffer (pH 6.5) were recorded separately as control

A series of 1D ¹H NMR spectra were also recorded after addition of the peptide solution to the cell suspension. Cells in the NMR tube were monitored every 15 min for

precipitation and mixed thoroughly to prevent sedimentation. New peaks were instantly observed as early as 5 min of incubation due to metabolites efflux from the cells.

Two-dimensional ^1H - ^{13}C heteronuclear single quantum coherence (HSQC) NMR analysis was performed using the standard pulse sequences, using a spectral width of 12 ppm (^1H) and 236 ppm (^{13}C). The peptides and their WS_2 conjugates were dissolved in 100% D_2O at 25 °C. ^1H was referenced to TSP and ^{13}C was referenced by using the indirect referencing procedure [284].

^{31}P NMR experiments were conducted to observe the interactions between WS_2 -conjugated KG18 and VR18 with *P. aeruginosa* LPS. A series of one-dimensional ^{31}P NMR spectra of LPS were collected using 0.2 mM of LPS in water at pH 4.5, along with QD-conjugated peptides, using concentrations that of 0.05, 0.1, 0.2, and 0.4 mM. The data was recorded at 298K on a Bruker Avance III 500 MHz spectrometer.

5.2.8.2. NMR-Derived Structure Calculation

Three-dimensional solution structure of the WS_2 -conjugated peptides in LPS were determined by following the procedures described previously [44]. Briefly, the volume integrals of their respective NOE cross-peaks were qualitatively differentiated into strong, medium, and weak, depending on their intensities in the *tr*NOESY spectra [125]. This information was further transformed to inter-proton upper bound distances of 3.0, 4.0, and 5.0 Å for strong, medium, and weak peaks, respectively, while the lower bound distance was fixed to 2.0 Å. The backbone dihedral angles of the peptides, phi (φ) and psi (ψ) were kept flexible (-30° to 120° and 120° to -120° , respectively) for all non-glycine residues to limit the conformational space. CYANA v2.1 was used for all structure calculations with iterative refinement of the structure based on distance violation [179]. Hydrogen bonding constraints were excluded from structure calculation. NMR-derived ensemble structures were analyzed using PyMol and Chimera. PROCHECK NMR was used to check the stereochemistry of the structures [225].

5.2.9. Ion channel formation assay using patch clamp technique

Bilayer membrane (BLM) was formed using diphytanoylphosphatidylcholine (DPhPC; Avanti Polar Lipids, AL, USA) and cholesterol (Sigma-Aldrich, St. Louis, USA), 10:1 wt/wt. The lipids, dissolved in chloroform, were taken in a glass Eppendorf tube. The solvent was removed completely by flushing with nitrogen gas. N-decane was added to obtain a lipid concentration 20 mg/ml. The membrane was formed on the aperture (150 μm diameter) of a polystyrene bilayer cup (Warner Instruments, CT, USA) by panting the lipid,

as described before [285]. Both trans- and cis-compartments had a symmetric solution of 1 M KCl, 5 mM MgCl₂, 10 mM HEPES (pH 7.4). Cis- and trans- chambers were connected with the ground electrode and recording electrode, respectively. Patch clamp amplifier PC-501A (Warner Instruments, CT, USA) was used. The thinning of the membrane was monitored by following the capacitance change. 50-60 µg of peptide or QD or QD-conjugated peptide (dissolved in water) was added to the cis- chamber (volume 1.5 ml) and stirred. Channel incorporation in the BLM was monitored using membrane current in response to different applied voltages. Currents were low-pass filtered at 1 kHz and digitized at 5 kHz using Digidata 1322A (Molecular Probes, USA). pClamp 10.1 software (Molecular devices, CA, USA) was used for data acquisition and analysis. This experiment was done in IIT Madras, India.

5.2.10. Statistics

Experiments were repeated as indicated in each method description above. Origin Pro v8.0 (OriginLab Corporation, Northampton, MA, USA), SigmaPlot v11.0 (Systat Software, Inc., CA, USA), and Kyplot v2.0 beta (KyensLab Inc. Japan) were used for data analysis. Student's t-test for parametric paired values (two sided) was calculated for determination of significance in values where ns, non-significant; *, $p \leq 0.05$; **, $p \leq 0.01$; ***, $p \leq 0.001$.

5.3. Results and Discussion

5.3.1. Preparation of WS₂-AMP conjugates

WS₂ QD were synthesized using lithium-intercalated WS₂ nanosheets in dimethylformamide (DMF) solution [277]. The resulting nanoparticles were then transferred to water containing 5% methanol via solvent exchange and their retained structure confirmed by the appearance of fringe-like pattern in high-resolution Transmission Electron Microscopy (HR-TEM), with a fringe distance of 0.27 nm [263]. The average size of the individual nanoparticles was ~2-3 nm [263,286], obtained from HR-TEM (Figure 5.1 (A)). The QDs were subsequently incubated with the designed antimicrobial peptides, KG18 or VR18, to obtain the peptide-QD conjugates (Scheme 5.1).

5.3.2. Physical characterization of the conjugates

Matrix-assisted laser desorption/ionization (MALDI) mass spectrometry (MS) of free KG18 and WS₂-QD conjugated KG18 showed distinct sharp peaks near m/z ratio of 2064 and 4442 respectively. MALDI analysis of free WS₂-QD showed several peaks at very low m/z ratio depicting its low molecular weight due to ultrasmall size. The MALDI

spectra of free KG18 showed one major peak at 2064 correlating its theoretical mass value and one minor peak at 4135 which corresponds either two peptides or a dimer reached to the MS detector at a time. The WS₂-QD conjugated KG18 peptide showed one single peak at 4442 which is greater than the mass of a dimer. Thus, it can be inferred that two peptide can attach to a single WS₂ QD at a time as shown in Figure 5.1 (B), where the QD-conjugated peptide resulted a more than two-fold mass increase compared to its unconjugated form. In the inset of Figure 5.1 (B) the HR-TEM image of WS₂-QD conjugated KG18 is shown where the fringe pattern of WS₂ remained un-altered before and after conjugation, demonstrating that the internal structure of the QDs does not change on peptide conjugation. In line with the MALDI results, DLS analysis showed that the hydrodynamic radius of free KG18, free WS₂-QD and WS₂-QD conjugated KG18 was 0.7±0.15, 8.44±2.23 and 18.51±6.59 d.nm respectively. In case of VR18 and WS₂-QD conjugated VR18 the hydrodynamic radius was 0.68±0.47 and 8.76±4.63 d.nm respectively. These findings suggests that the conjugation of the peptides with WS₂-QD results in an increased hydrodynamic size in case of WS₂-KG18 but not for WS₂-VR18 as shown in Figure 5.1 (C) and Figure S5.1 (A), Appendix V. Further, thermogravimetric analysis (TGA) supports that the inorganic WS₂ part is found to be 64.35% in WS₂-KG18 and that of 55.70% in WS₂-VR18 (Appendix V, Figure S5.2).

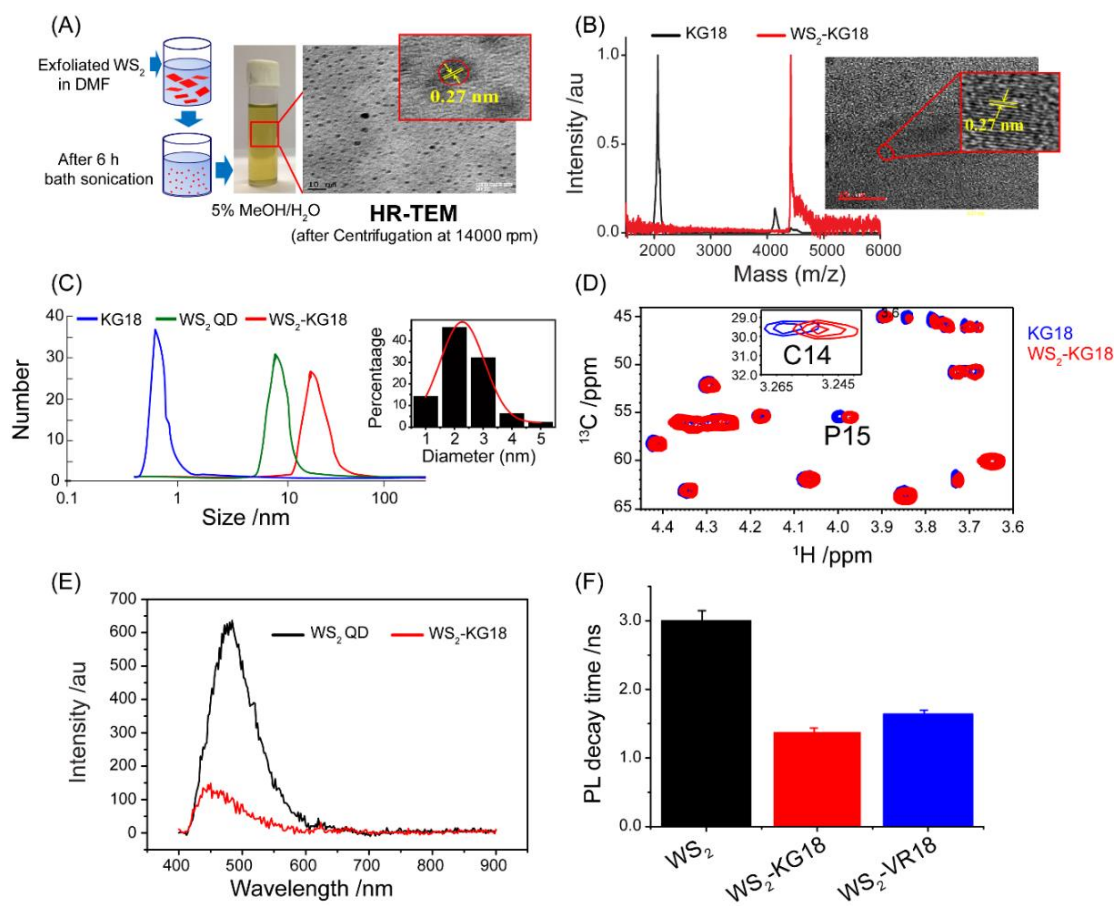


Figure 5.1. Physical characterization of peptide-QD conjugates: (A) Schematic illustration of the synthesis of WS₂-QD, displaying a fringe width of 0.27 nm (inset) in HR-TEM. (B-C) MALDI (normalized plot) and DLS analysis confirmed the formation of QD-KG18 conjugates., while TEM showed WS₂ QD diameters of ~2-3 nm, shown in inset of C. (D) The 2D heteronuclear ¹H-¹³C NMR spectra show chemical shift perturbation in the presence of AMP, suggesting the conjugate formation through Cys14 and Pro15 residues of KG18. € Photoluminescence (PL) and (F) PL decay time also confirmed QD-peptide conjugation via charge transfer from QD to peptide.

In order to better understand the interactions of WS₂ QD with KG18 or VR18, two-dimensional ¹H-¹³C heteronuclear single quantum coherence (HSQC) NMR experiments were next performed. From these, specific chemical shift perturbations were observed for ¹³CβHs of Cys14 (for KG18) or Cys9 (for VR18) and ¹³CδHs of Pro15 (for KG18) or Pro10 (for VR18) for both peptides upon interaction with WS₂ QD (Figure 5.1 (D) and Figure S5.1 (B) (Appendix V). This clearly demonstrated that the interaction is quite specific, whereby the thiol group (-SH) of the Cys residue remained in a favorable position for such conjugation to occur [60]. This was further supported by a slight blue shift and the concomitant intensity decrease observed for WS₂ QD after peptide conjugation, as evidenced by photoluminescence (PL). This indicated charge transfer from WS₂ QD to the

aromatic peptides (Figure 5.1 (E) and Figure S5.1 (C) (Appendix V). The fluorescence quantum yield was calculated for WS₂, WS₂-KG18 and WS₂-VR18 and found to be 3.62%, 2.44% and 2.22%, respectively. Additionally, time-resolved photoluminescence (PL) decay for WS₂ QD, WS₂-KG18, and WS₂-VR18 showed the decay time of free WS₂-QD to be 3.00±0.17 ns, suppressed after conjugation with KG18 and VR18 to 1.39±0.05, and 1.64±0.05 ns, respectively (Figure 5.1 (F) and Figure S5.1 (D) (Appendix V), reporting on the formation of stable QD-AMP conjugates.

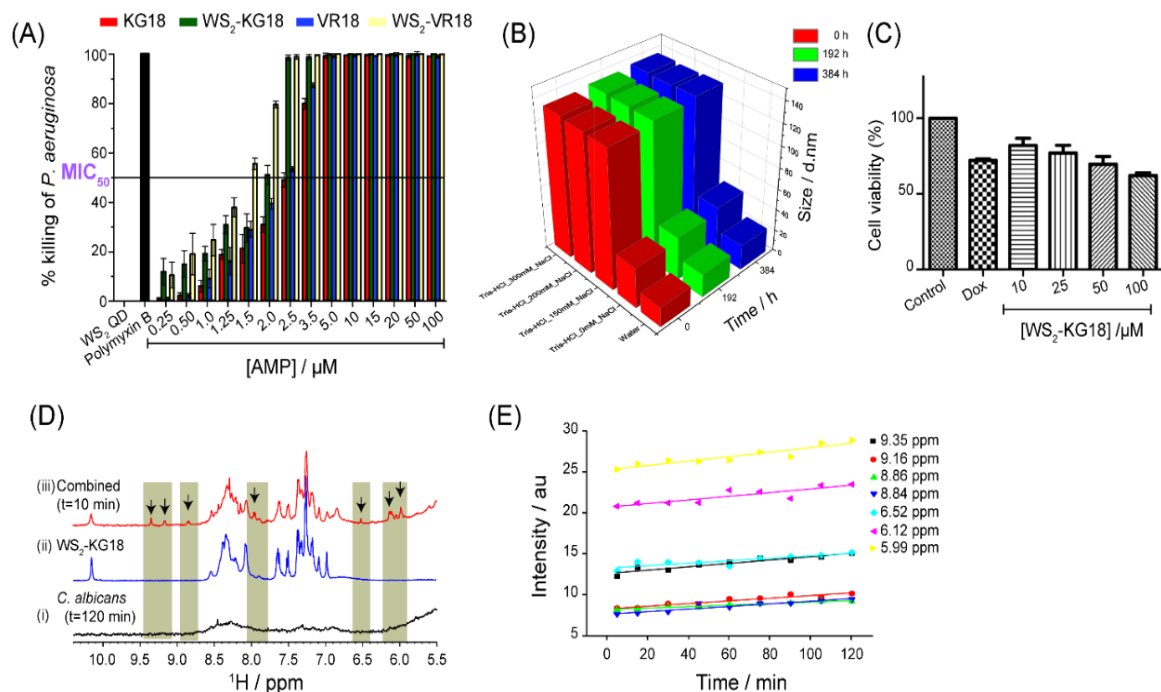


Figure 5.2. Biological activity of peptide-QD conjugates: (A) Histogram plot showing MIC_{99%} values of WS₂-KG18 against *P. aeruginosa*; Polymyxin B (100 μM) and WS₂-QD were used as positive and negative control, respectively. (B) The conjugated peptides WS₂-KG18/ WS₂-VR18 are stable in physiological condition, supported by the single size distribution pattern over time (t = 384 h). (C) The WS₂-KG18/VR18 displayed low toxicity against WI38 cells at their MIC_{99%} concentration. (D) One-dimensional ¹H NMR spectra of (i) *C. albicans* (after 120 min of incubation); (ii) WS₂-KG18 and (iii) WS₂-KG18 in presence of *C. albicans* cells, demonstrating the occurrence of metabolite peaks (indicated by arrows) as early as 10 min after incubation. (E) The intensity of the metabolite peaks in the one-dimensional ¹H NMR spectra, increases with increasing incubation time, illustrating time-dependent membrane disruption and release of intracellular metabolites.

5.3.3. Biological assays

Next, a series of biological assays were performed with KG18 and VR18 peptides along with their WS₂-QD conjugates. Both KG18 and VR18 were potent (MIC_{99%}=5 μM) against *P. aeruginosa* and *C. albicans* (Table 4.1 in chapter 4). In contrast, the parent

VG16KRRP peptide was inactive against *P. aeruginosa* [169]. However, the antimicrobial potency of QD-conjugated KG18 or VR18 was two times stronger than their free peptide counterparts (Figure 5.2 (A) and S5.3 (A), (Appendix V), also against *P. aeruginosa*. In contrast, non-conjugated WS₂ QDs displayed no antimicrobial activity of its own (Figure 5.2 (A)). It is also noteworthy that the WS₂-peptide conjugates and the free counterparts (KG18 or VR18) displayed high selectivity against bacteria and fungi (Figure 5.2 (A) and S5.3 (A) (Appendix V). Of note, the peptides KG18 and VR18 as well as their WS₂ conjugates are not only stable in physiological condition (Figure 5.2 (B) and S5.5, Appendix V), but also, they are non-hemolytic and non-cytotoxic in nature. Figure S5.4, (Appendix V) shows that 5-8% hemolysis was observed using peptide and its QD-conjugates, whereas cell viability assay (Figure 5.2 (C) and S5.3 (B), Appendix V) against normal human lung epithelial cells (WI38) shows that the compounds display low toxicity against human cells at the MIC_{99%} concentration (2.5-5 μM).

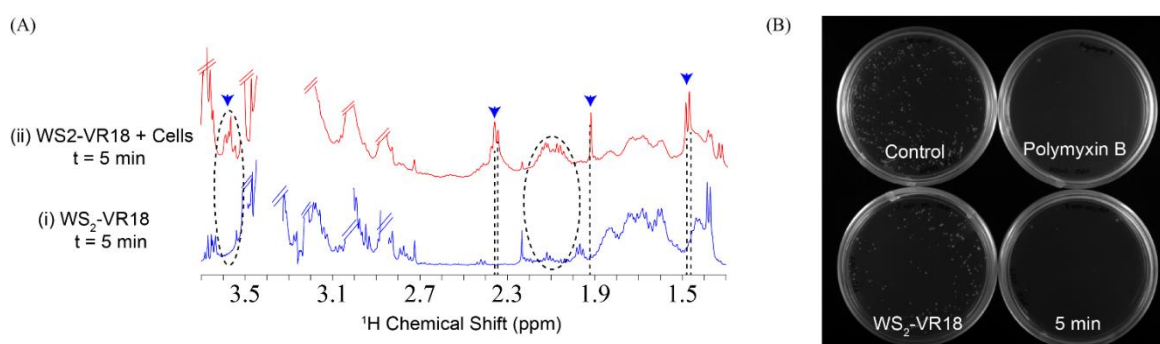


Figure 5.3. (A) The 1D ¹H NMR spectra of (i) free WS₂-VR18 and in (ii) presence of 1 O.D₆₃₀ *C. albicans* cells colored in blue and red respectively. New peaks (marked by arrows) appeared within 10 min of treatment indicating potent antimicrobial activity of WS₂-VR18. (B) Time kinetics plates of WS₂-VR18 after 0 min and 5 min treatment is compared with Negative (no treatment) and positive (100 μM Polymyxin B) control plates. Clear cell killing was observed in WS₂-VR18 treated plates after 5 min of incubation.

Addressing the molecular mechanisms underlying these effects, real-time NMR experiments were performed in the presence of live fungal cells. Such experiments revealed immediate line broadening for all peptide residues due to longer T₂ relaxation times (Figure 5.2 (D)). Additionally, metabolite release was observed from dead or wounded cells as early as 5-10 min after incubation (Figure 5.2 (D), 5.3 (A) and S5.6, Appendix V). The intensity of metabolites increased with increasing incubation time (Figure 5.2 (E)). Under similar conditions, untreated control cells did not show any metabolite release (Figure 5.2 (D) and S5.6, Appendix V). Further information on the time-kill kinetics for *C. albicans*

was provided by spread plate techniques, where the cells were initially incubated for different time points in the presence of WS₂ QD-conjugated peptide from which 5 μ l suspensions were plated on YPD agar plates. No fungal colonies appeared after 5 min of incubation (Figure 5.3 (B)), confirming the results of the live cell NMR experiments. Also, in line with the live-cell NMR experiments, scanning electron microscopy (SEM) was performed using *P. aeruginosa* and *C. albicans* cells treated with KG18 and WS₂ QD-conjugated peptide (WS₂-KG18 and/or WS₂-VR18), demonstrating membrane perturbation and leakage of the intracellular constituents as early as 15 min after incubation with the peptides (Figure 5.4 (A-B)). In contrast, untreated control cells remained unaffected even up to 90 min as shown in Figure 5.4 (A-B, (i)).

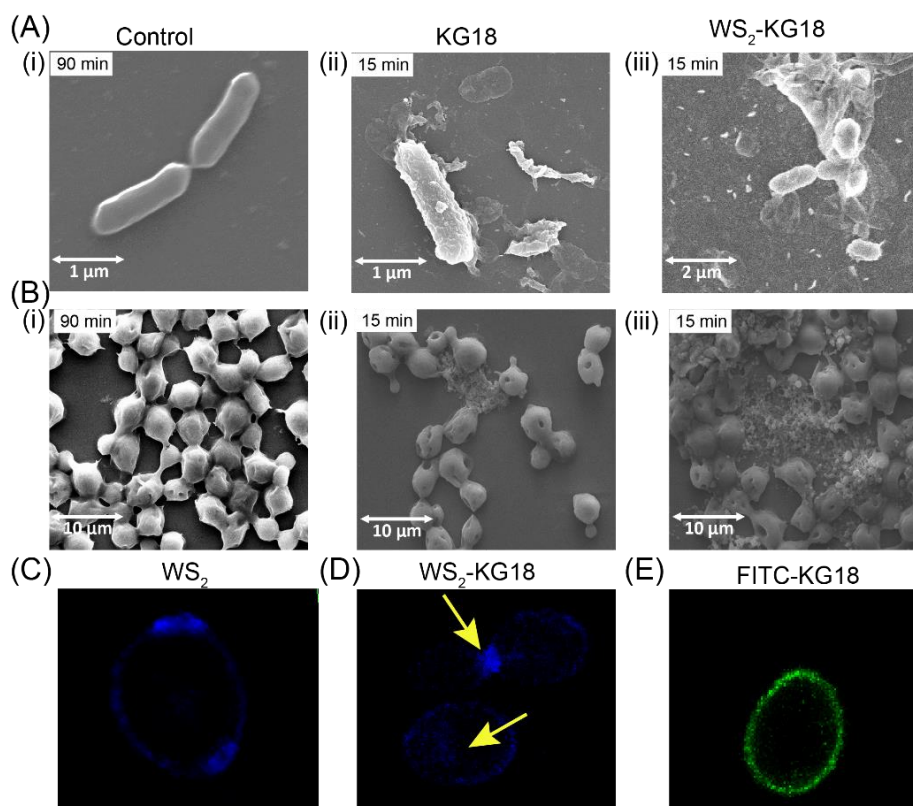


Figure 5.4. SEM images of (A) *P. aeruginosa* and (B) *C. albicans* cells. (i) Untreated cells showing no change in cell morphology after 90 min. In contrast, pronounced membrane perturbation was observed after exposure to with KG18 (ii) or WS₂-conjugated KG18 (iii) for 15 min. The morphological changes were more pronounced for WS₂-conjugated KG18 than for free KG18 peptide. Shown also are representative confocal microscopy images along the z-axis cross-section of *C. albicans* cells in the presence of (C) WS₂ QD or (D) WS₂-KG18. While WS₂-KG18 permeabilizes the *C. albicans* cell (yellow arrow) as early as 10 min of incubation (D), WS₂ QD alone remained at the surface of the *C. albicans* cells after the same time point (Scale - 2 μ m). (E)

A similar effect was observed for FITC-KG18 peptide, which remained on the surface of the *C. albicans* cells even after 60 min of incubation.

Next, we investigated the localization of QD-conjugated peptide in *P. aeruginosa* and *C. albicans* cells, utilizing the intrinsic fluorescence property of QD [287]. Figure 5.4 (D) and 5.5 (A) show confocal images where cross-sections across the z-axis of the fungal cells clearly depict the localization of the peptide-QD conjugates inside the fungal cells within 10 min of treatment, again illustrating the membrane permeabilizing activity of the QD-conjugated peptide. In contrast, WS₂-QD and FITC-KG18/VR18 (FITC-tagged at the N-terminal of respective peptide), used as controls, remained at the cell surface (Figure 5.4 (C-E) and 5.5 (B)) upon incubation with the cells for 60 min under similar conditions. Collectively, our results show that the antimicrobial activity of QD-conjugated peptides relies on direct membrane disruption, and that QD conjugation promotes membrane destabilization.

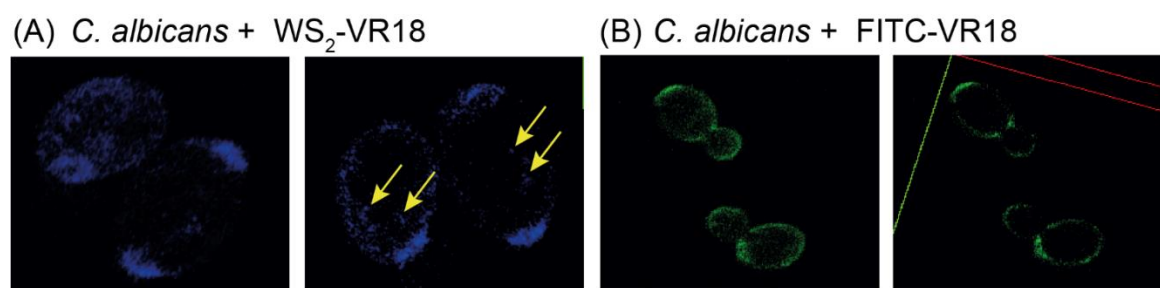


Figure 5.5. Confocal laser scanning microscopy images of the cells treated with either (A) WS₂-VR18 or (B) FITC-VR18. Left panel shows the overall 2D image of the cells, and the right panel shows the cross section along the z-axis to visualize the localization of the fluorophore attached peptides at a particular plane of the cells (Scale - 2 μ m). The arrow head show that WS₂-VR18 resides inside the cells, while FITC-VR18 remains localized in the cell membrane at same time scale.

5.3.4. Interaction of Microbial model membranes with QD-AMP conjugates

In order to provide deeper mechanistic insights into the origin of these effects, notably the difference between free and QD-conjugated peptides, the interaction between peptide and model membranes was next investigated at an atomic resolution using NMR spectroscopy. Since lipopolysaccharide (LPS) is the major component of the outer membrane of Gram-negative bacteria [288], ³¹P NMR experiments were performed for *P. aeruginosa* LPS in the presence of increasing concentrations of peptide conjugates (Figure 5.6 (A-B)). LPS forms heterogeneous aggregates in solution but in the presence of

conjugated peptides, a drastic conformational change was observed for the phosphate head groups of LPS (Figure 5.6 (A)). Apart from the small chemical shift change at one of the monophosphate residues of *P. aeruginosa* LPS resonating at -1.00 ppm, significant broadening at a second monophosphate group of LPS (resonating at -1.29 ppm) was also obtained upon increasing the concentration of conjugated peptides (Figure 5.6 (A)). The phosphate head group dynamics using real-time NMR experiments further suggested structural re-arrangement of LPS micelle through conformational changes, and/or dissociation of LPS aggregates into smaller fragments (Figure 5.6 (B)), in line with previous findings on the molecular rearrangement and/or disruption of *Escherichia coli* LPS by paradaxin [125]. In order to investigate membrane defect formation induced by the presently investigated peptides and their QD-conjugates, membrane destabilization effects were also investigated. It was observed that KG18 can readily form ion channels (Figure 5.6 (C) (i)) in model bilayer membranes (BLM). The channels exhibited clear transitions between closed (0 pA) and different open states (C1 and C2). The major conductance states observed were $\sim 9 \pm 1$ pS (C1) and 38 ± 5 pS in 1 M KCl and 80 mV. QD-conjugated KG18 also formed channels with conductance of $\sim 6 \pm 2$ and 81 ± 6 pS (Figure 5.6 (C) (ii)). Interestingly, channels formed by the QD-conjugated peptide exhibited initial rapid fluctuation between the open and closed states before stabilizing at higher conductance state (Figure 5.6 (C) (ii)). Additionally, QD-KG18 causes rupturing of BLM frequently, in contrast to unmodified QD, which did not show any channel forming activity (Figure 5.6 (C) (iii)). Similar observations were made for WS₂-VR18 (data not shown). Taken together, these results not only demonstrate the boosted membrane disruptive capacity of the QD-peptide conjugate, but also that the type and/or number of defects differ between free and QD-conjugated peptides.

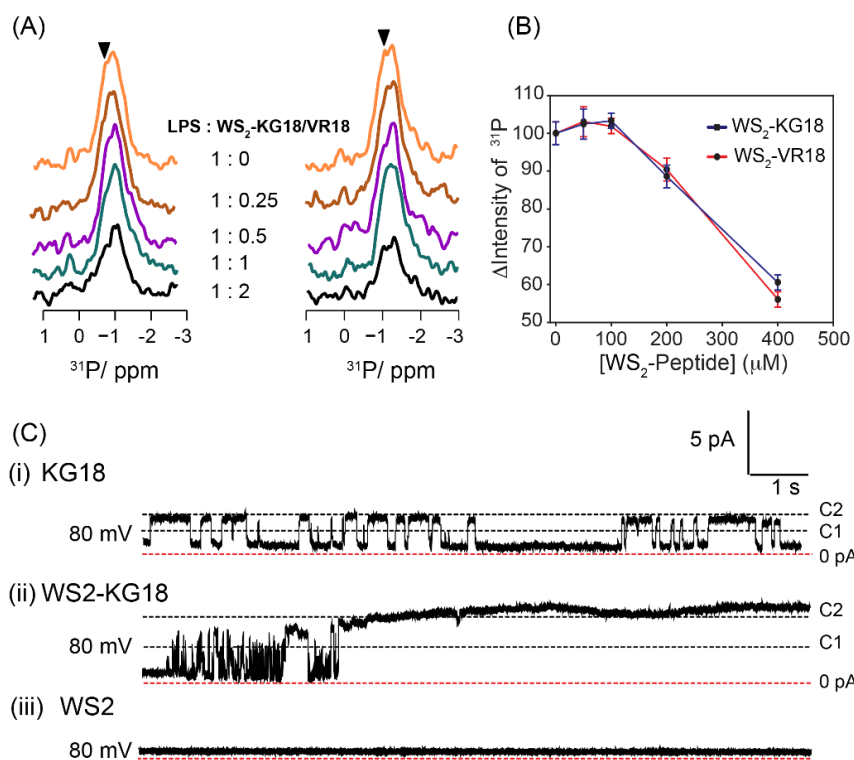


Figure 5.6. (A) One-dimensional ^{31}P NMR spectra of 200 μM LPS in the presence of different concentrations of WS₂-conjugated KG18 (left panel) or WS₂-VR18 (right panel), showing chemical shift changes as well as line broadening of ^{31}P resonances (arrowhead) of LPS. (B) Difference of ^{31}P NMR peak intensity with increasing concentrations of WS₂-peptide conjugates. (C) Current traces at 80 mV, exhibited by (i) KG18, (ii) QD-KG18, and (iii) WS₂ QD in BLM. Red broken lines indicate the baselines (0 pA, closed state), while different conductance states are represented as C1 and C2. While WS₂ QD alone did not form any channels, WS₂ QD-KG18 formed larger channels compared to the free peptide, which were stabilized at higher conductance states for longer time.

5.3.5. Three-dimensional structure determination using solution state NMR

To gain insight into structural aspects of WS₂ QD-conjugated peptides, high-resolution NMR spectroscopy of LPS-bound WS₂-KG18, and WS₂-VR18 was performed. Although the methodology applied may be used to determine the three-dimensional structure of the QD-conjugated peptides in live cell experiments, the release of metabolites within few min of treatment restricted us from employing this methodology in the presence of live *P. aeruginosa* and *C. albicans* cells. Instead, *P. aeruginosa* LPS was used for structural characterization of QD-conjugated peptides. The NOESY NMR spectra of conjugated peptides did not exhibit pronounced NOEs except for certain intra αN (i,i) or sequential αN (i,i+1) NOEs, indicating that QD-conjugated peptides remain highly dynamic in solution (Appendix V, Figure S5.7 (A-B)). In contrast, LPS forms large

molecular weight micelle at very low concentration (critical “micelle” concentration of LPS is $<1 \mu\text{M}$) [289], hence, addition of LPS to the QD-conjugated peptides resulted in a concentration-dependent line broadening, without affecting chemical shifts in the 1D ^1H NMR spectra (Appendix V, Figure S5.8 (A-B)). When the free peptides interact with LPS micelles they undergo a fast -intermediate exchange with the LPS-bound form under the NMR time-scale, creating an ideal situation for *transferred* NOESY (*tr*NOESY) experiments [215], to determine the three-dimensional structure of the conjugated peptides in the presence of LPS.

Interestingly, 2D *tr*NOESY spectra of KG18 and WS₂ QD-conjugated KG18 were almost identical in the presence of LPS, indicating that WS₂ QDs do not substantially affect the conformation of the peptide in the LPS-bound form (Figure 5.7 (A-B)). This result was further supported by CD spectra (Figure 5.7, inset), demonstrating free and WS₂-conjugated peptides to show similar secondary structure in absence and presence of LPS. The statistical analysis of the NOEs, as well as the structures in presence of LPS, are summarized in Table 5.1, which shows several medium ($i, i+2/i+3/i+4$) and long-range ($i, \geq i+5$) NOEs, in addition to sequential αN ($i, i+1$) NOEs (Figure 5.8 (A-D) and Table 5.1). Interestingly, αN ($i, i+3$) NOEs were observed between A7-W10 for WS₂-KG18 or W5-K8 for WS₂-VR18 (Figure 5.9 (A-B)). This confirms the formation of a well-folded conformation by both peptides in presence of LPS molecules. Additionally, several aromatic/aromatic, aromatic/aliphatic, and side chain/side chain NOEs were observed for QD-conjugated KG18/VR18 in LPS micelles (Figure 5.9 (A-B)). The 20-ensemble structure of WS₂-KG18 (Figure 5.10 (A)) shows a satisfactory superimposition with a root mean square deviation (RMSD) value of 0.2 \AA (Table 5.1), whereas in case of WS₂-VR18 (Figure 5.10 (A)) the RMSD value remained comparably high (1.28 \AA) due to insufficient medium- and long-range NOEs obtained (Table 5.1). The three-dimensional solution NMR structure of the WS₂ conjugated KG18 and VR18 (Figure 5.10 (B)) shows an amphipathic ordering with a clear separation of the orientation of charged and hydrophobic residues towards the polar and non-polar sides, respectively. Most strikingly, Trp5 (for VR18) and Trp10 (for KG18), as well as their indole ring protons ($\text{N}\epsilon\text{H}$), played crucial roles in the stabilization of the QD-conjugated peptides in the presence of LPS through the hydrophobic triad composed of “Trp-Leu-Phe” (Figure 5.10 (C)). This packing was also supported by other hydrophobic residues (Ala, Val, and Pro), which contributed to maintain the amphipathicity of the peptides in LPS micelle. In contrast, the positively charged

residues Lys and Arg were highly dynamic and faced the solvent, maintaining a distance of 10-15 Å between their head groups (Figure 5.10 (D)). This distance closely correlates with the distance between two terminal phosphate groups of LPS [229]. Furthermore, the presence of Cys C^αH/ Pro C^δH NOE established the occurrence of Cys-Pro bond in a trans-conformation.

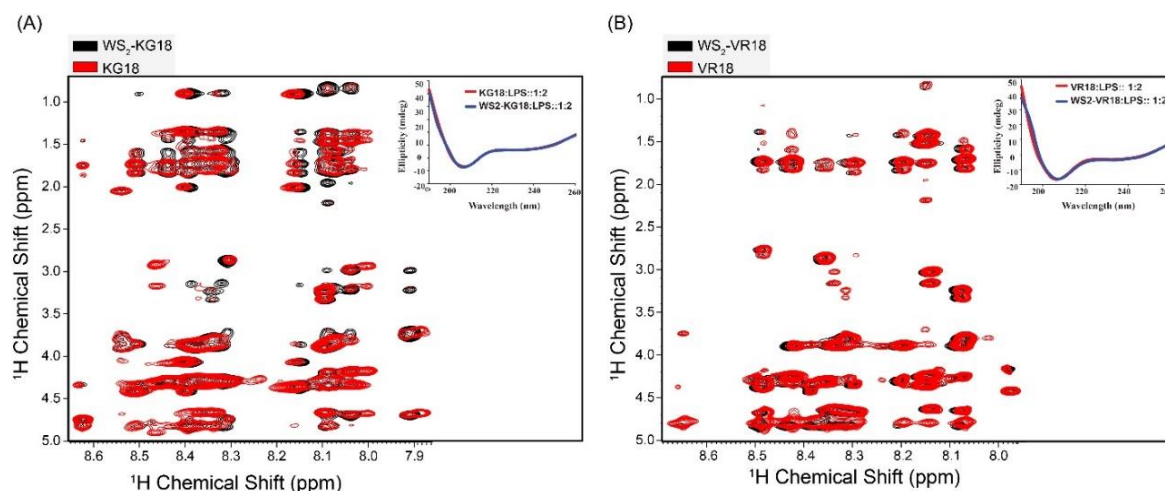


Figure 5.7. Overlay of signature NOE regions of (A) KG18, WS₂-KG18 and (B) VR18, WS₂-VR18 in the context of LPS, obtained from the *tr*NOESY spectra suggesting no spectral change. The CD spectra of the peptides and their WS₂ conjugates (inset) also showed similar profiles. All the NMR experiments were performed using Bruker Avance III 700 MHz, equipped with cryoprobe and at 298K.

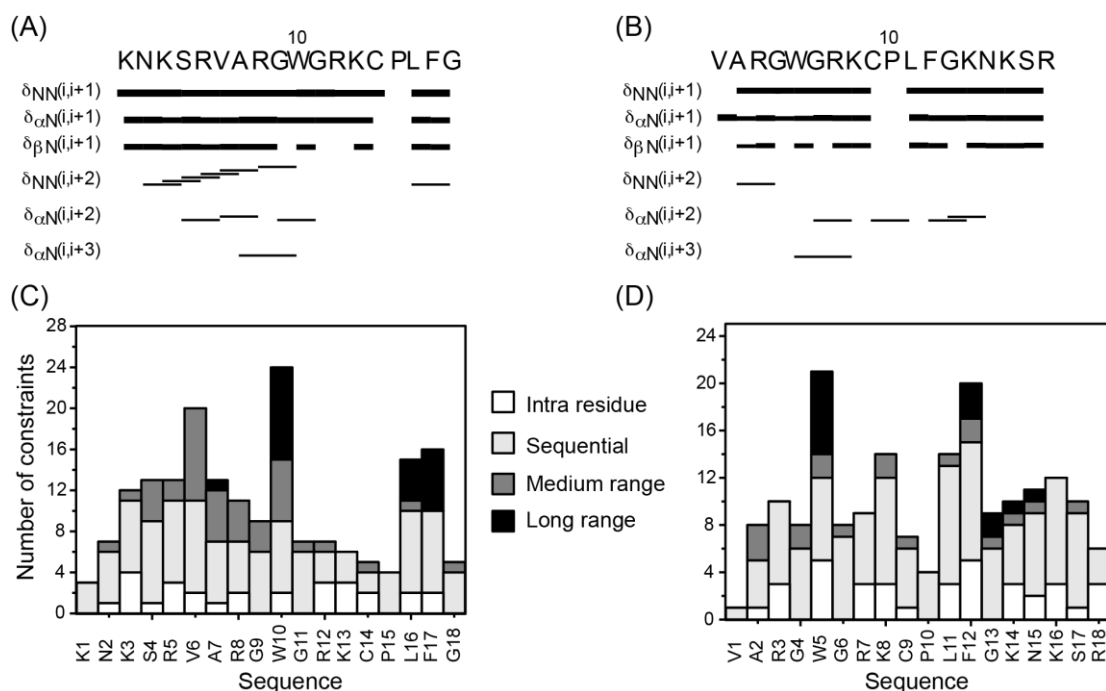


Figure 5.8. Bar diagram showing sequential and medium-range NOEs of WS₂-QD conjugated KG18 (A) and VR18 (B) in presence of *P. aeruginosa* LPS. The thickness of the bars indicates relative intensities of the NOE cross peaks, which are assigned as strong, medium, and weak. Amino acid sequences of both the peptides are shown at the top. (C-D) Histogram plots showing the number of *tr*-NOEs of the QD-conjugated peptides as a function of residue number in complex with LPS micelles.

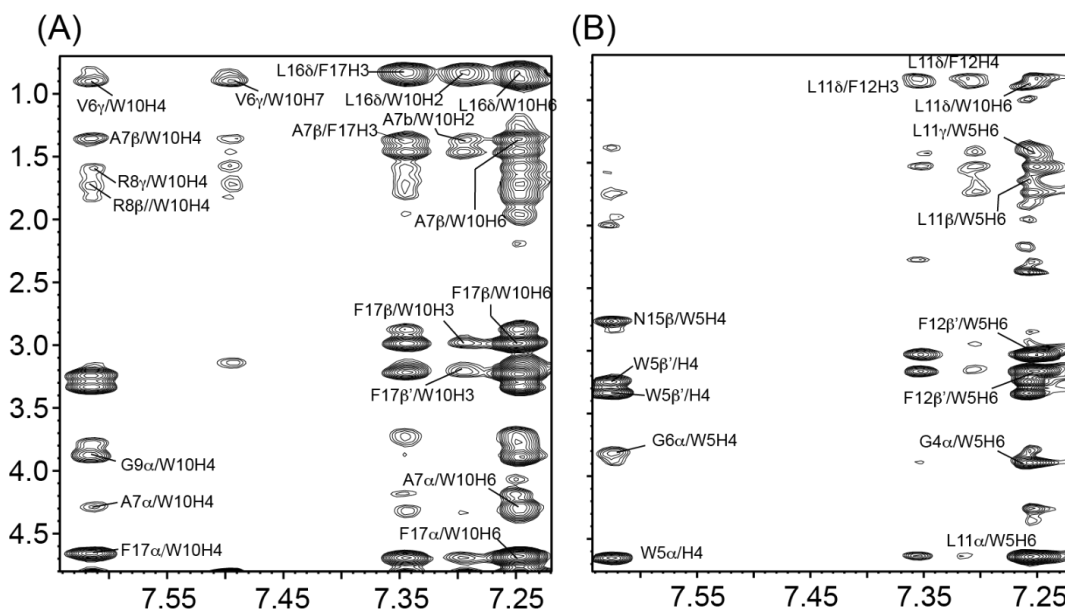


Figure 5.9. Two-dimensional ¹H-¹H *tr*NOESY spectra of (A) WS₂-KG18 and (B) WS₂-VR18 in the presence of LPS. Several side chain/side chain, aliphatic/aromatic and aromatic/aromatic NOEs between Val6, Ala7, Arg8, Gly9, Leu16, Trp10 and Phe17 were observed for WS₂-KG18 in LPS (A). In case of WS₂-VR18, the number of such NOEs were suppressed in comparison to WS₂-KG18.

The overlaid PDB structures of WS₂-KG18 and WS₂-VR18 showed that the VG13 region forms a folded loop type structure in presence of LPS micelle in both the peptides (Figure 5.10 (E)). This fold occurs due to the presence of proline residue in the primary sequence of the peptides. Based on these results, we infer that the “KNKSR” moiety of KG18/VR18 forms an initial anchoring to the membrane through electrostatic interactions, subsequently translocating the rest of the peptide into the outer leaflet, using hydrophobic interactions with acyl chains of the membrane, thereby inducing membrane defects (Figure 5.10 (F)). Since two molecules of the peptide are attached to each WS₂ QD, a larger surface area perturbation is generated compared to free peptides, promoting membrane disruption, resulting in higher membrane disruptive capacity and antimicrobial activity than the corresponding non-conjugated peptides.

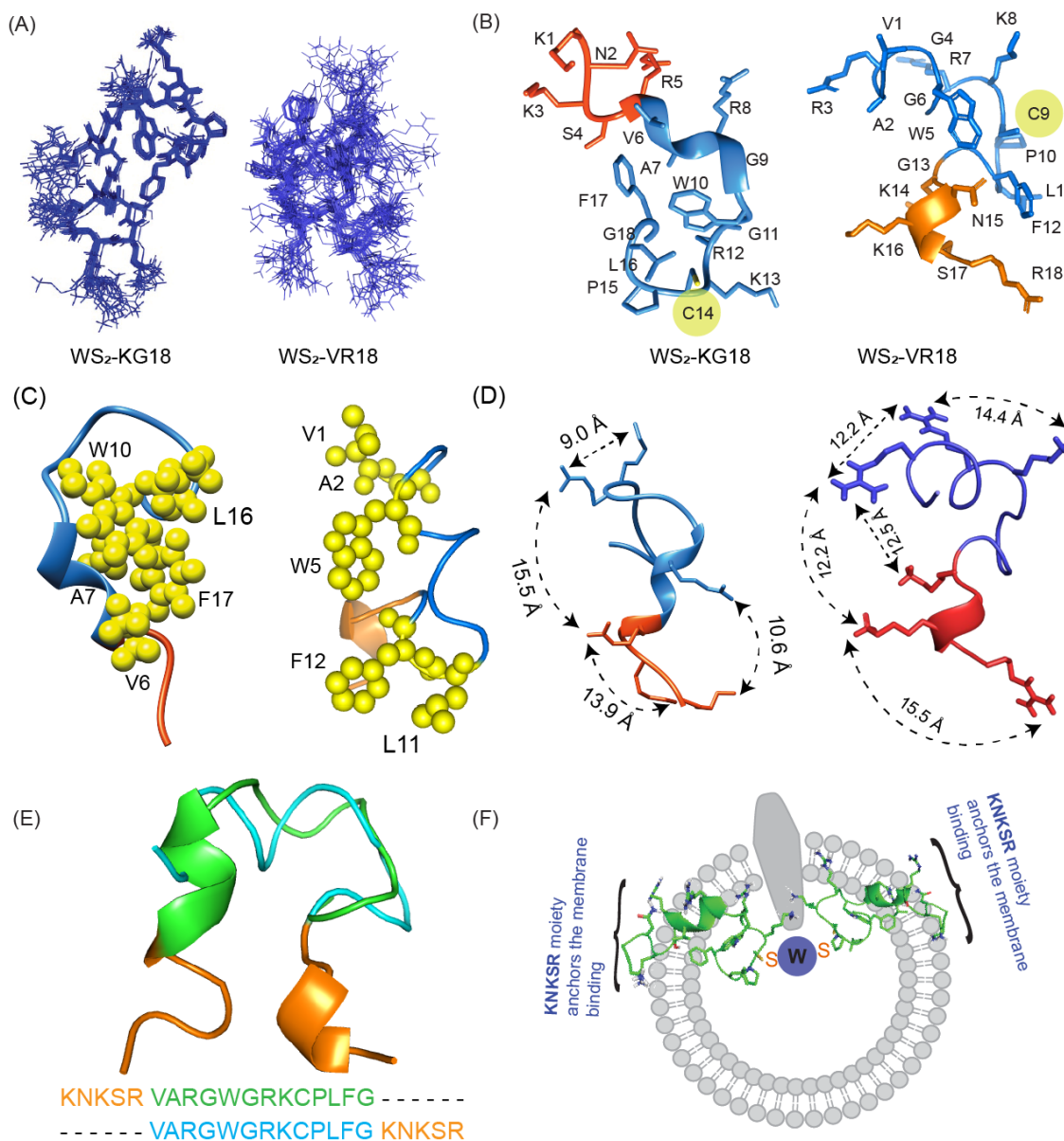


Figure 5.10. (A) Twenty ensemble structures of QD-conjugated KG18 and VR18 in LPS. The LPS-bound structure of WS_2 QD-KG18 (PDB acquisition codes 5Z31 and 5Z32 for WS_2 -KG18 and WS_2 -VR18, respectively) showed a rigid backbone conformation but (B) adopt an amphipathic structure displaying pronounced charge separation. (C) Aromatic-aromatic packing formed by W10 and F17 for WS_2 -KG18 and W5-F12 for WS_2 -VR18, which was further assisted by Val, Ala and Leu residues, forming a hydrophobic hub shown in yellow colour. (D) The distance between two positive charge residues of KG18 or VR18 is almost identical to the distance between head groups of LPS (~ 13 - 15 Å). (E) Overlaid single PDB structures of WS_2 -KG18 and WS_2 -VR18. (F) Initially, the "KNKSR" moiety anchors the membrane, binding through electrostatic interaction with the negatively charged phosphate head groups, followed by the hydrophobic interaction between acyl chain of lipids and "hydrophobic hub" of QD-conjugated peptide. Larger surface area perturbation

caused by QD-conjugated peptide results in more efficient membrane disruption and microbial killing.

Table 5.1. Summary of structural statistics for the 20 lowest energy ensemble structures of WS₂-conjugated KG18 and VR18 peptides in LPS.

Distance restraints	WS₂-KG18	WS₂-VR18
Intra residue ($i - j = 0$)	44	43
Sequential ($ i - j = 1$)	41	42
Medium range ($2 \leq i - j \leq 4$)	7	6
Long range ($ i - j \geq 5$)	31	18
Total	123	109
Angular restraints		
Φ	15	15
ψ	15	15
Distance restraints from violation ($\geq 0.4 \text{ \AA}$)	0	0
Deviation from mean structure (\AA)		
Average backbone to mean structure	0.20 ± 0.05	1.28 ± 0.42
Average heavy atom to mean structure	0.95 ± 0.17	2.30 ± 0.60
Ramachandran plot*		
% residues in the most favoured regions and additionally allowed region	61.5	41.7
% residues in the generously allowed region	38.5	58.3
% residues in the disallowed region	0.0	0.0

5.3.6. Anti-biofilm activity

Apart from exhibiting increasing resistance to various antimicrobials, *P. aeruginosa* and *C. albicans* cells are able to form biofilms (Figure 5.11 (A) and 5.12 (A-C)), rendering them largely non-susceptible to conventional antimicrobial agents and antimicrobial peptides alike.[290] This motivated us to investigate potential anti-biofilm properties of WS₂ QD-conjugated KG18 and VR18 (Figure 5.11 (B) and 5.12 (A-C)). Strikingly, both peptide conjugates showed complete removal of preformed matured *Pseudomonas* and *Candida* biofilms at 200 μM concentration (which is almost $2\times$ lower than for the free peptides) when assayed using MBEC assay, comparable to 100 μM Polymyxin-B or Amphotericin B (20 $\mu\text{g/ml}$) treated as a positive control (Figure 5.11 (C) and 5.12 (A-C)). Further quantification using MTT-based viability assay and biomass measurement using

crystal violet staining supported the microscopic data (Figure 5.11 (D-E), and 5.12 (D-G)). This illustrated another potentially important venue for peptide-conjugated WS₂ QD.

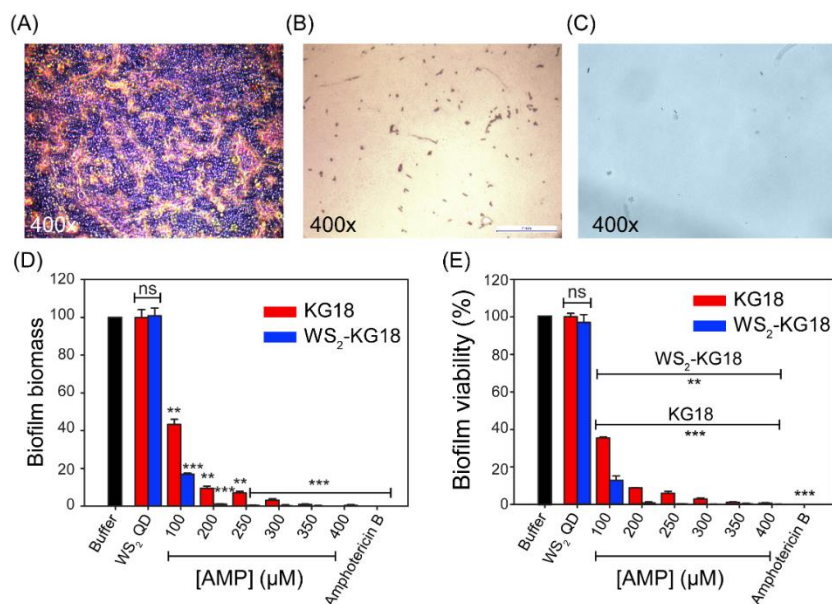


Figure 5.11. Matured *C. albicans* biofilm before (A) and after treatment with either (B) WS₂-conjugated peptide or (C) Amphotericin B (20 μg/ml). Bar graph of crystal violet staining of biofilms and (D) MTT assay showing potent anti-biofilm activity of KG18/WS₂-conjugated KG18 against matured *C. albicans* biofilms as compared with negative (no AMP conjugates) and positive (200 μM polymyxin B) controls (ns, non significant; *, p≤0.05; **, p≤0.01; ***, p≤0.001).

Complementing classical drug delivery approaches, nanoparticles have attracted strongly increasing interest as drug delivery agents in the last decade in particular as reported by several reviews by Malmsten M, Elzoghby *et al.*, Rai *et al.*, Tonga *et al.* and many more [291-294]. There is also several research articles published which explained about the application of such nanomaterials as antimicrobial agents, either on their own, or in combination with antibiotics [258]. For example, Brown *et al.*, reported upon the functionalization of ampicillin with silver and gold nanoparticles (AgNPs and AuNPs, respectively), and found the latter to display increased activity against a broad spectrum of pathogens compared to non-conjugated nanoparticles [295]. Similarly, Payne *et al* showed that the conjugation of Kanamycin to AuNP enhanced its activity against a series of gram-positive and gram-negative bacteria including Kanamycin resistant *Staphylococcus epidermidis*, *Streptococcus bovis*, *Enterobacter aerogenes*, *Pseudomonas aeruginosa* PA01, *P. aeruginosa* UNC-D and *Yersinia pestis* [296]. Vancomycin-conjugated porous silicon nanoparticles also showed targeted healing of *Staphylococcus aureus* infections *in-vivo* as reported by Hussain *et al* [297]. Expanding such studies to

AMPs, our group conjugated AuNPs with a 16 residue AMP, VG16KRKP, and reported upon its anti-*Salmonella* activity and enhanced stability *via* structure functional correlation.[44]

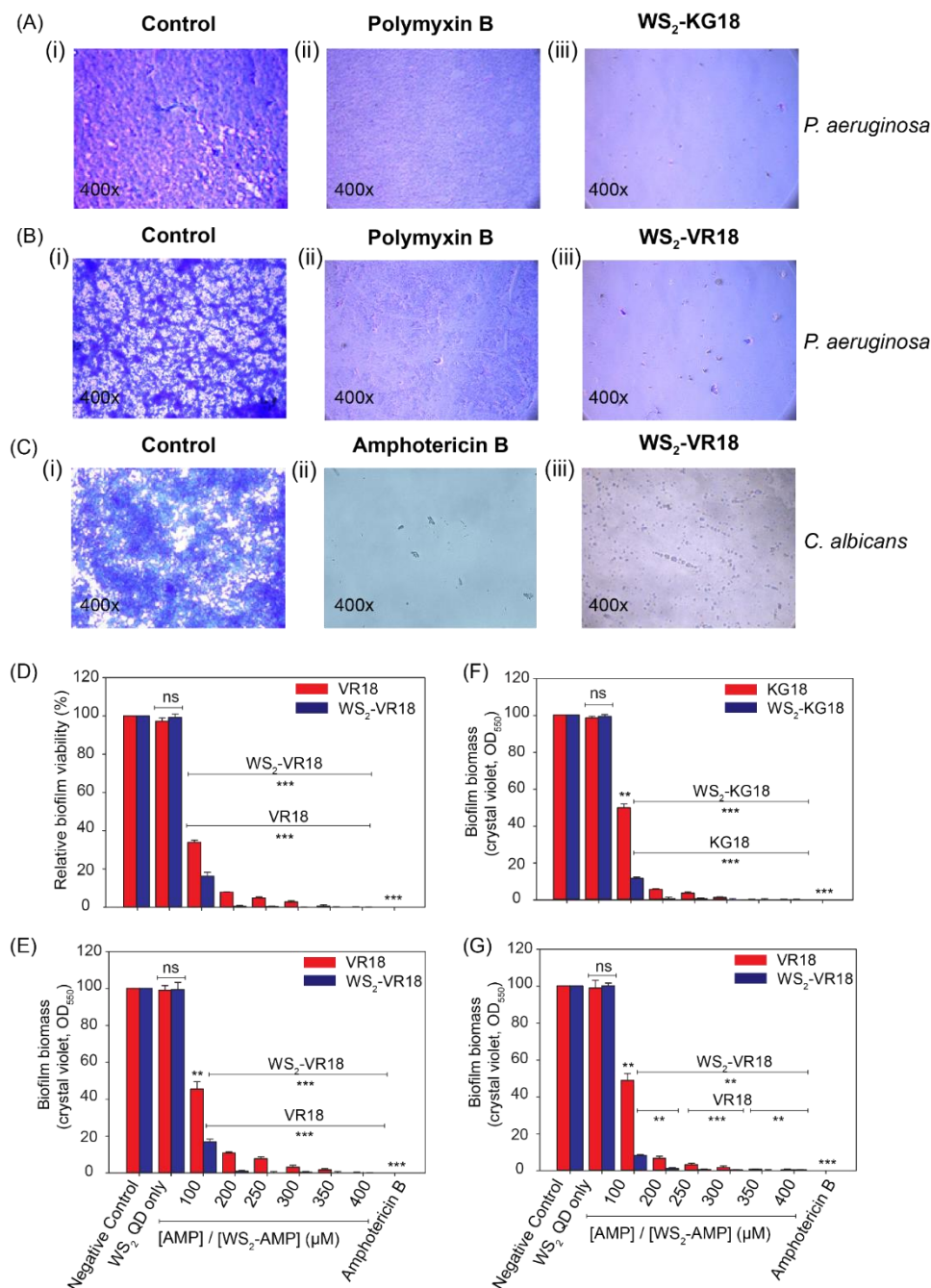


Figure 5.12. Images (A-C) showing the matured biofilm in the absence of presence of WS₂-conjugated AMPs. The biofilm was prepared either from *P. aeruginosa* or *C. albicans* and MBEC assay performed. Amphotericin B (20 μg/ml) was used as negative control. Histogram plot of (D) MTT assay against *C. albicans* biofilm and (E-G) crystal violet staining of *C. albicans* and *P. aeruginosa* biofilms. The potent anti-biofilm activity was compared between free and WS₂-conjugated KG18 or VR18 peptides. The negative and positive control of the experiments were

cells without peptide and in the presence of Amphotericin B (20 $\mu\text{g/ml}$), respectively (ns, non significant; *, $p \leq 0.05$; **, $p \leq 0.01$; ***, $p \leq 0.001$).

Various QDs have been reported to display antimicrobial properties, including CdTe, CdSe/ZnS, and ZnO QDs. Furthermore, QDs have been combined with antibiotics or antimicrobial peptides for improved performance [61,297-299]. For example, Luo *et al.* studied antibacterial effects of Rocephin in combination with CdTe QDs against *E. coli* [300]. It was found that CdTe QDs and Rocephin form a stable complex, which display more potent antimicrobial effects than expected for the combination of the individual compounds. Importantly, however, many QDs, especially those containing Cd^{2+} and other heavy metal ions, have been found to display high toxicity against human cells [301-305]. Recently, several groups have therefore focused their attention on QDs displaying lower toxicity, including, InAs/InP/ZnSe, InAs/ZnSe, and MoS_2 [306-308]. In our pursuit of designing nanoparticles that could be used for selective targeting of bacteria and fungi through AMP conjugation, we here extend on the latter studies by investigating a special class of transition metal quantum dots, displaying advantages of highly efficient fluorescent properties, very small size (~ 2 nm), straightforward AMP conjugation, and low toxicity against human cells.

As with other inorganic nanoparticles, membrane interactions of QDs are highly influenced by their surface properties. While membrane composition effects such as presence of anionic phospholipids (enriched in bacteria) and sterols (cholesterol and ergosterol in mammalian and fungal cells, respectively) [309-312], designing bare nanoparticles displaying good selectivity for pathogens, with potent antimicrobial effects and low toxicity against human cells, is difficult. Considering this, conjugating such nanoparticles with selective AMPs presents a promising alternative, since AMPs allow a wider range of approaches for reaching such selectivity, including quantitative structure-activity relationship approaches as shown by Pasupuleti *et al* and Fjell *et al* [40,313], AMPs generated from endogenous proteins [314,315], and Trp/Phe-tagged AMPs [41,127], to mention a few. Indeed, both the conjugated peptides investigated in our study displayed low toxicity against human cells, yet simultaneously a two-fold higher activity due to peptide clustering when compared to their free counterparts, the latter demonstrated by NMR-based live cell experiment and SEM micrographs to result from membrane rupture, loss of morphology, and metabolite release within few min of treatment. From this, conjugation of the WS_2 QDs with selective AMPs seems to represent a viable approach for

effectively ‘targeting’ such nanoparticles to bacteria and fungi, either for antimicrobial effects in a therapeutic setting, or for monitoring infections in diagnostics. A similar approach was previously used by coating fluorescent polymer nanoparticles with the Trp-tagged antimicrobial peptide GRR10W4 for selective uptake of these particles in melanoma cells [316].

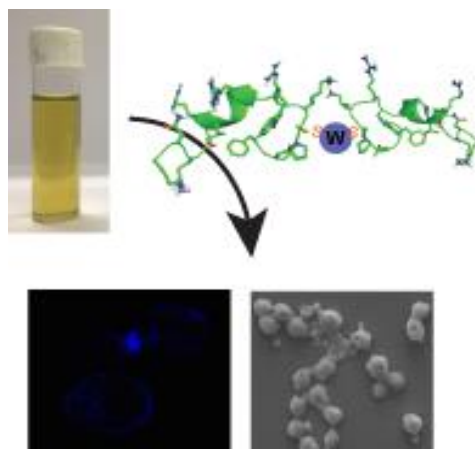
In addition to such functional ‘targeting’ resulting in potent antimicrobial effects against both planktonic and biofilm-forming pathogens, the present study provides novel insight into the mechanisms, by which such effects are reached. Thus, detailed comparative analysis of the structures of free and conjugated peptides showed adoption of an amphipathic orientation with clear charge separation. Furthermore, the conformation of the peptides remained unaltered before and after conjugation with WS₂-QD, as evidenced from *tr*NOESY spectra, whereas MALDI demonstrated each WS₂ QD to bind two AMP molecules. As the structure of a membrane active peptide plays important role for its activity, the unaltered conformation of our peptides, as well as the effectively bi-dentate formation, provides an added advantage of using such ultra-small nanoparticles, resulting in enhance membrane lysis and antimicrobial/antibiofilm activities.

This approach for combining low-toxic ultra-small QDs with potent and selective AMPs represents a promising tool not only for suppression of infections caused by bacterial and fungal pathogens, but also a probe for localization of such conjugates inside live cells., and for monitoring of treatment outcome. Here, it should also be noted that the ability to conjugate WS₂ QD with peptides containing thiol group allows a broad range of AMPs and other peptides to be conjugated, thus potentially supporting a broad range of applications within infection treatment and imaging.

5.4. Conclusion

In conclusion, this study demonstrates the successful design of two potent 18-residue antimicrobial peptides, as well as their conjugation to highly fluorescent, photostable and ultrasmall tungsten disulfide QD. Such peptide conjugation opens up a new platform for fluorescent tagging of bioactive molecules, notably AMPs. Our findings highlight a new powerful antimicrobial system, the favourable toxicity profile of which allows their usage as antimicrobial agents against challenging pathogens, both in planktonic form and in biofilms. Based on a series of detailed NMR studies, QD conjugation was demonstrated to result in enhanced interactions with both model lipid membranes, key membrane components (LPS), and pathogen cell membranes through a bi-dentate

configuration. Together with the favourable imaging properties of WS₂ QDs, these results demonstrate that conjugation of AMPs with such QDs represent a promising approach for boosting their antimicrobial effects, and for modification of such QDs with AMPs for selective pathogen imaging.



5.5. Appendix V

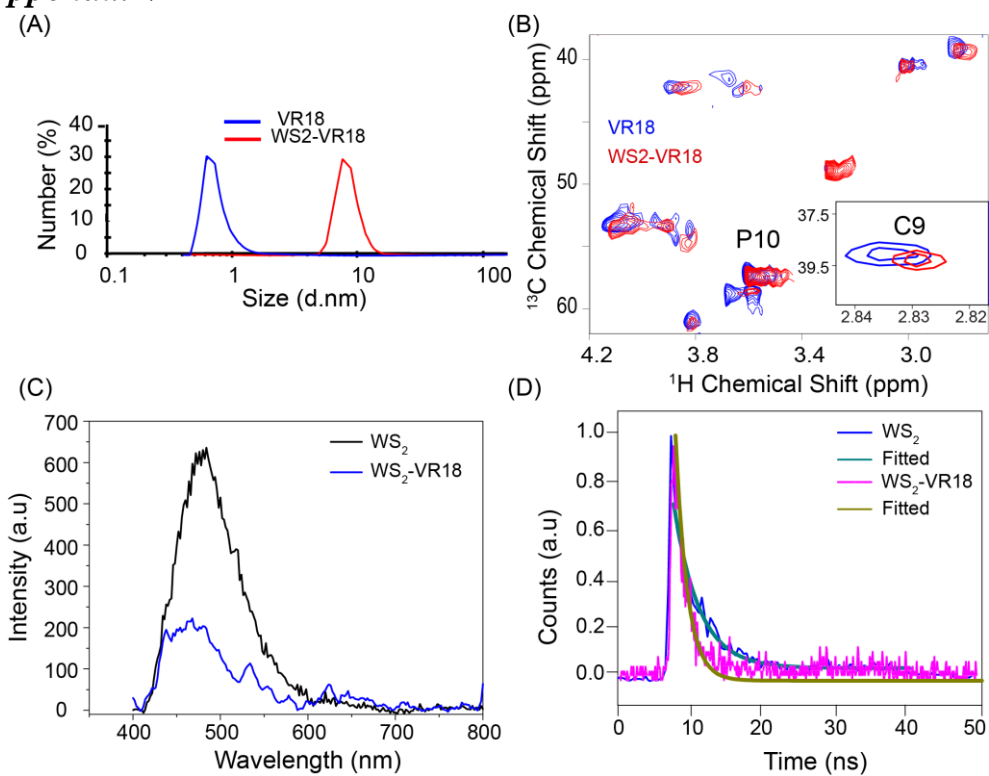


Figure S5.1. Physical characterization of WS₂-VR18: (A) Hydrodynamic size, obtained from dynamic light scattering (DLS), confirms the WS₂-VR18 conjugation. (B) The 2D heteronuclear ¹H-¹³C NMR spectra show chemical shift perturbation in the presence of WS₂-QD, demonstrating conjugate formation through Cys9 and Pro10 residues of VR18. (C-D) Photoluminescence (PL) and PL decay also confirmed conjugation of QD to the respective peptide via charge transfer.

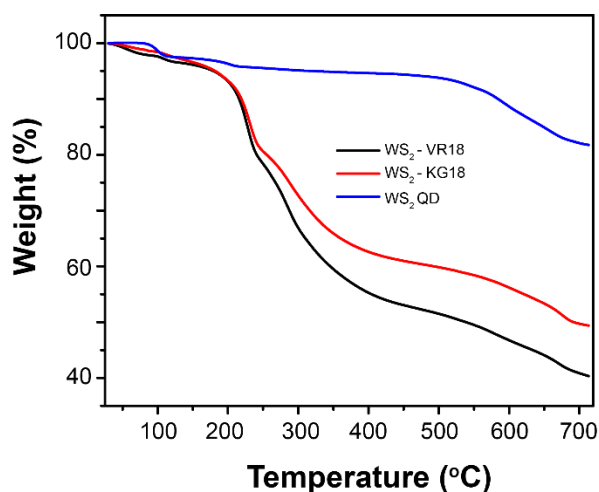


Figure S5.2. Thermogravimetric analysis (TGA) of WS₂ and its conjugated peptides. The weight loss of WS₂ QD was 5.8% at 470 °C. We assume that the composite has only inorganic residues at 470°C and the compositions of inorganic parts were calculated based on this.

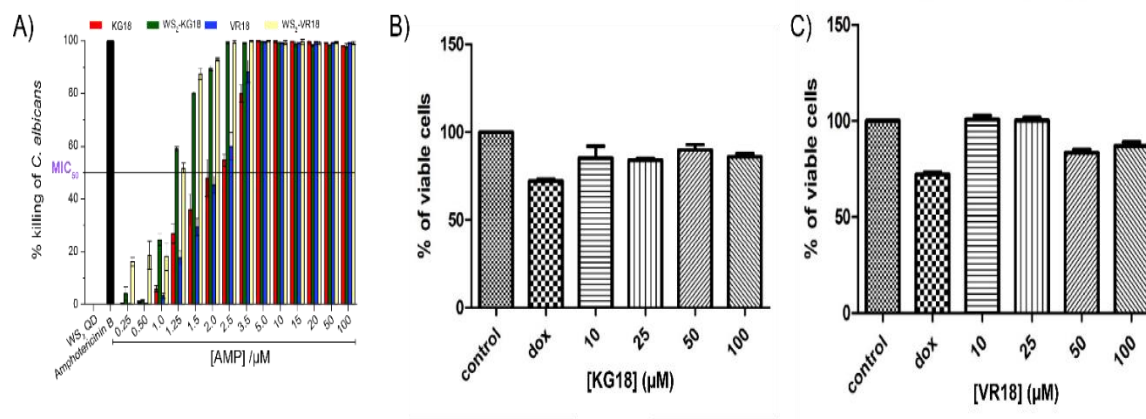


Figure S5.3. (A) Histogram plot showing MIC_{99%} values of WS₂-KG18 and WS₂-VR18 against *C. albicans* SC5314. Furthermore, as shown for KG18 (B) and VR18 (C), the free peptides did not exhibit any cytotoxicity against normal human WI38 cell line. Doxorubicin (dox) (3 μM) was used as a positive control.

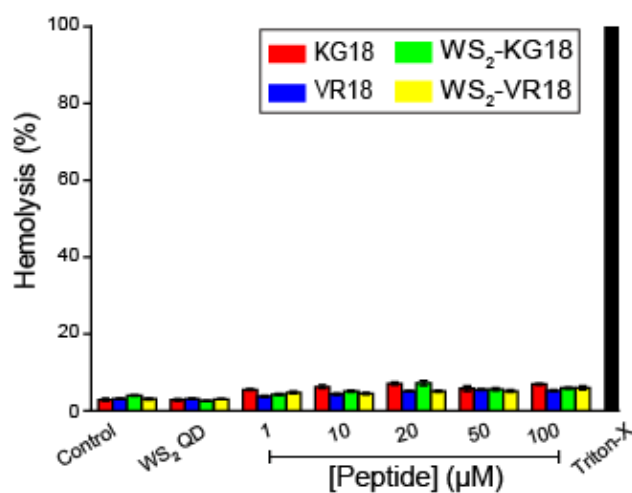


Figure S5.4. Free KG18, VR18 as well as WS₂-KG18 and WS₂-VR18 displayed low toxicity against human erythrocytes as obtained from hemolysis assay. The experiment was done in triplicate and the error bar represents \pm SD.

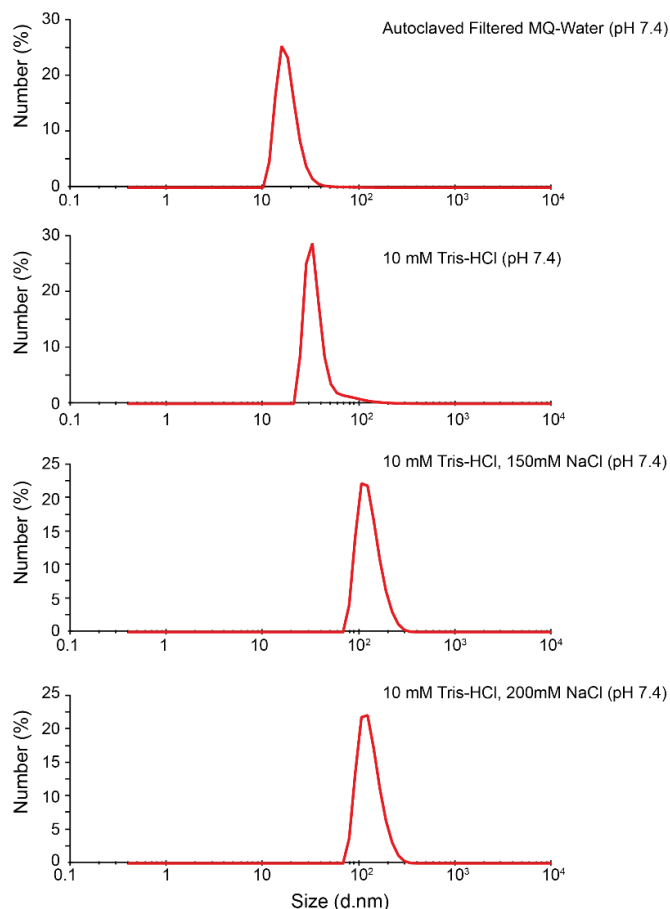


Figure S5.5. DLS analysis of WS2-KG18 either in aqueous solution (pH 7.4) or in 10mM Tris-HCl (pH 7.4) with different salt concentration after $t=16$ days.

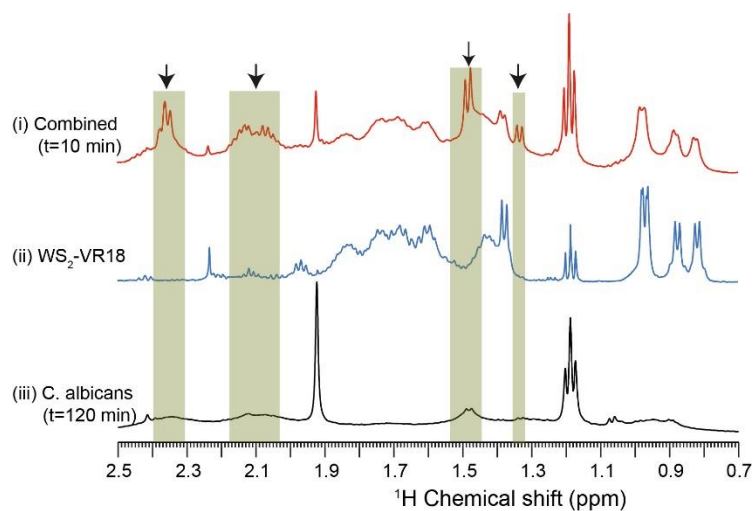


Figure S5.6. (A) One-dimensional ^1H NMR spectrum of WS₂-VR18 (i) in the presence of live *C. albicans* (O.D₆₃₀=1) cells; (ii) in the absence of cells, and (iii) with only cells in the absence of peptide. New peaks (marked by arrows) with sharp signal appeared within 10 min after treatment, indicating potent antimicrobial activity of WS₂-VR18. In contrast, no such peaks were obtained from the cells even after 120 min of incubation.

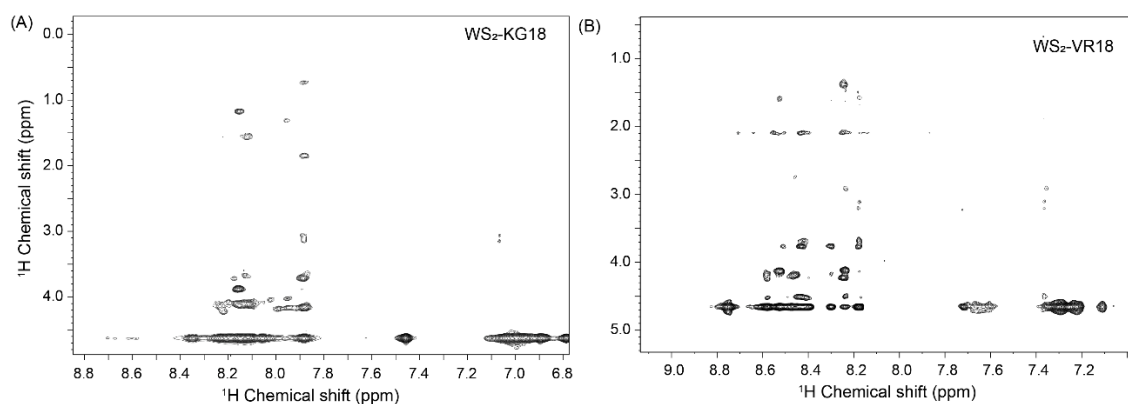


Figure S5.7. Free NOESY spectrum of WS₂-KG18 and WS₂-VR18 in H₂O (pH- 4.5, 298 K). The data was obtained in a Bruker 700 MHz spectrometer.

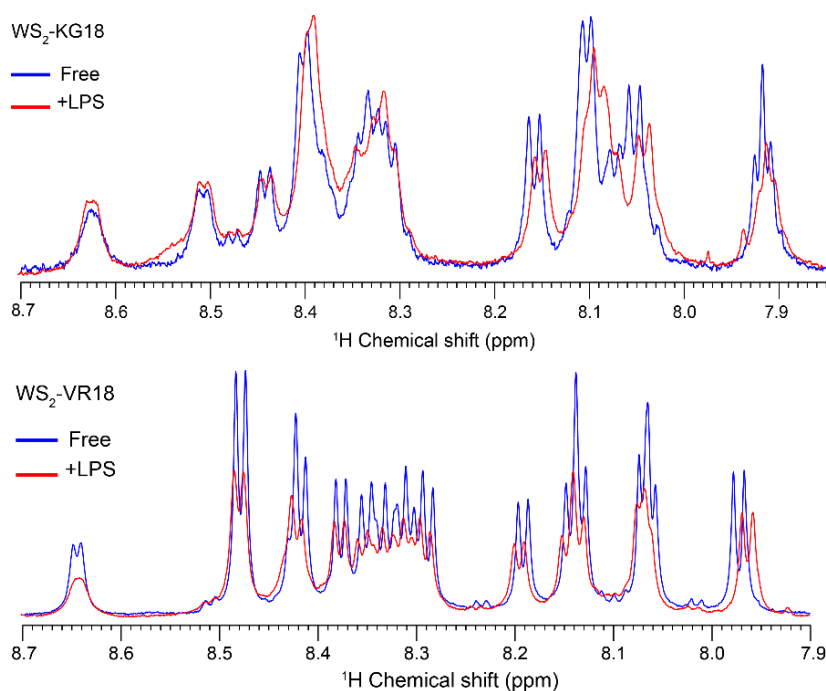


Figure S5.8. One-dimensional ¹H NMR spectrum of WS₂-KG18 (A) and WS₂-VR18 (B) in aqueous solution (blue colour) and in the presence of *P. aeruginosa* LPS (red colour) (stock concentration=1 mM). Peak broadening and change of intensities were observed after addition of *P. aeruginosa* LPS, suggesting a conformational exchange between free and bound form at NMR time scale.

Chapter VI

6. 7-Methoxytacrine and 2-Aminobenzothiazole Heterodimers: Structure-Mechanism Relationship of Amyloid Inhibitors Based on Rational Design

This chapter has been adapted from the following publication:

Gancar, M., Ho, K., **Mohid, S.A.**, Thai, N.Q., Bednarikova, Z., Nguyen, H.L., Bhunia, A., Nepovimova, E., Li, M.S. and Gazova, Z., **2020**. 7-Methoxytacrine and 2-Aminobenzothiazole Heterodimers: Structure–Mechanism Relationship of Amyloid Inhibitors Based on Rational Design. *ACS Chemical Neuroscience*, *11*(5), pp.715-729.

6.1. Introduction

All living things and viruses include the universally present enzyme lysozyme, which has a wide range of origin, amount, structural, chemical, and enzymatic characteristics [317]. It is a 14 kDa protein that is found in several mucosal secretions, including tissues from animals and plants as well as tears, saliva, and mucus. It is crucial for innate immunity since it protects against bacteria, viruses, and fungus [318]. It is also known as N-acetylmuramic acid hydrolase or muramidase (E.C. 3.2.1.17). The enzymatic activity of lysozyme is mediated by the hydrolysis of β -1,4-glycosidic linkages between N-acetylglucosamide (NAG) and N-acetylmuramic acid (NAM), which are found in the polysaccharide backbone of the peptidoglycans of Gram-positive bacteria [319]. Since its discovery by A. Fleming in 1921, lysozyme has been regarded as an endogenous antibiotic, intrinsically vital in the fight against microorganisms due to its ability to destroy the bacterial cell wall.

Human lysozyme is associated with lysozyme hereditary systemic non-neuropathic amyloidosis. It has been reported that amyloidogenic variants of the human lysozyme are encoded by six different mutations of the lysozyme gene. The phenotype of lysozyme systemic amyloidosis is heterogeneous and includes gastrointestinal symptoms, sicca syndrome, hepatic rupture, petechiae and purpura, renal failure, and lymphadenopathy [320]. Hen egg white lysozyme (HEWL) represents an interesting model system to investigate formation of amyloid aggregates and identify novel inhibitors with potential to deal with this disease [321]. This 129-residue-long anti-bacterial protein has been extensively used in studies as its structure and folding properties are well known and it is

highly homologous to human lysozyme. *In vitro*, it undergoes amyloid aggregation when exposed to high temperatures in acidic conditions [322].

After decades of research, protein amyloid aggregation remains one of the biggest challenges for the scientific community because of its association with amyloid-related diseases as well as recently obtained knowledge that protein amyloids also play physiological roles in organisms. Now, it is believed all peptide and polypeptide sequences can adopt the amyloid state under appropriate conditions [323]. Although the precise molecular mechanism of amyloid aggregation *in vivo* is still unknown, there are a lot of factors affecting the propensity of peptides and proteins to be transformed from a soluble state into almost insoluble amyloid structures [193]. They include genetic mutations, post-translational modifications, high protein concentration, and the presence of metal ions [324]. *In vitro* exposure of proteins to amyloid-inducing conditions such as high temperature or protein concentration, pH, and the presence of salts or denaturants results in the formation of amyloid fibrils with cross- β architecture common to amyloid aggregates formed *in vivo* [323].

It is generally accepted that the formation and accumulation of amyloid deposits in various tissues can have a toxic effect on different cell types, leading to cell dysfunction. Amyloidosis can represent a serious health problem leading to life-threatening organ failure and finally, death [325]. Alzheimer's and Parkinson's diseases, the most common forms of dementia, as well as diabetes mellitus are some of the more than 50 currently known amyloid diseases.

Currently, there is no cure for amyloid diseases. Treatment is mainly focused on alleviating symptoms, thus improving the quality of the patient's life. Therefore, a great emphasis is placed on the development of effective strategies for their successful treatment. One of the prospective therapeutic approaches involves inhibition of amyloid fibrillization or clearance of amyloid aggregates.

Many small molecules have proved to be capable of inhibition of amyloid aggregation. Most of the studied compounds possess structural features known to be important for their interaction with core regions of early-formed amyloid species and mature amyloid fibrils. These characteristics include the presence of aromatic rings, the substitution pattern of these aromatics, and the length and flexibility of the linker connecting the functional groups [326]. Curcumin and its derivatives exhibit the ability to interfere with β -amyloid fibrils and

aggregates. Derreumaux et al. reported the effects of many drugs targeting mainly A β peptide obtained from *in vitro* and *in vivo* experiments and clinical trials [327]. Glycoacridines inhibit amyloid aggregation of human insulin as well as HEWL [328]. Siddiqi et al. showed that capreomycin effectively suppresses the insulin amyloid fibrillization [329]. The ability of polyphenols to affect the amyloid aggregation of HEWL *in vitro* has been reported [330].

Tacrine was the first cholinesterase inhibitor approved by the U.S. FDA and also one of the most popular aromatic structures tested for possible anti-amyloid properties. However, its use has been restricted due to its hepatotoxicity [330]. Therefore, the search for more effective, secure, and multifunctional tacrine derivatives is still of interest [326]. It has been demonstrated that the tacrine analogue 7-methoxytacrine (7-MEOTA) and its derivatives have the ability to inhibit the amyloid formation of A β 1–40 peptide while being less toxic than but having pharmacological activity equal to that of tacrine. The other interesting molecule is benzothiazole, one of the most important chemical structures featured in a variety of natural and pharmaceutical agents and, its derivatives [331].

Heterodimerization remains an attractive concept leading to preservation, combination, or improvement of beneficial biological properties of parent compounds. It is believed that it is a valid concept when dealing with diseases as complex as amyloidosis. Furthermore, it provides an opportunity to take advantage of the active linker region which connects parent molecules and, thus, enhance the effects of uniquely designed anti-amyloid compounds [332].

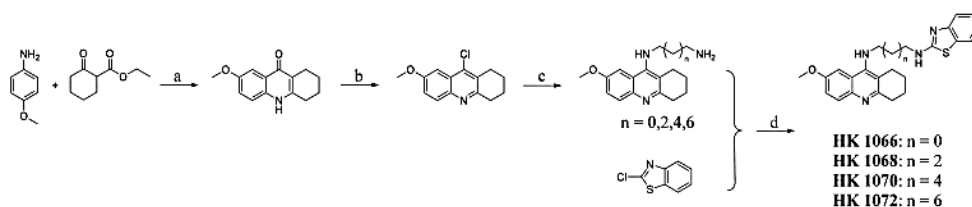
In this chapter, the main focus is to investigate into the effects of hybrid heterodimers on amyloid aggregation of HEWL. A novel series of heterodimers (HK compounds) was prepared through linkage of functional molecules 7-MEOTA and 2-aminobenzothiazole (BTZ) using aliphatic linkers varying in length. The results obtained using various *in vitro* and biophysical methods to show that HK compounds are capable of effective dose dependent inhibition of HEWL amyloid aggregation at acceptable toxicity levels. It was found that heterodimerization greatly improves the anti-amyloid ability of the parent compounds. Moreover, we investigated the structure–activity relationships of the studied molecules. Binding of heterodimers to HEWL mostly depends on a compound's aromatic groups and leads to blocking of the interaction between the β -domain and C-helix regions essential for formation of amyloid cross- β structure. Despite this fact, the length of the

linker is a decisive factor among the HK compounds in terms of their affinity to HEWL as well as their inhibitory activity.

6.2 Materials and methods

6.2.1 Chemicals and reagents

HEWL (L6876, activity ~40,000 units/mg protein, E.C. number 3.2.1.17), thioflavin T (ThT), dimethyl sulfoxide (DMSO), glycine, NaCl, and Dulbecco's Modified Eagle Medium (DMEM) were purchased from the Sigma-Aldrich Chemical Co. (St. Louis, MO, USA). SH-SY5Y human neuroblastoma cell line was purchased from German Collection of Microorganisms and Cell Culture, DSMZ (Braunschweig, Germany), and WST-1 Cell Proliferation Assay Kit (WST-1) from Roche Diagnostics GmbH (Mannheim, Germany). 4,4-Dimethyl-4-silapentane-5-sulfonate sodium salt (DSS), d₆-DMSO, and D₂O were obtained from Cambridge Isotope Laboratories, Inc. (Tewksbury, MA, USA). Citrate was purchased from Merck Millipore (Burlington, MA, USA), and disodium hydrogen phosphate was purchased from HiMedia Laboratories Pvt. Ltd. (Mumbai, India). All chemicals were of analytical reagent grade. Studied 7-MEOTA-2-aminobenzothiazole (BTZ) heterodimers (HK compounds) (Table 6.1) were synthesized at the Department of Chemistry, Faculty of Science, University of Hradec Kralove, Hradec Kralove, Czech Republic. All chemical reagents used for synthesis were purchased from Sigma-Aldrich. Solvents for synthesis were obtained from Penta Chemicals (Prague, Czech Republic).



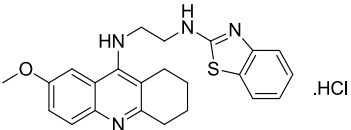
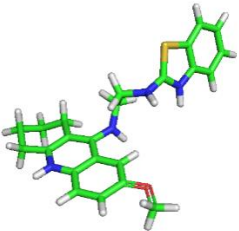
Scheme 6.1. ^aReagents and conditions: (a) toluene, H₂O, diphenyl ether, EtOH, Dean–Stark trap; (b) POCl₃; (c) α , ω -diaminoalkane, phenol; (d) DIPEA, DMF.

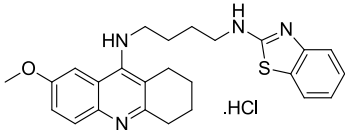
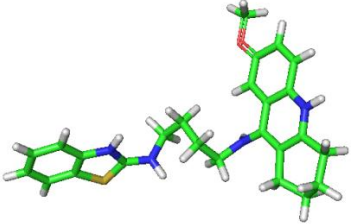
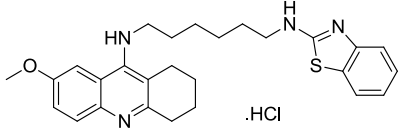
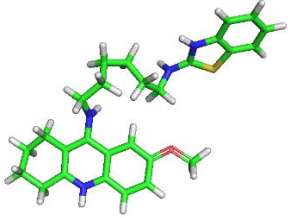
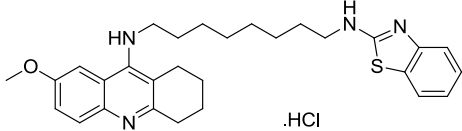
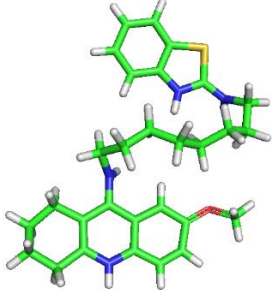
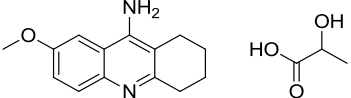

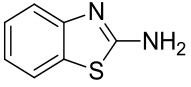
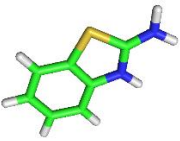
6.2.2 Synthesis of HK Compounds

Novel 7-MEOTA-BTZ heterodimers (HK 1066, HK 1068, HK 1070, and HK 1072) were obtained as depicted in Scheme 6.1. 7-Methoxy-1,3,4,10-tetrahydroacridin-9(2H)-one, 9-chloro-7-methoxy-1,2,3,4-tetrahydroacridine, and N-(7-methoxy-1,2,3,4-tetrahydroacridin-9-yl) alkane diamines were synthesized according to the procedures already reported in the literature [333]. Subsequent coupling with 2-chloro-1,3-benzothiazole in the presence of N, N-diisopropylethylamine (DIPEA) in dimethylformamide (DMF) at 110 °C for 2 h provided target compounds in moderate

yields. All new hybrids were finally structurally characterized in the form of hydrochloride salts by their analytical and spectroscopic data. Round-bottom flask with 2-chlorobenzothiazole (1 equiv.) was purged with argon and treated with DMF (5 ml). Thereafter, N, N diisopropylethylamine (2 equiv.) was added to the mixture. Finally, appropriate α , ω -diaminotacrine derivative (1 equiv.) dissolved in a small amount of DMF was added to the flask. Formed solution was then heated to 110 °C and stirred for 2 h. After cooling to room temperature, the mixture was dissolved in CH₂Cl₂ (3 × 100 ml) and extracted with water (100 ml). Collected organic layers were dried over Na₂SO₄, filtered, and evaporated to give crude product. Purification by column chromatography using ethyl acetate/MeOH/26% aqueous ammonia solution (60/1/0.2) as eluent provided a pure base. Obtained base was dissolved in MeOH and saturated with gaseous HCl. Solvent removal afforded an oily residue which was subsequently washed with acetonitrile to give the final product in the form of hydrochloride salt. The course of the reactions was monitored by thin-layer chromatography on aluminium plates precoated with silica gel 60 F254 (Merck, Czech Republic) and then visualized by UV 254. Melting points were determined on a melting point apparatus M-565 (Büchi, Switzerland) and are uncorrected. Uncalibrated purity was ascertained by LC-UV (at the wavelength of 254 nm) using a reverse phase C₁₈ chromatographic column. All the biologically tested compounds exhibited purity 99% at a wavelength 254 nm. NMR spectra of target compounds were recorded on Varian S500 spectrometer (operating at 500 MHz for ¹H and 126 MHz for ¹³C; Varian Corp., Palo Alto, CA, USA). Chemical shifts are reported in parts per million (ppm). Spin multiplicities are given as s (singlet), d (doublet), dd (doublet of doublets), t (triplet), p (pentet), or m (multiplet). The coupling constants (J) are reported in hertz (Hz). High-resolution mass spectra (HRMS) were determined by Q Exactive Plus hybrid quadrupole-orbitrap spectrometer. All the synthesis and characterization of the HK compounds, 7-MEOTA and BTZ, was done in the Slovak Academy of Sciences, Slovakia.

Table 6.1. The structures of studied HK compounds and 7-MEOTA and BTZ molecules.

Name	2D Structure	3D Structure
<i>HK 1066</i>		

HK 1068		
HK 1070		
HK 1072		
7-MEOTA		
BTZ		

6.2.3 *In vitro* Lysozyme Amyloid Aggregation: ThT Fluorescence Assay

HEWL was dissolved in 70 mM glycine buffer with an addition of 80 mM NaCl at pH 2.7 to a final concentration of 10 μ M. The HEWL solution was incubated at 65 °C for 2 h and stirred at 1200 rpm in thermomixer. After the incubation, the amyloid-specific dye ThT was added, and samples were incubated for another 60 min at 37 °C in dark. The formation of HEWL amyloid fibrils was confirmed by a significant increase in the ThT fluorescence. Measurements were performed in a 96-well plate using a Synergy MX (BioTek) spectrofluorometer. The excitation wavelength was set at 440 nm and the emission recorded at 485 nm. The excitation and emission slits were adjusted to 9.0/9.0

nm, and the top probe vertical offset was 6 mm. This experiment was done in the Slovak Academy of Sciences, Slovakia.

6.2.4 Effect of Compounds on HEWL Amyloid Fibrillization: Determination of IC_{50} Values

Interference of BTZ, 7-MEOTA, and HK compounds with an amyloid aggregation of HEWL was studied using ThT fluorescence assay in the concentration range of 100 pM to 1 mM at the fixed 10 μ M protein concentration. All compounds were dissolved in DMSO. The recorded ThT fluorescence intensities were normalized to the ThT fluorescence of lysozyme amyloid fibrils in the absence of studied compounds. This analysis was performed in the Slovak Academy of Sciences, Slovakia.

6.2.5 Atomic Force Microscopy (AFM)

The sample preparation, data acquisition and analysis was done in the Slovak Academy of Sciences, Slovakia. Samples for AFM were applied on freshly cleaved mica. After 5 min adsorption period the surface of mica was rinsed several times with ultrapure water and left to dry. AFM images were obtained using a scanning probe microscope (Veeco di Innova) in a tapping mode using the NCHV cantilever with a specific resistance 0.01–0.025 $\Omega \cdot \text{cm}^{-1}$. All images are unfiltered.

6.2.6 Attenuated Total Reflectance Fourier Transform Infrared (ATR-FTIR) Spectroscopy

ATR-FTIR spectra were recorded using a Nicolet 8700 Fourier transform infrared spectrometer (Thermo Fisher Scientific) equipped with Smart OMNI-Sampler (diamond crystal). 5 μ l of the sample (50 μ M HEWL, 500 μ M compound) was spread on the diamond surface. Each spectrum represents an average of 254 repetitions, recorded at the resolution of 2 cm^{-1} in amide I region (1700–1600 cm^{-1}). Recorded spectra were smoothed using OMNIC 8 software (Thermo Fisher Scientific) to achieve the quality of spectra adequate for deconvolution. 11-point Savitzky–Golay filter (10.607 cm^{-1}) followed by 7-point Savitzky–Golay filter (6.750 cm^{-1}) was applied. Spectra were subsequently deconvoluted by peak analyzer in OriginPro 8 software (OriginLab Corp.). Baseline was subtracted, and the positions of peaks in amide I region were added manually in correlation with the raw data. To assign peak positions to the secondary structures, measurements were compared against the published literature.[334] Gaussian peak function was used to fit the data, and particular secondary structures content was obtained by Gaussian curves area integration. This experiment was done in the Slovak Academy of Sciences, Slovakia.

6.2.7 Nuclear Magnetic Resonance (NMR)

All NMR experiments were done at 25 °C either on a Bruker Avance III 500 MHz equipped with a 5 mm SMART probe or 700 MHz NMR spectrometer equipped with the RT probe. HEWL samples (500 μ M) were prepared using 10 mM citrate–phosphate buffer with 100 mM NaCl (pH 2.8), and 10% D₂O was added for locking purpose. DSS was used as an internal standard (0.00 ppm). HK 1066 and HK 1072 were first dissolved in d₆-DMSO and then diluted into the same buffer for all the experiments. Two-dimensional (¹H) total correlation spectroscopy (2D TOCSY) and nuclear Overhauser spectroscopy (2D NOESY) were recorded for HEWL in free and bound (1:1 HEWL and ligand) forms with a mixing time of 80 and 150 ms, respectively, and the spectral width was set to 15 ppm in both directions. One dimensional STD NMR was performed using 1 mM concentration of ligand molecules. The chemical shifts of the HEWL from 2D ¹H-¹H TOCSY (mixing time 80 ms) and NOESY (mixing time 150 ms) experiments were assessed and compared with the reference chemical shift, deposited in BMRB [318]. The identity of the chemical shifts of the HEWL residues interacting with HK compounds obtained from MD simulation study has been also subsequently cross validated. STD NMR spectra were acquired at a ligand/HEWL mixture ratio of 300:1. Selective irradiation of HEWL was achieved by a train of Gaussian-shaped pulses with a 1% truncation and each of 49 ms in duration and separated by a 1 ms delay. A total of 40 selected pulses were applied, leading to a total time of saturation of 2 s. The so-called on resonance for HEWL was fixed at 0.2 ppm, and off-resonance was at 40 ppm, where neither protein nor the ligand resonances were present. Subtraction of the two spectra (on-resonance–off-resonance) by phase cycling leads to the difference spectrum that contains signals arising from the saturation transfer. The reference spectrum was recorded with 640 scans, while the difference spectrum was obtained with 1280 scans. Data processing was performed using TOPSPIN program suite for all the spectra, and peak assignment was done using the SPARKY software.

6.3 Results and discussion

Heterodimerization of small molecules represents a novel approach allowing researchers to improve anti-amyloid activities of compounds. We synthesized heterodimeric 7- MEOTA–BTZ molecules (HK compounds 1066, 1068, 1070, and 1072) by linking parent molecules 7-MEOTA and BTZ using variable length aliphatic linkers (C_n; n = 2, 4, 6, or 8). The chemical structures of the compounds are displayed in Table 6.1. The parent molecules (7-MEOTA and BTZ) as well as four heterodimers were investigated to determine whether they are able to inhibit HEWL amyloid aggregation. *In vitro*

experiments were used to examine their mechanism of action and to identify relationships between the molecular structure of heterodimers and their inhibitory activity.

6.3.1 Inhibition of HEWL Amyloid Fibrils Formation and Determination of IC_{50} Values.

The ability of the studied compounds to inhibit amyloid aggregation of HEWL was examined using the Thioflavin T (ThT) based fluorescence assay. The extent of inhibition of amyloid fibrillization was studied for all six compounds individually and an equimolar mixture of 7-MEOTA and BTZ at concentration gradients ranging from 100 pM to 1 mM and fixed 10 μ M HEWL concentration. The relative fluorescence intensities normalized to the fluorescence signal of HEWL amyloid fibrils alone (taken as 100%) are presented in Figure 6.1. As a decrease in fluorescence indicates the ability of compounds to inhibit the amyloid fibrils' formation, we could conclude that all of the studied compounds inhibit HEWL amyloid fibrillization to some extent. The efficiency is affected by the compound's concentration, heterodimerization, and structure.

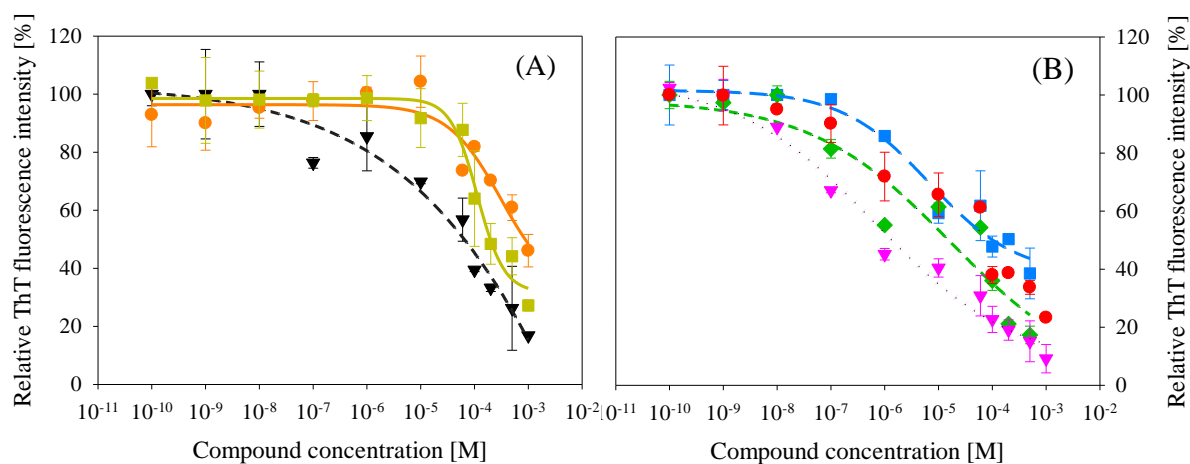


Figure 6.1. ThT fluorescence intensities of HEWL fibrillization in presence of increasing concentration of (A) 7-MEOTA (black triangles), BTZ (orange circles) and their equimolar mixture (dark yellow squares); (B) HK 1066 (blue circles), HK 1068 (red circles), HK 1070 (green prisms) and HK 1072 (magenta triangles). ThT fluorescence intensities were normalized to fluorescence of 10 μ M HEWL fibrils without added compounds (taken as 100 %). Experiments were performed as triplicates; error bars represent the average deviation of three separate samples.

A concentration gradient of 7-MEOTA resulted in a steady decline of ThT fluorescence intensity starting at 100 nM concentration (Figure 6.1 (A), black triangles). Regarding BTZ (Figure 6.1 (A), orange circles) and an equimolar mixture of parent molecules (Figure 6.1 (A), dark yellow squares), we observed a steep decline of ThT fluorescence intensity starting from \sim 80 μ M concentration. Moreover, the efficiency of the equimolar mixture

was worse than 7-MEOTA alone, suggesting a competitive binding of parent molecules. At the highest used concentration (1 mM) the fluorescence intensity reached ~15% for 7-MEOTA, ~40% for BTZ, and ~30% for their mixture, relative to the signal observed for untreated HEWL amyloid fibrils. That corresponds to ~85%, ~60%, and 70% inhibitory activity for 7-MEOTA, BTZ, and their mixture, respectively. On the other hand, data collected for heterodimer HK 1072 (Figure 6.1 (B), magenta triangles) showed a steady decline of the ThT fluorescence with increasing compound concentration starting from the picomolar region. At the highest (1 mM) concentration only ~10% fluorescence signal was observed in comparison to fluorescence detected for untreated lysozyme fibrils. That corresponds to ~90% inhibition of HEWL amyloid aggregation. The inhibitory activity of compounds with shorter linker slightly decreased, namely ~80% inhibition for HK 1070 (Figure 6.1 (B), green diamonds) and ~75% inhibition for HK 1068 (Figure 6.1 (B), red circles), respectively. The heterodimer with the shortest linker, HK 1066 (Figure 6.1 (B), blue squares), inhibited the HEWL amyloid aggregation by roughly 60%. Overall, the obtained data suggest that the inhibitory activity of parent molecules 7-MEOTA, BTZ, and their mixture without heterodimerization is significantly lower in comparison to that of the heterodimers. Moreover, an effect of linker length on the inhibitory activity of amyloid aggregation of HEWL was observed. The data presented in Figure 6.1 (B) suggest that elongation of the linker had a positive effect on a compound's capability to suppress amyloid aggregation of HEWL. The highest inhibition was observed for compound HK 1072 with the longest linker, eight carbons long. The gradual decline in inhibitory activity was observed for heterodimers with a shorter linker length. For better quantification of inhibitory properties of studied compounds, the fluorescence intensity values were fitted. The obtained curves were used for calculation of IC_{50} values (half-maximal inhibitory concentrations of compounds), which are summarized in Table 6.2. BTZ showed the lowest inhibitory potential, with the highest IC_{50} value equal to 871 μ M. The second parent molecule, 7-MEOTA, exhibited better anti-amyloid properties with an $IC_{50} \approx 67$ μ M. Their equimolar mixture had a higher IC_{50} value than all the heterodimers, equal to 196.7 μ M. Importantly, all heterodimers with the exception of HK 1066 were more effective at inhibiting HEWL amyloid aggregation than parent molecules BTZ and 7-MEOTA or their equimolar mixture.

Table 6.2. IC₅₀ values of 7-MEOTA, BTZ, HK compounds corresponding to their ability to inhibit amyloid aggregation of HEWL. Data represent the mean value obtained from three independent measurements and an average deviation.

Compound	IC₅₀ [μM]
<i>7-MEOTA</i>	66.8 ± 4.4
<i>BTZ</i>	871.4 ± 64.3
<i>eq. mixture</i>	196.7 ± 16.5
<i>HK 1066</i>	115.6 ± 11.3
<i>HK 1068</i>	48.7 ± 7.6
<i>HK 1070</i>	15.4 ± 0.9
<i>HK 1072</i>	1.6 ± 0.3

Moreover, it was found that, with longer aliphatic linker of heterodimers, the inhibitory efficiency of the compounds increased in correspondence to the decline of their IC₅₀ values. The most effective compound was the heterodimer HK 1072 with an IC₅₀ ≈ 1.6 μM, which is 2 orders of magnitude better than that of BTZ and 1 order enhancement in comparison to 7-MEOTA. The obtained results suggest that both the heterodimerization and linker length are important factors determining a compound's inhibitory ability.

6.3.2 Morphology of Amyloid Aggregates.

Atomic force microscopy (AFM) was used to visualize morphological changes of HEWL amyloid fibrils forming in the presence of the studied compounds (Figure 6.2). For BTZ (Figure 6.2 (C)) the quantity and morphology of the amyloid fibrils were comparable to those of HEWL amyloid aggregates formed alone, confirming very low inhibitory activity of this compound (Figure 6.2 (A)). A reduction of the number of amyloid aggregates was detected for lysozyme fibrillization in the presence of compound 7-MEOTA (Figure 6.2 (B)). Among the heterodimers, the lowest amount reduction of the amyloid fibrils was observed for HEWL fibrillization in the presence of HK 1066 (Figure 6.2 (D)) corresponding to its higher IC₅₀ value. Addition of HK 1068 (Figure 6.2 (E)) caused morphology and quantity changes similar to those observed for 7-MEOTA. Considerably fewer aggregates were formed in the presence of compound HK 1070 (Figure 6.2 (F)), and aggregates formed in the presence of HK 1072 (Figure 6.2 (G)) in particular

appeared much shorter and more amorphous compared to other samples. AFM images of formed aggregates are in a very good correlation with calculated IC₅₀ values and support results obtained from ThT fluorescent assay.

6.3.3 Secondary Structure Determination: ATR FTIR Spectroscopy.

In order to analyse differences in the content of secondary structure of HEWL amyloid fibrils formed alone and in the presence of studied compounds, samples were examined using ATR FTIR spectroscopy. The FTIR spectra recorded for native and untreated HEWL amyloid fibrils as well as for lysozyme aggregates formed in the presence of parent molecules BTZ, 7-MEOTA, and heterodimers HK 1068 (representing compounds with the short linker) and HK 1072 (compound with the longest linker and the best inhibitory activity) are presented in Figure 6.3 (A).

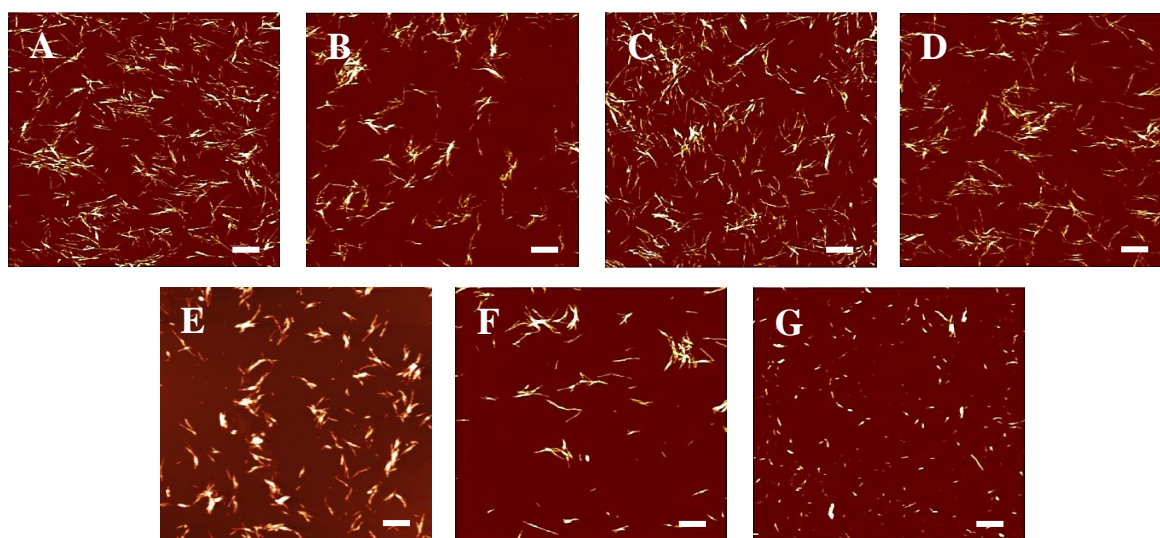


Figure 6.2. AFM images of HEWL fibrils formed alone (A) or in a presence of studied compounds 7-MEOTA (B), BTZ (C), HK 1066 (D), HK 1068 (E), HK 1070 (F) and HK 1072 (E). The concentration of HEWL was 10 μ M and the concentration of added compounds was 500 μ M. Bars represent 1 μ m.

The spectra were deconvoluted to calculate the particular protein secondary structures (Table 6.3). The α -helical and β -sheet content has been determined for all samples and is presented in Figure 6.3 (B). The absorption spectrum of native HEWL in the amide I region (Figure 6.3 (A), green dashed line) shows wide bands at 1653 and 1661 cm^{-1} corresponding to \sim 41% α -helical content (Figure 6.3 (B), green patterned column), which is in agreement with other studies. Bands at 1625 and 1636 cm^{-1} represent \sim 24% β -sheet content (Figure 6.3 (B), green full-colour column). In contrast, HEWL amyloid fibrils formed alone (Figure 6.3 (A), blue dotted line) have bands at 1624 and 1636 cm^{-1} , indicating a significant

increase in β -sheet content, characteristic for HEWL amyloid fibrils. Calculated β -sheet content for HEWL amyloid fibrils was $\sim 46\%$ (Figure 6.3 (B), blue full-colour column). This significant increase was mainly at the expense of lower α -helical content in HEWL amyloid fibrils ($\sim 15\%$) (Figure 6.3 (B), blue patterned column). Addition of studied parent molecules BTZ (Figure 6.3 (A), orange line) and 7-MEOTA (Figure 6.3 (A), black line) led to slight changes in the spectra compared to the ones detected for HEWL fibrils; interestingly, the β -sheet content was higher (58% for 7-MEOTA and 52% for BTZ) (Figure 6.3 (B), black and orange full-colour columns) than we observed for lysozyme fibrils alone (46%). An effect of HK 1068 and HK 1072 heterodimers on the secondary structure content of HEWL amyloid aggregates was significantly different. Bands at 1623 and 1636 cm^{-1} (Figure 6.3 (A), red and magenta lines) related to the β -sheet secondary structure were still observed, however at much lower intensity. The spectral deconvolution (Figure 6.3 (B), red and magenta full-coloured columns) determined $\sim 29\%$ and $\sim 22\%$ β -sheet content for HK 1068 and HK 1072, respectively. Interestingly, the observed decrease in β -sheet content in comparison to HEWL amyloid fibrils prepared alone was mostly at the cost of an extensive increase of random coil ($\sim 10\%$), β -turn content ($\sim 4\text{--}10\%$), and a minor increase of the α -helical structures ($\sim 5\%$). These results indicate that the heterodimers HK 1068 and HK 1072 were able to prevent the formation of cross- β structures unique for amyloid fibrils, while also conserving part of α -helical structure. The content of secondary structures is shown in Table 6.3.

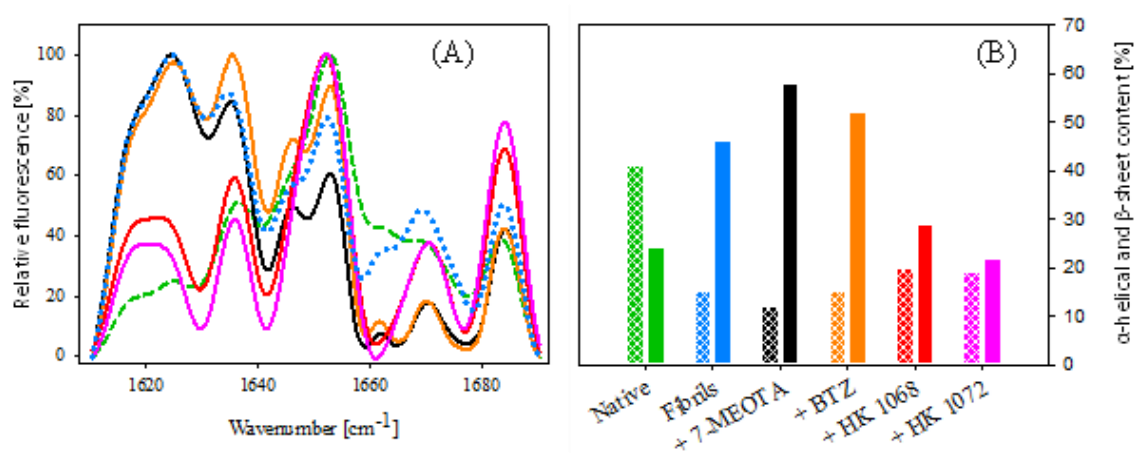


Figure 6.3. (A) ATR FTIR spectra of native $50\ \mu\text{M}$ HEWL (green dashed line) and $50\ \mu\text{M}$ HEWL amyloid fibrils after fibrillization without added compound (blue dotted line) or in presence of $500\ \mu\text{M}$ compound BTZ (orange line), 7-MEOTA (black line), HK 1068 (red line) and HK 1072 (magenta line). (B) α -helical (patterned columns) and β -sheet (full-colour columns) content

determined for native HEWL, HEWL fibrils and HEWL fibrillized in presence of compounds BTZ, 7-MEOTA, HK 1068 and HK 1072.

6.3.4 Binding Epitope of HEWL: Small Molecule Interaction.

Two-dimensional homonuclear NOESY experiment was done to elucidate the structural perturbation of HEWL in the presence of HK 1066 and HK 1072 at an equimolar ratio. Figure 6.4 depicts the superimposed spectra of HEWL in the absence and presence of ligands (HK 1066 and HK 1072). After careful investigation, several chemical shift perturbations (CSPs) were observed in both cases, but HK 1066 showed peak broadening effect against several amino acid residues such as Asp48, Asp52, Asn59, and Trp108 (Figure 6.4 (A)). The same effect was also observed for C α H of Ile98 and C β Hs of Gln57. On the contrary, in the presence of HK 1072 residues, Asn59 and Trp108 showed a downfield CSP of \sim 0.06 and 0.02 ppm, respectively (Figure 6.4 (B)).

Table 6.3. Secondary structure percentage distributions of samples measured by FTIR with corresponding peak positions.

HEWL	Native		Fibrils		+7-MEOTA		+BTZ		+HK 1068		+HK 1072	
	Peak [cm ⁻¹]	%	Peak [cm ⁻¹]	%	Peak [cm ⁻¹]	%	Peak [cm ⁻¹]	%	Peak [cm ⁻¹]	%	Peak [cm ⁻¹]	%
α-helical	1653 1661	41	1653 1661	15	1653 1662	12	1653 1662	15	1653	20	1654	19
β-sheet	1625 1636	24	1624 1636	46	1625 1636	58	1625 1636	52	1623 1636	29	1623 1636	22
β-turn	1670 1683	17	1669 1684	23	1771 1683	12	1670 1684	10	1670 1684	27	1670 1684	33
Side chain	1617	3	1616	8	1616	7	1617	8	1616	7	1617	7
Random coil	1646	14	1645	8	1646	11	1646	14	1648	18	1648	18

Other amino acid residues responsible for binding to HK 1072 remained unchanged in the NOESY spectrum. Additionally, the remarkable CSPs were observed for the indole (N ϵ H) ring protons of Trp62 and Trp111 of HEWL in the presence of the ligands HK 1066 and

HK 1072 (Figure 6.5). Trp62 showed ~ 0.13 and 0.08 ppm downfield CSP for HK 1066 and HK 1072, respectively, while Trp111 showed ~ 0.07 and 0.04 upfield CSPs after addition of equimolar concentrations of HK 1066 (Figure 6.5 (A)) and HK 1072 (Figure 6.5 (B)), respectively. It is noteworthy that the Trp63 and Trp108 of HEWL have been shown to interact with the HK compounds in molecular docking analysis (Appendix VI, Figure S6.1), but these residues showed minimal (in presence of HK 1066) to no (in presence of HK 1072) CSPs in the NOESY spectrum. Surprisingly, their neighbouring residues, such as Trp62 and Trp111, showed significant chemical shift perturbation upon addition of the equimolar concentration of the HK ligands. Generally, aromatic–aromatic interactions along with hydrophobic stacking plays a crucial role to halt the amyloid aggregation of HEWL molecules. Next, saturation transfer difference (STD) NMR was performed to define the epitope of the ligands, binding to HEWL. In this study, the ligand to HEWL concentration was kept at 300:1 ratio to enhance the “STD amplification factor”. Careful analysis of the data suggests that both HK compounds interact with HEWL as evidenced by strong STD peaks of the $-\text{CH}_2/-\text{CH}_3$ groups along with comparatively low signals from aromatic ring protons (Figure 6.6). Interestingly, the acyl chain protons (linker protons) of HK 1072 have shown comparatively stronger interaction than those associated with HK 1066 (as shown in inset), correlating well with the previous observations like ThT assays. One of the generally accepted therapeutic strategies for amyloidosis is the inhibition of amyloid aggregation of peptides and polypeptides and/or removal of insoluble amyloid fibrils from the affected tissue.

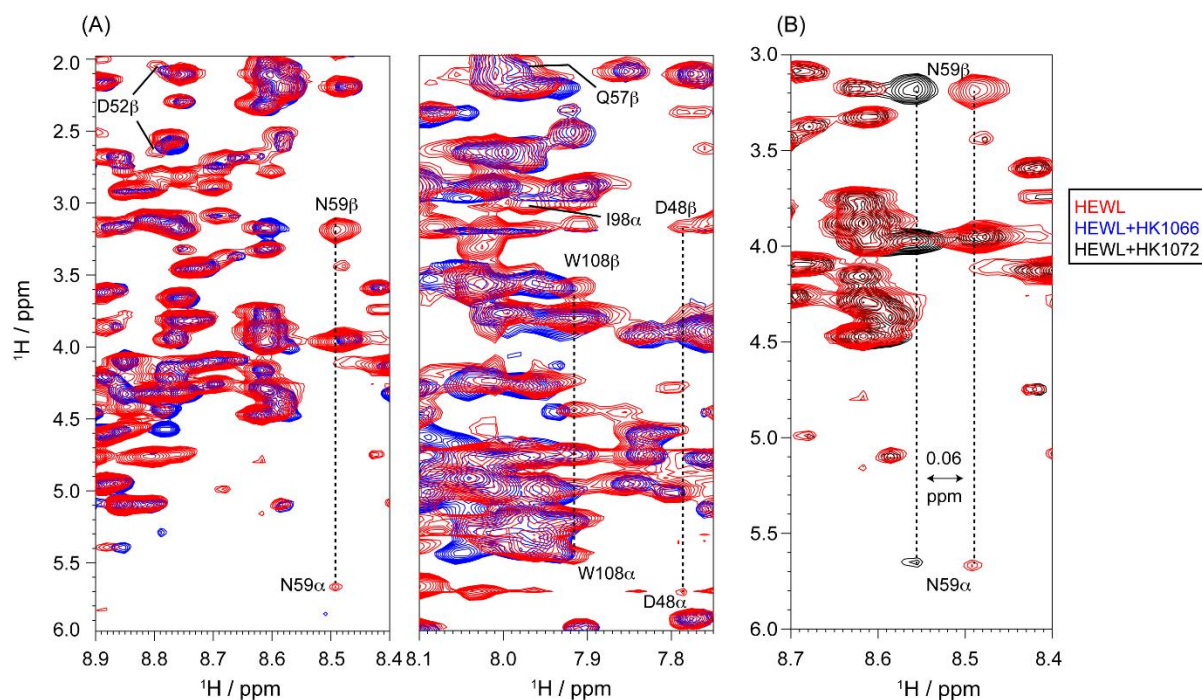


Figure 6.4. 2D NOESY spectra of free HEWL (red) and in the presence of either (A) HK1066 (blue) or (B) HK1072 (black). The superimposed spectra confirm the residue-specific chemical shift changes. CSPs were obtained for several residues that are involved in binding with the ligands that were obtained by the molecular docking and are marked by arrows. The experiment was performed using Bruker Avance III 700 MHz spectrometer and at 25 °C.

There are many reports documenting a great potential of small molecules to interfere with amyloid fibrillization of peptides and polypeptides leading to decreasing of the amount of the amyloid aggregates [335,336]. It was found that small molecules interfere with amyloid fibrillization through interaction with various amyloidogenic species produced in the aggregation process, and several mechanisms of action were suggested concerning their anti-amyloid activity [337]. Re *et al.* suggested that intercalation of a small molecule within grooves created by β -sheets in both soluble oligomeric forms as well as in the mature amyloid fibrils leads to inhibitory activity [338]. Another proposed mode of action rests on the binding of a small molecule into the hydrophobic region of peptides and polypeptides and interaction with neighbouring amyloidogenic residues, subsequently leading to inhibition of self-assembly process and amyloid polymerization [332]. In 2014, Takai *et al.* discussed the effects of amino acids on the amyloid aggregation of lysozyme showing that the presence of cysteine significantly contributes to the inhibition of amyloid formation by noncovalent interaction between the thiol group of cysteine and the core sequence of lysozyme [339]. Ascorbic acid inhibited amyloid fibrillization of lysozyme. Proposed

mechanism of action suggests binding to the aggregation-prone region of lysozyme, stabilizing its partially unfolded state, and thus preventing further conformational changes leading to fibrillization [335].

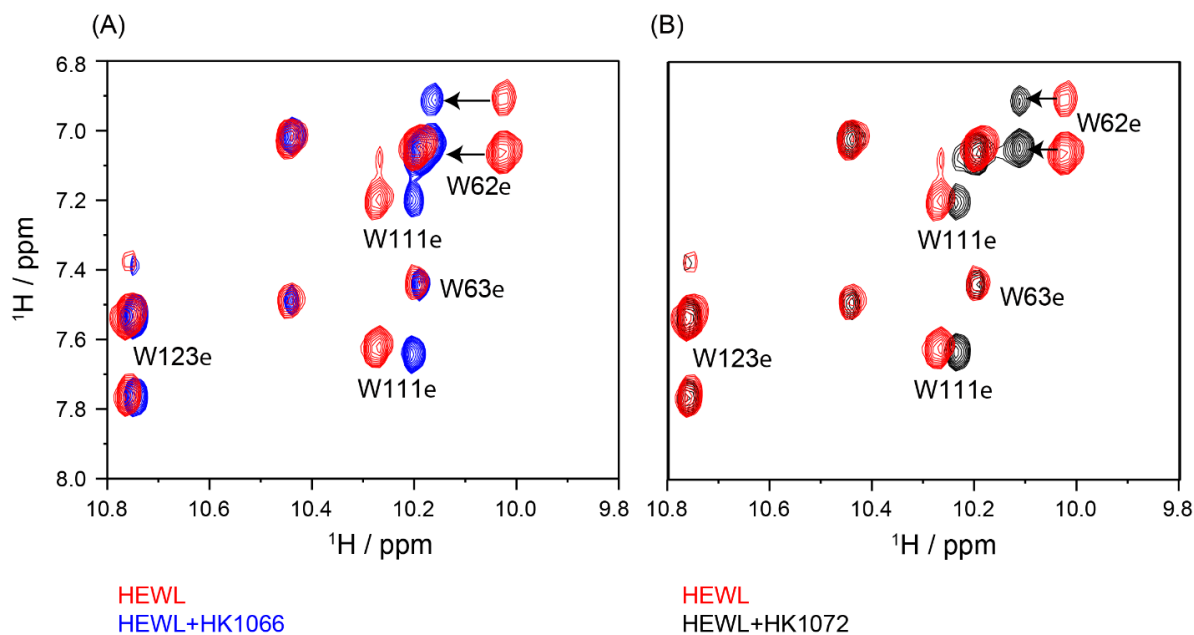


Figure 6.5. Chemical shift perturbation of indole (NεH) ring proton belonging to tryptophan residues of HEWL in the presence of either HK 1066 (A) or HK 1072 (B), indicating that these moieties play a crucial role during binding of the ligand molecules.

Structure–activity relationship study of several small molecules toward the amyloid aggregation of peptides and polypeptides has been performed. It was found that presence of aromatic structures in small molecules represents important factor for anti-amyloid properties of many compounds. To improve the effectivity of small compounds to influence amyloid aggregation the accumulation of cyclic structures into one multiple cyclic compounds was suggested. Lieu *et al.* demonstrated that the formation of lysozyme amyloid fibrils was markedly inhibited by the presence of rifampicin and its analogue p-benzoquinone in a dose-dependent fashion [340,341]. Phenolic and polyphenolic compounds have been reported to inhibit the amyloid formation of peptides and polypeptides [335,336]. Catechol and hydroquinone inhibited lysozyme amyloid aggregation by covalent binding to the peptide chain, forming quinoproteins [335]. A number of acridine derivatives have shown the ability to inhibit lysozyme amyloid aggregation [337]. Many other small polycyclic compounds have been tested and acknowledged as potential drug candidate prototypes for the treatment of amyloidosis [342]. Based on this knowledge, we decided to study the effect of two compounds 7-MEOTA and BTZ on the amyloid aggregation of

HEWL. Both molecules consist of two (BTZ) or three (7-MEOTA) cyclic structures. Moreover, 7-MEOTA belongs to tacrine analogues for which the anti-amyloid activities have already been reported. We have found that these molecules were able to affect lysozyme amyloid fibrillization to some extent. The 7-MEOTA is quite effective with an IC_{50} value of 66.8 μM . Surprisingly, the efficiency of BTZ to inhibit HEWL fibrillization is significantly lower corresponding to an IC_{50} value of 871.4 μM . We suggest that the reason behind this difference is lack of vdW interaction leading to lower total affinity. Overall, our data support finding that small molecules containing multiple cycles are able to interfere with amyloid aggregation. Currently, there is a new strategy to improve the inhibitory efficiency of small compounds based on combining multiple cyclic functional molecules into one heterodimeric compound. The aim is an enhancement of anti-aggregation capabilities due to the synergy of two or more active structures. Besides the aromatic multicycles, a linker connecting two functional molecules has proven to be another promising structure to optimize and modulate the effects of heterodimers. The relationship between inhibitory potency of heterodimers designed against amyloid aggregation, the structure of functional molecules and properties of the linker has been already reported [321]. In 2007, Reinke and Gestwicki defined a narrow region of optimal linker length and flexibility in case of curcumin derivatives [326]. Both these parameters strongly influenced the potency of studied compounds against amyloid-beta aggregation. In 2018, Ulicna *et al.* described a series of tacrine–coumarine heterodimers effective against amyloid aggregation of lysozyme [337]. These derivatives differed in linker length as well as its structure. Compounds containing plain aliphatic linker have shown the greatest inhibition efficiency. It has been demonstrated that linker longer than $\sim 9 \text{ \AA}$ inhibited the formation of lysozyme amyloid fibrils at lower potency, suggesting an upper limit to the effective length of linker region.

Our results obtained for the studied heterodimers consisting of 7-MEOTA and BTZ functional molecules connected by aliphatic linker point to their significantly higher inhibitory activity compared to separate parent molecules. The IC_{50} values of studied heterodimers were lower (HK 1068, 48.7 μM ; HK 1070, 15.4 μM ; HK 1072, 1.6 μM) than the IC_{50} of functional molecules (BTZ, 871.4 μM ; 7-MEOTA, 66.8 μM) with exception of derivative HK 1066 (115.6 μM). These results indicate that heterodimerization improves the anti-amyloid properties of the parent molecules. The detailed analysis of the obtained results suggests that elongating the linker region increased the efficiency of the

heterodimers. Considering the functional molecules in heterodimers were identical, we suggest that the length of the linker region plays an important role in compounds anti-amyloid potency. The data obtained using ThT fluorescence assay were confirmed by microscopy, namely by AFM. Negligible changes in the amount and morphology of amyloid fibrils were observed after treatment of HEWL fibrillization with BTZ alone. Moderate inhibitory efficiency was detected for the second parent molecule 7-MEOTA. The effect of heterodimerization and elongation of the linker was evident as changes in the amount and also morphology got more apparent in the presence of the heterodimers HK 1070 and HK 1072.

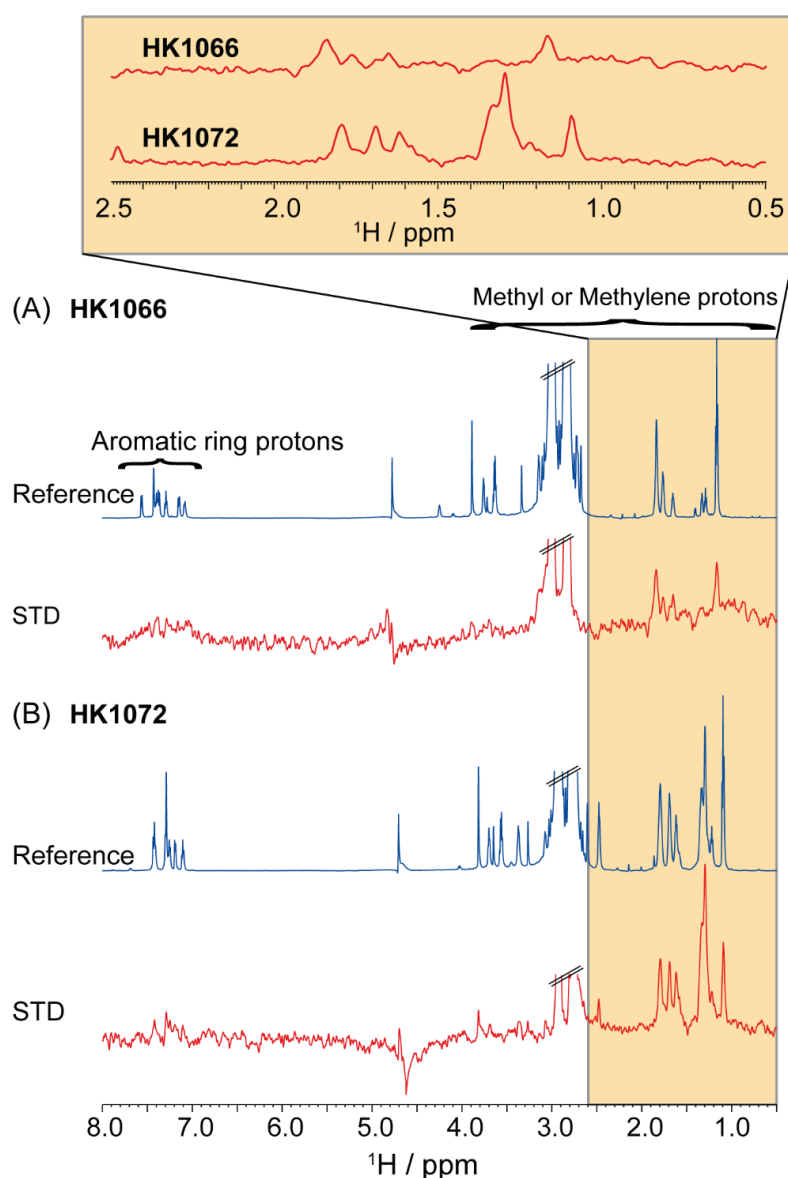


Figure 6.6. 1D STD NMR analysis of free and bound HK 1066 and HK 1072 in the presence of HEWL. The aliphatic (CH₂/CH₃) and aromatic ring protons of HK compounds are in close

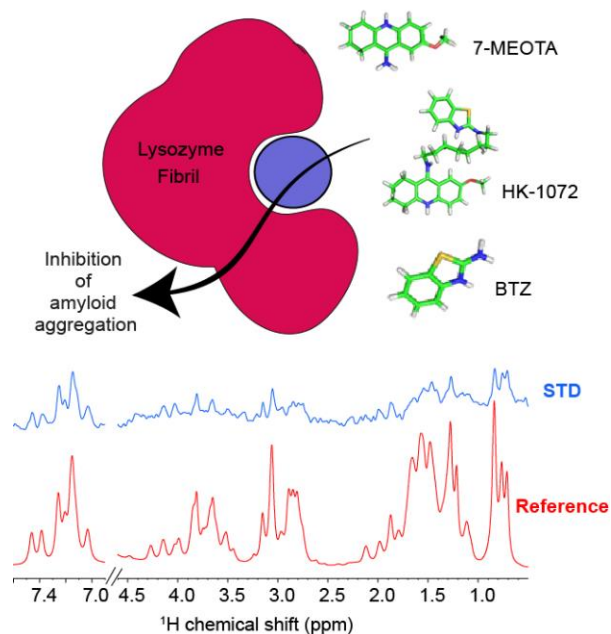
proximity to the HEWL; however, relatively stronger STD signal was observed for methylene protons of HK 1072 in comparison to HK 1066.

ATR FTIR data supported the previous results since HEWL fibrillization in the presence of parent molecules, BTZ and 7-MEOTA, leads to subtle changes in the protein secondary structure and notable β -sheet content increase. On the other hand, the inhibitory activity of the heterodimers HK 1068 and HK 1072 resulted in an extensive decrease in the β -sheet content and minor preservation of the α -helical structure in produced HEWL amyloid fibrils. The two dimensional NMR analysis revealed the atomistic details of the interactions between the HK compounds and HEWL. The chemical shift perturbations indicates that the specific residues directly interact with the HK compounds in the solution. Furthermore, The STD analysis shed more light into the binding mechanisms. The results indicates that the linker region interacts with residues in close proximity to the C-helix domain (residue 98-109). The presence of heterodimer in binding site possibly inhibits the interaction between b-domain and C-helix, halting the formation of the cross-beta structure. Elongation of the linker ultimately enhances a compound's ability to prevent this interaction by greater steric obstruction.

6.4 Conclusion

Combining multiple functional moieties while conserving their fundamental properties in one molecule with enhanced activity is a novel approach to target amyloidoses. In this study, the activity of 7-MEOTA–BTZ heterodimers, HK compounds, toward amyloid aggregation of lysozyme was investigated. Using several *in vitro* techniques, it is showed that heterodimerization has a substantial impact on the effectiveness of the compounds. As a result, HK compounds exhibited a much higher ability to inhibit amyloid aggregation of HEWL in comparison to their parent molecules. When certain conditions are met, namely the linker length, inhibitory efficacy improvement was observed. We suggest that this dependency is connected to the interaction of the aliphatic linker with residues in the C-helix sequence (98–109) of the HEWL molecule. It has been demonstrated that elongation of the linker leads to the higher affinity of HK compounds. As the Vander Waal's interaction of the linker region increases, it helps the BTZ moiety to bind more effectively with HEWL. We also suggest that their anti-amyloid activity is related to the steric obstruction between the β -sheet-rich and C-helix regions of the HEWL molecule, which are considered essential for the formation of the amyloid structures.

The obtained results represent an important contribution for the recent rational design of potential lead small molecules with anti-amyloid properties, and the studied heterodimers are prospective candidates for the treatment of systemic lysozyme amyloidosis and other amyloid-related diseases.



6.5. Appendix VI

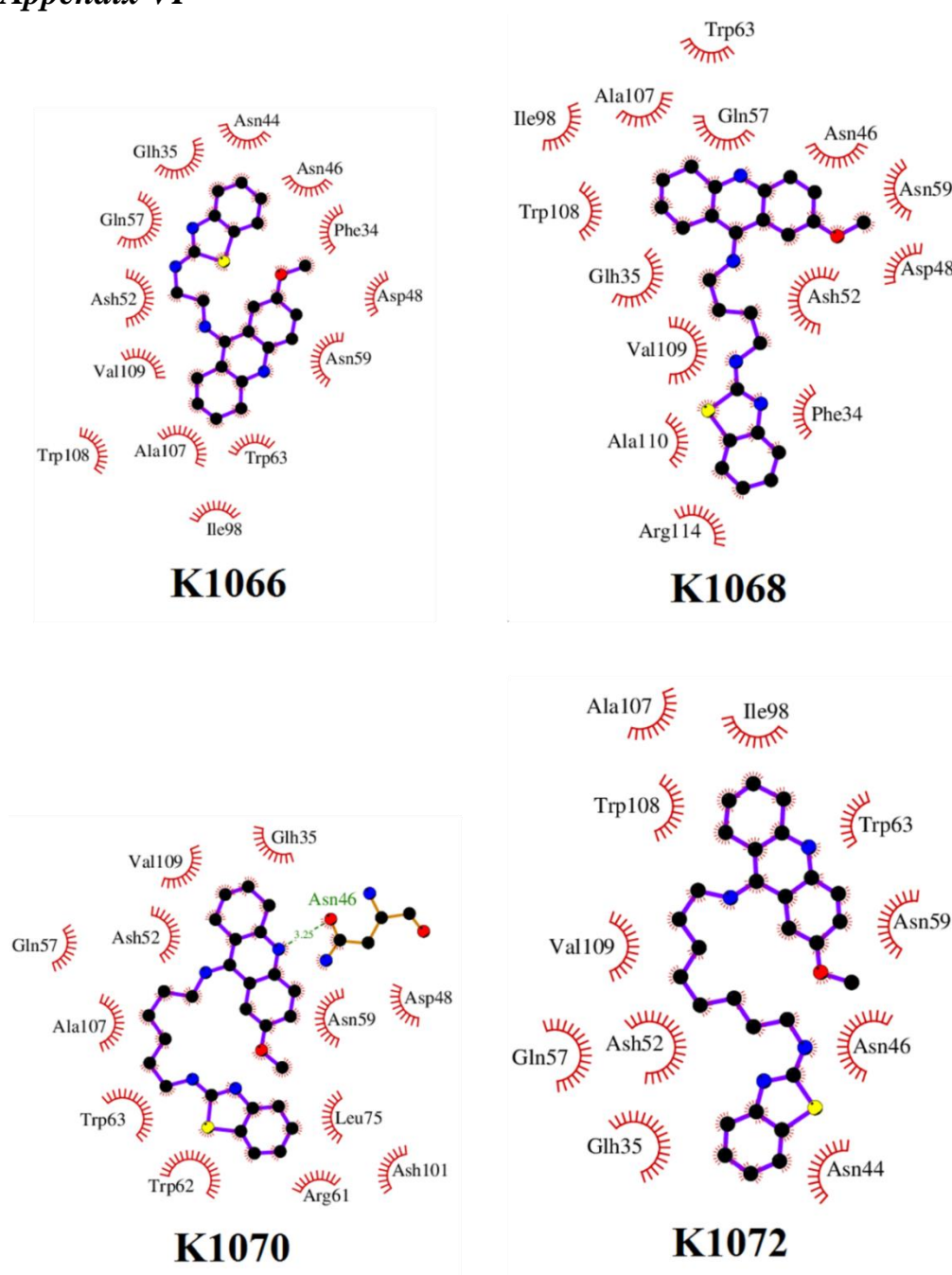


Figure S6.1. Contact networks of four compounds *HK 1066*, *HK 1068*, *HK 1070*, and *HK 1072* in the best docking mode. Red “eyes” refer to non-bonded contacts, while the green dashed line denotes *hydrogen bonds*. The plots were created by using LigPlot+ version 1.4.4.

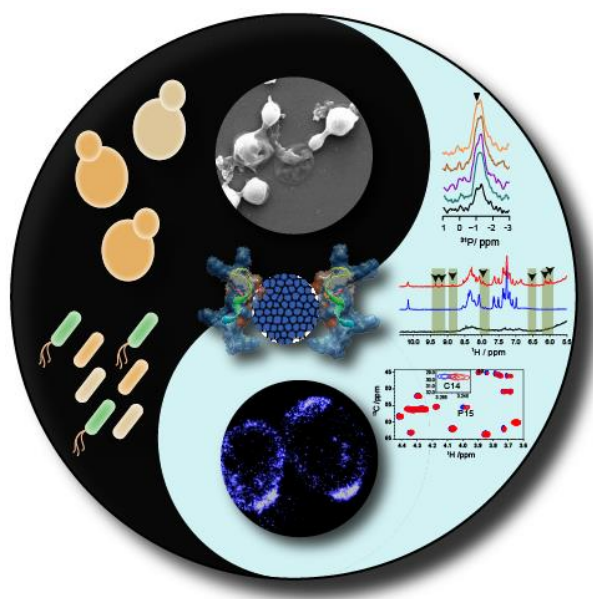
Summary and future outlook

Quick and powerful actions are urgently needed to combat the continuous uprising of MDR pathogens otherwise we will be helpless in the forthcoming antimicrobial crisis. AMPs have already proven their potency to be used as an alternative arsenal against a broad range of pathogens including viruses, bacteria, fungus and protozoa. Despite past failures, in recent years a steady increase of both AMPs and AMP mimicked antimicrobial in clinical trials is highly encouraging. Failures of AMPs in clinical trials could be attributed to less clear efficacy, inappropriate study design or inferiority over conventional antibiotics. As a result, in future clinical testing of AMPs, practical techniques should be addressed, as we have gained the following lessons: (1) The use of AMPs may go beyond FDA-approved clinical indications; (2) determining the most effective dose and administration regimen may reduce cytotoxicity of AMPs; (3) molecules efficacy can be demonstrated in equivalence or non-inferiority trials with an antibiotic as a comparator; (4) bacterial resistance development should be included as one of the primary outcome parameters in clinical trials of AMPs; (5) bioavailability and effectiveness need to be increased by employing appropriate delivery methods and, (6) clinical trials may include combinations of AMPs with conventional antibiotics or other drug modalities for enhanced antibacterial activity. Taking these lessons into account, a growing number of AMPs may enter into the market as multi-functional, powerful, and long-lasting antimicrobial agents against a variety of infectious disorders.

Incorporation of nanotechnology in the AMP field has opened endless opportunities starting from potent antimicrobial drug against MDR strains to targeted drug delivery, multimodal imaging, and rapid diagnostics as discussed in this thesis. However, these kinds of nanoparticle conjugated peptide-based drugs are still stuck in clinical trials and not available in the market to date. The following reasons are the main obstacles that mainly hinder the pathway. (1) The physical and chemical interaction of such AMP-NP conjugates in biological systems like bloodstream and intracellular regions, is not fully explored. (2) AMPs are not adequately protected even after conjugation with NPs and often the whole system either gets entrapped in the lysosomal pathway, or the peptides get degraded after unloading from carrier molecules. (3) The extent of immunogenicity of the designed AMP-NP complex should be addressed, which is one of the main reasons for the failure of such drugs in clinical trials. (4) Conjugation of AMPs with NPs via covalent bonds often compromises with its activity and changes the three-dimensional structure. Lastly, (5) the

production cost of both AMPs and NPs at industrial scale is still a significant problem, rendering them commercially non-viable.

After proper addressing the above concerns, the AMP-NP system will also undoubtedly provide a new arsenal to fight against MDR and XDR pathogens in clinical and healthcare systems along with AMPs itself. Furthermore, with the advancement in nanotechnology, one day, it will be possible to diagnose any disease very quickly and accurately, which will lead to rapid treatment at an early stage of a particular disease.



The above theme is mainly based on ancient Chinese philosophical concept of dualism termed as ‘yin & yang’, which stands for negative and positive, respectively. Some bacteria and fungus are good and beneficial but on the other side some are bad for human health. Similarly, some traditional antibiotics have severe side effects but at the same time they save lives. The major focus of this thesis was to study some efficient peptide-based antibiotics that have lower toxicity but have higher antimicrobial activity. The quantum dot conjugated system provided additional features to be used as a diagnostic tool for imaging purposes.

References

1. Phelps, M.; Perner, M.L.; Pitzer, V.E.; Andreasen, V.; Jensen, P.K.M.; Simonsen, L. Cholera Epidemics of the Past Offer New Insights Into an Old Enemy. *J Infect Dis* **2018**, *217*, 641-649, doi:10.1093/infdis/jix602.
2. Strebhardt, K.; Ullrich, A. Paul Ehrlich's magic bullet concept: 100 years of progress. *Nat Rev Cancer* **2008**, *8*, 473-480, doi:10.1038/nrc2394.
3. Tan, S.Y.; Tatsumura, Y. Alexander Fleming (1881-1955): Discoverer of penicillin. *Singapore Med J* **2015**, *56*, 366-367, doi:10.11622/smedj.2015105.
4. Davies, J.; Davies, D. Origins and evolution of antibiotic resistance. *Microbiol Mol Biol Rev* **2010**, *74*, 417-433, doi:10.1128/MMBR.00016-10.
5. Livermore, D.M. The need for new antibiotics. *Clin Microbiol Infect* **2004**, *10 Suppl 4*, 1-9, doi:10.1111/j.1465-0691.2004.1004.x.
6. Savage, N. Overcoming resistance. *Antimicrobial resistance 2020*, pp. S55-S56.
7. Kupferschmidt, K. Resistance fighters. *Science* **2016**, *352*, 758-761, doi:10.1126/science.352.6287.758.
8. Terreni, M.; Tacani, M.; Pregnolato, M. New Antibiotics for Multidrug-Resistant Bacterial Strains: Latest Research Developments and Future Perspectives. *Molecules* **2021**, *26*, doi:10.3390/molecules26092671.
9. Ung, L.; Bispo, P.J.M.; Shanbhag, S.S.; Gilmore, M.S.; Chodosh, J. The persistent dilemma of microbial keratitis: Global burden, diagnosis, and antimicrobial resistance. *Surv Ophthalmol* **2019**, *64*, 255-271, doi:10.1016/j.survophthal.2018.12.003.
10. Dahlgren, M.A.; Lingappan, A.; Wilhelmus, K.R. The clinical diagnosis of microbial keratitis. *Am J Ophthalmol* **2007**, *143*, 940-944, doi:10.1016/j.ajo.2007.02.030.
11. Mills, R. Microbial keratitis: what's the preferred initial therapy? View 1: corneal scraping and combination antibiotic therapy is indicated. *Br J Ophthalmol* **2003**, *87*, 1167-1169, doi:10.1136/bjo.87.9.1167-a.
12. Maung, N.; Thant, C.C.; Srinivasan, M.; Upadhyay, M.P.; Priyadarsini, B.; Mahalakshmi, R.; Whitcher, J.P. Corneal ulceration in South East Asia. II: a strategy for the prevention of fungal keratitis at the village level in Burma. *Br J Ophthalmol* **2006**, *90*, 968-970, doi:10.1136/bjo.2006.094706.
13. Hoffman, J.J.; Burton, M.J.; Leck, A. Mycotic Keratitis-A Global Threat from the Filamentous Fungi. *J Fungi (Basel)* **2021**, *7*, doi:10.3390/jof7040273.
14. Samreen; Ahmad, I.; Malak, H.A.; Abulreesh, H.H. Environmental antimicrobial resistance and its drivers: a potential threat to public health. *J Glob Antimicrob Resist* **2021**, *27*, 101-111, doi:10.1016/j.jgar.2021.08.001.
15. Mitchell, J.; Purohit, M.; Jewell, C.P.; Read, J.M.; Marrone, G.; Diwan, V.; Stålsby Lundborg, C. Trends, relationships and case attribution of antibiotic resistance between children and environmental sources in rural India. *Sci Rep* **2021**, *11*, 22599, doi:10.1038/s41598-021-01174-w.
16. O'NEILL, J. Tackling drug-resistant infections globally: final report and recommendations. **2016**.
17. Brown, K.L.; Hancock, R.E. Cationic host defense (antimicrobial) peptides. *Curr Opin Immunol* **2006**, *18*, 24-30, doi:10.1016/j.coi.2005.11.004.
18. Groenink, J.; Walgreen-Weterings, E.; van 't Hof, W.; Veerman, E.C.; Nieuw Amerongen, A.V. Cationic amphipathic peptides, derived from bovine and human lactoferrins, with antimicrobial activity against oral pathogens. *FEMS Microbiol Lett* **1999**, *179*, 217-222, doi:10.1111/j.1574-6968.1999.tb08730.x.
19. Harris, F.; Dennison, S.R.; Phoenix, D.A. Anionic antimicrobial peptides from eukaryotic organisms. *Curr Protein Pept Sci* **2009**, *10*, 585-606.

20. Hotchkiss, R.D.; Dubos, R.J. Fractionation of the bactericidal agent from cultures of a soil Bacillus. *J. Biol. Chem* **1940**, *132*, 791–792.
21. Dubos, R.J.; Hotchkiss, R.D. THE PRODUCTION OF BACTERICIDAL SUBSTANCES BY AEROBIC SPORULATING BACILLI. *J Exp Med* **1941**, *73*, 629-640.
22. Ohtani, S.; Okada, T.; Yoshizumi, H.; Kagamiyama, H. Complete primary structures of two subunits of purothionin A, a lethal protein for brewer's yeast from wheat flour. *J Biochem* **1977**, *82*, 753-767.
23. Pirtskhalava, M.; Gabrielian, A.; Cruz, P.; Griggs, H.L.; Squires, R.B.; Hurt, D.E.; Grigolava, M.; Chubinidze, M.; Gogoladze, G.; Vishnepolsky, B.; et al. DBAASP v.2: an enhanced database of structure and antimicrobial/cytotoxic activity of natural and synthetic peptides. *Nucleic Acids Res* **2016**, *44*, D1104-1112, doi:10.1093/nar/gkv1174.
24. Zasloff, M. Antimicrobial peptides of multicellular organisms. *Nature* **2002**, *415*, 389-395, doi:10.1038/415389a.
25. Sohlenkamp, C.; Geiger, O. Bacterial membrane lipids: diversity in structures and pathways. *FEMS Microbiol Rev* **2016**, *40*, 133-159, doi:10.1093/femsre/fuv008.
26. Wang, G. *Antimicrobial peptides: Discovery, design, and novel therapeutic strategies*; CABI Publishing: 2010; p. 230.
27. Khamis, A.M.; Essack, M.; Gao, X.; Bajic, V.B. Distinct profiling of antimicrobial peptide families. *Bioinformatics* **2015**, *31*, 849-856, doi:10.1093/bioinformatics/btu738.
28. Bechinger, B.; Gorr, S.U. Antimicrobial Peptides: Mechanisms of Action and Resistance. *J Dent Res* **2017**, *96*, 254-260, doi:10.1177/0022034516679973.
29. Lee, T.H.; Hall, K.N.; Aguilar, M.I. Antimicrobial Peptide Structure and Mechanism of Action: A Focus on the Role of Membrane Structure. *Curr Top Med Chem* **2016**, *16*, 25-39.
30. Shai, Y. Mode of action of membrane active antimicrobial peptides. *Biopolymers* **2002**, *66*, 236-248, doi:10.1002/bip.10260.
31. Kosikowska, P.; Lesner, A. Antimicrobial peptides (AMPs) as drug candidates: a patent review (2003-2015). *Expert Opin Ther Pat* **2016**, *26*, 689-702, doi:10.1080/13543776.2016.1176149.
32. Rivas-Santiago, B.; Rivas Santiago, C.E.; Castañeda-Delgado, J.E.; León-Contreras, J.C.; Hancock, R.E.; Hernandez-Pando, R. Activity of LL-37, CRAMP and antimicrobial peptide-derived compounds E2, E6 and CP26 against Mycobacterium tuberculosis. *Int J Antimicrob Agents* **2013**, *41*, 143-148, doi:10.1016/j.ijantimicag.2012.09.015.
33. Myhrman, E.; Håkansson, J.; Lindgren, K.; Björn, C.; Sjöstrand, V.; Mahlapuu, M. The novel antimicrobial peptide PXL150 in the local treatment of skin and soft tissue infections. *Appl Microbiol Biotechnol* **2013**, *97*, 3085-3096, doi:10.1007/s00253-012-4439-8.
34. Savini, F.; Luca, V.; Bocedi, A.; Massoud, R.; Park, Y.; Mangoni, M.L.; Stella, L. Cell-Density Dependence of Host-Defense Peptide Activity and Selectivity in the Presence of Host Cells. *ACS Chem Biol* **2017**, *12*, 52-56, doi:10.1021/acscchembio.6b00910.
35. Datta, A.; Yadav, V.; Ghosh, A.; Choi, J.; Bhattacharyya, D.; Kar, R.K.; Ilyas, H.; Dutta, A.; An, E.; Mukhopadhyay, J.; et al. Mode of Action of a Designed Antimicrobial Peptide: High Potency against Cryptococcus neoformans. *Biophysical journal* **2016**, *111*, 1724-1737, doi:10.1016/j.bpj.2016.08.032.
36. Björn, C.; Noppa, L.; Näslund Salomonsson, E.; Johansson, A.L.; Nilsson, E.; Mahlapuu, M.; Håkansson, J. Efficacy and safety profile of the novel antimicrobial peptide PXL150 in a mouse model of infected burn wounds. *Int J Antimicrob Agents* **2015**, *45*, 519-524, doi:10.1016/j.ijantimicag.2014.12.015.
37. Zelezetsky, I.; Tossi, A. Alpha-helical antimicrobial peptides--using a sequence template to guide structure-activity relationship studies. *Biochim Biophys Acta* **2006**, *1758*, 1436-1449, doi:10.1016/j.bbamem.2006.03.021.
38. Falagas, M.E.; Kasiakou, S.K. Toxicity of polymyxins: a systematic review of the evidence from old and recent studies. *Crit Care* **2006**, *10*, R27, doi:10.1186/cc3995.

39. Vlieghe, P.; Lisowski, V.; Martinez, J.; Khrestchatisky, M. Synthetic therapeutic peptides: science and market. *Drug Discov Today* **2010**, *15*, 40-56, doi:10.1016/j.drudis.2009.10.009.
40. Fjell, C.D.; Hiss, J.A.; Hancock, R.E.; Schneider, G. Designing antimicrobial peptides: form follows function. *Nat Rev Drug Discov* **2011**, *11*, 37-51, doi:10.1038/nrd3591.
41. Malmsten, M.; Kasetty, G.; Pasupuleti, M.; Alenfall, J.; Schmidtchen, A. Highly selective end-tagged antimicrobial peptides derived from PRELP. *PLoS One* **2011**, *6*, e16400, doi:10.1371/journal.pone.0016400.
42. Brinckerhoff, L.H.; Kalashnikov, V.V.; Thompson, L.W.; Yamshchikov, G.V.; Pierce, R.A.; Galavotti, H.S.; Engelhard, V.H.; Slingluff, C.L. Terminal modifications inhibit proteolytic degradation of an immunogenic MART-1(27-35) peptide: implications for peptide vaccines. *Int J Cancer* **1999**, *83*, 326-334.
43. Rink, R.; Arkema-Meter, A.; Baudoin, I.; Post, E.; Kuipers, A.; Nelemans, S.A.; Akanbi, M.H.; Moll, G.N. To protect peptide pharmaceuticals against peptidases. *J Pharmacol Toxicol Methods* **2010**, *61*, 210-218, doi:10.1016/j.vascn.2010.02.010.
44. Chowdhury, R.; Ilyas, H.; Ghosh, A.; Ali, H.; Ghorai, A.; Midya, A.; Jana, N.R.; Das, S.; Bhunia, A. Multivalent gold nanoparticle-peptide conjugates for targeting intracellular bacterial infections. *Nanoscale* **2017**, *9*, 14074-14093, doi:10.1039/c7nr04062h.
45. Pal, I.; Bhattacharyya, D.; Kar, R.K.; Zarena, D.; Bhunia, A.; Atreya, H.S. A Peptide-Nanoparticle System with Improved Efficacy against Multidrug Resistant Bacteria. *Sci Rep* **2019**, *9*, 4485, doi:10.1038/s41598-019-41005-7.
46. Baptista, P.V.; McCusker, M.P.; Carvalho, A.; Ferreira, D.A.; Mohan, N.M.; Martins, M.; Fernandes, A.R. Nano-Strategies to Fight Multidrug Resistant Bacteria-"A Battle of the Titans". *Front Microbiol* **2018**, *9*, 1441, doi:10.3389/fmicb.2018.01441.
47. Arias, L.S.; Pessan, J.P.; Vieira, A.P.M.; Lima, T.M.T.; Delbem, A.C.B.; Monteiro, D.R. Iron Oxide Nanoparticles for Biomedical Applications: A Perspective on Synthesis, Drugs, Antimicrobial Activity, and Toxicity. *Antibiotics (Basel)* **2018**, *7*, doi:10.3390/antibiotics7020046.
48. Vinzant, N.; Scholl, J.L.; Wu, C.M.; Kindle, T.; Koodali, R.; Forster, G.L. Iron Oxide Nanoparticle Delivery of Peptides to the Brain: Reversal of Anxiety during Drug Withdrawal. *Front Neurosci* **2017**, *11*, 608, doi:10.3389/fnins.2017.00608.
49. Kim, I.T.; Nunnery, G.A.; Jacob, K.; Schwartz, J.; Liu, X.; Tannenbaum, R. Synthesis, Characterization, and Alignment of Magnetic Carbon Nanotubes Tethered with Maghemite Nanoparticles. *The Journal of Physical Chemistry C* **2010**, *114*, 6944-6951, doi:10.1021/jp9118925.
50. Hartgerink, J.D.; Granja, J.R.; Milligan, R.A.; Ghadiri, M.R. Self-Assembling Peptide Nanotubes. *Journal of the American Chemical Society* **1996**, *118*, 43-50, doi:10.1021/ja953070s.
51. Liu, L.; Xu, K.; Wang, H.; Tan, P.K.; Fan, W.; Venkatraman, S.S.; Li, L.; Yang, Y.Y. Self-assembled cationic peptide nanoparticles as an efficient antimicrobial agent. *Nat Nanotechnol* **2009**, *4*, 457-463, doi:10.1038/nnano.2009.153.
52. Wang, H.; Xu, K.; Liu, L.; Tan, J.P.; Chen, Y.; Li, Y.; Fan, W.; Wei, Z.; Sheng, J.; Yang, Y.Y.; et al. The efficacy of self-assembled cationic antimicrobial peptide nanoparticles against *Cryptococcus neoformans* for the treatment of meningitis. *Biomaterials* **2010**, *31*, 2874-2881, doi:10.1016/j.biomaterials.2009.12.042.
53. Lam, S.J.; Wong, E.H.; O'Brien-Simpson, N.M.; Pantarat, N.; Blencowe, A.; Reynolds, E.C.; Qiao, G.G. Bionano Interaction Study on Antimicrobial Star-Shaped Peptide Polymer Nanoparticles. *ACS Appl Mater Interfaces* **2016**, *8*, 33446-33456, doi:10.1021/acsami.6b11402.

54. Mi, G.; Shi, D.; Herchek, W.; Webster, T.J. Self-assembled arginine-rich peptides as effective antimicrobial agents. *J Biomed Mater Res A* **2017**, *105*, 1046-1054, doi:10.1002/jbm.a.35979.
55. Schneider, A.; Garlick, J.A.; Egles, C. Self-assembling peptide nanofiber scaffolds accelerate wound healing. *PLoS One* **2008**, *3*, e1410, doi:10.1371/journal.pone.0001410.
56. Almaaytah, A.; Mohammed, G.K.; Abualhajaa, A.; Al-Balas, Q. Development of novel ultrashort antimicrobial peptide nanoparticles with potent antimicrobial and antibiofilm activities against multidrug-resistant bacteria. *Drug Des Devel Ther* **2017**, *11*, 3159-3170, doi:10.2147/DDDT.S147450.
57. Lauster, D.; Glanz, M.; Bardua, M.; Ludwig, K.; Hellmund, M.; Hoffmann, U.; Hamann, A.; Böttcher, C.; Haag, R.; Hackenberger, C.P.R.; et al. Multivalent Peptide-Nanoparticle Conjugates for Influenza-Virus Inhibition. *Angew Chem Int Ed Engl* **2017**, *56*, 5931-5936, doi:10.1002/anie.201702005.
58. Teleanu, D.M.; Chircov, C.; Grumezescu, A.M.; Volceanov, A.; Teleanu, R.I. Impact of Nanoparticles on Brain Health: An Up to Date Overview. *J Clin Med* **2018**, *7*, doi:10.3390/jcm7120490.
59. Vignoni, M.; de Alwis Weerasekera, H.; Simpson, M.J.; Phopase, J.; Mah, T.F.; Griffith, M.; Alarcon, E.I.; Scaiano, J.C. LL37 peptide@silver nanoparticles: combining the best of the two worlds for skin infection control. *Nanoscale* **2014**, *6*, 5725-5728, doi:10.1039/c4nr01284d.
60. Pal, I.; Brahmkhatri, V.P.; Bera, S.; Bhattacharyya, D.; Quirishi, Y.; Bhunia, A.; Atreya, H.S. Enhanced stability and activity of an antimicrobial peptide in conjugation with silver nanoparticle. *J Colloid Interface Sci* **2016**, *483*, 385-393, doi:10.1016/j.jcis.2016.08.043.
61. Wadhwani, P.; Heidenreich, N.; Podeyn, B.; Bürck, J.; Ulrich, A.S. Antibiotic gold: tethering of antimicrobial peptides to gold nanoparticles maintains conformational flexibility of peptides and improves trypsin susceptibility. *Biomater Sci* **2017**, *5*, 817-827, doi:10.1039/c7bm00069c.
62. Casciaro, B.; d'Angelo, I.; Zhang, X.; Loffredo, M.R.; Conte, G.; Cappiello, F.; Quaglia, F.; Di, Y.P.; Ungaro, F.; Mangoni, M.L. Poly(lactide- co-glycolide) Nanoparticles for Prolonged Therapeutic Efficacy of Esculentin-1a-Derived Antimicrobial Peptides against *Pseudomonas aeruginosa* Lung Infection: in Vitro and in Vivo Studies. *Biomacromolecules* **2019**, *20*, 1876-1888, doi:10.1021/acs.biomac.8b01829.
63. Maleki, H.; Rai, A.; Pinto, S.; Evangelista, M.; Cardoso, R.M.; Paulo, C.; Carvalheiro, T.; Paiva, A.; Imani, M.; Simchi, A.; et al. High Antimicrobial Activity and Low Human Cell Cytotoxicity of Core-Shell Magnetic Nanoparticles Functionalized with an Antimicrobial Peptide. *ACS Appl Mater Interfaces* **2016**, *8*, 11366-11378, doi:10.1021/acsami.6b03355.
64. Lakshminarayanan, R.; Ye, E.; Young, D.J.; Li, Z.; Loh, X.J. Recent Advances in the Development of Antimicrobial Nanoparticles for Combating Resistant Pathogens. *Adv Healthc Mater* **2018**, *7*, e1701400, doi:10.1002/adhm.201701400.
65. Tan, X.W.; Lakshminarayanan, R.; Liu, S.P.; Goh, E.; Tan, D.; Beuerman, R.W.; Mehta, J.S. Dual functionalization of titanium with vascular endothelial growth factor and β -defensin analog for potential application in keratoprosthesis. *J Biomed Mater Res B Appl Biomater* **2012**, *100*, 2090-2100, doi:10.1002/jbm.b.32774.
66. Tan, X.W.; Goh, T.W.; Saraswathi, P.; Nyein, C.L.; Setiawan, M.; Riau, A.; Lakshminarayanan, R.; Liu, S.; Tan, D.; Beuerman, R.W.; et al. Effectiveness of antimicrobial peptide immobilization for preventing perioperative cornea implant-associated bacterial infection. *Antimicrob Agents Chemother* **2014**, *58*, 5229-5238, doi:10.1128/AAC.02859-14.
67. Rahimi, H.; Roudbarmohammadi, S.; Delavari, H.; Roudbary, M. Antifungal effects of indolicidin-conjugated gold nanoparticles against fluconazole-resistant strains of. *Int J Nanomedicine* **2019**, *14*, 5323-5338, doi:10.2147/IJN.S207527.

68. Bucki, R.; Niemirowicz-Laskowska, K.; Deptuła, P.; Wilczewska, A.Z.; Misiak, P.; Durnaś, B.; Fiedoruk, K.; Piktel, E.; Mystkowska, J.; Janmey, P.A. Susceptibility of microbial cells to the modified PIP. *J Nanobiotechnology* **2019**, *17*, 81, doi:10.1186/s12951-019-0511-1.
69. Zheng, Y.; Liu, W.; Chen, Y.; Li, C.; Jiang, H.; Wang, X. Conjugating gold nanoclusters and antimicrobial peptides: From aggregation-induced emission to antibacterial synergy. *J Colloid Interface Sci* **2019**, *546*, 1-10, doi:10.1016/j.jcis.2019.03.052.
70. Mei, L.; Lu, Z.; Zhang, W.; Wu, Z.; Zhang, X.; Wang, Y.; Luo, Y.; Li, C.; Jia, Y. Bioconjugated nanoparticles for attachment and penetration into pathogenic bacteria. *Biomaterials* **2013**, *34*, 10328-10337, doi:10.1016/j.biomaterials.2013.09.045.
71. Torres, L.M.F.C.; Almeida, M.T.; Santos, T.L.; Marinho, L.E.S.; de Mesquita, J.P.; da Silva, L.M.; Dos Santos, W.T.P.; Martins, H.R.; Kato, K.C.; Alves, E.S.F.; et al. Antimicrobial alumina nanobiostructures of disulfide- and triazole-linked peptides: Synthesis, characterization, membrane interactions and biological activity. *Colloids Surf B Biointerfaces* **2019**, *177*, 94-104, doi:10.1016/j.colsurfb.2019.01.052.
72. Niemirowicz, K.; Surel, U.; Wilczewska, A.Z.; Mystkowska, J.; Piktel, E.; Gu, X.; Namiot, Z.; Kułakowska, A.; Savage, P.B.; Bucki, R. Bactericidal activity and biocompatibility of ceragenin-coated magnetic nanoparticles. *J Nanobiotechnology* **2015**, *13*, 32, doi:10.1186/s12951-015-0093-5.
73. Sharma, R.; Raghav, R.; Priyanka, K.; Rishi, P.; Sharma, S.; Srivastava, S.; Verma, I. Exploiting chitosan and gold nanoparticles for antimycobacterial activity of in silico identified antimicrobial motif of human neutrophil peptide-1. *Sci Rep* **2019**, *9*, 7866, doi:10.1038/s41598-019-44256-6.
74. Palmieri, G.; Tatè, R.; Gogliettino, M.; Balestrieri, M.; Rea, I.; Terracciano, M.; Proroga, Y.T.; Capuano, F.; Anastasio, A.; De Stefano, L. Small Synthetic Peptides Bioconjugated to Hybrid Gold Nanoparticles Destroy Potentially Deadly Bacteria at Submicromolar Concentrations. *Bioconjug Chem* **2018**, *29*, 3877-3885, doi:10.1021/acs.bioconjchem.8b00706.
75. Alghair, Z.K.; Fernig, D.G.; Ebrahimi, B. Enhanced inhibition of influenza virus infection by peptide-noble-metal nanoparticle conjugates. *Beilstein J Nanotechnol* **2019**, *10*, 1038-1047, doi:10.3762/bjnano.10.104.
76. Silva, N.C.; Silva, S.; Sarmiento, B.; Pintado, M. Chitosan nanoparticles for daptomycin delivery in ocular treatment of bacterial endophthalmitis. *Drug Deliv* **2015**, *22*, 885-893, doi:10.3109/10717544.2013.858195.
77. de Alteriis, E.; Maselli, V.; Falanga, A.; Galdiero, S.; Di Lella, F.M.; Gesuele, R.; Guida, M.; Galdiero, E. Efficiency of gold nanoparticles coated with the antimicrobial peptide indolicidin against biofilm formation and development of. *Infect Drug Resist* **2018**, *11*, 915-925, doi:10.2147/IDR.S164262.
78. Sun, T.; Zhan, B.; Zhang, W.; Qin, D.; Xia, G.; Zhang, H.; Peng, M.; Li, S.A.; Zhang, Y.; Gao, Y.; et al. Carboxymethyl chitosan nanoparticles loaded with bioactive peptide OH-CATH30 benefit nonscar wound healing. *Int J Nanomedicine* **2018**, *13*, 5771-5786, doi:10.2147/IJN.S156206.
79. Cuellar, M.; Cifuentes, J.; Perez, J.; Suarez-Arnedo, A.; Serna, J.A.; Groot, H.; Muñoz-Camargo, C.; Cruz, J.C. Novel BUF2-magnetite nanobioconjugates with cell-penetrating abilities. *Int J Nanomedicine* **2018**, *13*, 8087-8094, doi:10.2147/IJN.S188074.
80. Vijayan, A.; James, P.P.; Nanditha, C.K.; Kumar, G.S.V. Multiple cargo deliveries of growth factors and antimicrobial peptide using biodegradable nanopolymer as a potential wound healing system. *Int J Nanomedicine* **2019**, *14*, 2253-2263, doi:10.2147/IJN.S190321.
81. Fan, D.; Yao, C.; Zhou, W.; Li, X. Ultrashort Lipopeptides Self-Assembled with Gold Nanoparticles as Potent Antimicrobial Agents. *J Nanosci Nanotechnol* **2018**, *18*, 8124-8132, doi:10.1166/jnn.2018.16411.

82. Wilson, D.; Materón, E.; Ibáñez-Redín, G.; Faria, R.C.; Correa, D.S.; Oliveira, O.N. Erratum to "Electrical detection of pathogenic bacteria in food samples using information visualization methods with a sensor based on magnetic nanoparticles functionalized with antimicrobial peptides" [Talanta 194 (2019) 611-618]. *Talanta* **2019**, *200*, 562, doi:10.1016/j.talanta.2019.03.085.
83. Tenland, E.; Pochert, A.; Krishnan, N.; Umashankar Rao, K.; Kalsum, S.; Braun, K.; Glegola-Madejska, I.; Lerm, M.; Robertson, B.D.; Lindén, M.; et al. Effective delivery of the anti-mycobacterial peptide NZX in mesoporous silica nanoparticles. *PLoS One* **2019**, *14*, e0212858, doi:10.1371/journal.pone.0212858.
84. Zhou, Y.; Dai, Z. New Strategies in the Design of Nanomedicines to Oppose Uptake by the Mononuclear Phagocyte System and Enhance Cancer Therapeutic Efficacy. *Chem Asian J* **2018**, *13*, 3333-3340, doi:10.1002/asia.201800149.
85. Lamprecht, A.; Ubrich, N.; Yamamoto, H.; Schäfer, U.; Takeuchi, H.; Maincent, P.; Kawashima, Y.; Lehr, C.M. Biodegradable nanoparticles for targeted drug delivery in treatment of inflammatory bowel disease. *J Pharmacol Exp Ther* **2001**, *299*, 775-781.
86. Wnętrzak, A.; Makyła-Juzak, K.; Chachaj-Brekiesz, A.; Lipiec, E.; Romeu, N.V.; Dynarowicz-Latka, P. Cyclosporin A distribution in cholesterol-sphingomyelin artificial membranes modeled as Langmuir monolayers. *Colloids Surf B Biointerfaces* **2018**, *166*, 286-294, doi:10.1016/j.colsurfb.2018.03.031.
87. Romero, G.B.; Arntjen, A.; Keck, C.M.; Müller, R.H. Amorphous cyclosporin A nanoparticles for enhanced dermal bioavailability. *Int J Pharm* **2016**, *498*, 217-224, doi:10.1016/j.ijpharm.2015.12.019.
88. El-Shabouri, M.H. Positively charged nanoparticles for improving the oral bioavailability of cyclosporin-A. *Int J Pharm* **2002**, *249*, 101-108.
89. Kamarajan, P.; Hayami, T.; Matte, B.; Liu, Y.; Danciu, T.; Ramamoorthy, A.; Worden, F.; Kapila, S.; Kapila, Y. Nisin ZP, a Bacteriocin and Food Preservative, Inhibits Head and Neck Cancer Tumorigenesis and Prolongs Survival. *PLoS One* **2015**, *10*, e0131008, doi:10.1371/journal.pone.0131008.
90. de Abreu, L.C.; Todaro, V.; Sathler, P.C.; da Silva, L.C.; do Carmo, F.A.; Costa, C.M.; Toma, H.K.; Castro, H.C.; Rodrigues, C.R.; de Sousa, V.P.; et al. Development and Characterization of Nisin Nanoparticles as Potential Alternative for the Recurrent Vaginal Candidiasis Treatment. *AAPS PharmSciTech* **2016**, *17*, 1421-1427, doi:10.1208/s12249-016-0477-3.
91. Wang, H.; She, Y.; Chu, C.; Liu, H.; Jiang, S.; Sun, M.; Jiang, S. *Preparation, antimicrobial and release behaviors of nisin-poly (vinyl alcohol)/wheat gluten/ZrO2 nanofibrous membranes*; 2015; Volume 50.
92. Kinik, H.; Karaduman, M. Cierny-Mader Type III chronic osteomyelitis: the results of patients treated with debridement, irrigation, vancomycin beads and systemic antibiotics. *Int Orthop* **2008**, *32*, 551-558, doi:10.1007/s00264-007-0342-9.
93. Yousry, C.; Elkheshen, S.A.; El-Laithy, H.M.; Essam, T.; Fahmy, R.H. Studying the influence of formulation and process variables on Vancomycin-loaded polymeric nanoparticles as potential carrier for enhanced ophthalmic delivery. *Eur J Pharm Sci* **2017**, *100*, 142-154, doi:10.1016/j.ejps.2017.01.013.
94. Iooss, P.; Le Ray, A.M.; Grimandi, G.; Daculsi, G.; Merle, C. A new injectable bone substitute combining poly(epsilon-caprolactone) microparticles with biphasic calcium phosphate granules. *Biomaterials* **2001**, *22*, 2785-2794.
95. Yang, Z.; Liu, J.; Gao, J.; Chen, S.; Huang, G. Chitosan coated vancomycin hydrochloride liposomes: Characterizations and evaluation. *Int J Pharm* **2015**, *495*, 508-515, doi:10.1016/j.ijpharm.2015.08.085.
96. Severino, P.; Silveira, E.F.; Loureiro, K.; Chaud, M.V.; Antonini, D.; Lancellotti, M.; Sarmento, V.H.; da Silva, C.F.; Santana, M.H.A.; Souto, E.B. Antimicrobial activity of polymyxin-loaded solid lipid nanoparticles (PLX-SLN): Characterization of physicochemical

- properties and in vitro efficacy. *Eur J Pharm Sci* **2017**, *106*, 177-184, doi:10.1016/j.ejps.2017.05.063.
97. Alipour, M.; Halwani, M.; Omri, A.; Suntres, Z.E. Antimicrobial effectiveness of liposomal polymyxin B against resistant Gram-negative bacterial strains. *Int J Pharm* **2008**, *355*, 293-298, doi:10.1016/j.ijpharm.2007.11.035.
 98. Peng, L.H.; Huang, Y.F.; Zhang, C.Z.; Niu, J.; Chen, Y.; Chu, Y.; Jiang, Z.H.; Gao, J.Q.; Mao, Z.W. Integration of antimicrobial peptides with gold nanoparticles as unique non-viral vectors for gene delivery to mesenchymal stem cells with antibacterial activity. *Biomaterials* **2016**, *103*, 137-149, doi:10.1016/j.biomaterials.2016.06.057.
 99. Liu, C.; Kou, Y.; Zhang, X.; Cheng, H.; Chen, X.; Mao, S. Strategies and industrial perspectives to improve oral absorption of biological macromolecules. *Expert Opin Drug Deliv* **2018**, *15*, 223-233, doi:10.1080/17425247.2017.1395853.
 100. Rao, Y.; Kwok, S.J.; Lombardi, J.; Turro, N.J.; Eisenthal, K.B. Label-free probe of HIV-1 TAT peptide binding to mimetic membranes. *Proc Natl Acad Sci U S A* **2014**, *111*, 12684-12688, doi:10.1073/pnas.1411817111.
 101. He, B.; Ma, S.; Peng, G.; He, D. TAT-modified self-assembled cationic peptide nanoparticles as an efficient antibacterial agent. *Nanomedicine* **2018**, *14*, 365-372, doi:10.1016/j.nano.2017.11.002.
 102. Bera, S.; Kar, R.K.; Mondal, S.; Pahan, K.; Bhunia, A. Structural Elucidation of the Cell-Penetrating Penetratin Peptide in Model Membranes at the Atomic Level: Probing Hydrophobic Interactions in the Blood-Brain Barrier. *Biochemistry* **2016**, *55*, 4982-4996, doi:10.1021/acs.biochem.6b00518.
 103. Kwon, E.J.; Skalak, M.; Bertucci, A.; Braun, G.; Ricci, F.; Ruoslahti, E.; Sailor, M.J.; Bhatia, S.N. Porous Silicon Nanoparticle Delivery of Tandem Peptide Anti-Infectives for the Treatment of Pseudomonas aeruginosa Lung Infections. *Adv Mater* **2017**, *29*, doi:10.1002/adma.201701527.
 104. Water, J.J.; Smart, S.; Franzyk, H.; Foged, C.; Nielsen, H.M. Nanoparticle-mediated delivery of the antimicrobial peptide plectasin against Staphylococcus aureus in infected epithelial cells. *Eur J Pharm Biopharm* **2015**, *92*, 65-73, doi:10.1016/j.ejpb.2015.02.009.
 105. Yeom, J.H.; Lee, B.; Kim, D.; Lee, J.K.; Kim, S.; Bae, J.; Park, Y.; Lee, K. Gold nanoparticle-DNA aptamer conjugate-assisted delivery of antimicrobial peptide effectively eliminates intracellular Salmonella enterica serovar Typhimurium. *Biomaterials* **2016**, *104*, 43-51, doi:10.1016/j.biomaterials.2016.07.009.
 106. Zhao, Z.; Yan, R.; Yi, X.; Li, J.; Rao, J.; Guo, Z.; Yang, Y.; Li, W.; Li, Y.Q.; Chen, C. Bacteria-Activated Theranostic Nanoprobes against Methicillin-Resistant Staphylococcus aureus Infection. *ACS Nano* **2017**, *11*, 4428-4438, doi:10.1021/acs.nano.7b00041.
 107. Jin, Y.; Kim, D.; Roh, H.; Kim, S.; Hussain, S.; Kang, J.; Pack, C.G.; Kim, J.K.; Myung, S.J.; Ruoslahti, E.; et al. Tracking the Fate of Porous Silicon Nanoparticles Delivering a Peptide Payload by Intrinsic Photoluminescence Lifetime. *Adv Mater* **2018**, *30*, e1802878, doi:10.1002/adma.201802878.
 108. Yu, X.; Wang, J.; Liu, J.; Shen, S.; Cao, Z.; Pan, J.; Zhou, S.; Pang, Z.; Geng, D.; Zhang, J. A multimodal Pepstatin A peptide-based nanoagent for the molecular imaging of P-glycoprotein in the brains of epilepsy rats. *Biomaterials* **2016**, *76*, 173-186, doi:10.1016/j.biomaterials.2015.10.050.
 109. Walther, C.; Meyer, K.; Rennert, R.; Neundorff, I. Quantum dot-carrier peptide conjugates suitable for imaging and delivery applications. *Bioconjug Chem* **2008**, *19*, 2346-2356, doi:10.1021/bc800172q.
 110. Mohid, S.A.; Ghorai, A.; Ilyas, H.; Mroue, K.H.; Narayanan, G.; Sarkar, A.; Ray, S.K.; Biswas, K.; Bera, A.K.; Malmsten, M.; et al. Application of tungsten disulfide quantum dot-conjugated antimicrobial peptides in bio-imaging and antimicrobial therapy. *Colloids Surf B Biointerfaces* **2019**, *176*, 360-370, doi:10.1016/j.colsurfb.2019.01.020.

111. Taubes, G. The bacteria fight back. *Science* **2008**, *321*, 356-361, doi:10.1126/science.321.5887.356.
112. Chan, L.W.; Hern, K.E.; Ngambenjawong, C.; Lee, K.; Kwon, E.J.; Hung, D.T.; Bhatia, S.N. Selective Permeabilization of Gram-Negative Bacterial Membranes Using Multivalent Peptide Constructs for Antibiotic Sensitization. *ACS Infect Dis* **2021**, *7*, 721-732, doi:10.1021/acsinfecdis.0c00805.
113. Magana, M.; Pushpanathan, M.; Santos, A.L.; Leanse, L.; Fernandez, M.; Ioannidis, A.; Giulianotti, M.A.; Apidianakis, Y.; Bradfute, S.; Ferguson, A.L.; et al. The value of antimicrobial peptides in the age of resistance. *Lancet Infect Dis* **2020**, *20*, e216-e230, doi:10.1016/S1473-3099(20)30327-3.
114. Zgurskaya, H.I.; López, C.A.; Gnanakaran, S. Permeability Barrier of Gram-Negative Cell Envelopes and Approaches To Bypass It. *ACS Infect Dis* **2015**, *1*, 512-522, doi:10.1021/acsinfecdis.5b00097.
115. Sani, M.A.; Separovic, F. How Membrane-Active Peptides Get into Lipid Membranes. *Acc Chem Res* **2016**, *49*, 1130-1138, doi:10.1021/acs.accounts.6b00074.
116. Tsubery, H.; Ofek, I.; Cohen, S.; Fridkin, M. N-terminal modifications of Polymyxin B nonapeptide and their effect on antibacterial activity. *Peptides* **2001**, *22*, 1675-1681, doi:10.1016/s0196-9781(01)00503-4.
117. Majerle, A.; Kidric, J.; Jerala, R. Enhancement of antibacterial and lipopolysaccharide binding activities of a human lactoferrin peptide fragment by the addition of acyl chain. *J Antimicrob Chemother* **2003**, *51*, 1159-1165, doi:10.1093/jac/dkg219.
118. De Zoysa, G.H.; Cameron, A.J.; Hegde, V.V.; Raghothama, S.; Sarojini, V. Antimicrobial peptides with potential for biofilm eradication: synthesis and structure activity relationship studies of battacin peptides. *J Med Chem* **2015**, *58*, 625-639, doi:10.1021/jm501084q.
119. Varnava, K.G.; Reynisson, J.; Raghothama, S.; Sarojini, V. Synthesis, antibacterial, and antibiofilm potential of human autophagy 16 polypeptide and analogues. *Peptide Science* **2018**, *110*, e24076, doi:<https://doi.org/10.1002/pep2.24076>.
120. Chan, W.C.; White, P.D.; Beythien, J.; Steinauer, R. Facile synthesis of protected C-terminal peptide segments by Fmoc/But solid-phase procedures on N-Fmoc-9-amino-xanthen-3-ylloxymethyl polystyrene resin. *Journal of the Chemical Society, Chemical Communications* **1995**, 589-592, doi:10.1039/C39950000589.
121. Swedan, S.; Shubair, Z.; Almaaytah, A. Synergism of cationic antimicrobial peptide WLBU2 with antibacterial agents against biofilms of multi-drug resistant. *Infect Drug Resist* **2019**, *12*, 2019-2030, doi:10.2147/IDR.S215084.
122. Lakshminarayanan, R.; Liu, S.; Li, J.; Nandhakumar, M.; Aung, T.T.; Goh, E.; Chang, J.Y.; Saraswathi, P.; Tang, C.; Safie, S.R.; et al. Synthetic multivalent antifungal peptides effective against fungi. *PLoS One* **2014**, *9*, e87730, doi:10.1371/journal.pone.0087730.
123. Mukai, Y.; Matsushita, Y.; Niidome, T.; Hatekeyama, T.; Aoyag, H. Parallel and antiparallel dimers of magainin 2: their interaction with phospholipid membrane and antibacterial activity. *J Pept Sci* **2002**, *8*, 570-577, doi:10.1002/psc.416.
124. D, G.T.; G, K.D. *Sparky*, SPARKY 3; University of California: San Francisco.
125. Bhunia, A.; Domadia, P.N.; Torres, J.; Hallock, K.J.; Ramamoorthy, A.; Bhattacharjya, S. NMR structure of pardaxin, a pore-forming antimicrobial peptide, in lipopolysaccharide micelles: mechanism of outer membrane permeabilization. *J Biol Chem* **2010**, *285*, 3883-3895, doi:10.1074/jbc.M109.065672.
126. Varnava, K.G.; Mohid, S.A.; Calligari, P.; Stella, L.; Reynison, J.; Bhunia, A.; Sarojini, V. Design, Synthesis, Antibacterial Potential, and Structural Characterization of N-Acylated Derivatives of the Human Autophagy 16 Polypeptide. *Bioconjug Chem* **2019**, *30*, 1998-2010, doi:10.1021/acs.bioconjchem.9b00290.

127. Schmidtchen, A.; Pasupuleti, M.; Mörgelin, M.; Davoudi, M.; Alenfall, J.; Chalupka, A.; Malmsten, M. Boosting antimicrobial peptides by hydrophobic oligopeptide end tags. *J Biol Chem* **2009**, *284*, 17584-17594, doi:10.1074/jbc.M109.011650.
128. Izadpanah, A.; Gallo, R.L. Antimicrobial peptides. *J Am Acad Dermatol* **2005**, *52*, 381-390; quiz 391-382, doi:10.1016/j.jaad.2004.08.026.
129. Guilhelmelli, F.; Vilela, N.; Albuquerque, P.; Derengowski, L.D.; Silva-Pereira, I.; Kyaw, C.M. Antibiotic development challenges: the various mechanisms of action of antimicrobial peptides and of bacterial resistance. *Front Microbiol* **2013**, *4*, doi:ARTN 353 10.3389/fmicb.2013.00353.
130. Eband, R.M.; Walker, C.; Eband, R.F.; Magarvey, N.A. Molecular mechanisms of membrane targeting antibiotics. *Bba-Biomembranes* **2016**, *1858*, 980-987, doi:10.1016/j.bbamem.2015.10.018.
131. Kapoor, G.; Saigal, S.; Elongavan, A. Action and resistance mechanisms of antibiotics: A guide for clinicians. *J Anaesthesiol Clin Pharmacol* **2017**, *33*, 300-305, doi:10.4103/joacp.JOACP_349_15.
132. Yu, Z.L.; Qin, W.R.; Lin, J.X.; Fang, S.S.; Qiu, J.P. Antibacterial Mechanisms of Polymyxin and Bacterial Resistance. *Biomed Res Int* **2015**, doi:Artn 679109 10.1155/2015/679109.
133. Johnstone, R.W.; Licht, J.D. Histone deacetylase inhibitors in cancer therapy: is transcription the primary target? *Cancer Cell* **2003**, *4*, 13-18.
134. Gryder, B.E. Targeted cancer therapy: giving histone deacetylase inhibitors all they need to succeed (vol 4, pg 505, 2012). *Future Med Chem* **2012**, *4*, 1369-1370.
135. Johnstone, R.W. Histone-deacetylase inhibitors: Novel drugs for the treatment of cancer. *Nat Rev Drug Discov* **2002**, *1*, 287-299, doi:10.1038/nrd772.
136. Lin, H.Y.; Chen, C.S.; Lin, S.P.; Weng, J.R.; Chen, C.S. Targeting histone deacetylase in cancer therapy. *Med Res Rev* **2006**, *26*, 397-413, doi:10.1002/med.20056.
137. Anuchin, A.M.; Goncharenko, A.V.; Demidenok, O.I.; Kaprelyants, A.S. Histone-Like Proteins of Bacteria (Review). *Appl Biochem Micro+* **2011**, *47*, 580-585, doi:10.1134/S0003683811060020.
138. Drlica, K.; Rouviereyaniv, J. Histone-Like Proteins of Bacteria. *Microbiol Rev* **1987**, *51*, 301-319.
139. Balandina, A.; Kamashev, D.; Rouviere-Yaniv, J. The bacterial histone-like protein HU specifically recognizes similar structures in all nucleic acids - DNA, RNA, and their hybrids. *Journal of Biological Chemistry* **2002**, *277*, 27622-27628, doi:10.1074/jbc.M201978200.
140. Slesarev, A.I.; Belova, G.I.; Kozyavkin, S.A.; Lake, J.A. Evidence for an early prokaryotic origin of histones H2A and H4 prior to the emergence of eukaryotes. *Nucleic Acids Research* **1998**, *26*, 427-430, doi:DOI 10.1093/nar/26.2.427.
141. Rack, J.G.M.; Morra, R.; Barkauskaite, E.; Kraehenbuehl, R.; Ariza, A.; Qu, Y.; Ortmayer, M.; Leidecker, O.; Cameron, D.R.; Matic, I.; et al. Identification of a Class of Protein ADP-Ribosylating Sirtuins in Microbial Pathogens. *Molecular Cell* **2015**, *59*, 309-320, doi:10.1016/j.molcel.2015.06.013.
142. AbouElfetouh, A.; Kuhn, M.L.; Hu, L.I.; Scholle, M.D.; Sorensen, D.J.; Sahu, A.K.; Becher, D.; Antelmann, H.; Mrksich, M.; Anderson, W.F.; et al. The E. coli sirtuin CobB shows no preference for enzymatic and nonenzymatic lysine acetylation substrate sites. *Microbiologyopen* **2015**, *4*, 66-83, doi:10.1002/mbo3.223.
143. Appel, C.D.; Feld, G.K.; Wallace, B.D.; Williams, R.S. Structure of the sirtuin-linked macrodomain SAV0325 from Staphylococcus aureus. *Protein Sci* **2016**, *25*, 1682-1691, doi:10.1002/pro.2974.

144. Gregorette, I.V.; Lee, Y.M.; Goodson, H.V. Molecular evolution of the histone deacetylase family: Functional implications of phylogenetic analysis. *J Mol Biol* **2004**, *338*, 17-31, doi:10.1016/j.jmb.2004.02.006.
145. Ma, C.; Yang, X.; Lewis, P.J. Bacterial Transcription as a Target for Antibacterial Drug Development. *Microbiol Mol Biol R* **2016**, *80*, 139-160, doi:10.1128/Mmbr.00055-15.
146. Turecka, K.; Waleron, K. Inhibitors of Bacterial Transcription are Compounds for Potent Antimicrobial Drugs. *Curr Pharm Biotechno* **2013**, *14*, 1275-1286.
147. Zhang, P.; Cheetham, A.G.; Lin, Y.A.; Cui, H. Self-assembled Tat nanofibers as effective drug carrier and transporter. *ACS Nano* **2013**, *7*, 5965-5977, doi:10.1021/nn401667z.
148. Buda De Cesare, G.; Cristy, S.A.; Garsin, D.A.; Lorenz, M.C. Antimicrobial Peptides: a New Frontier in Antifungal Therapy. *mBio* **2020**, *11*, doi:10.1128/mBio.02123-20.
149. Delattin, N.; Brucker, K.; Cremer, K.; Cammue, B.P.; Thevissen, K. Antimicrobial Peptides as a Strategy to Combat Fungal Biofilms. *Curr Top Med Chem* **2017**, *17*, 604-612, doi:10.2174/1568026616666160713142228.
150. Makovitzki, A.; Avrahami, D.; Shai, Y. Ultrashort antibacterial and antifungal lipopeptides. *Proc Natl Acad Sci U S A* **2006**, *103*, 15997-16002, doi:10.1073/pnas.0606129103.
151. Seddon, A.M.; Casey, D.; Law, R.V.; Gee, A.; Templer, R.H.; Ces, O. Drug interactions with lipid membranes. *Chem Soc Rev* **2009**, *38*, 2509-2519, doi:10.1039/b813853m.
152. Porcelli, F.; Buck-Koehntop, B.A.; Thennarasu, S.; Ramamoorthy, A.; Veglia, G. Structures of the dimeric and monomeric variants of magainin antimicrobial peptides (MSI-78 and MSI-594) in micelles and bilayers, determined by NMR spectroscopy. *Biochemistry* **2006**, *45*, 5793-5799, doi:10.1021/bi0601813.
153. Gottler, L.M.; Ramamoorthy, A. Structure, membrane orientation, mechanism, and function of pexiganan--a highly potent antimicrobial peptide designed from magainin. *Biochim Biophys Acta* **2009**, *1788*, 1680-1686, doi:10.1016/j.bbamem.2008.10.009.
154. Sani, M.A.; Separovic, F. Antimicrobial Peptide Structures: From Model Membranes to Live Cells. *Chemistry* **2018**, *24*, 286-291, doi:10.1002/chem.201704362.
155. Glukhov, E.; Stark, M.; Burrows, L.L.; Deber, C.M. Basis for selectivity of cationic antimicrobial peptides for bacterial versus mammalian membranes. *J Biol Chem* **2005**, *280*, 33960-33967, doi:10.1074/jbc.M507042200.
156. Shukla, R.; Medeiros-Silva, J.; Parmar, A.; Vermeulen, B.J.A.; Das, S.; Paioni, A.L.; Jekhmane, S.; Lorent, J.; Bonvin, A.M.J.J.; Baldus, M.; et al. Mode of action of teixobactins in cellular membranes. *Nat Commun* **2020**, *11*, 2848, doi:10.1038/s41467-020-16600-2.
157. Lakshminarayanan, R.; Tan, W.X.; Aung, T.T.; Goh, E.T.; Muruganatham, N.; Li, J.; Chang, J.Y.; Dikshit, N.; Saraswathi, P.; Lim, R.R.; et al. Branched Peptide, B2088, Disrupts the Supramolecular Organization of Lipopolysaccharides and Sensitizes the Gram-negative Bacteria. *Sci Rep* **2016**, *6*, 25905, doi:10.1038/srep25905.
158. Mason, A.J.; Marquette, A.; Bechinger, B. Zwitterionic phospholipids and sterols modulate antimicrobial peptide-induced membrane destabilization. *Biophys J* **2007**, *93*, 4289-4299, doi:10.1529/biophysj.107.116681.
159. Sood, R.; Kinnunen, P.K. Cholesterol, lanosterol, and ergosterol attenuate the membrane association of LL-37(W27F) and temporin L. *Biochim Biophys Acta* **2008**, *1778*, 1460-1466, doi:10.1016/j.bbamem.2008.02.014.
160. Girois, S.B.; Chapuis, F.; Decullier, E.; Revol, B.G. Adverse effects of antifungal therapies in invasive fungal infections: review and meta-analysis. *Eur J Clin Microbiol Infect Dis* **2006**, *25*, 138-149, doi:10.1007/s10096-005-0080-0.
161. Matsumori, N.; Tahara, K.; Yamamoto, H.; Morooka, A.; Doi, M.; Oishi, T.; Murata, M. Direct interaction between amphotericin B and ergosterol in lipid bilayers as revealed by ²H NMR spectroscopy. *J Am Chem Soc* **2009**, *131*, 11855-11860, doi:10.1021/ja9033473.
162. Kasai, Y.; Matsumori, N.; Umegawa, Y.; Matsuoka, S.; Ueno, H.; Ikeuchi, H.; Oishi, T.; Murata, M. Self-assembled amphotericin B is probably surrounded by ergosterol:

- bimolecular interactions as evidenced by solid-state NMR and CD spectra. *Chemistry* **2008**, *14*, 1178-1185, doi:10.1002/chem.200701256.
163. Yamamoto, T.; Umegawa, Y.; Yamagami, M.; Suzuki, T.; Tsuchikawa, H.; Hanashima, S.; Matsumori, N.; Murata, M. The Perpendicular Orientation of Amphotericin B Methyl Ester in Hydrated Lipid Bilayers Supports the Barrel-Stave Model. *Biochemistry* **2019**, *58*, 2282-2291, doi:10.1021/acs.biochem.9b00180.
164. Bui, T.T.; Suga, K.; Kuhl, T.L.; Umakoshi, H. Melting-Temperature-Dependent Interactions of Ergosterol with Unsaturated and Saturated Lipids in Model Membranes. *Langmuir* **2019**, *35*, 10640-10647, doi:10.1021/acs.langmuir.9b01538.
165. Bolard, J. How do the polyene macrolide antibiotics affect the cellular membrane properties? *Biochim Biophys Acta* **1986**, *864*, 257-304, doi:10.1016/0304-4157(86)90002-x.
166. Paquet, M.J.; Fournier, I.; Barwicz, J.; Tancrede, P.; Auger, M. The effects of amphotericin B on pure and ergosterol- or cholesterol-containing dipalmitoylphosphatidylcholine bilayers as viewed by 2H NMR. *Chem Phys Lipids* **2002**, *119*, 1-11, doi:10.1016/s0009-3084(02)00071-3.
167. Hamill, R.J. Amphotericin B formulations: a comparative review of efficacy and toxicity. *Drugs* **2013**, *73*, 919-934, doi:10.1007/s40265-013-0069-4.
168. Fernández de Ullivarri, M.; Arbulu, S.; Garcia-Gutierrez, E.; Cotter, P.D. Antifungal Peptides as Therapeutic Agents. *Front Cell Infect Microbiol* **2020**, *10*, 105, doi:10.3389/fcimb.2020.00105.
169. Datta, A.; Ghosh, A.; Airoidi, C.; Sperandeo, P.; Mroue, K.H.; Jiménez-Barbero, J.; Kundu, P.; Ramamoorthy, A.; Bhunia, A. Antimicrobial Peptides: Insights into Membrane Permeabilization, Lipopolysaccharide Fragmentation and Application in Plant Disease Control. *Sci Rep* **2015**, *5*, 11951, doi:10.1038/srep11951.
170. Bhattacharyya, D.; Kim, M.; Mroue, K.H.; Park, M.; Tiwari, A.; Saleem, M.; Lee, D.; Bhunia, A. Role of non-electrostatic forces in antimicrobial potency of a dengue-virus derived fusion peptide VG16KRKP: Mechanistic insight into the interfacial peptide-lipid interactions. *Biochim Biophys Acta Biomembr* **2019**, *1861*, 798-809, doi:10.1016/j.bbamem.2019.01.011.
171. Ilyas, H.; Kim, J.; Lee, D.; Malmsten, M.; Bhunia, A. Structural insights into the combinatorial effects of antimicrobial peptides reveal a role of aromatic-aromatic interactions in antibacterial synergism. *J Biol Chem* **2019**, *294*, 14615-14633, doi:10.1074/jbc.RA119.009955.
172. Behrendt, R.; White, P.; Offer, J. Advances in Fmoc solid-phase peptide synthesis. *J Pept Sci* **2016**, *22*, 4-27, doi:10.1002/psc.2836.
173. Loreto, E.S.; Mario, D.A.; Denardi, L.B.; Alves, S.H.; Santurio, J.M. In vitro susceptibility of *Pythium insidiosum* to macrolides and tetracycline antibiotics. *Antimicrob Agents Chemother* **2011**, *55*, 3588-3590, doi:10.1128/AAC.01586-10.
174. Dave, A.; Samarth, A.; Karolia, R.; Sharma, S.; Karunakaran, E.; Partridge, L.; MacNeil, S.; Monk, P.N.; Garg, P.; Roy, S. Characterization of Ocular Clinical Isolates of. *Microorganisms* **2020**, *8*, doi:10.3390/microorganisms8020260.
175. Santra, A.; Ghosh, T.; Misra, A.K. Removal of benzylidene acetal and benzyl ether in carbohydrate derivatives using triethylsilane and Pd/C. *Beilstein J Org Chem* **2013**, *9*, 74-78, doi:10.3762/bjoc.9.9.
176. **H. Kim, T.H.L., H. Park, H. Oh.** Preparation of novel ergosterol glycoside derivatives for treating dermatitis. 20190337976, Mar 24, 2017 2019.
177. Weinberger, A.; Tsai, F.C.; Koenderink, G.H.; Schmidt, T.F.; Itri, R.; Meier, W.; Schmatko, T.; Schröder, A.; Marques, C. Gel-assisted formation of giant unilamellar vesicles. *Biophys J* **2013**, *105*, 154-164, doi:10.1016/j.bpj.2013.05.024.

178. Mescola, A.; Marín-Medina, N.; Ragazzini, G.; Accolla, M.; Alessandrini, A. Magainin-H2 effects on the permeabilization and mechanical properties of giant unilamellar vesicles. *J Colloid Interface Sci* **2019**, *553*, 247-258, doi:10.1016/j.jcis.2019.06.028.
179. Güntert, P.; Mumenthaler, C.; Wüthrich, K. Torsion angle dynamics for NMR structure calculation with the new program DYANA. *J Mol Biol* **1997**, *273*, 283-298, doi:10.1006/jmbi.1997.1284.
180. Pettersen, E.F.; Goddard, T.D.; Huang, C.C.; Couch, G.S.; Greenblatt, D.M.; Meng, E.C.; Ferrin, T.E. UCSF Chimera--a visualization system for exploratory research and analysis. *J Comput Chem* **2004**, *25*, 1605-1612, doi:10.1002/jcc.20084.
181. Chen, H.; Gordon, D.; Heinemann, S.H. Modulation of cloned skeletal muscle sodium channels by the scorpion toxins Lqh II, Lqh III, and Lqh alphaIT. *Pflugers Arch* **2000**, *439*, 423-432, doi:10.1007/s004249900181.
182. Zhou, G.; Deng, X.; Tian, J.; Fazil, M.H.U.T.; Lakshminarayanan, R.; Srinivasan, R. SnAP reagents for the synthesis of selenomorpholines and 1,4-selenazepanes and their biological evaluation. *Chem Commun (Camb)* **2020**, *56*, 1780-1783, doi:10.1039/c9cc09337k.
183. Sun, R.L.; Jones, D.B.; Wilhelmus, K.R. Clinical characteristics and outcome of Candida keratitis. *Am J Ophthalmol* **2007**, *143*, 1043-1045, doi:10.1016/j.ajo.2007.02.016.
184. Tummanapalli, S.S.; Willcox, M.D. Antimicrobial resistance of ocular microbes and the role of antimicrobial peptides. *Clin Exp Optom* **2021**, *104*, 295-307, doi:10.1111/cxo.13125.
185. Sharma, P.; Sharma, N.; Mishra, P.; Joseph, J.; Mishra, D.K.; Garg, P.; Roy, S. Differential Expression of Antimicrobial Peptides in Streptococcus pneumoniae Keratitis and STAT3-Dependent Expression of LL-37 by Streptococcus pneumoniae in Human Corneal Epithelial Cells. *Pathogens* **2019**, *8*, doi:10.3390/pathogens8010031.
186. Sharma, P.; Guha, S.; Garg, P.; Roy, S. Differential expression of antimicrobial peptides in corneal infection and regulation of antimicrobial peptides and reactive oxygen species by type III secretion system of Pseudomonas aeruginosa. *Pathog Dis* **2018**, *76*, doi:10.1093/femspd/fty001.
187. Terlau, H.; Olivera, B.M. Conus venoms: a rich source of novel ion channel-targeted peptides. *Physiol Rev* **2004**, *84*, 41-68, doi:10.1152/physrev.00020.2003.
188. Tietze, A.A.; Tietze, D.; Ohlenschläger, O.; Leipold, E.; Ullrich, F.; Köhl, T.; Mischo, A.; Buntkowsky, G.; Görlach, M.; Heinemann, S.H.; et al. Structurally diverse μ -conotoxin PIIIA isomers block sodium channel NaV 1.4. *Angew Chem Int Ed Engl* **2012**, *51*, 4058-4061, doi:10.1002/anie.201107011.
189. Lu, L. Stress-induced corneal epithelial apoptosis mediated by K⁺ channel activation. *Prog Retin Eye Res* **2006**, *25*, 515-538, doi:10.1016/j.preteyeres.2006.07.004.
190. Kim, H.; Lee, T.H.; Park, H.; Oh, H. Ergosterol glycoside derivative. 2021.
191. de Almeida, R.F.; Fedorov, A.; Prieto, M. Sphingomyelin/phosphatidylcholine/cholesterol phase diagram: boundaries and composition of lipid rafts. *Biophys J* **2003**, *85*, 2406-2416, doi:10.1016/S0006-3495(03)74664-5.
192. M'Baye, G.; Mély, Y.; Duportail, G.; Klymchenko, A.S. Liquid ordered and gel phases of lipid bilayers: fluorescent probes reveal close fluidity but different hydration. *Biophys J* **2008**, *95*, 1217-1225, doi:10.1529/biophysj.107.127480.
193. Niu, Z.; Prade, E.; Malideli, E.; Hille, K.; Jussupow, A.; Mideksa, Y.G.; Yan, L.M.; Qian, C.; Fleisch, M.; Messias, A.C.; et al. Structural Insight into IAPP-Derived Amyloid Inhibitors and Their Mechanism of Action. *Angew Chem Int Ed Engl* **2020**, *59*, 5771-5781, doi:10.1002/anie.201914559.
194. Junior, E.F.C.; Guimarães, C.F.R.C.; Franco, L.L.; Alves, R.J.; Kato, K.C.; Martins, H.R.; de Souza Filho, J.D.; Bemquerer, M.P.; Munhoz, V.H.O.; Resende, J.M.; et al. Glycotriazole-peptides derived from the peptide HSP1: synergistic effect of triazole and saccharide rings

- on the antifungal activity. *Amino Acids* **2017**, *49*, 1389-1400, doi:10.1007/s00726-017-2441-2.
195. O'Connor, C.; White, K.L.; Doncescu, N.; Didenko, T.; Roth, B.L.; Czaplicki, G.; Stevens, R.C.; Wüthrich, K.; Milon, A. NMR structure and dynamics of the agonist dynorphin peptide bound to the human kappa opioid receptor. *Proc Natl Acad Sci U S A* **2015**, *112*, 11852-11857, doi:10.1073/pnas.1510117112.
196. Gizachew, D.; Dratz, E. Transferred NOESY NMR studies of biotin mimetic peptide (FSHPQNT) bound to streptavidin: a structural model for studies of peptide-protein interactions. *Chem Biol Drug Des* **2011**, *78*, 14-24, doi:10.1111/j.1747-0285.2011.01096.x.
197. Linser, R.; Dasari, M.; Hiller, M.; Higman, V.; Fink, U.; Lopez del Amo, J.M.; Markovic, S.; Handel, L.; Kessler, B.; Schmieder, P.; et al. Proton-detected solid-state NMR spectroscopy of fibrillar and membrane proteins. *Angew Chem Int Ed Engl* **2011**, *50*, 4508-4512, doi:10.1002/anie.201008244.
198. Wang, G. Structures of human host defense cathelicidin LL-37 and its smallest antimicrobial peptide KR-12 in lipid micelles. *J Biol Chem* **2008**, *283*, 32637-32643, doi:10.1074/jbc.M805533200.
199. Bechinger, B.; Zasloff, M.; Opella, S.J. Structure and orientation of the antibiotic peptide magainin in membranes by solid-state nuclear magnetic resonance spectroscopy. *Protein Sci* **1993**, *2*, 2077-2084, doi:10.1002/pro.5560021208.
200. Ramirez, L.S.; Pande, J.; Shekhtman, A. Helical Structure of Recombinant Melittin. *J Phys Chem B* **2019**, *123*, 356-368, doi:10.1021/acs.jpbc.8b08424.
201. Bhattacharjya, S.; Domadia, P.N.; Bhunia, A.; Malladi, S.; David, S.A. High-resolution solution structure of a designed peptide bound to lipopolysaccharide: transferred nuclear Overhauser effects, micelle selectivity, and anti-endotoxic activity. *Biochemistry* **2007**, *46*, 5864-5874, doi:10.1021/bi6025159.
202. Bhunia, A.; Mohanram, H.; Domadia, P.N.; Torres, J.; Bhattacharjya, S. Designed beta-boomerang antiendotoxic and antimicrobial peptides: structures and activities in lipopolysaccharide. *J Biol Chem* **2009**, *284*, 21991-22004, doi:10.1074/jbc.M109.013573.
203. Ting, D.S.J.; Ho, C.S.; Deshmukh, R.; Said, D.G.; Dua, H.S. Infectious keratitis: an update on epidemiology, causative microorganisms, risk factors, and antimicrobial resistance. *Eye (Lond)* **2021**, *35*, 1084-1101, doi:10.1038/s41433-020-01339-3.
204. Li, N.; Zhu, Z.; Yi, G.; Li, S.; Han, X. Corneal Opacity Leading to Multiple Myeloma Diagnosis: A Case Report and Literature Review. *Am J Case Rep* **2018**, *19*, 421-425, doi:10.12659/ajcr.908475.
205. Taylor, H.R.; Burton, M.J.; Haddad, D.; West, S.; Wright, H. Trachoma. *Lancet* **2014**, *384*, 2142-2152, doi:10.1016/S0140-6736(13)62182-0.
206. Austin, A.; Lietman, T.; Rose-Nussbaumer, J. Update on the Management of Infectious Keratitis. *Ophthalmology* **2017**, *124*, 1678-1689, doi:10.1016/j.ophtha.2017.05.012.
207. Kam, K.W.; Yung, W.; Li, G.K.H.; Chen, L.J.; Young, A.L. Infectious keratitis and orthokeratology lens use: a systematic review. *Infection* **2017**, *45*, 727-735, doi:10.1007/s15010-017-1023-2.
208. Aydin, B.; Cubuk, M.O.; Ucgul, A.; Ertop, M.; Ozmen, M.C.; Atalay, T.; Akata, F. Combined Intrastromal Voriconazole and Amphotericin B Treatment for Persistent Fungal Keratitis. *Eye Contact Lens* **2020**, *46*, 269-273, doi:10.1097/ICL.0000000000000723.
209. Chang, V.S.; Dhaliwal, D.K.; Raju, L.; Kowalski, R.P. Antibiotic Resistance in the Treatment of Staphylococcus aureus Keratitis: a 20-Year Review. *Cornea* **2015**, *34*, 698-703, doi:10.1097/ICO.0000000000000431.
210. Barceló-Vidal, J.; Rodríguez-García, E.; Grau, S. Extremely high levels of vancomycin can cause severe renal toxicity. *Infect Drug Resist* **2018**, *11*, 1027-1030, doi:10.2147/IDR.S171669.

211. Nikaido, H. Multidrug resistance in bacteria. *Annu Rev Biochem* **2009**, *78*, 119-146, doi:10.1146/annurev.biochem.78.082907.145923.
212. Haney, E.F.; Mansour, S.C.; Hancock, R.E. Antimicrobial Peptides: An Introduction. *Methods Mol Biol* **2017**, *1548*, 3-22, doi:10.1007/978-1-4939-6737-7_1.
213. Lazzaro, B.P.; Zasloff, M.; Rolff, J. Antimicrobial peptides: Application informed by evolution. *Science* **2020**, *368*, doi:10.1126/science.aau5480.
214. Malmsten, M. Antimicrobial peptides. *Ups J Med Sci* **2014**, *119*, 199-204, doi:10.3109/03009734.2014.899278.
215. Datta, A.; Jaiswal, N.; Ilyas, H.; Debnath, S.; Biswas, K.; Kumar, D.; Bhunia, A. Structural and Dynamic Insights into a Glycine-Mediated Short Analogue of a Designed Peptide in Lipopolysaccharide Micelles: Correlation Between Compact Structure and Anti-Endotoxin Activity. *Biochemistry* **2017**, *56*, 1348-1362, doi:10.1021/acs.biochem.6b01229.
216. Halder, S.; Yadav, K.K.; Sarkar, R.; Mukherjee, S.; Saha, P.; Haldar, S.; Karmakar, S.; Sen, T. Alteration of Zeta potential and membrane permeability in bacteria: a study with cationic agents. *Springerplus* **2015**, *4*, 672, doi:10.1186/s40064-015-1476-7.
217. Ratha, B.N.; Kar, R.K.; Bednarikova, Z.; Gazova, Z.; Kotler, S.A.; Raha, S.; De, S.; Maiti, N.C.; Bhunia, A. Molecular Details of a Salt Bridge and Its Role in Insulin Fibrillation by NMR and Raman Spectroscopic Analysis. *J Phys Chem B* **2020**, *124*, 1125-1136, doi:10.1021/acs.jpcc.9b10349.
218. Jung, G.B.; Nam, S.W.; Choi, S.; Lee, G.J.; Park, H.K. Evaluation of antibiotic effects on *Pseudomonas aeruginosa* biofilm using Raman spectroscopy and multivariate analysis. *Biomed Opt Express* **2014**, *5*, 3238-3251, doi:10.1364/BOE.5.003238.
219. Patel, K.D.; Mohid, S.A.; Dutta, A.; Arichthota, S.; Bhunia, A.; Haldar, D.; Sarojini, V. Synthesis and antibacterial study of cell-penetrating peptide conjugated trifluoroacetyl and thioacetyl lysine modified peptides. *Eur J Med Chem* **2021**, *219*, 113447, doi:10.1016/j.ejmech.2021.113447.
220. Cranfield, C.G.; Henriques, S.T.; Martinac, B.; Duckworth, P.; Craik, D.J.; Cornell, B. Kalata B1 and Kalata B2 Have a Surfactant-Like Activity in Phosphatidylethanolamine-Containing Lipid Membranes. *Langmuir* **2017**, *33*, 6630-6637, doi:10.1021/acs.langmuir.7b01642.
221. Cranfield, C.; Carne, S.; Martinac, B.; Cornell, B. The assembly and use of tethered bilayer lipid membranes (tBLMs). *Methods Mol Biol* **2015**, *1232*, 45-53, doi:10.1007/978-1-4939-1752-5_4.
222. Cranfield, C.G.; Bettler, T.; Cornell, B. Nanoscale ion sequestration to determine the polarity selectivity of ion conductance in carriers and channels. *Langmuir* **2015**, *31*, 292-298, doi:10.1021/la504057z.
223. Roumestand, C.; Canet, D. Extending the excitation sculpting concept for selective excitation. *J Magn Reson* **2000**, *147*, 331-339, doi:10.1006/jmre.2000.2206.
224. Datta, A.; Bhattacharyya, D.; Singh, S.; Ghosh, A.; Schmidtchen, A.; Malmsten, M.; Bhunia, A. Role of Aromatic Amino Acids in Lipopolysaccharide and Membrane Interactions of Antimicrobial Peptides for Use in Plant Disease Control. *J Biol Chem* **2016**, *291*, 13301-13317, doi:10.1074/jbc.M116.719575.
225. Laskowski, R.A.; Rullmann, J.A.; MacArthur, M.W.; Kaptein, R.; Thornton, J.M. AQUA and PROCHECK-NMR: programs for checking the quality of protein structures solved by NMR. *J Biomol NMR* **1996**, *8*, 477-486.
226. Sharma, P.; Elofsson, M.; Roy, S. Attenuation of. *Virulence* **2020**, *11*, 795-804, doi:10.1080/21505594.2020.1776979.
227. Hong, Y.; Zeng, J.; Wang, X.; Drlica, K.; Zhao, X. Post-stress bacterial cell death mediated by reactive oxygen species. *Proc Natl Acad Sci U S A* **2019**, *116*, 10064-10071, doi:10.1073/pnas.1901730116.

228. Su, L.J.; Zhang, J.H.; Gomez, H.; Murugan, R.; Hong, X.; Xu, D.; Jiang, F.; Peng, Z.Y. Reactive Oxygen Species-Induced Lipid Peroxidation in Apoptosis, Autophagy, and Ferroptosis. *Oxid Med Cell Longev* **2019**, *2019*, 5080843, doi:10.1155/2019/5080843.
229. Ghosh, A.; Datta, A.; Jana, J.; Kar, R.K.; Chatterjee, C.; Chatterjee, S.; Bhunia, A. Sequence context induced antimicrobial activity: insight into lipopolysaccharide permeabilization. *Mol Biosyst* **2014**, *10*, 1596-1612, doi:10.1039/c4mb00111g.
230. Sawa, T.; Ohara, M.; Kurahashi, K.; Twining, S.S.; Frank, D.W.; Doroques, D.B.; Long, T.; Gropper, M.A.; Wiener-Kronish, J.P. In vitro cellular toxicity predicts *Pseudomonas aeruginosa* virulence in lung infections. *Infect Immun* **1998**, *66*, 3242-3249, doi:10.1128/IAI.66.7.3242-3249.1998.
231. Kugadas, A.; Christiansen, S.H.; Sankaranarayanan, S.; Surana, N.K.; Gauguier, S.; Kunz, R.; Fichorova, R.; Vorup-Jensen, T.; Gadjeva, M. Impact of Microbiota on Resistance to Ocular *Pseudomonas aeruginosa*-Induced Keratitis. *PLoS Pathog* **2016**, *12*, e1005855, doi:10.1371/journal.ppat.1005855.
232. Kłodzińska, E.; Szumski, M.; Dziubakiewicz, E.; Hryniewicz, K.; Skwarek, E.; Janusz, W.; Buszewski, B. Effect of zeta potential value on bacterial behavior during electrophoretic separation. *Electrophoresis* **2010**, *31*, 1590-1596, doi:10.1002/elps.200900559.
233. Bridges, D.F.; Lacombe, A.; Wu, V.C.H. Integrity of the. *Front Microbiol* **2020**, *11*, 888, doi:10.3389/fmicb.2020.00888.
234. Kasibhatla, S.; Amarante-Mendes, G.P.; Finucane, D.; Brunner, T.; Bossy-Wetzel, E.; Green, D.R. Propidium Iodide (PI) Uptake Assay to Detect Apoptosis. *CSH Protoc* **2006**, *2006*, doi:10.1101/pdb.prot4495.
235. Pahlow, S.; Meisel, S.; Cialla-May, D.; Weber, K.; Rösch, P.; Popp, J. Isolation and identification of bacteria by means of Raman spectroscopy. *Adv Drug Deliv Rev* **2015**, *89*, 105-120, doi:10.1016/j.addr.2015.04.006.
236. Schiller, J.; Muller, M.; Fuchs, B.; Arnold, K.; Huster, D. 31P NMR Spectroscopy of Phospholipids: From Micelles to Membranes. *Current Analytical Chemistry* **2007**, *3*, 283-301, doi:<http://dx.doi.org/10.2174/157341107782109635>.
237. Meikle, T.G.; Conn, C.E.; Separovic, F.; Drummond, C.J. Exploring the structural relationship between encapsulated antimicrobial peptides and the bilayer membrane mimetic lipidic cubic phase: studies with gramicidin A'. *RSC Advances* **2016**, *6*, 68685-68694, doi:10.1039/C6RA13658C.
238. Mankoci, S.; Ewing, J.; Dalai, P.; Sahai, N.; Barton, H.A.; Joy, A. Bacterial Membrane Selective Antimicrobial Peptide-Mimetic Polyurethanes: Structure-Property Correlations and Mechanisms of Action. *Biomacromolecules* **2019**, *20*, 4096-4106, doi:10.1021/acs.biomac.9b00939.
239. Biswas, K.; Ilyas, H.; Datta, A.; Bhunia, A. NMR Assisted Antimicrobial Peptide Designing: Structure Based Modifications and Functional Correlation of a Designed Peptide VG16KRKP. *Curr Med Chem* **2020**, *27*, 1387-1404, doi:10.2174/0929867326666190624090817.
240. Bhunia, A.; Ramamoorthy, A.; Bhattacharjya, S. Helical hairpin structure of a potent antimicrobial peptide MSI-594 in lipopolysaccharide micelles by NMR spectroscopy. *Chemistry* **2009**, *15*, 2036-2040, doi:10.1002/chem.200802635.
241. Domadia, P.N.; Bhunia, A.; Ramamoorthy, A.; Bhattacharjya, S. Structure, interactions, and antibacterial activities of MSI-594 derived mutant peptide MSI-594F5A in lipopolysaccharide micelles: role of the helical hairpin conformation in outer-membrane permeabilization. *J Am Chem Soc* **2010**, *132*, 18417-18428, doi:10.1021/ja1083255.
242. Shukla, V.K.; Siemons, L.; Gervasio, F.L.; Hansen, D.F. Aromatic side-chain flips orchestrate the conformational sampling of functional loops in human histone deacetylase 8. *Chem Sci* **2021**, *12*, 9318-9327, doi:10.1039/d1sc01929e.

243. Pritchard, R.B.; Hansen, D.F. Characterising side chains in large proteins by protonless. *Nat Commun* **2019**, *10*, 1747, doi:10.1038/s41467-019-09743-4.
244. Kneller, J.M.; Lu, M.; Bracken, C. An effective method for the discrimination of motional anisotropy and chemical exchange. *J Am Chem Soc* **2002**, *124*, 1852-1853, doi:10.1021/ja017461k.
245. Sun, Y.; Karmakar, M.; Roy, S.; Ramadan, R.T.; Williams, S.R.; Howell, S.; Shive, C.L.; Han, Y.; Stopford, C.M.; Rietsch, A.; et al. TLR4 and TLR5 on corneal macrophages regulate *Pseudomonas aeruginosa* keratitis by signaling through MyD88-dependent and -independent pathways. *J Immunol* **2010**, *185*, 4272-4283, doi:10.4049/jimmunol.1000874.
246. Gandhi, A.; Kariyat, R.R.; Chappa, C.; Tayal, M.; Sahoo, N. Tobacco Hornworm (*Int J Mol Sci* **2020**, *21*, doi:10.3390/ijms21218297.
247. Resch-Genger, U.; Grabolle, M.; Cavaliere-Jaricot, S.; Nitschke, R.; Nann, T. Quantum dots versus organic dyes as fluorescent labels. *Nature Methods* **2008**, *5*, 763, doi:10.1038/nmeth.1248<https://www.nature.com/articles/nmeth.1248#supplementary-information>.
248. Flessau, S.; Wolter, C.; Pöselt, E.; Kröger, E.; Mews, A.; Kipp, T. Fluorescence spectroscopy of individual semiconductor nanoparticles in different ethylene glycols. *Phys Chem Chem Phys* **2014**, *16*, 10444-10455, doi:10.1039/c4cp00443d.
249. Zwijnenburg, M.A. Photoluminescence in semiconductor nanoparticles: an atomistic view of excited state relaxation in nanosized ZnS. *Nanoscale* **2012**, *4*, 3711-3717, doi:10.1039/c2nr30191a.
250. Abdel-Mottaleb, M.M.; Beduneau, A.; Pellequer, Y.; Lamprecht, A. Stability of fluorescent labels in PLGA polymeric nanoparticles: Quantum dots versus organic dyes. *Int J Pharm* **2015**, *494*, 471-478, doi:10.1016/j.ijpharm.2015.08.050.
251. Zheng, Q.; Lavis, L.D. Development of photostable fluorophores for molecular imaging. *Curr Opin Chem Biol* **2017**, *39*, 32-38, doi:10.1016/j.cbpa.2017.04.017.
252. R., L.J. Quenching of Fluorescence. In *Principles of Fluorescence Spectroscopy*; Springer US: 1983; pp. 257-301.
253. Chen, H.; Ahsan, S.S.; Santiago-Berrios, M.B.; Abruña, H.D.; Webb, W.W. Mechanisms of quenching of Alexa fluorophores by natural amino acids. *J Am Chem Soc* **2010**, *132*, 7244-7245, doi:10.1021/ja100500k.
254. Ghose, M.; Mandal, S.; Roy, D.; Mandal, R.K.; Basu, G. Dielectric relaxation in a single tryptophan protein. *FEBS Lett* **2001**, *509*, 337-340.
255. Pierce, D.W.; Boxer, S.G. Dielectric relaxation in a protein matrix. *The Journal of Physical Chemistry* **1992**, *96*, 5560-5566, doi:10.1021/j100192a069.
256. Toseland, C.P. Fluorescent labeling and modification of proteins. *J Chem Biol* **2013**, *6*, 85-95, doi:10.1007/s12154-013-0094-5.
257. Swenson, E.S.; Price, J.G.; Brazelton, T.; Krause, D.S. Limitations of green fluorescent protein as a cell lineage marker. *Stem Cells* **2007**, *25*, 2593-2600, doi:10.1634/stemcells.2007-0241.
258. Malekhaïat Häffner, S.; Malmsten, M. Membrane interactions and antimicrobial effects of inorganic nanoparticles. *Adv Colloid Interface Sci* **2017**, *248*, 105-128, doi:10.1016/j.cis.2017.07.029.
259. Fortina, P.; Kricka, L.J.; Graves, D.J.; Park, J.; Hyslop, T.; Tam, F.; Halas, N.; Surrey, S.; Waldman, S.A. Applications of nanoparticles to diagnostics and therapeutics in colorectal cancer. *Trends Biotechnol* **2007**, *25*, 145-152, doi:10.1016/j.tibtech.2007.02.005.
260. Delehanty, J.B.; Breger, J.C.; Gemmill, K.B.; Stewart, M.H.; Medintz, I.L. Controlling the actuation of therapeutic nanomaterials: enabling nanoparticle-mediated drug delivery. *Ther Deliv* **2013**, *4*, 1411-1429, doi:10.4155/tde.13.110.

261. Boschi, F.; De Sanctis, F. Overview of the optical properties of fluorescent nanoparticles for optical imaging. *Eur J Histochem* **2017**, *61*, 2830, doi:10.4081/ejh.2017.2830.
262. Li, R.; Yan, R.; Bao, J.; Tu, W.; Dai, Z. A localized surface plasmon resonance-enhanced photoelectrochemical biosensing strategy for highly sensitive and scatheless cell assay under red light excitation. *Chemical Communications* **2016**, *52*, 11799-11802, doi:10.1039/C6CC05964C.
263. Ghorai, A.; Bayan, S.; Gogurla, N.; Midya, A.; Ray, S.K. Highly Luminescent WS₂ Quantum Dots/ZnO Heterojunctions for Light Emitting Devices. *ACS Appl Mater Interfaces* **2017**, *9*, 558-565, doi:10.1021/acsami.6b12859.
264. Park, S.C.; Park, Y.; Hahm, K.S. The role of antimicrobial peptides in preventing multidrug-resistant bacterial infections and biofilm formation. *Int J Mol Sci* **2011**, *12*, 5971-5992, doi:10.3390/ijms12095971.
265. Hancock, R.E.; Sahl, H.G. Antimicrobial and host-defense peptides as new anti-infective therapeutic strategies. *Nat Biotechnol* **2006**, *24*, 1551-1557, doi:10.1038/nbt1267.
266. Shai, Y. Mechanism of the binding, insertion and destabilization of phospholipid bilayer membranes by alpha-helical antimicrobial and cell non-selective membrane-lytic peptides. *Biochim Biophys Acta* **1999**, *1462*, 55-70.
267. Loffredo, M.R.; Ghosh, A.; Harmouche, N.; Casciaro, B.; Luca, V.; Bortolotti, A.; Cappiello, F.; Stella, L.; Bhunia, A.; Bechinger, B.; et al. Membrane perturbing activities and structural properties of the frog-skin derived peptide Esculentin-1a(1-21)NH₂ and its Diastereomer Esc(1-21)-1c: Correlation with their antipseudomonal and cytotoxic activity. *Biochim Biophys Acta* **2017**, *1859*, 2327-2339, doi:10.1016/j.bbamem.2017.09.009.
268. Bechinger, B.; Lohner, K. Detergent-like actions of linear amphipathic cationic antimicrobial peptides. *Biochim Biophys Acta* **2006**, *1758*, 1529-1539, doi:10.1016/j.bbamem.2006.07.001.
269. Knappe, D.; Henklein, P.; Hoffmann, R.; Hilpert, K. Easy strategy to protect antimicrobial peptides from fast degradation in serum. *Antimicrob Agents Chemother* **2010**, *54*, 4003-4005, doi:10.1128/AAC.00300-10.
270. Jenssen, H.; Aspmo, S.I. Serum stability of peptides. *Methods Mol Biol* **2008**, *494*, 177-186, doi:10.1007/978-1-59745-419-3_10.
271. Carmona, G.; Rodriguez, A.; Juarez, D.; Corzo, G.; Villegas, E. Improved protease stability of the antimicrobial peptide Pin2 substituted with D-amino acids. *Protein J* **2013**, *32*, 456-466, doi:10.1007/s10930-013-9505-2.
272. Bhattacharjya, S.; Ramamoorthy, A. Multifunctional host defense peptides: functional and mechanistic insights from NMR structures of potent antimicrobial peptides. *FEBS J* **2009**, *276*, 6465-6473, doi:10.1111/j.1742-4658.2009.07357.x.
273. Hancock, R.E. Resistance mechanisms in *Pseudomonas aeruginosa* and other nonfermentative gram-negative bacteria. *Clin Infect Dis* **1998**, *27 Suppl 1*, S93-99.
274. Pappas, P.G.; Lionakis, M.S.; Arendrup, M.C.; Ostrosky-Zeichner, L.; Kullberg, B.J. Invasive candidiasis. *Nat Rev Dis Primers* **2018**, *4*, 18026, doi:10.1038/nrdp.2018.26.
275. Elbing, K.; Brent, R. Media preparation and bacteriological tools. *Curr Protoc Mol Biol* **2002**, *Chapter 1*, Unit 1.1, doi:10.1002/0471142727.mb0101s59.
276. Pierce, C.G.; Uppuluri, P.; Tristan, A.R.; Wormley, F.L.; Mowat, E.; Ramage, G.; Lopez-Ribot, J.L. A simple and reproducible 96-well plate-based method for the formation of fungal biofilms and its application to antifungal susceptibility testing. *Nat Protoc* **2008**, *3*, 1494-1500, doi:10.1038/nprot.2008.141.
277. Ghorai, A.; Midya, A.; Maiti, R.; Ray, S.K. Exfoliation of WS₂ in the semiconducting phase using a group of lithium halides: a new method of Li intercalation. *Dalton Trans* **2016**, *45*, 14979-14987, doi:10.1039/c6dt02823c.
278. MacGowan, A.P.; Wootton, M.; Hedges, A.J.; Bowker, K.E.; Holt, H.A.; Reeves, D.S. A new time-kill method of assessing the relative efficacy of antimicrobial agents alone and in

- combination developed using a representative beta-lactam, aminoglycoside and fluoroquinolone. *J Antimicrob Chemother* **1996**, *38*, 193-203.
279. Müssen, M.; Di Fiore, S.; Römling, U.; Häußler, S. A 96-well-plate-based optical method for the quantitative and qualitative evaluation of *Pseudomonas aeruginosa* biofilm formation and its application to susceptibility testing. *Nat Protoc* **2010**, *5*, 1460-1469, doi:10.1038/nprot.2010.110.
280. Brandenburg, K.S.; Rodriguez, K.J.; McAnulty, J.F.; Murphy, C.J.; Abbott, N.L.; Schurr, M.J.; Czuprynski, C.J. Tryptophan inhibits biofilm formation by *Pseudomonas aeruginosa*. *Antimicrob Agents Chemother* **2013**, *57*, 1921-1925, doi:10.1128/AAC.00007-13.
281. O'Toole, G.A. Microtiter dish biofilm formation assay. *J Vis Exp* **2011**, doi:10.3791/2437.
282. Chauhan, N.M.; Shinde, R.B.; Karuppaiyil, S.M. Effect of alcohols on filamentation, growth, viability and biofilm development in *Candida albicans*. *Braz J Microbiol* **2013**, *44*, 1315-1320, doi:10.1590/S1517-83822014005000012.
283. Sklenar, V.; Píotko, M.; Leppik, R.; Saudek, V. Journal of Magnetic Resonance. *Journal of Magnetic Resonance* **1993**, *102*, 241-245.
284. Harris, R.K.; Becker, E.D.; Cabral de Menezes, S.M.; Goodfellow, R.; Granger, P. NMR Nomenclature: Nuclear Spin Properties and Conventions for Chemical Shifts. IUPAC Recommendations 2001. *Solid State Nucl Magn Reson* **2002**, *22*, 458-483, doi:10.1006/snmr.2002.0063.
285. Saha, T.; Dasari, S.; Tewari, D.; Prathap, A.; Sureshan, K.M.; Bera, A.K.; Mukherjee, A.; Talukdar, P. Hopping-mediated anion transport through a mannitol-based rosette ion channel. *J Am Chem Soc* **2014**, *136*, 14128-14135, doi:10.1021/ja506278z.
286. Ghorai, A.; Midya, A.; Ray, S.K. Superior charge storage performance of WS₂ quantum dots in a flexible solid state supercapacitor. *New Journal of Chemistry* **2018**, *42*, 3609-3613, doi:10.1039/C7NJ03869K.
287. Guo, X.; Wang, Y.; Wu, F.; Ni, Y.; Kokot, S. The use of tungsten disulfide dots as highly selective, fluorescent probes for analysis of nitrofurazone. *Talanta* **2015**, *144*, 1036-1043, doi:10.1016/j.talanta.2015.07.055.
288. Wang, X.; Quinn, P.J. Endotoxins: lipopolysaccharides of gram-negative bacteria. *Subcell Biochem* **2010**, *53*, 3-25, doi:10.1007/978-90-481-9078-2_1.
289. Li, P.; Sun, M.; Wohland, T.; Ho, B.; Ding, J.L. The molecular mechanism of interaction between sushi peptide and *Pseudomonas* endotoxin. *Cell Mol Immunol* **2006**, *3*, 21-28.
290. Sadekuzzaman, M.; S. Yang, M.F.R.M.; Ha., S.D. Current and Recent Advanced Strategies for Combating Biofilms. *Comprehensive Reviews in Food Science and Food Safety* **2015**, *14*, 491-509, doi:10.1111/1541-4337.12144.
291. Malmsten, M. Inorganic nanomaterials as delivery systems for proteins, peptides, DNA, and siRNA. *Current Opinion in Colloid & Interface Science* **2013**, *18*, 468-480, doi:<https://doi.org/10.1016/j.cocis.2013.06.002>.
292. Elzoghby, A.O.; Hemasa, A.L.; Freag, M.S. Hybrid protein-inorganic nanoparticles: From tumor-targeted drug delivery to cancer imaging. *J Control Release* **2016**, *243*, 303-322, doi:10.1016/j.jconrel.2016.10.023.
293. Rai, M.; Ingle, A.P.; Gupta, I.; Brandelli, A. Bioactivity of noble metal nanoparticles decorated with biopolymers and their application in drug delivery. *Int J Pharm* **2015**, *496*, 159-172, doi:10.1016/j.ijpharm.2015.10.059.
294. Tonga, G.Y.; Moyano, D.F.; Kim, C.S.; Rotello, V.M. Inorganic Nanoparticles for Therapeutic Delivery: Trials, Tribulations and Promise. *Curr Opin Colloid Interface Sci* **2014**, *19*, 49-55, doi:10.1016/j.cocis.2014.03.004.
295. Brown, A.N.; Smith, K.; Samuels, T.A.; Lu, J.; Obare, S.O.; Scott, M.E. Nanoparticles functionalized with ampicillin destroy multiple-antibiotic-resistant isolates of *Pseudomonas aeruginosa* and *Enterobacter aerogenes* and methicillin-resistant

- Staphylococcus aureus. *Appl Environ Microbiol* **2012**, *78*, 2768-2774, doi:10.1128/AEM.06513-11.
296. Payne, J.N.; Waghvani, H.K.; Connor, M.G.; Hamilton, W.; Tockstein, S.; Moolani, H.; Chavda, F.; Badwaik, V.; Lawrenz, M.B.; Dakshinamurthy, R. Novel Synthesis of Kanamycin Conjugated Gold Nanoparticles with Potent Antibacterial Activity. *Front Microbiol* **2016**, *7*, 607, doi:10.3389/fmicb.2016.00607.
297. Hussain, S.; Joo, J.; Kang, J.; Kim, B.; Braun, G.B.; She, Z.G.; Kim, D.; Mann, A.P.; Mölder, T.; Teesalu, T.; et al. Antibiotic-loaded nanoparticles targeted to the site of infection enhance antibacterial efficacy. *Nat Biomed Eng* **2018**, *2*, 95-103, doi:10.1038/s41551-017-0187-5.
298. Thakur, M.; Pandey, S.; Mewada, A.; Patil, V.; Khade, M.; Goshi, E.; Sharon, M. Antibiotic conjugated fluorescent carbon dots as a theranostic agent for controlled drug release, bioimaging, and enhanced antimicrobial activity. *J Drug Deliv* **2014**, *2014*, 282193, doi:10.1155/2014/282193.
299. Chen, H.; Zhang, M.; Li, B.; Chen, D.; Dong, X.; Wang, Y.; Gu, Y. Versatile antimicrobial peptide-based ZnO quantum dots for in vivo bacteria diagnosis and treatment with high specificity. *Biomaterials* **2015**, *53*, 532-544, doi:10.1016/j.biomaterials.2015.02.105.
300. Luo, Z.; Wu, Q.; Zhang, M.; Li, P.; Ding, Y. Cooperative antimicrobial activity of CdTe quantum dots with rocephin and fluorescence monitoring for Escherichia coli. *J Colloid Interface Sci* **2011**, *362*, 100-106, doi:10.1016/j.jcis.2011.06.039.
301. Tsoi, K.M.; Dai, Q.; Alman, B.A.; Chan, W.C. Are quantum dots toxic? Exploring the discrepancy between cell culture and animal studies. *Acc Chem Res* **2013**, *46*, 662-671, doi:10.1021/ar300040z.
302. Liu, J.; Hu, R.; Zhang, B.; Wang, Y.; Liu, X.; Law, W.C.; Liu, L.; Ye, L.; Yong, K.T. Cytotoxicity assessment of functionalized CdSe, CdTe and InP quantum dots in two human cancer cell models. *Mater Sci Eng C Mater Biol Appl* **2015**, *57*, 222-231, doi:10.1016/j.msec.2015.07.044.
303. Bradburne, C.E.; Delehanty, J.B.; Boeneman Gemmill, K.; Mei, B.C.; Mattoussi, H.; Susumu, K.; Blanco-Canosa, J.B.; Dawson, P.E.; Medintz, I.L. Cytotoxicity of quantum dots used for in vitro cellular labeling: role of QD surface ligand, delivery modality, cell type, and direct comparison to organic fluorophores. *Bioconjug Chem* **2013**, *24*, 1570-1583, doi:10.1021/bc4001917.
304. Winnik, F.M.; Maysinger, D. Quantum dot cytotoxicity and ways to reduce it. *Acc Chem Res* **2013**, *46*, 672-680, doi:10.1021/ar3000585.
305. Yong, K.T.; Law, W.C.; Hu, R.; Ye, L.; Liu, L.; Swihart, M.T.; Prasad, P.N. Nanotoxicity assessment of quantum dots: from cellular to primate studies. *Chem Soc Rev* **2013**, *42*, 1236-1250, doi:10.1039/c2cs35392j.
306. Xie, R.; Chen, K.; Chen, X.; Peng, X. InAs/InP/ZnSe Core/Shell/Shell Quantum Dots as Near-Infrared Emitters: Bright, Narrow-Band, Non-Cadmium Containing, and Biocompatible. *Nano Res* **2008**, *1*, 457-464.
307. Zimmer, J.P.; Kim, S.W.; Ohnishi, S.; Tanaka, E.; Frangioni, J.V.; Bawendi, M.G. Size series of small indium arsenide-zinc selenide core-shell nanocrystals and their application to in vivo imaging. *J Am Chem Soc* **2006**, *128*, 2526-2527, doi:10.1021/ja0579816.
308. Yang, X.; Li, J.; Liang, T.; Ma, C.; Zhang, Y.; Chen, H.; Hanagata, N.; Su, H.; Xu, M. Antibacterial activity of two-dimensional MoS₂ sheets. *Nanoscale* **2014**, *6*, 10126-10133, doi:10.1039/c4nr01965b.
309. Lin, T.Y.; Weibel, D.B. Organization and function of anionic phospholipids in bacteria. *Appl Microbiol Biotechnol* **2016**, *100*, 4255-4267, doi:10.1007/s00253-016-7468-x.
310. Oliver, P.M.; Crooks, J.A.; Leidl, M.; Yoon, E.J.; Saghatelian, A.; Weibel, D.B. Localization of anionic phospholipids in Escherichia coli cells. *J Bacteriol* **2014**, *196*, 3386-3398, doi:10.1128/JB.01877-14.

311. Xu, F.; Rychnovsky, S.D.; Belani, J.D.; Hobbs, H.H.; Cohen, J.C.; Rawson, R.B. Dual roles for cholesterol in mammalian cells. *Proc Natl Acad Sci U S A* **2005**, *102*, 14551-14556, doi:10.1073/pnas.0503590102.
312. Parks, L.W.; Smith, S.J.; Crowley, J.H. Biochemical and physiological effects of sterol alterations in yeast—a review. *Lipids* **1995**, *30*, 227-230.
313. Pasupuleti, M.; Walse, B.; Svensson, B.; Malmsten, M.; Schmidtchen, A. Rational design of antimicrobial C3a analogues with enhanced effects against Staphylococci using an integrated structure and function-based approach. *Biochemistry* **2008**, *47*, 9057-9070, doi:10.1021/bi800991e.
314. Kalle, M.; Papareddy, P.; Kasetty, G.; Tollefsen, D.M.; Malmsten, M.; Mörgelin, M.; Schmidtchen, A. Proteolytic activation transforms heparin cofactor II into a host defense molecule. *J Immunol* **2013**, *190*, 6303-6310, doi:10.4049/jimmunol.1203030.
315. Malmsten, M.; Davoudi, M.; Walse, B.; Rydengård, V.; Pasupuleti, M.; Mörgelin, M.; Schmidtchen, A. Antimicrobial peptides derived from growth factors. *Growth Factors* **2007**, *25*, 60-70, doi:10.1080/08977190701344120.
316. Duong, D.T.; Singh, S.; Bagheri, M.; Verma, N.K.; Schmidtchen, A.; Malmsten, M. Pronounced peptide selectivity for melanoma through tryptophan end-tagging. *Sci Rep* **2016**, *6*, 24952, doi:10.1038/srep24952.
317. Matsushita, I.; Yanase, H. A novel thermophilic lysozyme from bacteriophage phiIN93. *Biochem Biophys Res Commun* **2008**, *377*, 89-92, doi:10.1016/j.bbrc.2008.09.101.
318. Redfield, C.; Dobson, C.M. Sequential 1H NMR assignments and secondary structure of hen egg white lysozyme in solution. *Biochemistry* **1988**, *27*, 122-136, doi:10.1021/bi00401a020.
319. Hancock, R.E.; Scott, M.G. The role of antimicrobial peptides in animal defenses. *Proc Natl Acad Sci U S A* **2000**, *97*, 8856-8861, doi:10.1073/pnas.97.16.8856.
320. Nasr, S.H.; Dasari, S.; Mills, J.R.; Theis, J.D.; Zimmermann, M.T.; Fonseca, R.; Vrana, J.A.; Lester, S.J.; McLaughlin, B.M.; Gillespie, R.; et al. Hereditary Lysozyme Amyloidosis Variant p.Leu102Ser Associates with Unique Phenotype. *J Am Soc Nephrol* **2017**, *28*, 431-438, doi:10.1681/ASN.2016090951.
321. Mocanu, M.M.; Ganea, C.; Siposova, K.; Filippi, A.; Demjen, E.; Marek, J.; Bednarikova, Z.; Antosova, A.; Baran, I.; Gazova, Z. Polymorphism of hen egg white lysozyme amyloid fibrils influences the cytotoxicity in LLC-PK1 epithelial kidney cells. *Int J Biol Macromol* **2014**, *65*, 176-187, doi:10.1016/j.ijbiomac.2014.01.030.
322. Ramazzotti, M.; Melani, F.; Marchi, L.; Mulinacci, N.; Gestri, S.; Tiribilli, B.; Degl'Innocenti, D. Mechanisms for the inhibition of amyloid aggregation by small ligands. *Biosci Rep* **2016**, *36*, doi:10.1042/BSR20160101.
323. Dobson, C.M. Protein folding and misfolding. *Nature* **2003**, *426*, 884-890, doi:10.1038/nature02261.
324. Miller, Y. Molecular Insights into the Effect of Metals on Amyloid Aggregation. *Methods Mol Biol* **2022**, *2340*, 121-137, doi:10.1007/978-1-0716-1546-1_7.
325. Khlitunova, I.; Biernat, J.; Wang, Y.; Pickhardt, M.; von Bergen, M.; Gazova, Z.; Mandelkow, E.; Mandelkow, E.M. Inducible expression of Tau repeat domain in cell models of tauopathy: aggregation is toxic to cells but can be reversed by inhibitor drugs. *J Biol Chem* **2006**, *281*, 1205-1214, doi:10.1074/jbc.M507753200.
326. Reinke, A.A.; Gestwicki, J.E. Structure-activity relationships of amyloid beta-aggregation inhibitors based on curcumin: influence of linker length and flexibility. *Chem Biol Drug Des* **2007**, *70*, 206-215, doi:10.1111/j.1747-0285.2007.00557.x.
327. Doig, A.J.; Derreumaux, P. Inhibition of protein aggregation and amyloid formation by small molecules. *Curr Opin Struct Biol* **2015**, *30*, 50-56, doi:10.1016/j.sbi.2014.12.004.
328. Kunitomi, R.; Pradipta, A.R.; Kawabe, H.; Lobsiger, N.; Tanaka, K.; Zako, T. Inhibition of amyloid formation of amyloid β (1-42), amylin and insulin by 1,5-diazacyclooctanes, a

- spermine-acrolein conjugate. *Bioorg Med Chem* **2021**, *46*, 116391, doi:10.1016/j.bmc.2021.116391.
329. Siddiqi, M.K.; Alam, P.; Chaturvedi, S.K.; Khan, M.V.; Nusrat, S.; Malik, S.; Khan, R.H. Capreomycin inhibits the initiation of amyloid fibrillation and suppresses amyloid induced cell toxicity. *Biochim Biophys Acta Proteins Proteom* **2018**, *1866*, 549-557, doi:10.1016/j.bbapap.2018.02.005.
330. Summers, W.K. Tacrine, and Alzheimer's treatments. *J Alzheimers Dis* **2006**, *9*, 439-445, doi:10.3233/jad-2006-9s350.
331. Keri, R.S.; Patil, M.R.; Patil, S.A.; Budagumpi, S. A comprehensive review in current developments of benzothiazole-based molecules in medicinal chemistry. *Eur J Med Chem* **2015**, *89*, 207-251, doi:10.1016/j.ejmech.2014.10.059.
332. Thai, N.Q.; Bednarikova, Z.; Gancar, M.; Linh, H.Q.; Hu, C.K.; Li, M.S.; Gazova, Z. Compound CID 9998128 Is a Potential Multitarget Drug for Alzheimer's Disease. *ACS Chem Neurosci* **2018**, *9*, 2588-2598, doi:10.1021/acchemneuro.8b00091.
333. Korabecny, J.; Dolezal, R.; Cabelova, P.; Horova, A.; Hrubá, E.; Ricny, J.; Sedlacek, L.; Nepovimova, E.; Spilovska, K.; Andrs, M.; et al. 7-MEOTA-donepezil like compounds as cholinesterase inhibitors: Synthesis, pharmacological evaluation, molecular modeling and QSAR studies. *Eur J Med Chem* **2014**, *82*, 426-438, doi:10.1016/j.ejmech.2014.05.066.
334. Yang, H.; Yang, S.; Kong, J.; Dong, A.; Yu, S. Obtaining information about protein secondary structures in aqueous solution using Fourier transform IR spectroscopy. *Nat Protoc* **2015**, *10*, 382-396, doi:10.1038/nprot.2015.024.
335. Gazova, Z.; Siposova, K.; Kurin, E.; Mučaji, P.; Nagy, M. Amyloid aggregation of lysozyme: the synergy study of red wine polyphenols. *Proteins* **2013**, *81*, 994-1004, doi:10.1002/prot.24250.
336. Gazova, Z.; Bellova, A.; Daxnerova, Z.; Imrich, J.; Kristian, P.; Tomascikova, J.; Bagelova, J.; Fedunova, D.; Antalík, M. Acridine derivatives inhibit lysozyme aggregation. *Eur Biophys J* **2008**, *37*, 1261-1270, doi:10.1007/s00249-008-0313-0.
337. Ulicna, K.; Bednarikova, Z.; Hsu, W.T.; Holztragerova, M.; Wu, J.W.; Hamulakova, S.; Wang, S.S.; Gazova, Z. Lysozyme amyloid fibrillization in presence of tacrine/acridone-coumarin heterodimers. *Colloids Surf B Biointerfaces* **2018**, *166*, 108-118, doi:10.1016/j.colsurfb.2018.03.010.
338. Biancalana, M.; Koide, S. Molecular mechanism of Thioflavin-T binding to amyloid fibrils. *Biochim Biophys Acta* **2010**, *1804*, 1405-1412, doi:10.1016/j.bbapap.2010.04.001.
339. Takai, E.; Uda, K.; Matsushita, S.; Shikiya, Y.; Yamada, Y.; Shiraki, K.; Zako, T.; Maeda, M. Cysteine inhibits amyloid fibrillation of lysozyme and directs the formation of small worm-like aggregates through non-covalent interactions. *Biotechnol Prog* **2014**, *30*, 470-478, doi:10.1002/btpr.1866.
340. Re, F.; Airolidi, C.; Zona, C.; Masserini, M.; La Ferla, B.; Quattrocchi, N.; Nicotra, F. Beta amyloid aggregation inhibitors: small molecules as candidate drugs for therapy of Alzheimer's disease. *Curr Med Chem* **2010**, *17*, 2990-3006, doi:10.2174/092986710791959729.
341. Lieu, V.H.; Wu, J.W.; Wang, S.S.; Wu, C.H. Inhibition of amyloid fibrillization of hen egg-white lysozymes by rifampicin and p-benzoquinone. *Biotechnol Prog* **2007**, *23*, 698-706, doi:10.1021/bp060353n.
342. de Freitas Silva, M.; Dias, K.S.T.; Gontijo, V.S.; Ortiz, C.J.C.; Viegas, C. Multi-Target Directed Drugs as a Modern Approach for Drug Design Towards Alzheimer's Disease: An Update. *Curr Med Chem* **2018**, *25*, 3491-3525, doi:10.2174/0929867325666180111101843.

Peer-reviewed publications.

Journal of
Medicinal Chemistry

Subscriber access provided by UNIV OF DURHAM

Article

Insights into the Mechanism of Antimicrobial Activity of Seven-Residue Peptides

Gopal Pandit, Humaira Ilyas, Suvankar Ghosh, Anil Parsram Bidkar, Sk. Abdul Mohid, Anirban Bhunia, Priyadarshi Satpati, and Sunanda Chatterjee

J. Med. Chem., **Just Accepted Manuscript** • DOI: 10.1021/acs.jmedchem.8b00353 • Publication Date (Web): 02 Aug 2018

Downloaded from <http://pubs.acs.org> on August 3, 2018

Just Accepted

"Just Accepted" manuscripts have been peer-reviewed and accepted for publication. They are posted online prior to technical editing, formatting for publication and author proofing. The American Chemical Society provides "Just Accepted" as a service to the research community to expedite the dissemination of scientific material as soon as possible after acceptance. "Just Accepted" manuscripts appear in full in PDF format accompanied by an HTML abstract. "Just Accepted" manuscripts have been fully peer reviewed, but should not be considered the official version of record. They are citable by the Digital Object Identifier (DOI®). "Just Accepted" is an optional service offered to authors. Therefore, the "Just Accepted" Web site may not include all articles that will be published in the journal. After a manuscript is technically edited and formatted, it will be removed from the "Just Accepted" Web site and published as an ASAP article. Note that technical editing may introduce minor changes to the manuscript text and/or graphics which could affect content, and all legal disclaimers and ethical guidelines that apply to the journal pertain. ACS cannot be held responsible for errors or consequences arising from the use of information contained in these "Just Accepted" manuscripts.

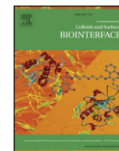


is published by the American Chemical Society, 1155 Sixteenth Street N.W., Washington, DC 20036
Published by American Chemical Society. Copyright © American Chemical Society.
However, no copyright claim is made to original U.S. Government works, or works produced by employees of any Commonwealth realm Crown government in the course of their duties.



Contents lists available at ScienceDirect

Colloids and Surfaces B: Biointerfaces

journal homepage: www.elsevier.com/locate/colsurfb

Application of tungsten disulfide quantum dot-conjugated antimicrobial peptides in bio-imaging and antimicrobial therapy



Sk. Abdul Mohid^{a,1}, Arup Ghorai^{b,1}, Humaira Ilyas^a, Kamal H. Mroue^c, Gomathy Narayanan^d, Abhisek Sarkar^e, Samit K. Ray^f, Kaushik Biswas^e, Amal Kanti Bera^d, Martin Malmsten^{g,h,**}, Anupam Midya^{b,*}, Anirban Bhunia^{a,*}

^a Department of Biophysics, Bose Institute, Kolkata, 700054, India

^b School of Nanoscience and Technology, IIT Kharagpur, Kharagpur, 721302, India

^c Department of Chemistry, University of Waterloo, Waterloo, Ontario, N2L3G1, Canada

^d Department of Biotechnology, IIT Madras, Chennai, 600036, India

^e Division of Molecular Medicine, Bose Institute, Kolkata, 700054, India

^f Department of Physics, IIT Kharagpur, Kharagpur, 721302, India

^g Department of Pharmacy, Uppsala University, SE-75232, Uppsala, Sweden

^h Department of Pharmacy, University of Copenhagen, DK-2100, Copenhagen, Denmark

ARTICLE INFO

Keywords:

Anti-biofilm
Antimicrobial peptide
Ion channel
Peptide NMR
Quantum dots

ABSTRACT

Two-dimensional (2D) tungsten disulfide (WS₂) quantum dots offer numerous promising applications in materials and optoelectronic sciences. Additionally, the catalytic and photoluminescence properties of ultra-small WS₂ nanoparticles are of potential interest in biomedical sciences. Addressing the use of WS₂ in the context of infection, the present study describes the conjugation of two potent antimicrobial peptides with WS₂ quantum dots, as well as the application of the resulting conjugates in antimicrobial therapy and bioimaging. In doing so, we determined the three-dimensional solution structure of the quantum dot-conjugated antimicrobial peptide by a series of high-resolution nuclear magnetic resonance (NMR) techniques, correlating this to the disruption of both model lipid and bacterial membranes, and to several key biological performances, including antimicrobial and anti-biofilm effects, as well as cell toxicity. The results demonstrate that particle conjugation enhances the antimicrobial and anti-biofilm potency of these peptides, effects inferred to be due to multi-dendate interactions for the conjugated peptides. As such, our study provides information on the mode-of-action of such conjugates, laying the foundation for their potential use in treatment and monitoring of infections.

1. Introduction

Fluorescence and photoluminescence are powerful techniques that are widely used in biological and biochemical experiments via microscopy and spectroscopy [1]. Key advantages of these techniques typically include high sensitivity, as well as compatibility with non-invasive and non-destructive protocols, the latter key for live cell and *in vivo* imaging [2]. Unfortunately, numerous fluorophores are prone to photobleaching [2], while others have quantum yields sensitive to quenching [3], and/or to ambient dielectric properties [4]. Fluorescent proteins such as Green Fluorescence Protein (GFP), on the other hand, suffer from disadvantages related to their bulky size [5]. Considering

advantages relating to high sensitivity and photostability, optical nanomaterials have received considerable attention in materials science and nanomedicine, e.g., in diagnostics and drug delivery, as well as in their theranostic combinations [6]. Quantum dots (QDs) prepared from II/VI and IIIA/V semiconductors have received particular recent attention [7]. In this context, low-dimensional inorganic transition metal dichalcogenides (TMDC), consisting of triatomic building blocks (MX₂, where M = Mo or W, and X = S or Se), represent a new and promising class of semiconducting materials, which are environmentally benign, highly fluorescent, and optically stable [8]. MoS₂ and WS₂ are two members of TMDCs, sharing key properties such as small size (1–6 nm), high fluorescence intensity (20–30 times higher than organic dyes), and

* Corresponding authors.

** Corresponding author at: Department of Pharmacy, Uppsala University, SE-75232, Uppsala, Sweden.

E-mail addresses: martin.malmsten@farmaci.uu.se, martin.malmsten@sund.ku.dk (M. Malmsten), anupam.midya@iitkgp.ac.in (A. Midya), bhunia@jcbse.ac.in (A. Bhunia).

¹ Contributed equally.

<https://doi.org/10.1016/j.colsurfb.2019.01.020>

Received 11 September 2018; Received in revised form 24 December 2018; Accepted 7 January 2019

Available online 08 January 2019

0927-7765/© 2019 Elsevier B.V. All rights reserved.

Enhanced Silkworm Cecropin B Antimicrobial Activity against *Pseudomonas aeruginosa* from Single Amino Acid Variation

Ottavia Romoli,^{†,¶} Shruti Mukherjee,^{‡,¶} Sk Abdul Mohid,[‡] Arkajyoti Dutta,[§] Aurora Montali,^{||} Elisa Franzolin,[†] Daniel Brady,[†] Francesca Zito,[⊥] Elisabetta Bergantino,[†] Chiara Rampazzo,[†] Gianluca Tettamanti,^{||} Anirban Bhunia,^{*,‡,¶} and Federica Sandrelli^{*,†,¶}

[†]Department of Biology, University of Padova, Via Ugo Bassi 58/B, 35131 Padova, Italy

[‡]Department of Biophysics, Bose Institute, P-1/12 CIT Scheme VII (M), 700 054 Kolkata, India

[§]Department of Chemistry, Bose Institute, 93/1 A P C Road, 700 009 Kolkata, India

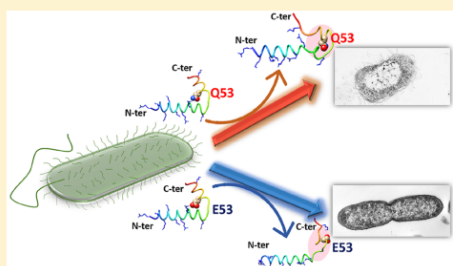
^{||}Department of Biotechnology and Life Sciences, University of Insubria, Via Jean Henry Dunant, 3, 21100 Varese, Italy

[⊥]Laboratoire de Biologie Physico-Chimique des Protéines Membranaires, Institut de Biologie Physico-Chimique, CNRS, UMR7099, University Paris Diderot, Sorbonne Paris Cité, Paris Sciences et Lettres Research University, F-75005 Paris, France

Supporting Information

ABSTRACT: *Pseudomonas aeruginosa* is an opportunistic bacterial pathogen causing severe infections in hospitalized and immunosuppressed patients, particularly individuals affected by cystic fibrosis. Several clinically isolated *P. aeruginosa* strains were found to be resistant to three or more antimicrobial classes indicating the importance of identifying new antimicrobials active against this pathogen. Here, we characterized the antimicrobial activity and the action mechanisms against *P. aeruginosa* of two natural isoforms of the antimicrobial peptide cecropin B, both isolated from the silkworm *Bombyx mori*. These cecropin B isoforms differ in a single amino acid substitution within the active portion of the peptide, so that the glutamic acid of the E53 CecB variant is replaced by a glutamine in the Q53 CecB isoform. Both peptides showed a high antimicrobial and membranolytic activity against *P. aeruginosa*, with Q53 CecB displaying greater activity compared with the E53 CecB isoform. Biophysical analyses, live-cell NMR, and molecular-dynamic-simulation studies indicated that both peptides might act as membrane-interacting elements, which can disrupt outer-membrane organization, facilitating their translocation toward the inner membrane of the bacterial cell. Our data also suggest that the amino acid variation of the Q53 CecB isoform represents a critical factor in stabilizing the hydrophobic segment that interacts with the bacterial membrane, determining the highest antimicrobial activity of the whole peptide. Its high stability to pH and temperature variations, tolerance to high salt concentrations, and low toxicity against human cells make Q53 CecB a promising candidate in the development of CecB-derived compounds against *P. aeruginosa*.

KEYWORDS: antimicrobial peptides, cecropin B, *Bombyx mori*, NMR, *Pseudomonas aeruginosa*



The extensive use and misuse of conventional antibiotics have led to the emergence of multidrug-resistant (MDR) pathogens, causing a dramatic health burden worldwide. As a result, many initiatives for the discovery and development of new drugs have been promoted.¹ In the urgent need for new therapeutics, antimicrobial peptides (AMPs) are considered interesting candidates as potential alternatives to treat MDR bacterial infections.¹

AMPs are molecules produced by virtually all organisms as effectors of the innate immune response, representing the first line of defense against infections. Insects possess numerous AMPs, which are classified on the basis of their amino acid (aa) sequences and structures.^{2,3} Among AMPs, the cecropin (Cec) group includes five subtypes (A–E) as well as other peptides indicated with different names, such as sarcotoxins,

stomoxins, papiliocins, enbocins, and spodopsins isolated from different insect species and some synthetically derived variants.^{2–5} Structurally, Cec AMPs are linear, cationic peptides with variable lengths from 31 to 39 residues; they have random-coil structures in aqueous solutions but form amphipathic helical structures upon interaction with cell membranes.^{2,3}

Within the Cec group, the CecB subtype is active against both Gram-positive and Gram-negative bacteria and displays antitumor properties.^{6–10} CecB antimicrobial activity is related to interactions with bacterial membranes and to pore

Received: February 1, 2019

Published: May 2, 2019

Design, Synthesis, Antibacterial Potential, and Structural Characterization of N-Acylated Derivatives of the Human Autophagy 16 Polypeptide

Kyriakos Gabriel Varnava,[†] Sk. Abdul Mohid,[‡] Paolo Calligari,[§] Lorenzo Stella,[§] Jóhannes Reynison,^{†,||} Anirban Bhunia,^{*,‡,¶} and Vijayalekshmi Sarojini^{*,†,⊥,||}

[†]School of Chemical Sciences, The University of Auckland, Private Bag 92019, Auckland, New Zealand

[‡]Department of Biophysics, Bose Institute, P-1/12 CIT Scheme VII (M), Kolkata 700054, India

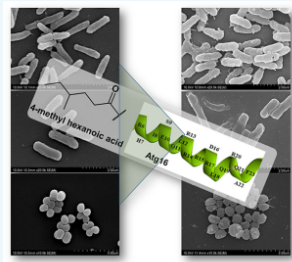
[§]Department of Chemical Science and Technologies, University of Rome Tor Vergata, 00133 Rome, Italy

^{||}School of Pharmacy, Hornbeam Building, Keele University, Staffordshire ST5 5BG, United Kingdom

[⊥]The MacDiarmid Institute for Advanced Materials and Nanotechnology, Wellington 6140, New Zealand

Supporting Information

ABSTRACT: A synthetic antimicrobial peptide library based on the human autophagy 16 polypeptide has been developed. Designed acetylated peptides bearing lipids of different chain lengths resulted in peptides with enhanced potency compared to the parent Atg16. A 21-residue fragment of Atg16 conjugated to 4-methylhexanoic acid (K30) emerged as the most potent antibacterial, with negligible hemolysis. Several studies, including microscopy, dye leakage, and ITC, were conducted to gain insight into the antibacterial mechanism of action of the peptide. Visual inspection using both SEM and TEM revealed the membranolytic effect of the peptide on bacterial cells. The selectivity of the peptide against bacterial cell membranes was also proven using dye leakage assays. ITC analysis revealed the exothermic nature of the binding interaction of the peptide to D8PG micelles. The three-dimensional solution NMR structure of K30 in complex with dioctanoylphosphatidylglycerol (D8PG) micelles revealed that the peptide adopts a helix–loop–helix structure in the presence of anionic membrane lipids mimicking bacterial membranes. Intermolecular NOEs between the peptide and lipid deciphered the location of the peptide in the bound state, which was subsequently supported by the paramagnetic relaxation enhancement (PRE) NMR experiment. Collectively, these results describe the structure–function relationship of the peptide in the bacterial membrane.



INTRODUCTION

Increased morbidity and mortality from bacterial infections¹ and the ability of bacteria to mutate and become resistant to successive generations of antibiotics² necessitate the development of novel antibacterial drugs. Novel platforms that help to deepen our current understanding of antibacterial drug discovery and create drugs that can be used as weapons against lethal bacterial infections are urgently needed. *Pseudomonas aeruginosa*, *Staphylococcus aureus*, and *Escherichia coli* are bacterial pathogens implicated in numerous severe health conditions and infections.^{3–8}

Antimicrobial peptides (AMPs) are widely distributed in humans, plants, and animals and play crucial roles in protecting the host from bacterial infections.^{9–13} AMPs primarily target the bacterial cell membrane and either create pores or cover the membrane like a carpet, ultimately causing bacterial cell lysis. Pore-forming AMPs insert part of the peptide into bacterial phospholipid membranes, bind to a component of the membrane causing membrane lysis, or enter the cells and bind to intracellular targets such as DNA, enzymes, or pro-

teins.^{10,14–16} The overall net positive charge possessed by many AMPs facilitates the interactions with the negatively charged bacterial membrane.¹⁷ The design of a library of peptide antibiotics is usually done using a parent peptide (naturally occurring or designed in the laboratory), followed by structure–activity relationship (SAR) studies and fine-tuning the activity of the peptide.¹⁸ The conjugation of fatty acids is often used to enhance the activity and serum stability of AMPs and is a strategy inspired by lipopeptide antibiotics such as polymyxin.¹⁹ N-Acylated derivatives of other AMPs have been reported in the literature and have generally led to enhancements in antibacterial activity.^{20–23} Our ongoing work in this area has led to fine-tuning the structure and length of the fatty acid component of the antimicrobial lipopeptide bactacin.²⁴

The work reported in this article continues on from our recent report on the antibacterial activity of the human

Received: April 20, 2019

Revised: May 15, 2019

Published: May 30, 2019

7-Methoxytacrine and 2-Aminobenzothiazole Heterodimers: Structure–Mechanism Relationship of Amyloid Inhibitors Based on Rational Design

Miroslav Gancar,[†] Kiet Ho,[†] Sk. Abdul Mohid, Nguyen Quoc Thai, Zuzana Bednarikova, H. Linh Nguyen, Anirban Bhunia, Eugenie Nepovimova, Mai Suan Li,^{*} and Zuzana Gazova^{*}

Cite This: *ACS Chem. Neurosci.* 2020, 11, 715–729

Read Online

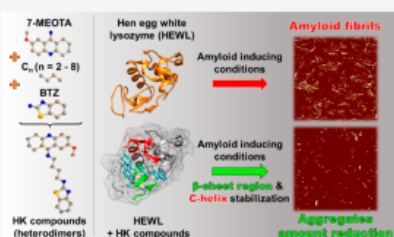
ACCESS |

Metrics & More

Article Recommendations

Supporting Information

ABSTRACT: The formation and accumulation of amyloid aggregates are the phenomena that accompany amyloidoses, which are currently untreatable and include Alzheimer's and Parkinson's diseases, diabetes mellitus, non-neuropathic lysozyme systemic amyloidosis, and others. One of the very promising therapeutic approaches seems to be an inhibition of amyloid formation and/or clearance of amyloid aggregates. Small molecules have a great potential to interfere with amyloid fibrillation of peptides and polypeptides, which can be improved by connection of cyclic structures into single multicyclic molecules and their dimerization. In our study, we focused on heterodimers consisting of 7-methoxytacrine (7-MEOTA) and 2-aminobenzothiazole (BTZ) parent molecules connected by an aliphatic linker. Using *in vitro* and *in silico* methods, we investigated



the ability of studied compounds to inhibit the amyloid aggregation of hen egg white lysozyme. Heterodimerization led to significant improvement of inhibitory activity compared to that of the parent molecules. The efficiency of the heterodimers varied; the most effective inhibitor contained the longest linker, eight carbons long. We suggest that binding of a heterodimer to a lysozyme blocks the interaction between the β -domain and C-helix region essential for the formation of amyloid cross- β structure. Elongation of the linker ultimately enhances the compound's ability to prevent this interaction by allowing the BTZ part of the heterodimer to bind more effectively, increasing the compound's binding affinity, and also by greater steric obstruction. This study represents an important contribution to the recent rational design of potential lead small molecules with anti-amyloid properties, and the heterodimers studied are prospective candidates for the treatment of systemic lysozyme amyloidosis and other amyloid-related diseases.

KEYWORDS: Protein aggregation, amyloid, heterodimerization, inhibition, lysozyme, small molecules

INTRODUCTION

After decades of research, protein amyloid aggregation remains one of the biggest challenges for the scientific community because of its association with amyloid-related diseases as well as recently obtained knowledge that protein amyloids also play physiological roles in organisms. Now, it is believed all peptide and polypeptide sequences can adopt the amyloid state under appropriate conditions.¹ Although the precise molecular mechanism of amyloid aggregation *in vivo* is still unknown, there are a lot of factors affecting the propensity of peptides and polypeptides to be transformed from a soluble state into almost insoluble amyloid structures. They include genetic mutations, post-translational modifications, high protein concentration, and the presence of metal ions.² *In vitro* exposure of proteins to amyloid-inducing conditions such as high temperature or protein concentration, pH, and the presence of salts or denaturants results in the formation of

amyloid fibrils with cross- β architecture common to amyloid aggregates formed *in vivo*.

It is generally accepted that the formation and accumulation of amyloid deposits in various tissues can have a toxic effect on different cell types, leading to cell dysfunction. Amyloidosis can represent a serious health problem leading to life-threatening organ failure and finally, death.³ Alzheimer's and Parkinson's diseases, the most common forms of dementia, as well as diabetes mellitus are some of the more than 50 currently known amyloid diseases. Human lysozyme is associated with lysozyme hereditary systemic non-neuropathic amyloidosis. It has been reported that amyloidogenic variants of the human

Received: July 29, 2019

Accepted: February 3, 2020

Published: February 3, 2020

REVIEW ARTICLE

Combining Antimicrobial Peptides with Nanotechnology: An Emerging Field in Theranostics

Sk Abdul Mohid¹ and Anirban Bhunia^{1,*}

¹Department of Biophysics, Bose Institute, P-1/12 CIT Scheme VII (M), Kolkata 700054, India

Abstract: The emergence of multidrug-resistant pathogens and their rapid adaptation against new antibiotics is a major challenge for scientists and medical professionals. Different approaches have been taken to combat this problem, which includes rationally designed potent antimicrobial peptides (AMPs) and several nanoparticles and quantum dots. AMPs are considered as a new generation of super antibiotics that hold enormous potential to fight against bacterial resistance by the rapidly killing planktonic as well as their biofilm form while keeping low toxicity profile against eukaryotic cells. Various nanoparticles and quantum dots have proved their effectiveness against a vast array of infections and diseases. Conjugation and functionalization of nanoparticles with potentially active antimicrobial peptides have added advantages that widen their applications in the field of drug discovery as well as delivery system including imaging and diagnostics. This article reviews the current progress and implementation of different nanoparticles and quantum dots conjugated antimicrobial peptides in terms of bio-stability, drug delivery, and therapeutic applications.

ARTICLE HISTORY

Received: June 13, 2019
Revised: September 11, 2019
Accepted: October 18, 2019

DOI:
10.2174/1389203721666191231111634

Keywords: Antimicrobial peptides (AMPs), Nanoparticles (NPs), Antimicrobial peptide-nanoparticle conjugates, Diagnosis, Drug delivery, Bio-imaging.

1. INTRODUCTION

Human civilization has faced the challenge of several pathogenic microorganisms since its beginning. The effect of infections and the related rate of morbidity or mortality during the pre-antibiotic era was severe when the history witnessed the deadliest epidemic diseases like plague and cholera [1]. However, a major milestone was reached when the famous German scientist Paul Ehrlich hypothesized the concept of 'magic bullet' [2] in 1900 and the first true antibiotic Penicillin was discovered by Alexander Fleming in 1928 [3]. This successfully cured numerous life-threatening infections for decades along with its modified derivatives. Following the 'golden era' of antibiotics [4] from 1950 to 1970, the rapid emergence of multidrug or extensive drug-resistant (MDR and XDR) pathogenic microorganisms started to emerge. Drug-resistant virus, bacteria, fungus, and protozoa continue to be reported regularly against the first-line clinical drugs while the arsenal for new and potent alternatives are very limited [5].

Antimicrobial peptides (AMPs) are gene encoded universal defense systems of all kinds of organisms. AMPs have

various properties and modes of action against microbial cells which is widely reported as a potential alternative against traditional antibiotics [6-8]. These short polypeptides (<50) hold several unique attributes including amphipathicity that plays a crucial role after interacting with microbial membranes while forming different secondary structures like α -helix, β -sheet/strand, loop or turn and extended conformations [9]. The cumulative effects of length, charge, hydrophobicity, and helicity also allow these AMPs to selectively interact with anionic bacterial and zwitterionic mammalian membranes [10]. The principal target of most of the reported AMPs is the membrane of microorganisms. This is because it requires a large amount of energy for a bacterial cell to change bilayer lipid composition and architecture to produce complete resistance [11, 12].

More than 12000 natural and synthetic AMPs are reported to date. However, only few are commercially available in the market for clinical uses [13]. Despite the promising characteristics of AMPs as stated above, there are a few limitations that impeded progress, which includes (i) instability in serum or cells and tissues due to the action of peptidases, [14] (ii) cytotoxicity to some extent [15] and (iii) ineffective drug delivery [16] to internal organs across the basement or endothelial cell membranes. Different approaches like cyclization, incorporation of D- or unusual amino acids, acetylation, amidation, lipidation as well as reducing cationic

*Address correspondence to this author at the Department of Biophysics, Bose Institute, P-1/12 CIT Scheme VII (M), Kolkata 700054, India; Tel: +91-33-2569 3336; E-mails: bhunias@jcbose.ac.in; anirbanbhunia@gmail.com

Comparison of Synthetic Neuronal Model Membrane Mimics in Amyloid Aggregation at Atomic Resolution

Swapna Bera, Nilanjan Gayen, Sk Abdul Mohid, Dipita Bhattacharyya, Janarthanan Krishnamoorthy, Dibakar Sarkar, Jihye Choi, Nirakar saho, Atin K Mandal, DongKuk Lee, and Anirban Bhunia

ACS Chem. Neurosci., **Just Accepted Manuscript** • DOI: 10.1021/acchemneuro.0c00166 • Publication Date (Web): 03 Jun 2020

Downloaded from pubs.acs.org on June 17, 2020

Just Accepted

"Just Accepted" manuscripts have been peer-reviewed and accepted for publication. They are posted online prior to technical editing, formatting for publication and author proofing. The American Chemical Society provides "Just Accepted" as a service to the research community to expedite the dissemination of scientific material as soon as possible after acceptance. "Just Accepted" manuscripts appear in full in PDF format accompanied by an HTML abstract. "Just Accepted" manuscripts have been fully peer reviewed, but should not be considered the official version of record. They are citable by the Digital Object Identifier (DOI®). "Just Accepted" is an optional service offered to authors. Therefore, the "Just Accepted" Web site may not include all articles that will be published in the journal. After a manuscript is technically edited and formatted, it will be removed from the "Just Accepted" Web site and published as an ASAP article. Note that technical editing may introduce minor changes to the manuscript text and/or graphics which could affect content, and all legal disclaimers and ethical guidelines that apply to the journal pertain. ACS cannot be held responsible for errors or consequences arising from the use of information contained in these "Just Accepted" manuscripts.

Nonthermal Atmospheric Plasma-Induced Cellular Envelope Damage of *Staphylococcus aureus* and *Candida albicans* Biofilms: Spectroscopic and Biochemical Investigations

Soumendra Singh¹, Animesh Halder², SK. Abdul Mohid, Damayanti Bagchi, Oindrila Sinha, Amrita Banerjee, Probir Kumar Sarkar, Anirban Bhunia, Sanjay K. Ghosh, Amitabha Mitra, and Samir Kumar Pal³

Abstract—Objective: Nonthermal plasma at atmospheric condition using dielectric barrier discharge (DBD) is reported to be useful in many applications. Here, we have developed a strategy to generate nonthermal atmospheric plasma (NTAP) at ambient conditions for potential biomedical applications. **Methods:** We have explored the active ingredients of the nonthermal plasma using atomic emission spectroscopy. The potential mechanism of the generation of reactive oxygen species (ROS) and reactive nitrogen species (RNS) from the generated plasma for therapeutic use has been demonstrated. Major results: The antimicrobial efficacy of the nonthermal plasma application to model *Staphylococcus aureus* and *Candida albicans* biofilms has been investigated. Our detailed electron microscopic studies followed by biochemical investigation reveal the mechanism of bacterial/fungal deactivation process. The nuclear magnetic resonance (NMR) studies on the live cell of *C. albicans* before and after NTAP treatment clearly conclude the disruption of cellular envelope leading to necrosis as evidenced by fluorescence-assisted

cell sorting (FACS) studies. **Conclusions:** The proposed NTAP setup may find relevance in novel strategies in bacterial and fungal biofilm destruction in the future development of nonfluid hand sanitization.

Index Terms—Antibiofilm effects, cancer therapeutics, dielectric breakdown, nonthermal atmospheric plasma (NTAP), reactive oxygen species (ROS) and reactive nitrogen species (RNS), water electrode.

I. INTRODUCTION

ANTIBIOTICS are the main source of therapy against various microorganisms. However, excessive and uncontrolled use of antibiotics has led to the emergence of various multidrug-resistant strains of microorganisms [1]. Therefore, to find alternatives for existing antibiotics is of paramount importance [2]. Nonthermal atmospheric plasma (NTAP) promises to be a very suitable alternative method of conventional topical medication of a variety of drug-resistant microbial organisms [3]. NTAP in the biological field has various medical applications like sterilization, blood coagulation, bacterial inactivation, and cancer therapy [4]. The essential advantages of NTAP in biomedical applications include selectivity, targeted activity, and minimal damage to the surrounding living tissues of the target area [5]. It is known that NTAP-induced treatment employs reactive oxygen species (ROS) and reactive nitrogen species (RNS) that are formed during the dielectric barrier discharge (DBD) [6] leading to DNA damage of the living target cells including various harmful microbes.

The coappearance of ultraviolet (UV) radiation with NTAP is obvious. The wavelength of radiation depends on the strategy of NTAP generation (the energy content), which includes voltage, power, frequency of operation, and finally, the composition and the concentration of gas used (in case of plasma jet). While a few of the advances in these areas have demonstrated the feasibility of producing UV-C radiation along with the plasma [7], most researchers have demonstrated the availability of UV-B only [8]. The use of the UV light for the inactivation of microorganism is well studied [9], [10]. The effect of UV alone was found to be weak for the purpose, but UV was found to behave as an assistant with NTAP facilitating the plasma for DNA damage [9]. UV-C although is known to have antimicrobial properties [11], it is potentially harmful and can act as a mutating agent for short- and long-term cell

Manuscript received December 11, 2019; revised June 10, 2020; accepted July 3, 2020. This work was supported Indian Council of Medical Research (ICMR) under Grant 5/3/8/247/2014ITR, in part by the Department of Science and Technology-Science and Engineering Research Board (DST-SERB) under Grant EMR/2016/004698, and in part by the Department of Biotechnology (DBT) under Grant BT/PR11534/NNT/28/776/2014. The review of this article was arranged by Senior Editor J. L. Lopez. (Soumendra Singh and SK. Abdul Mohid contributed equally to this work.) (Corresponding author: Samir Kumar Pal.)

Soumendra Singh, and Amrita Banerjee are with the Technical Research Centre, S. N. Bose National Centre for Basic Sciences, Kolkata 700106, India.

Animesh Halder is with the Technical Research Centre, S. N. Bose National Centre for Basic Sciences, Kolkata 700106, India, and also with the Department of Applied Optics and Photonics, University of Calcutta, Kolkata 700106, India.

SK. Abdul Mohid and Anirban Bhunia are with the Department of Biophysics, Bose Institute, Kolkata 700091, India.

Damayanti Bagchi is with the Department of Chemical, Biological and Macromolecular Sciences, S. N. Bose National Centre for Basic Sciences, Kolkata 700106, India.

Oindrila Sinha is with the Department of Life Sciences, Presidency University Kolkata, Kolkata 700073, India.

Probir Kumar Sarkar is with the Department of Physics, Ananda Mohan College, Kolkata 700009, India.

Sanjay K. Ghosh is with the Department of Physics, Bose Institute, Kolkata 700091, India.

Amitabha Mitra is with the Center for Astroparticle Physics and Space Science, Bose Institute, Kolkata 700091, India.

Samir Kumar Pal is with the Department of Chemical Biological and Macromolecular Sciences, S. N. Bose National Centre for Basic Sciences, Kolkata 700106, India, and also with the Technical Research Centre, S. N. Bose National Centre for Basic Sciences, Kolkata 700106, India (e-mail: skpal@bose.res.in).

Color versions of one or more of the figures in this article are available online at <http://ieeexplore.ieee.org>.

Digital Object Identifier 10.1109/TPS.2020.3008282

0093-3813 © 2020 IEEE. Personal use is permitted, but republication/redistribution requires IEEE permission. See <https://www.ieee.org/publications/rights/index.html> for more information.

Special Collection

Effect of Secondary Structure and Side Chain Length of Hydrophobic Amino Acid Residues on the Antimicrobial Activity and Toxicity of 14-Residue-Long de novo AMPs

Gopal Pandit^{+, [a]}, Nabarupa Chowdhury^{+, [b]}, Sk. Abdul Mohid,^[b] Anil P. Bidkar,^[c] Anirban Bhunia,^{*, [b]} and Sunanda Chatterjee^{*, [a]}

Herein we report the efficacy and toxicity of three de novo designed cationic antimicrobial peptides (AMPs) LL-14, VV-14 and $\beta\beta$ -14, where side chains of the hydrophobic amino acids were reduced gradually. The AMPs showed broad-spectrum antimicrobial activity against three pathogens from the ESKAPE group and two fungal strains. This study showed that side chains which are either too long or too short increase toxicity and lower antimicrobial activity, respectively. VV-14 was found to be non-cytotoxic and highly potent under physiological salt concentrations against several pathogens, especially Salmonella

typhi TY2. These AMPs acted via membrane deformation, depolarization, and lysis. The activity of the AMPs is related to their ability to take on amphipathic helical conformations in the presence of microbial membrane mimics. Among AMPs with the same charge, hydrophobic interactions between the side chains of the residues with cell membrane lipids determine their antimicrobial potency and cytotoxicity. Strikingly, an optimum hydrophobic interaction is the crux of generating highly potent non-cytotoxic AMPs.

Introduction

The emergence of multidrug-resistant pathogens and their rapid adaptation against new antibiotics have been a great challenge for scientist and medical professionals lately.^[1–5] Colistin, an antibiotic that is used as the last line of defence against multidrug resistant Gram-negative pathogens, have also started being rendered inefficient by the plasmid mediated dissemination of the *mcr-1* gene.^[6–7] In contrast, the development of new antibiotics is an extremely slow process. The last new class of antibiotic (Daptomycin, a lipopeptide) was introduced in the year 2003.^[8] Different approaches have been explored to combat this alarming situation^[9–14] One of the major remedial approaches involves development of rationally designed potent antimicrobial peptides (AMPs).^[15–18] AMPs are considered as new generation antibiotics that holds huge potentials to fight against bacterial resistance by the rapid

killing of planktonic microbial cells as well as their biofilm form, while keeping a low toxicity profile against eukaryotic cells.^[19–20]

AMPs are present ubiquitously in nature as the first line of defence in several life forms from invertebrates to the plants or mammals.^[21–24] Natural AMPs show broad-spectrum antimicrobial activity against microbes like bacteria, fungi, protozoa and even several classes of pathologically relevant viruses.^[25] AMPs have an additional strength over the conventional antibiotics in having diverse modes of action in contrast to the fixed intracellular targets for antibiotics.^[26–27] This in turn leads to delayed or no development of resistance at all against the microbes, in contrast to the antibiotics. One of the most important mechanism of action of the AMPs involve membranolysis of the microbial membrane,^[28–33] while other mechanisms involve translocation of the AMPs across the cell membrane to work on intracellular targets.^[34] Some AMPs are also known to have an immunomodulatory function on the host systems.^[35] Though several natural AMPs have been isolated, reported and characterised till date, there are only a few that have been studied for their medical applications owing to their high systemic toxicity, less cell selectivity, poor plasma/serum stability and sensitivity towards high salt concentrations.^[36] Additionally, natural AMPs often have long primary sequences, which make them economically expensive and involve folding issues.^[37] To overcome this problem, researchers have developed the synthetic analogs of AMPs.^[38–40]

Cationic amphipathic alpha helical peptides are the most promising, well-characterized and abundant AMPs in nature. Leucine and Lysine residues which have strong helix promoting abilities are often used to design prototype alpha helices, called LK peptides with strong antimicrobial activities. Length of the LK peptides plays a crucial role in their antimicrobial activity and the cytotoxicity.^[41–46] Increasing the length promotes

[a] G. Pandit,* S. Chatterjee
Department of Chemistry
Indian Institute of Technology Guwahati
Guwahati, Assam (India)
E-mail: sunanda.c@iitg.ac.in

[b] N. Chowdhury,* S. Abdul Mohid, A. Bhunia
Department of Biophysics
Bose Institute
Kolkata, West Bengal (India)
E-mail: bhunia@jcbose.ac.in

[c] A. P. Bidkar
Department of Biosciences and Bioengineering
Indian Institute of Technology Guwahati
Guwahati, Assam (India)

[*] These authors contributed equally to this work.

Supporting information for this article is available on the WWW under <https://doi.org/10.1002/cmdc.202000550>

This article belongs to the Special Collection "MedChem in India"



Contents lists available at ScienceDirect

European Journal of Medicinal Chemistry

journal homepage: <http://www.elsevier.com/locate/ejmech>

Synthesis and antibacterial study of cell-penetrating peptide conjugated trifluoroacetyl and thioacetyl lysine modified peptides



Kamal D. Patel ^a, Sk Abdul Mohid ^b, Arkajyoti Dutta ^c, Shalini Arichthota ^d,
Anirban Bhunia ^b, Devyani Haldar ^d, Vijayalekshmi Sarojini ^{a, e, *}

^a School of Chemical Sciences, The University of Auckland, Private Bag 92019, Auckland, 1142, New Zealand

^b Department of Biophysics, Bose Institute, P-1/12 CIT Scheme VII (M), Kolkata, 700054, India

^c Department of Chemistry, Bose Institute, 93/1, APC Road, Kolkata, 700009, India

^d Laboratory of Chromatin Biology and Epigenetics Centre for DNA Fingerprinting and Diagnostics, Inner Ring Road, Uppal, Hyderabad, 500039, India

^e The MacDiarmid Institute for Advanced Materials and Nanotechnology, Wellington, 6140, New Zealand

ARTICLE INFO

Article history:

Received 22 January 2021

Received in revised form

18 March 2021

Accepted 1 April 2021

Available online 20 April 2021

Keywords:

Drug delivery

Antimicrobial peptide

Transcription

Biofilm

NMR

Calcein leakage assay

ABSTRACT

Substrate-based sirtuin inhibitors target bacterial genome and RNA and provide a promising approach to address bacterial resistance issues, if cellular internalisation can be achieved. We designed *N*-trifluoroacetyl lysine and *N*-thioacetyl lysine peptides (**KP 13**, **KP 15** and **KP 24**) as inhibitors of bacterial sirtuins and their cell-penetrating peptide conjugates **Tat KP 13**, **Tat KP 15** and **Tat KP 24**. The conjugated peptides were successfully internalised and showed signs of bacterial transcription inhibition resulting in enhanced antibacterial potency against model Gram negative and Gram positive pathogens. Synergistic activity in combination with streptomycin and polymyxin B has also been established. These peptides were effective in inhibiting biofilm formation and eradicating preformed biofilms. Morphological analysis using both SEM and TEM showed bacterial membrane disruption. Calcein dye leakage analysis established the selectivity of these peptides to bacterial membranes. This study documents the first report of the application of substrate-based sirtuin inhibitors as antimicrobial therapeutics.

© 2021 Published by Elsevier Masson SAS.

1. Introduction

Antimicrobial peptides (AMPs), also known as host defence peptides (HDPs) hold a prominent place as current and future broad-spectrum antibiotics in light of the emergence of multidrug resistance of pathogens towards conventional antibiotics [1]. The potential of AMPs to tackle infections caused by Gram-positive and Gram-negative bacteria, viruses and fungal pathogens has been reported in the literature [2]. AMPs act either by forming pores in the membranes, causing membrane lysis or by acting on intracellular targets like enzymes or nucleic acids [3,4]. Peptide antibiotics vancomycin and polymyxin B are used against infections caused by multidrug resistant pathogens as the last line of defence [2,5]. While emergence of resistance against peptide antibiotics by microbes is rare, it cannot be completely ruled out [6]. Innovative research ideas can help develop new AMPs which act on novel

targets that could also help address bacterial resistance issues.




Histone deacetylases (HDACs) identified in eukaryotes are broadly classified into four classes. Classes 1, 2, and 4 are called zinc-dependent HDACs. Class 3 also called as sirtuins (Sirt1-Sirt7) are NAD⁺ dependent enzymes. The intracellular target of these enzymes are histone proteins [7,8]. These positively charged proteins play a role in imparting compactness and rigidity to negatively charged DNA. The negatively charged DNA wraps around histone proteins resulting in transcription silencing. Acetylation of the lysine residues by histone acetyltransferases (HATs) neutralise the positively charged histone proteins and thus results in the unwrapping of DNA from histone resulting in chromatin and gene transcription activation. HDACs catalyse the reverse reaction instigated by HATs, removal of acetate from histones, increasing the overall positive charge of histones and reinstating their interactions with DNA, thereby arresting transcription and cell division [9,10].

Sirtuins are HDACs that regulate metabolic homeostasis, genomic integrity and longevity and are highly conserved among various forms of life. Thus, substrate-based sirtuin inhibitors hold promise as potential anti-bacterial agents with the potential to

* Corresponding author. School of Chemical Sciences, The University of Auckland, Private Bag 92019, Auckland, 1142, New Zealand.
E-mail address: v.sarojini@auckland.ac.nz (V. Sarojini).

Review

Atomic-Resolution Structures and Mode of Action of Clinically Relevant Antimicrobial Peptides

 Surajit Bhattacharjya ^{1,*} , Sk Abdul Mohid ²  and Anirban Bhunia ² 
¹ School of Biological Sciences, 60 Nanyang Drive, Nanyang Technological University, Singapore 637551, Singapore

² Department of Biophysics, Bose Institute, Unified Academic Campus, Saltlake, Sector V, EN 80, Kolkata 700091, India; skabdulmohid1992@gmail.com (S.A.M.); anirbanbhunia@gmail.com (A.B.)

* Correspondence: surajit@ntu.edu.sg

Abstract: Global rise of infections and deaths caused by drug-resistant bacterial pathogens are among the unmet medical needs. In an age of drying pipeline of novel antibiotics to treat bacterial infections, antimicrobial peptides (AMPs) are proven to be valid therapeutics modalities. Direct in vivo applications of many AMPs could be challenging; however, works are demonstrating encouraging results for some of them. In this review article, we discussed 3-D structures of potent AMPs e.g., polymyxin, thanatin, MSL, protegrin, OMP1A in complex with bacterial targets and their mode of actions. Studies on human peptide LL37 and de novo-designed peptides are also discussed. We have focused on AMPs which are effective against drug-resistant Gram-negative bacteria. Since treatment options for the infections caused by super bugs of Gram-negative bacteria are now extremely limited. We also summarize some of the pertinent challenges in the field of clinical trials of AMPs.

Keywords: antibiotics; multidrug resistant (MDR) bacteria; MDR Gram negative bacteria; antimicrobial peptides (AMPs); lipopolysaccharide (LPS); mechanism of AMPs



Citation: Bhattacharjya, S.; Mohid, S.A.; Bhunia, A. Atomic-Resolution Structures and Mode of Action of Clinically Relevant Antimicrobial Peptides. *Int. J. Mol. Sci.* **2022**, *23*, 4558. <https://doi.org/10.3390/ijms23094558>

Academic Editors: Ian A. Nicholls and Vladimir N. Uversky

Received: 15 March 2022

Accepted: 18 April 2022

Published: 20 April 2022

Publisher's Note: MDPI stays neutral with regard to jurisdictional claims in published maps and institutional affiliations.



Copyright: © 2022 by the authors. Licensee MDPI, Basel, Switzerland. This article is an open access article distributed under the terms and conditions of the Creative Commons Attribution (CC BY) license (<https://creativecommons.org/licenses/by/4.0/>).

1. Introduction

At present, antibiotics are the major drugs administered to eliminate infectious diseases caused by bacteria and other microbes. However, our dependence on the frontline antibiotics has now been challenged by the steady rise of bacterial antimicrobial resistance (AMR) problems. Although, the emergence of antibiotic resistance pathogens is a natural phenomenon [1–3]. Penicillinase, a bacterial enzyme that hydrolyzes penicillin antibiotic, was identified even before the therapeutic approval of penicillin [1–3]. Notably, resistant bacterial strains could be isolated within few years of the introduction of an antibiotic, for example the first methicillin resistant *S. aureus* (MRSA) was detected in 1961 only two years after methicillin was introduced [1–3]. Overuse and misuse of antibiotics over the decades have now been escalated to the occurrence of drug resistant, multi-drug-resistant (MDR) and extremely drug-resistant (XDR) bacterial pathogens. Bacterial AMR has been recognized as one of the major health issues of this century. Commissioned by the UK government, the O'Neill report made a thorough analysis of AMR and provided an estimate of 10 million deaths/year by 2050 [4]. In 2019, Centers for disease control and prevention (CDC) of USA indicated 2.8 million of antibiotic-resistant infections resulting in 35,000 annual deaths [5]. A very recent comprehensive analyses on the global burden of bacterial antimicrobial resistance in 2019 has reported 4.95 million deaths associated with bacterial AMR including 1.27 million more deaths attributable to bacterial AMR [6]. The six leading bacterial pathogens *Escherichia coli*, *Staphylococcus aureus*, *Klebsiella pneumoniae*, *Streptococcus pneumoniae*, *Acinetobacter baumannii*, and *Pseudomonas aeruginosa* have caused 929,000 deaths attributable to AMR and 3.57 million fatalities associated with AMR in 2019 [6]. In addition, AMR-associated deaths are found to be prevalent due to infections caused by six other pathogens namely *Mycobacterium tuberculosis*, *Enterococcus faecium*,



Contents lists available at ScienceDirect

BBA - Biomembranes

journal homepage: www.elsevier.com/locate/bbamem

Structural insights into the interaction of antifungal peptides and ergosterol containing fungal membrane

Sk Abdul Mohid^{a,1}, Karishma Biswas^{a,1}, TaeJun Won^b, Lakshmi S. Mallela^c, Arin Guichait^d, Lena Butzke^e, Riddhiman Sarkar^f, Timothy Barkham^g, Bernd Reif^f, Enrico Leipold^e, Sanhita Roy^c, Anup K. Misra^d, Rajamani Lakshminarayanan^h, DongKuk Lee^{b,*}, Anirban Bhunia^{a,*}

^a Department of Biophysics, Bose Institute, Unified Academic Campus, Salt Lake, EN 80, Sector V, Kolkata 700091, India

^b Department of Fine Chemistry, Seoul National University of Science and Technology, Seoul 01811, Republic of Korea

^c Prof. Brien Holden Eye Research Centre, LV Prasad Eye Institute, Hyderabad 500034, India

^d Division of Molecular Medicine, Bose Institute, Unified Academic Campus, Salt Lake, EN 80, Sector V, Kolkata 700091, India

^e Department of Anesthesiology and Intensive Care & Center of Brain, Behavior and Metabolism, University of Lübeck, Ratzeburger Allee 160, 23562 Lübeck, Germany

^f Technical University of Munich, 85748 Garching, Germany

^g Department of Laboratory Medicine, Tan Tock Seng Hospital, 11 Jalan Tan Tock Seng, Singapore

^h Singapore Eye Research Institute, 20 College Road, Discovery Tower Level 6, 169856, Singapore

ARTICLE INFO

Keywords:

Antimicrobial peptide
Sterols
Nuclear magnetic resonance
Candida albicans

ABSTRACT

The treatment of invasive drug-resistant and potentially life-threatening fungal infections is limited to few therapeutic options that are usually associated with severe side effects. The development of new effective antimicrobials with a more tolerable side effect profile is therefore of utmost clinical importance. Here, we used a combination of complementary *in vitro* assays and structural analytical methods to analyze the interaction of the *de novo* antimicrobial peptide VG16KRKP with the sterol moieties of biological cell membranes. We demonstrate that VG16KRKP disturbs the structural integrity of fungal membranes both *in vitro* and in model membrane system containing ergosterol along with phosphatidylethanolamine lipid and exhibits broad-spectrum antifungal activity. As revealed by systematic structure-function analysis of mutated VG16KRKP analogs, a specific pattern of basic and hydrophobic amino acid side chains in the primary peptide sequence determines the selectivity of VG16KRKP for fungal specific membranes.

1. Introduction

Membrane-active antimicrobial peptides (AMPs), which selectively disrupt the structural integrity of microbial membranes, are considered a new generation of antibiotics to combat multidrug-resistant pathogenic fungi [1–3]. A precise understanding of the interaction between membrane-active drugs with the components of biomembranes is a prerequisite to unravel their molecular mechanisms on one hand and to optimise their target specificity and thus reduce potential side effects on the other [4]. In a bilayer structure, membrane-active medicines or toxins may target the membrane lipids directly [5]. Naturally occurring and *de novo* designed AMPs are predominantly cationic, but also contain hydrophobic residues [6]. Hence, they interact via electrostatic and

hydrophobic interactions with negatively charged lipid headgroups and the hydrophobic acyl chains of their target membranes, respectively [7–10].

Microbial membranes are inherently anionic in composition and spatial geometry, making them structurally and functionally distinct from the host membranes [11–13]. On the other hand, fungal and mammalian cells share a similar membrane surface chemistry, which complicates the development of effective membrane-targeted antimicrobial therapeutics [12,13]. The need to develop new antimicrobial therapeutics is particularly evident in the global increase in antibiotic-resistant fungal infections. Apart from this, most antifungals available today show only limited target specificity and thus are associated with severe systemic toxicity in humans, which is observed especially in deep

* Corresponding author.

E-mail addresses: dongkuk@snut.ac.kr (D. Lee), bhunias@jcbiose.ac.in (A. Bhunia).

¹ Both authors contributed equally.

<https://doi.org/10.1016/j.bbamem.2022.183996>

Received 24 January 2022; Received in revised form 9 June 2022; Accepted 13 June 2022

Available online 23 June 2022

0005-2736/© 2022 Elsevier B.V. All rights reserved.



A rationally designed synthetic antimicrobial peptide against *Pseudomonas*-associated corneal keratitis: Structure-function correlation

Sk Abdul Mohid^a, Prerana Sharma^b, Amani Alghalayini^c, Tripti Saini^d, Debarun Datta^{e,f}, Mark D.P. Willcox^e, Haydar Ali^g, Sreyan Raha^h, Achintya Singha^h, DongKuk Leeⁱ, Nirakar Sahoo^d, Charles G. Cranfield^c, Sanhita Roy^b, Anirban Bhunia^{a,*}

^a Department of Biophysics, Bose Institute, EN 80, Sector V, Bidhan Nagar, Kolkata 700091, India

^b Prof Brien Holden Eye Research Centre, L V Prasad Eye Institute, Hyderabad-500034, India

^c School of Life Science, University of Technology Sydney, Ultimo, NSW 2007, Australia

^d Department of Biology, The University of Texas Rio Grande Valley, Edinburg, TX 78539, USA

^e School of Optometry and Vision Science, University of New South Wales, Sydney, Australia

^f Optometry and Vision Science Research Group, Aston University, UK

^g Indian Association for the Cultivation of Science, Jadavpur, Kolkata 700032, India

^h Department of Physics, Bose Institute, Kolkata 700009, India

ⁱ Seoul National University of Science and Technology, Seoul 01811, Republic of Korea

ARTICLE INFO

Keywords:

Contact lens
Bacterial keratitis
Antimicrobial peptide (AMP)
Nuclear magnetic resonance (NMR)
Pseudomonas aeruginosa

ABSTRACT

Contact lens wearers are at an increased risk of developing *Pseudomonas*-associated corneal keratitis, which can lead to a host of serious ocular complications. Despite the use of topical antibiotics, ocular infections remain a major clinical problem, and a strategy to avoid *Pseudomonas*-associated microbial keratitis is urgently required. The hybrid peptide VR18 (VARGWGRKCPLFGKNKSR) was designed to have enhanced antimicrobial properties in the fight against *Pseudomonas*-induced microbial keratitis, including contact lens-related keratitis. In this paper, VR18's modes of action against *Pseudomonas* membranes were shown by live cell Raman spectroscopy, live cell NMR, live-cell fluorescence microscopy and measures taken using sparsely tethered bilayer lipid membrane bacterial models to be via a bacterial-specific membrane disruption mechanism. The high affinity and selectivity of the peptide were then demonstrated using *in vivo*, *in vitro* and *ex vivo* models of *Pseudomonas* infection. The extensive data presented in this work suggests that topical employment of the VR18 peptide would be a potent therapeutic agent for the prevention or remedy of *Pseudomonas*-associated microbial keratitis.

1. Introduction

Corneal opacity is the fifth leading cause of blindness globally, accounting for ~3.2% of all cases [1,2]. The recent World Health Organisation (WHO) report highlighted that ~6 million of the world's population are affected by cornea-related blindness or moderate/severe visual impairment, including 2 million of those who are affected by

trachoma [3]. Infectious keratitis is considered a "silent epidemic" in the western world, with an annual incidence on the order of 25,000–30,000 in the US alone [4]. Being more abundant in developing countries, infectious keratitis has been designated as a "neglected tropical disease". To date, antibiotics like vancomycin, tobramycin and amphotericin B (AmB) are the best choices for treating microbial keratitis [5]. These drugs, however, are toxic to mammalian cells and cause membrane

Abbreviations: AMP, Antimicrobial peptide; NMR, Nuclear magnetic resonance; LPS, Lipopolysaccharides; PI, Propidium iodide; ROS, Reactive oxygen species; OD, Optical density; NOE, Nuclear Overhauser effect; TOCSY, Total correlation spectroscopy; NOESY, Nuclear Overhauser effect spectroscopy; *tr*NOESY, transferred Nuclear Overhauser effect spectroscopy; ALS, asymmetric least squares; LUV, Large unilamellar vesicle; GUV, Giant unilamellar vesicle; ITC, Isothermal titration calorimetry; MIC_{99%}, Minimal inhibitory concentration for 99% killing; HSQC, heteronuclear single quantum correlation; HCEC, Human corneal epithelial cells; MTT, (3-(4,5-Dimethylthiazol-2-yl)-2,5-Diphenyltetrazolium Bromide); POPE, 1-palmitoyl-2-oleoyl-sn-glycero-3-phosphoethanolamine; POPG, 1-palmitoyl-2-oleoyl-sn-glycero-3-phospho-(1-*rac*-glycerol); CHAPSO, 3-[(3-cholamidopropyl)dimethylammonio]-2-hydroxy-1-propanesulfonic acid; TSP, 3-(trimethylsilyl)propionic-2,2,3,3-*d4* acid sodium salt; CFU, Colony forming unit.

* Corresponding author.

E-mail address: bhunia@jcbose.ac.in (A. Bhunia).

<https://doi.org/10.1016/j.bpc.2022.106802>

Received 28 January 2022; Received in revised form 10 March 2022; Accepted 15 March 2022

Available online 22 March 2022

0301-4622/© 2022 Elsevier B.V. All rights reserved.